MECHANICAL AND FAILURE PROPERTIES OF RIGID POLYURETHANE FOAM UNDER TENSION

MUHAMMAD RIDHA

NATIONAL UNIVERSITY OF SINGAPORE
2007

MECHANICAL AND FAILURE PROPERTIES OF RIGID POLYURETHANE FOAM UNDER TENSION

MUHAMMAD RIDHA
(S.T., ITB)

A THESIS SUBMITTED FOR THE DEGREE OF DOCTOR OF PHILOSOPHY

DEPARTMENT ON MECHANICAL ENGINEERING
NATIONAL UNIVERSITY OF SINGAPORE

Acknowledgements

Table of contents

Summary

Solid foams have certain properties that cannot be elicited from many homogeneous solids; these include a low stiffness, low thermal conductivity, high compressibility at a constant load and adjustability of strength, stiffness and density. These properties have made solid foams useful for various applications, such as cushioning, thermal insulation, impact absorption and in lightweight structures. The employment of solid foams for load-bearing applications has motivated studies into their mechanical properties and this has involved experiments as well as theoretical modelling. However, many aspects of foam behaviour still remain to be fully understood.

This investigation is directed at identifying the mechanical properties of anisotropic rigid polyurethane foam and its response to tensile loading, as well as developing a simplified cell model that can describe its behaviour. The investigation encompasses experimental tests, visual observation of foam cells and their deformation and development of an idealized cell model. Three rigid polyurethane foams of different density are fabricated and subjected to tension in various directions. Quasi-static tensile tests are performed on an Instron$^{®}$ universal testing machine, while dynamic tension is applied using a split Hopkinson bar arrangement. The results show that the stiffness and tensile strength increase with density, but decrease with angle between the line of load application and the foam rise direction. Dynamic tensile test data indicates that for the rates of deformation imposed, the foam is not rate sensitive in terms of the stiffness and strength.

Observations are made using micro-CT scanning and optical microscopy to examine the internal structure of the rigid polyurethane and its behaviour under compressive and tensile loads. Micro-CT images of cells in the foam indicate that the

cells exhibit a good degree of resemblance with an elongated tetrakaidecahedron. Images of the cell struts show that their cross-sections are similar to that of a Plateau border [1], while microscopic examination of rigid polyurethane foam samples under tensile and compressive loading shows that cell struts are both bent and axially deformed, with bending being the main deformation mechanism. The images also reveal that strut segments immediately adjoining the cell vertices do not flex during deformation because they have a larger cross-section there and are constrained by the greater thickness of the cell wall membrane in that vicinity. With regard to fracture, the images show that fracture in foam occurs by crack propagation through struts and membranes perpendicular to the direction of loading.

Idealized foam cell models based on elongated rhombic dodecahedron and elongated tetrakaidecahedron cells are proposed and analysed to determine their load and deformation properties – elastic stiffness, Poisson's ratio, and tensile strength. A parametric study carried out by varying the values of structural parameters indicates that:

- The elastic stiffness and strength of foam are not influenced by cell size; they are governed by density, geometric anisotropy of the cells, shape of the cells and their struts, as well as the length of the rigid strut segments.

- Foam strength and stiffness increase with density but decreases with angle between the loading and foam rise directions.

- The anisotropic stiffness and strength ratios increase with greater anisotropy in cell geometry.

- The Poisson's ratios are primarily determined by the geometric anisotropy of the cells.

A comparison between the cell models with cells in actual foams indicates that the tetrakaidecahedron has a greater geometric resemblance with cells in actual foam compared to the rhombic dodecahedron. Moreover, good correlation between the tetrakaidecahedron cell model and actual foam in terms of elastic stiffness was observed.

Finite element simulations are undertaken to examine the behaviour of foam based on the tetrakaidecahedron cell model for cases that were not amenable to analytical solution – i.e. tensile loading in various directions and nonlinearity in cell strut material properties. The simulations show that although thin membranes in foams do not have much effect on the stiffness, they affect the fracture properties by influencing the direction of crack propagation. A comparison between foam properties predicted by the model and those of actual foam shows that they correlate reasonably well in terms of stiffness and the anisotropy ratio for tensile strength. FEM simulations are also performed to examine the influence of variations in cell geometry on the mechanical properties. The results show that the variations incorporated do not have much effect on the overall stiffness, but decrease the predicted tensile strength.

In essence, this study provides greater insight into the mechanical properties of rigid polyurethane foam and the mechanisms governing its deformation and failure. The proposed idealized cell models also constitute useful approaches to account for specific properties of foam.

List of figures

List of tables

List of symbols

A area of strut cross-section

A_y area corresponding to load in the y-direction

A_z area corresponding to load in the z-direction

A_b area of bar cross-section

A_s area of specimen cross-section

C_1 constant relating second moment of area to the area of the strut cross-section

C_2 constant relating distance from centroid to the extremities and the area of the strut cross-section

C_3 constant relating the length of the rigid strut segment to the distance from centroid to the extremities of the strut cross-section

C_f constant relating the mechanical properties to the density of foam

d length of rigid strut segment

E_b stiffness of bar

E_f overall stiffness of foam

E_s stiffness of solid cell strut material

E_{yy} overall foam stiffness in the y-direction

E_{zz} overall foam stiffness in the z-direction

F_y load in the y-direction

F_z load in the z-direction

I second moment of area of the strut cross-section

L length of strut in the tetrakaidecahedron cell

$\hat{L}$	length of strut in the rhombic dodecahedron cell
P_f	mechanical property of foam
P_s	mechanical property of solid material
R	distance from centroid to the extremities of the strut cross-section
$\overline{R}$	average distance from the centroid to the extremities of the strut cross-section
r	radius of a circle inscribed within a Plateau border
α	angle between a strut and the xy-plane
β	angle between a strut and the xz-plane
δ_x	deformation in the x-direction
δ_y	deformation in the y-direction
δ_z	deformation in the z-direction
$\varepsilon_{pl\,max}$	plastic strain at fracture of solid material
ε_{xx}	normal strain in the x-direction
ε_{yy}	normal strain in the y-direction
ε_{zz}	normal strain in the z-direction
θ	angle defining cell geometric anisotropy ratio
ρ	overall density of foam
ρ_s	density of solid material
$\sigma_{max\,f}$	tensile strength of foam
$\sigma_{max\,s}$	tensile strength of solid material in cells
σ_{yy}	normal stress in the y-direction

$\sigma_{y\,max}$	tensile strength in the y-direction
σ_{zz}	normal stress in the z-direction
$\sigma_{z\,max}$	tensile strength in the z-direction
υ_{yx}	Poisson's ratio of strain in the x-direction arising from normal stress in the y-direction
υ_{yz}	Poisson's ratio of strain in the z-direction arising from normal stress in the y-direction
υ_{zx}	Poisson's ratio of strain in the x-direction arising from normal stress in the z-direction
υ_{zy}	Poisson's ratio of strain in the y-direction arising from normal stress in the z-direction
u_n	displacement in the normal direction
u_t	displacement in the transverse direction
x_{flex}	length of the flexible segment of an inclined struts projected onto the x axes
X_1	fraction of strut that is flexible
X_2	fraction of strut that is rigid
y_{flex}	length of the flexible segment of an inclined struts projected onto the y axes
z_{flex}	length of the flexible segment of an inclined struts projected onto the z axes

Chapter 1   Introduction

A cellular material is defined as "one which is made of an interconnected network of solid struts or plates which form edges and faces of cells" [2]. Cellular materials can be natural occurring as well as man-made. They have been used in many engineering applications, e.g., sandwich structures, kinetic energy absorbers, heat insulators, etc. Man-made cellular materials generally come in two forms – solid foams with some variations in cell geometry and structures with regular cells such as honeycombs. Solid foams are cellular materials with a three-dimensional structural arrangement, while honeycombs essentially posses a two-dimensional pattern. Solid foams made from metals or polymers have been used in structural applications and kinetic energy absorptions devices, whereby they are subject to static and dynamic loads. Hence, the mechanical behaviour of foams under different rates of loading, as well as their failure properties, must be considered in engineering designs that incorporate their usage. Although numerous investigations on foams have been performed, their mechanical behaviour, especially with regard to failure, is still not fully understood. This motivates continued research with regard to these aspects.

1.1   Properties of solid foam and its applications

Solid foams possess certain unique properties that are different from those of homogeneous solid materials. Some of these properties and how they facilitate application are:

- Relatively low stiffness – Low stiffness foams made from elastic polymers are useful in cushioning applications such as bedding and seats.

- Low thermal conductivity – Non metallic foams are useful for thermal insulation, which are employed in applications ranging from lagging of industrial pipes to encapsulating frozen food.

- High compressibility at a constant load – Foams can be compressed to a relatively high strain under an approximately constant load. This makes them very useful for impact absorption because they can dissipate significant kinetic energy while limiting the magnitude of the force transferred to more fragile components that they shield. Hence, they are used in the packaging of electronic products and in car bumpers.

- Adjustable strength, stiffness and weight – The strength, stiffness and weight of foams depend on their density, which can be varied. Hence, the mechanical properties of foams can be controlled, making them attractive in structural application requiring particular strength or stiffness to weight ratios – e.g., composite structures used in aircraft.

The use of foams in kinetic energy absorption and structural applications, whereby they are subjected to static and dynamic loading, motivates the need to study their mechanical properties. Various approaches have been employed and these are briefly discussed in the following section.

1.2   Studies on mechanical behaviour

The mechanical behaviour of foam has been studied and analysed using several approaches. These include experimentation, analysis based on simplified cell models and development of constitutive relationships. Experiments involving three-dimensional mechanical tests have been performed by several researchers [3-10]. These yielded results in the form of empirical failure criteria of the foam. The failure criteria do not seem to agree with each other, and different researchers have defined

their failure criteria based on different types of stress. Experimental investigations have contributed significantly to understanding the mechanical behaviour of foam; however, they have not yielded much information on the micromechanics involved in the deformation and failure of foam material.

A number of researchers [2, 8, 11-46] have proposed simplified cell models for foam. They used these to predict mechanical properties such as stiffness, Poisson's ratio, failure criteria, etc. This approach is useful in describing some of the micromechanics involved in the deformation and failure of foam. However, most models involve some empirical constants that need to be determined from experiments and hence they do not give direct relationship between the properties of the cells – e.g. the overall foam density, the mechanical properties of the material the struts and membranes are made from, cell geometry and strut cross-section – with the overall mechanical properties of actual foam. Some of the models proposed are also not realistic because of several reasons – e.g. the models cannot fill space in three dimensions (i.e. they cannot be arranged to form large cell assemblies) and the cells do not resemble those in actual foams. Moreover, most of these cell models are isotropic and hence cannot be used to describe anisotropic foam behaviour, which often results from the manufacturing process.

Constitutive models for foams have been developed and analysed by several researchers [3, 47-51]. Some of them have also been implemented in finite element codes such as ABAQUS and LS-DYNA. These models seem to differ from one another because they are developed based on different types of stress and strain – e.g. Miller [50] used the von Mises stress and mean stress with a hardening model defined by a function of the volumetric and plastic strains; Deshpande and Fleck [3] on the other hand, used their own definitions of equivalent stress and strain based on a von

Mises criterion combined with a volumetric energy criterion. Hanssen et al. [49], who have examined several constitutive models and compared them with experiments on aluminium foam, suggested that these models are inaccurate because they do not consider local and global fracture for shear and tension.

1.3 Objectives

The extensive use of foam in many engineering applications, especially for kinetic energy absorption and in advanced structures, has motivated the study of their mechanical behaviour. Although many such investigations have been undertaken, various aspects of the mechanical behaviour of foam have yet to be fully understood, especially with regard to its response and failure under tension. Researchers have proposed constitutive models based on experimental results, cell model analysis, or combinations of both. However, these models do not seem to agree with one another particularly with regard to the types of stress and strain used to define the constitutive relationship. Moreover, a study by Hansenn et al. [49] shows that some of the models which have been implemented in finite element packages cannot represent actual foam, mainly because the models do not include fracture criteria for tension and shear. Simplified cell models have also been proposed, analysed and compared with actual foam; however, they do not seem to be able to fully represent and explain the mechanical behaviour observed. Moreover, the simplified cell models have limitations, such as the dependence on empirical constants, lack of geometrical realism, and current applicability only to isotropic foam.

Experimental studies and development of idealized cell models for solid foam have their particular distinctive advantages. Experimental studies provide good insight into the mechanical behaviour of foam but they are not able to explain the micromechanics behind its behaviour. On the other hand, idealized cell models are

able to explain the micromechanics. Thus, a study that combines both is expected to give a fuller insight into foam behaviour.

Consequently, this study aims to provide an understanding of several aspects that appear to be lacking in information; these include:

- the mechanical properties of rigid polyurethane foam under static and dynamic tension

- microscopic features of the rigid polyurethane foam, such as the size and geometry of constituent cells and cell struts, as well as stiffness and tensile strength of the struts

- micromechanics of the deformation and fracture of cells within foam subjected to tension, as revealed by microscopic observations

- development of a simplified cell geometry that can model the behaviour of rigid polyurethane foam under tension and which directly relates the overall mechanical properties of rigid polyurethane foam with the mechanical behaviour of the constituent cells

This study combines experimental testing, visual observation of cell deformation, and development of an idealized cell model. The information generated will help facilitate future development of constitutive models for foam. The focus includes an understanding of how rigid polyurethane responds to tension and the development of an idealized cell model. It is envisaged that the results of this study and the cell model proposed can be applied to investigation of other types of foam and loading.

The following chapter provides an overview of the basic mechanical properties of foam, aspects that influence their behaviour and other studies that have been conducted on the properties of foam.

Chapter 2 Literature review

2.1 Microstructure of polymer foam

Solid foams comprise cells with solid material defining their edges, and membrane walls in some cases (see Fig. 2.1). Foams that have membrane cell walls are considered closed cell foams (see Fig. 2.1(a)) while foams that do not have such membrane are called open cell foams (see Fig. 2.1(b)). Due to its structure, closed cell foams can have liquid or gas trapped inside it cells while open cell foam does not.
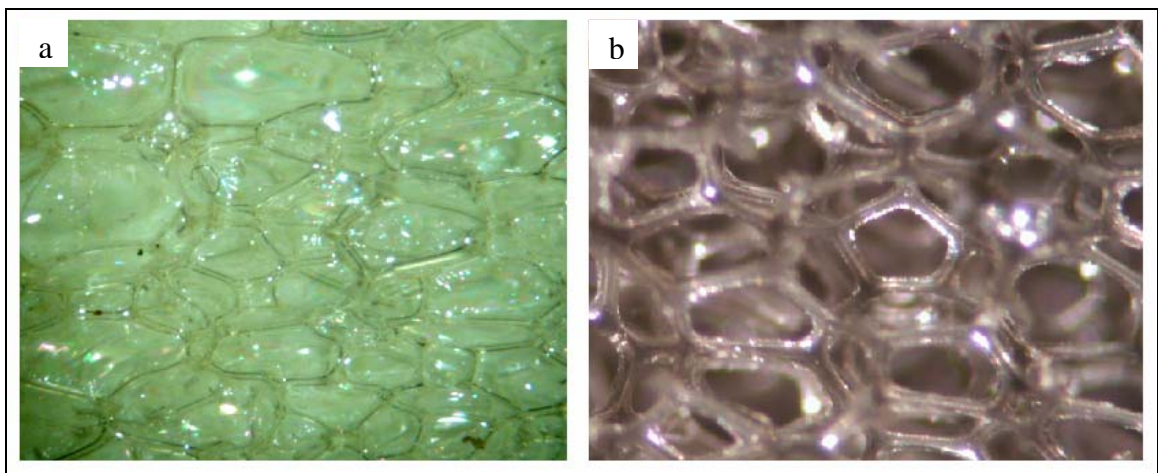
Fig. 2.1 (a) Close cell foam and (b) open cell foam

Fig. 2.1 shows that the dimensions and shapes of cells in foams vary even within a small area. This is because it is not possible to control the foaming process to produce uniform cells. Thermosetting polymeric foams are made by introducing a gassing agent to a mixture of polymer resin and hardener. This results in foaming process whereby the mixture expands and rises as the result of cell/bubble formation. This process produces foam cells that are elongated in the foam rise direction. Other processing parameters such as gravity [49] can also causes cells that have larger or smaller dimensions in certain directions. Cells with larger or smaller dimensions in one direction give rise to anisotropy in foam properties, such as a higher stiffness and strength in the direction of elongation.

2.2 Basic mechanical properties of solid foam

2.2.1 Compression

The mechanical behaviour of solid foam under compressive loading is probably the primary property that distinguishes it from non-cellular solids. Typical stress-strain curves for solid foams made from three different kinds of solid material – elastomeric foam, elastic-plastic foam and elastic-brittle foam – are shown in Fig. 2.2. They all have similar characteristics i.e. linear elasticity at low stresses, followed by an extended plateau terminating in a regime of densification, whereby the stress rises steeply. These characteristics are different from those of common solid materials such as metals, which normally do not have an extended stress-strain plateau under compression.
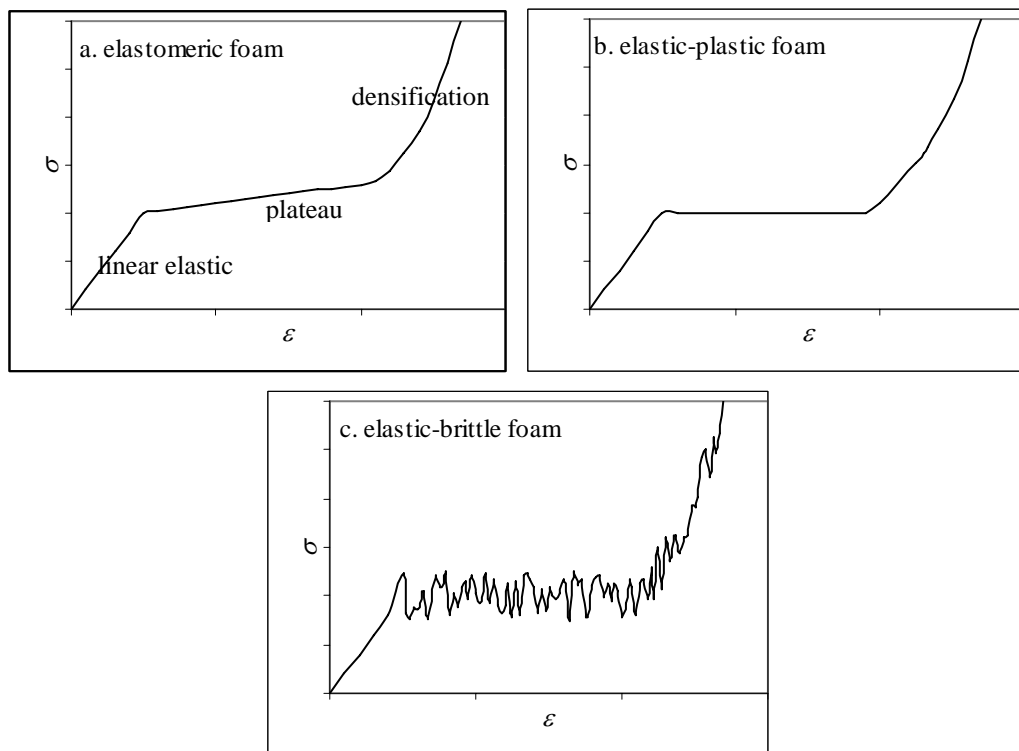
Fig. 2.2 Stress-strain relationships for foams under compression

In all the three types of solid foam, initial linear elasticity arises primarily from the bending of cell struts, and in closed cell foams, stretching of the membranes in the cell walls and changes in fluid pressure inside the cells [2]. On the other hand,

the mechanisms corresponding to the stress-strain plateau are different for the three types of foam – elastic buckling for elastomeric foams, formation of plastic hinges in elastic-plastic foams and brittle crushing in elastic-brittle foams [2].

The long plateau in the compressive stress-strain curve endows foams with a very high compressibility and enables them to exert a relatively constant stress up to a very high strain. These two characteristics make foam an ideal material for cushioning purposes because the low and constant stress contribute to comfort and for crash protection (e.g. in helmets), because the foam is able to absorb kinetic energy while limiting the stress transmitted to relatively low levels.

2.2.2 Tension

Typical stress-strain curves for three kinds of solid foam, i.e. elastomeric foam, elastic-plastic foam and elastic-brittle foam are shown in Fig. 2.3. At low strains, all the foams exhibit linear elasticity, similar to their compressive behaviour [2]. On the other hand, at higher strains, different deformation mechanisms occur in the three types of foam, causing differences in the shapes of their stress-strain curves. An increase in the modulus is experienced by elastomeric foams because of cell struts/wall re-alignment, whereby the deformation mechanism changes from bending to tension in cell struts. On the other hand, plastic yielding occurs in elastic-plastic foams, creating a short plateau in the stress-strain curve followed by a rapid increase of stress due to cell wall re-alignment. For brittle foams, their stress strain curves do not show any non-linearity, as brittle fracture occurs immediately at the end of the linear elasticity. [2]
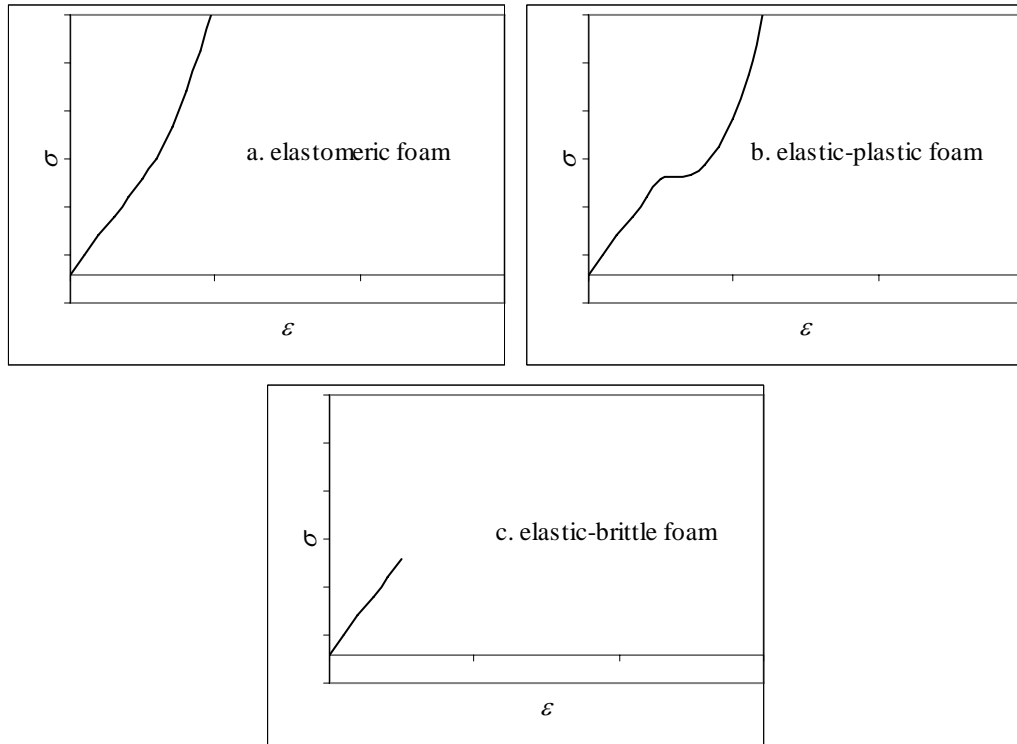
Fig. 2.3 Stress-strain curves of foams under tension [2]

Note that these behaviours typical of foams are not all-encompassing, since each foam has its own distinctive characteristics. Banhart and Baumeister [52] asserted that the linear portion is not really elastic, as some of the deformation is irreversible. The tensile stress-strain curve obtained by Motz and Pippan [53] for a closed-cell aluminium foam (an elastic-plastic foam) shows no rapid increase of stress after plastic collapse, which is expected according to Fig. 2.3. Instead, fracture occurs after plastic yielding resulting in a stress-strain curve which is similar to that for solid aluminium.

2.3   Factors influencing mechanical properties of solid foam

The mechanical properties of solid foams are influenced by several factors – the mechanical properties of the solid material defining the cell edges (struts) and walls (membranes), cell structure and properties of fluid inside the cells.

- Mechanical properties of the solid material – The mechanical properties of solid foams, such as stiffness, strength and viscoelasticity, depend largely on the mechanical properties of the solid material in the cell edges and walls – e.g. the stiffer and stronger the cell strut and wall material, the stiffer and the stronger the solid foam.

- Cells structure of the foam – The mechanical properties of solid foam depend not only on the mechanical properties of the solid material in the cell edges and walls, but also on cell structure. This is because how the cell struts and walls deform determines the overall mechanical behaviour of foam. When solid foams are loaded by compression/tension, the struts at the cell edges deform, and they undergo bending and tension/compression. Their compliance in bending is much higher than that in tension/compression; and hence, bending is the primary deformation mechanism [2] and consequently, stiffness of solid foam is strongly influenced by the bending of cell edges. As highlighted in Section 2.1, cells in many foams are usually geometrically anisotropic, with a larger dimension in one direction. Consequently, this causes anisotropy in the mechanical properties of foam. Usually, the foam is stiffer and stronger in the direction of cell elongation. Poisson's ratio is another mechanical property of solid foam that depends on cell structure, with values ranging from -0.5 to a large positive values [2].

- Fluid inside the foam cells – As mentioned in Section 2.1, solid foam can be classified into two types – closed celled and open celled. Due to the difference in their microstructure, these two types of foam behave differently when loaded. Closed cell foams have fluid trapped inside their cells and hence their mechanical properties are influenced by the properties of the fluid contained – e.g. a fluid with low compressibility can stiffen the foam. On the other hand, fluids can flow freely

through open cell foams, but, this does not mean that the fluid does not affect its mechanical properties. At high strain rates, the viscosity of the fluid flowing through the cells when foam is loaded can increase its stiffness, thus, introducing strain rate sensitivity.

2.4 Studies on mechanical properties of solid foam

The extensive use of foams in engineering applications, especially in kinetic energy absorption and composite structures, has motivated investigations into their mechanical behaviour. Different approaches have been used – experimentation, development of simplified cell models and formulation of continuum constitutive relationships for numerical modelling; some of these are now discussed

2.4.1 Experimental studies

Researchers, such as Zaslawsky [9], McIntyre and Anderton [7], Zhang et al. [10], Triantafillou et al. [8], Doyoyo and Wierzbicki [5], Deshpande and Fleck [3, 4] and Gdoutos et al. [6], have performed experiments on solid foam. These include uniaxial tension and compression, shear, and multiaxial loading, with most of these efforts are aimed at obtaining empirical failure criteria. Zaslawsky [9] carried out tests on thin walled tubes of rigid polyurethane foam to simulate multiaxial loading by imposing internal pressure together with axial tension or compression. These tests yielded an empirical failure criterion in form of a rectangular envelope with respect to axes defined by the two principal stresses, suggesting that the foam follows a maximum principal stress failure criterion. As with Zaslawsky [9], Zhang et al. [10, 54] also tested several polymeric foams. Their experiments included uniaxial compression, shear, and hydrostatic compression to establish a failure criterion and a constitutive model. Unlike the failure criterion by Zaslawsky [9] which is only

defined by the maximum principal stress, the failure criterion by Zhang et al. [10, 54] is quantified by the effective stress and hydrostatic pressure.

Triantafillou et al. [8] studied polymeric foams and determined a failure envelope based on the von Mises effective stress and mean stress. This failure envelope was then compared with analytical failure criteria derived from a cubic open cell model developed by Gibson et al. [21]. Triantafillou et al. [8] suggested that their model is able to describe yield in open cell polyurethane and closed cell polyethylene foams quite well, showing that the principal stress criterion proposed by Zaslawsky [9] is inadequate. Unlike Zaslawsky [9], Zhang et al. [10, 54] and Triantafillou et al. [8] who studied polymeric foam, Doyoyo and Wierzbicki [5] examined metallic foam and performed biaxial tests on isotropic Alporas® and anisotropic Hydro® closed cell aluminium foams. From these tests, they also proposed a failure criterion based on mean stress and von Mises effective stress. As with Zaslawsky [9], Zhang et al. [10, 54] and Doyoyo and Wierzbicki [5], Gdoutos et al. [6] also studied the mechanical behaviour of foam in order to propose failure criteria. They performed uniaxial tension, compression, shear and biaxial loading tests on Divinycell™ foam and found that failure could be described by the Tsai-Wu failure criterion [55] which is expressed as a second-order polynomial equation with principal stresses as the parameters. Again, this failure criterion differs from those described earlier, as it is defined using different stresses. Deshpande and Fleck [3, 4] performed multiaxial mechanical tests on PVC and aluminium foams, and compared their results with a phenomenological yield surface they proposed [3]. Their criterion also uses the von Mises-mean stress plane, similar to the failure criterion proposed by Gibson et al. [21], Triantafillou et al. [8] and Doyoyo and Wierzbicki [5].

The studies discussed so far have concentrated on obtaining empirical failure criterion. McIntyre and Anderton [7] and McCullough et al. [56] chose to use another approach, employing fracture mechanics and carried out fracture toughness tests on rigid polyurethane foams. They concluded that fracture in the foams they studied could be characterized by G_{Ic}, K_{Ic} and a crack opening displacement criterion. Although the foam used in their tests was anisotropic, they neglected this factor in their study. McCullough et al. [56], investigated aluminium foam and performed fracture toughness tests to get J-integral curve. They found that crack propagation in foams is interrupted by crack bridging by cell edges. This differentiates crack propagation in foams from that in solid material. Their approach of using fracture mechanics to analyse the properties of foam seems to be somewhat peculiar because fracture mechanics is a continuum-based approach while foam is not really a continuum material.

The experimental studies discussed have focused mainly on finding appropriate failure criteria. Some of these criteria have also been developed into a constitutive model and this is discussed later. It is noted that researchers have proposed failure criteria that differ one another because different types of stress are used. Although these studies have provided insights into the mechanical behaviour of foams, they have not yielded information on the micromechanics governing foam behaviour. An understanding of the underlying micromechanics is important in explaining the response of foam, thus leading to improved failure criteria and constitutive models. Hence, some researchers have also tried to describe the micromechanics governing foam deformation by analyzing idealized cell models. Some of these studies are now discussed.

2.4.2 Cell models

Cell models for solid foams have been proposed and analysed both analytically and numerically to find generic relationships between the overall mechanical properties of solid foam and its microstructural characteristics, such as cell shape and size, density and the mechanical properties of the solid defining cell struts and walls. This approach is also useful for relating the overall deformation of solid foam to the tension, bending and torsion experienced by cell struts and walls and describing how failure is governed by buckling, plastic deformation and fracture in cells.

Early cell models for foam by Gent and Thomas [18, 19], Lederman [29], Cunningham [15], Christensen [14] and Kanakkanatt [27] suggest that elastic deformation of foam is caused mainly by the stretching of cell struts/walls which leads to a linear dependence of stiffness on foam density. However, later developments by Ko [28], Gibson et al. [21], Triantafillou et al. [8], Gibson and Ashby [2, 20], Huber and Gibson [26], Maiti et al. [31] and Zhu et al. [40, 41] have shown that bending of cell struts/walls plays a major role in foam deformation. This results in a quadratic dependence of foam stiffness on density, which bears better correlation with actual foam.

Gent and Thomas [18] and Lederman [29] considered models in which struts with random orientations are interconnected via spheres; similarly, Cunningham [15] and Christensen [14] have also examined interconnected struts with random orientations. Gent and Thomas [18], Lederman [29], Cunningham [15], and Christensen [14] analysed these structures by determining the average stiffness of the struts that are randomly oriented. They took the stretching of struts to be the main mechanism governing foam deformation, while other modes of struts deformation – bending and torsion – were not considered. This led to a (nearly) linear relationship

between stiffness and density which is found to be unsatisfactory for actual foam, especially open cell foams and closed cell foams with thin cell walls.

Gent and Thomas [19] have proposed a simple cubic structure which Kanakkanatt [27] further developed to include geometric anisotropy. As with Gent and Thomas [18], Lederman [29] Cunningham [15] and Christensen [14], Gent and Thomas [19] and Kanakkannat [27] considered the stretching of cell struts as the main deformation mechanism in foam. Thus, they also found a linear relationship between stiffness and foam density. Kanakkannat [27] concluded that his model differs from experimental results on actual foams because it neglected bending of struts.

Warren and Kraynik [22] and Wang and Cuitino [38] analysed struts in a prescribed intersection pattern to represent foam. Warren and Kraynik [22] considered a tetrahedral arrangement of four struts intersecting at one point as the basic repeating unit. They considered stretching and bending of struts as well as random orientation of the tetrahedral units to model the variation of cells in actual foam. Their model could be arranged to fill space in three dimensions but lacked geometrical similarity with actual foam. This model was extended by Sahraoui [36] to account for anisotropy. Wang and Cuitino [38] derived equations for any number of struts originating from one point in their model and considered the stretching and bending of struts in their models. These models are semi isotropic with equal strut lengths and hence, cannot be used for anisotropic foams. They also lack geometric similarity with cells in actual foams.

The development of cell models also includes employing simplified repeating cell units and researchers have utilized such models to identify the main mechanisms governing foam deformation and failure, and devise equations to describe the mechanical properties of foams. A simplified cell model based on open cubic cells

have been proposed by Gibson et al. [21], Triantafillou et al. [8], Gibson and Ashby [2, 20], Maiti et al. [31] and Huber and Gibson [26] to describe the mechanical behaviour of foam (see Fig. 2.4). From these cell models, they suggested that the main mechanism for foam deformation is the bending of cell struts and walls. Other deformation mechanisms, such as cell wall stretching and compression of fluid inside cells, have also been incorporated into their models. They also developed a yield surface/failure model based on three distinctive mechanisms that can initiate nonlinearity in the stress-strain curve for foam, i.e. elastic buckling, plastic yielding and brittle crushing or fracture. They proposed constitutive models for anisotropic foams based on elongated versions of these cell models. Most of the constitutive models proposed for open or closed cell foams with thin cell walls were able to relate the properties of actual foam to the properties of the solid material and relative density of the foams via power law relationship of the form

$$P_f = C_f \ P_s \left(\frac{\rho_f}{\rho_s} \right)^n,$$

(2.1)

where P_f, P_s, ρ_f and ρ_s are respectively property of the foam, property of the solid defining the cells, foam density and density of the strut materials; C_f is a constant defined empirically from experiments, while n is a constant derived analytically. This model has been further extended by Andrews et al. [11] to analyse creep in foam. Although this cell model manages to describe the mechanical behaviour of foam, it does not provide a direct explanation for the value of the constant C_f for each mechanical property. The cell model is also not realistic because it cannot be assembled in three dimensions, i.e. this model cannot be arranged to fill space.
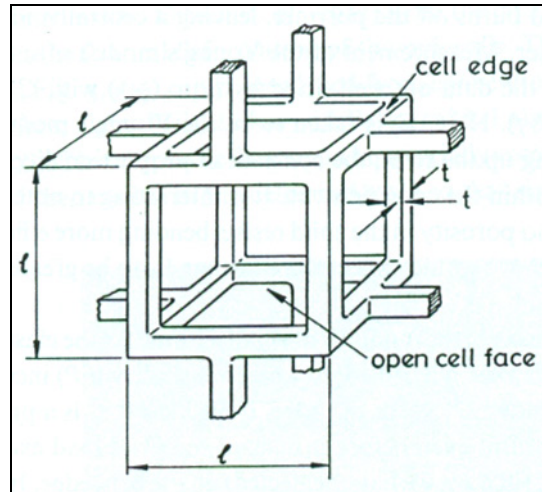
Fig. 2.4 Cubic cell model proposed by Gibson et al. [21], Triantafillou et al. [8], Gibson and Ashby [2, 20], Maiti et al. [31], Huber and Gibson [26]

Researchers have also made use of polyhedra to model cells in foam. Ko [28] considered a trapezo rhombic dodecahedron – a polyhedron with six equilateral trapezoids and six congruent rhombic faces arranged in a hexagonal closest packing arrangement, as well as a rhombic dodecahedron – a polyhedron with twelve rhombic faces arranged in a face-centred cubic packing arrangement. Ko [28] and Dawson and Shortall [57] suggested that actual rigid polyurethane foam cells are mostly pentagonal dodecahedra, i.e. polyhedra with twelve pentagonal faces each. However, pentagonal dodecahedra cannot be assembled in three-dimensions to fill space. Tetrakaidecahedra – a polyhedron with 14 faces – as shown in Fig. 2.5, have attracted many researchers such as Dement'ev and Tarakanov [16, 17], Zhu et al. [40], Warren and Kraynik [39], Choi and Lakes [13], Simone and Gibson [37], Grenestedt [24], Grenestedt and Tanaka [23], and Ridha et al. [44-46]. They have utilized this to model open and closed cell foam. This cell model can be arranged to fill space in a body-centred cubic arrangement. Patel and Finnie [33] asserted that in actual foam, five sided faces are found in abundance, while four and six sided faces are also found in a considerable quantities. This suggests that pentagonal dodecahedra and tetrakaidecahedra are similar to cells in actual foam.

17

Menges and Knipschild [30] carried out a theoretical analysis of the stiffness and strength of foam based on the pentagonal dodecahedron model. They consider bending and axial deformation of struts as the deformation mechanisms. Compressive strength was derived based on the buckling load, while the tensile strength was derived from the axial loading of struts. Their assumption of using only axial loading on struts as the main failure criterion for tensile loading seems to contradict with their assumption of employing both axial loading and bending as the main deformation mechanisms. This is because the bending of beams/struts usually initiates fracture earlier than axial loading. As with Menges and Knipschild [30], Chan and Nakamura [12] have also used pentagonal dodecahedra for their foam model. They used it to model the stiffness and yield strength of open and closed cell foam under compressive loading. The bending of cell struts and walls was considered the primary deformation mechanism while buckling was associated with yield. Both Menges and Knipschild [30] and Chan and Nakamura [12] only studied isotropic foam using their model.

Zhu et al. [40], Warren and Kraynik [39] and Choi and Lakes [13] used a tetrakaidecahedral geometry to model an open cell foam. Zhu et al. [40] asserted that a tetrakaidecahedron is the only polyhedron that can be assembled with identical units to fill space, and it nearly satisfies the minimum surface energy criterion. Warren and Kraynik [39] also concurred with this. They stated that "it is the only polyhedral bubble known that fills space to form dry soap foam (one that contains very little liquid) with perfect order", and also suggested that other polyhedra can fill space but do not satisfy the energy conditions stated in Plateau's law [1]. Both Zhu et al. [40] and Warren and Kraynik [39] obtained analytical expressions for the mechanical properties, i.e. Young's modulus, shear modulus, bulk modulus and Poisson's ratio, based on small deformation of this cell. Their model shows that for

low density foams, bending is the main deformation mechanism in the foam. The stiffness of this model can also be approximated using Eq. (2.1) with values of C_f and n approaching 1 and 2 when the cross section of the cell struts corresponds to a Plateau border [1], which is defined by three circular arc that touch each other. This is consistent with the semi empirical equation proposed by Gibson et al. [21], Triantafillou et al. [8], Gibson and Ashby [2, 20], Maiti et al. [31], Huber and Gibson [26]. Zhu et al. [40] concluded that the mechanical properties of this model are approximately isotropic. The model has also been used to analyse large deformation [41] and creep behaviour [58] and appears more realistic than the cubic cell model [2, 8, 20, 21, 26, 31] because the cells can be arranged to fill space. However, due to its geometric isotropy, this model can only be applied to isotropic foam.

Mills and Zhu [32], Simone and Gibson [37], Grenestedt [24], and Grenestedt and Tanaka [23] used a tetrakaidecahedron cell model for closed-cell foams. Mills and Zhu [32] derived equations that describe the mechanical properties of foam for high compressive strains. Simone and Gibson [37] performed numerical simulations using this model in order to see the influence of material distribution in metallic foams. Grenestedt [24] employed FEM simulation to obtain elastic properties based on this model, while the finite element analysis of Grenestedt and Tanaka [23] was directed at examining the effect of cell irregularity on the mechanical properties of closed cell foams. As with the model by Zhu et al. [40], those by Mills and Zhu [32], Simone and Gibson [37], Grenestedt [24] and Grenestedt and Tanaka [23] are isotropic.
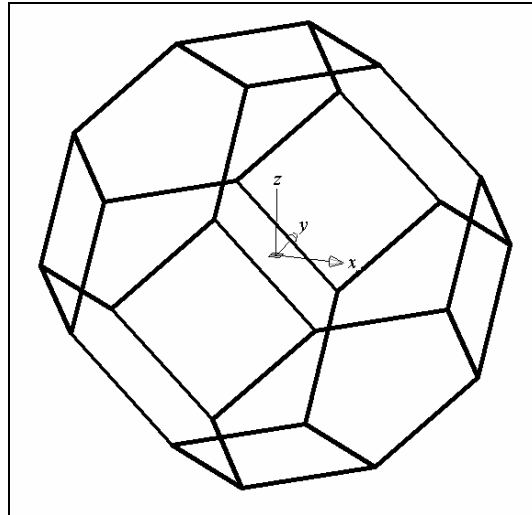
Fig. 2.5 Tetrakaidecahedral foam cell model

Other researchers such as Roberts and Garboczi [34, 35], Huang and Gibson [25], Zhu et al. [42] and Zhu and Windle [43] preferred to use a more random cell model because actual foams do not comprise identical repeating cells. Roberts and Garboczi [34] generated a foam model using Voronoi tessellations of distributed seed points in space to form a closed cell foam with planar faces. Fig. 2.6 shows the Voronoi model used by Roberts and Garboczi [34] who also employed other types of random cell models called Gaussian random fields to model closed cell foams with curved cell walls; Fig. 2.7 shows such a model. They performed FEM simulations of these models to obtain their elastic properties. Both models were for isotropic foam and cannot be applied to anisotropic cells.

In contrast to Roberts and Garboczi [34] who analysed random cell models for closed cell foams, Roberts and Garboczi [35], Huang and Gibson [25], Zhu et al. [42] and Zhu and Windle [43] have used random cells to model open cell foams. Roberts and Garboczi [35] used Voronoi tessellations, a node-bond model that connects random nodes to their nearest neighbours and Gaussian random fields to develop random cells for open cell foam model. They performed FEM simulations based on these models to obtain elastic properties. Zhu et al. [42], Zhu and Windle [43] used

the Voronoi tessellation technique to build foam models. They applied FEM simulations to these models to study the influence of cell irregularity in foams on their elastic properties and response to high strain compressive loading. Similarly, Huang and Gibson [25] used the Voronoi tessellation technique to build closed cell models and employed FEM simulation to study creep behaviour.

Although random cell models appear to better represent the microstructure of actual foams, these models cannot be analysed easily due to their complex geometries. Thus, numerical simulation is required. Moreover, the random models proposed have only been applied to isotropic foams and cannot be used to model anisotropic foams which commonly occur.
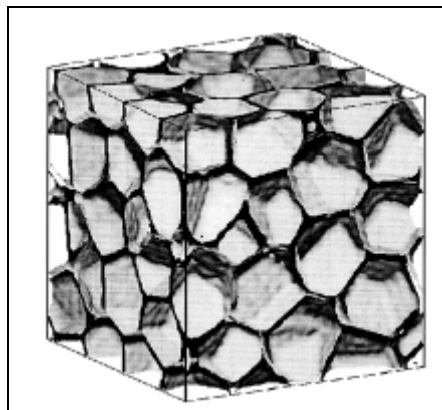
Fig. 2.6 Voronoi tessellation cell model [34]
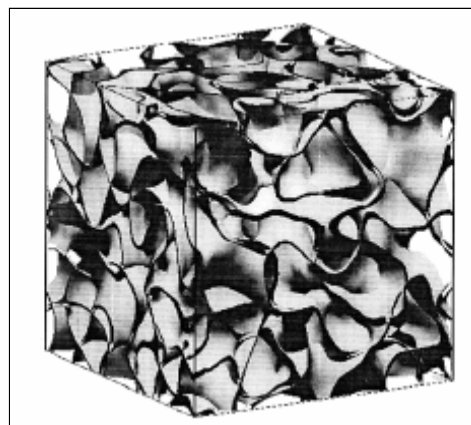
Fig. 2.7 Closed cell Gaussian random field model [34]

2.4.3 Constitutive models

A knowledge of constitutive material behaviour is essential in structural design involving foams. Implementation of appropriate constitutive material models into computer simulation codes facilitates the design and analysis of components. The development of constitutive models for foams has been of interest to researchers such as Deshpande and Fleck [3], Schreyer et al. [51], Ehlers [47] and Miller [50]. Some of the constitutive models developed have been implemented in finite element packages – e.g. LS-DYNA and ABAQUS. Hanssen et al. [49] have briefly described some constitutive models developed for solid foam, i.e. material models 26, 126, 63 and 75 in LS-DYNA, the crushable foam model in ABAQUS and the models by Deshpande and Fleck [3], Miller [50], Schreyer et al. [51] and Ehlers [47]. A comparison among the models is shown in Fig. 2.8 [49].
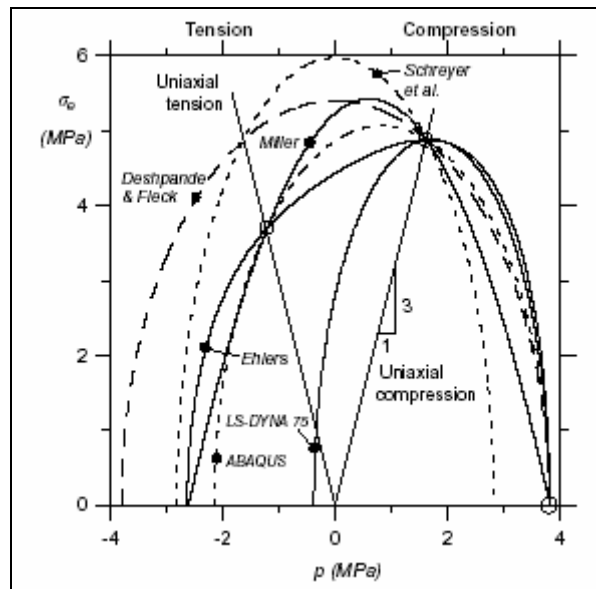
Fig. 2.8 Comparison of yield surface based on several models for foam [49]

Material models 26 and 126 in LS-DYNA use the orthogonal directions of the material (principal directions of anisotropy) as the basis for their hardening functions. Yield criterion is defined for each of the six stress components. The difference between the two is the hardening model: material model 26 uses the engineering

volumetric strain as the variable, while material model 126 uses the engineering strain. The main feature of both is that they can be used to model anisotropic foams. [49]

Material model 63 in LS-DYNA uses the principal stresses as the base of its strain hardening function. This model essentially employs a maximum principal stress criterion, whereby the compressive principal stress is a function of volumetric stress, while the tensile principal stress follows an elastic-perfectly plastic curve. This model cannot be used for anisotropic foams [49]. Material model 75 in LS-DYNA and the crushable foam model in ABAQUS involve yield functions that can be described by an ellipse in the von Mises-mean stress plane. The major difference between the two models is that the ellipse in ABAQUS has a fixed ratio between its major and minor axis, while the ratio is not fixed for material model 75 in LS-DYNA. Hence material model 75 in LS-DYNA requires a larger number input parameters than the crushable foam model in ABAQUS. The ABAQUS crushable foam model only requires the hardening curve in the form of a relationship between hydrostatic stress and volumetric strain, while material model 75 in LS-DYNA requires not only a definition of the hardening curve via a relationship between hydrostatic stress and volumetric strain, but also the uniaxial compressive stress-strain hardening curve. [49]

Deshpande and Fleck [3] modified the von Mises criterion by including the effect of elastic volumetric strain energy in the criterion (note that the von Mises criterion only considers elastic shear strain energy). Deshpande and Fleck's [3] criterion results in an ellipse when it is drawn in the von Mises-mean stress plane. Strain hardening is modelled via a function of equivalent plastic strain defined as the energy conjugate of Deshpande and Fleck's [3] equivalent stress. This criterion only

needs data from a uniaxial compression test on foam and can only be used to describe isotropic foam [3, 49].

Miller [50] combined the Drucker-Prager criterion and the yield surface proposed by Gibson et al. [21], Triantafillou et al. [8], and Gibson and Ashby [2, 20]. The result was a criterion in the form of a polynomial of the stress invariants – first order in the von Mises stress and second order in the mean stress. Miller's strain hardening model is defined in terms of a function of the volumetric strain and plastic strain. [49, 50]

Gioux et al. [48] presented a physical basis for the criterion proposed by Miller [50] and Deshpande and Fleck [3]. They found that the Miller [50] criterion can be derived from the mechanistic failure surface criterion developed by Gibson et al. [21], Triantafillou et al. [8], and Gibson and Ashby [2, 20], by taking into account the influence of cell wall curvature. They also found that Deshpande and Fleck's [3] criterion can be derived from the Miller [50] criterion by neglecting the effect of the linear term for the mean stress. Gioux et al. [48] suggested that both criteria, i.e. Deshpande and Fleck's [3] and Miller's [50], are able to describe the multiaxial failure surface for aluminium foam.

Hanssen et al. [49] have compared results from LS-DYNA models 26, 126, 75, and 63 with experimental results for aluminium foams under specific loading configurations. They concluded that none of the models can describe the experimental results with convincing accuracy. They believe that inaccuracy occurs because the models do not consider local and global fracture. Hence, an accurate, efficient and robust fracture criterion is needed to enhance the accuracy of the material models.

Chapter 3   Rigid Polyurethane Foam

As highlighted in Chapter 1, this study focuses on the tensile mechanical properties of rigid polyurethane foam and establishment of an appropriate cell model. The mechanical and structural properties of rigid polyurethane foam are discussed in this chapter, and the fabrication of rigid polyurethane foam is first presented.

3.1   Fabrication of rigid polyurethane foam

Rigid polyurethane foam blocks were fabricated by mixing polyurethane resin (polyol), a hardener (diisocyanate) and a gassing agent together. The chemicals used were DALTOFOAM® MM 6775 for the resin, SUPRASEC® 5005 for the hardener and HCFC 141b for the gassing agent. Three foam blocks were made by first mixing the resin and the gassing agent together thoroughly, followed by introducing the hardener to the mixture, which was then poured into a mould and left to cure. Mixing of the components caused a reaction, which resulted in a foaming process whereby bubbles are formed and rises causing the bubbles to elongate in the foam rise direction while the mixture hardens. The density of the three foam blocks was varied by using different amounts of gassing agent.

The foam made by this technique comprised primarily closed cells with struts defining the cell edges and thin membrane for cell walls. The cells were elongated in the foam rise direction, generating geometric anisotropy quantified by a geometric anisotropy ratio (i.e. the ratio between the cell length in the rise direction to that in the transverse direction) that varied with foam density. The material in each block was denser and less uniform near the outer surface. Thus, these portions at the surface were cut away and discarded. Nearer the middle of each block, the cell dimensions perpendicular to the rise direction were generally similar, making them roughly

axisymmetric. The overall density of the solid foam, average cell size and cell geometric anisotropy ratio are presented in Table 3.1. The characteristics of the foams are consistent with the conclusion by Dawson and Shortall [57] that the cell anisotropy ratio of rigid polyurethane foam decreases with a higher density.

Table 3.1 Solid foam data

	Foam A	Foam B	Foam C
Density (kg/m^3)	23.3	29.5	35.2
Average cell size $(mm \times mm)$	1×0.4	1×0.5	0.9×0.53
Average cell geometric anisotropy ratio	2.5	2	1.7

3.2 Quasi-static Tensile tests

Quasi–static tensile tests were performed on foam specimens to study the influence of loading direction, foam density and cell anisotropy ratio on the mechanical properties. Dog-bone shaped specimens were cut from foam blocks according to five directions – along the foam rise direction and 30°, 45°, 60° and 90° to the foam rise direction. Fig. 3.1 shows the specimen dimensions. The ends of the specimens were glued to acrylic blocks to facilitate gripping by an Instron$^®$ (model 5500) universal testing machine used to apply tension (see Fig. 3.2).
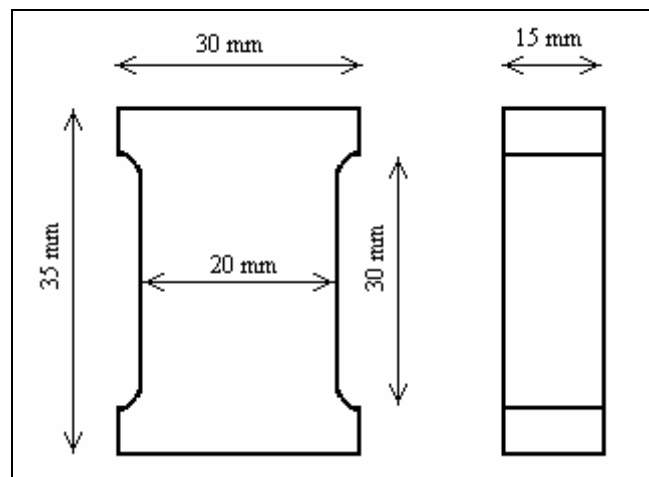
Fig. 3.1 Dog-bone shaped specimen
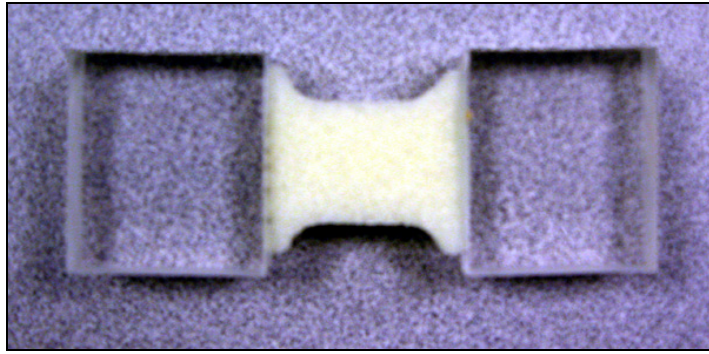
Fig. 3.2 Foam specimen attached to acrylic block

Results from these tests are presented in the form of engineering stress-strain curves and a typical stress-strain curve for these foams is illustrated in Fig. 3.3. The curve shows that the foam has an initial linear response followed by a shorter nonlinear response before fracture.
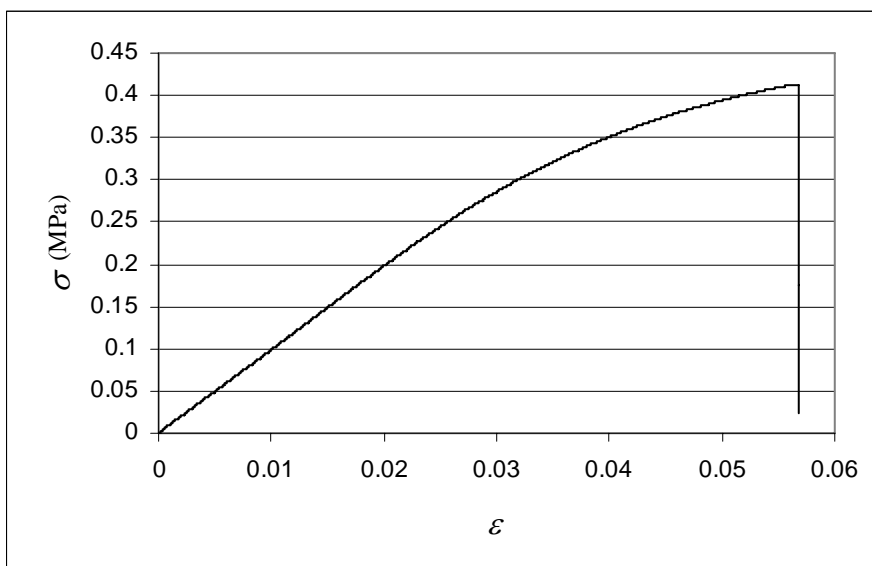
Fig. 3.3 Typical stress-strain curve

The stress-strain curves are converted into stiffness and tensile strength data as functions of loading direction. Foam stiffness was determined from the gradient of the initial linear portion, while foam strength was defined by the maximum stress before failure. Fig. 3.4 shows the stiffness as a function of loading direction, while Fig. 3.5 shows tensile strength as function of loading direction for the three foams.
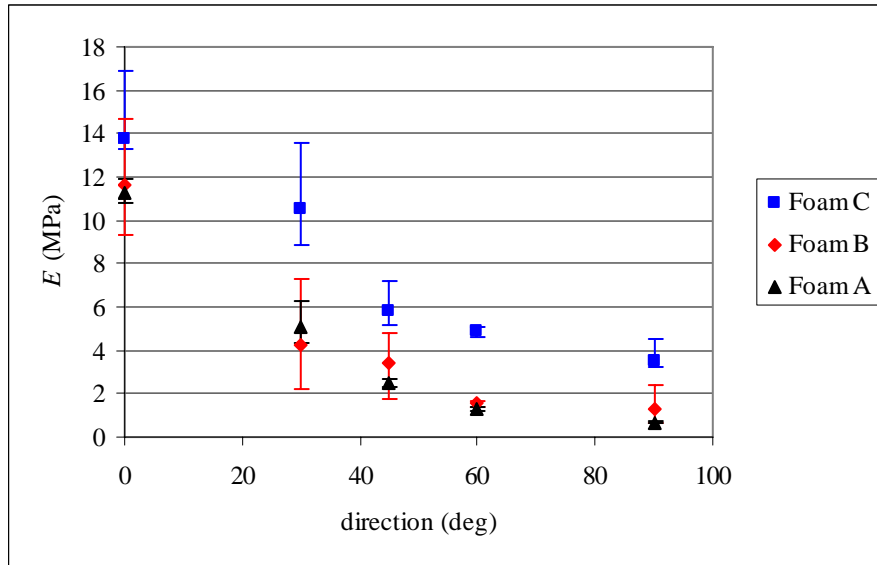
Fig. 3.4 Stiffness
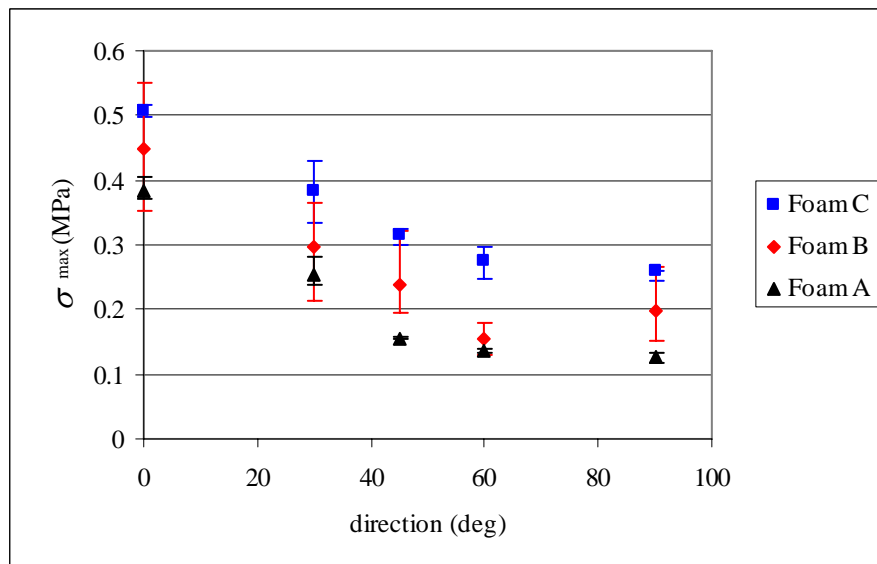
Fig. 3.5 Tensile strength

All the foams exhibited anisotropy in their mechanical properties – the stiffness and tensile strength depend on loading direction. The stiffness is highest in the rise direction (0°) and decreases with the angle to the rise direction. Minimum stiffness corresponds to loading perpendicular to the foam rise direction, i.e. the transverse direction. As with stiffness, foam strength is also highest in the foam rise direction and decreases with angle to the rise direction. Consequently, foam is also weakest in the transverse direction. These results are expected because the foam cells are anisotropic and elongated in the rise direction. The cell struts that are aligned in the

foam rise direction are longer; hence, they are relatively easier to bend when loaded in the transverse direction, making the foam more compliant in that direction. This also causes the foam to be weaker in the transverse direction. Moreover, the foam is also weaker in the transverse direction because fewer struts are required to be broken when failure occurs, as there is a smaller number of struts per unit area perpendicular to the transverse direction.

Foam C is stiffer and stronger than foam B, while foam B is stiffer than stronger than foam A, i.e. $E_{fC} > E_{fB} > E_{fA}$ and $\sigma_{fC\max} > \sigma_{fB\max} > \sigma_{fA\max}$. This is expected because foam C is denser than foam B, while foam B is denser than foam A ($\rho_{fC} > \rho_{fB} > \rho_{fA}$). The amount of solid material to carry the load increases with density, thus, increasing the stiffness and strength of the foam. Notable scatter in the stiffness and strength data was found from tests on the foam specimens, as presented via the I-shaped bars in Figs. 3.4 and 3.5 . This is expected because the cells within each type of foam were not uniform. Fig. 3.6 shows the average anisotropy ratios for strength and stiffness as a function of cell geometric anisotropy. It indicates that the cell geometric anisotropy ratio governs the degree of anisotropy in the mechanical properties of the foams – anisotropy in the strength and stiffness increases with cell geometric anisotropy.
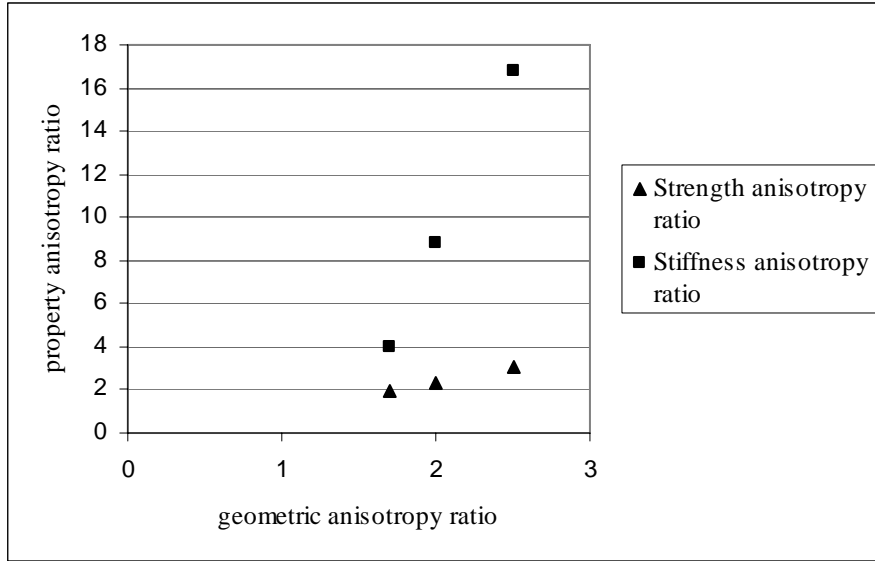
Fig. 3.6 Strength and stiffness anisotropy ratio

3.3 Dynamic tensile tests

In addition to quasi-static tensile tests, dynamic tensile tests were also undertaken. These tests were performed on foam B $\left(\rho = 29.5\,\mathrm{kg}/\mathrm{m}^3\right)$ to examine if strain rate influences its tensile mechanical properties. The specimens in these tests were also dog-bone shaped, similar to those in quasi-static tensile tests (see Fig. 3.1). Specimens were dynamically stretched using a tensile split Hopkinson bar arrangement (SPHB), as shown in Fig. 3.7. The input/output bars used in this experiment were made of polycarbonate (with stiffness $E = 2.2\,\mathrm{GPa}$; diameter = 16.5 mm) to reduce mismatch in impedance with the compliant specimens. A pendulum-driven system was employed, whereby a pendulum strikes anvil, generating a tensile pulse in the input bar, which propagates and loads the specimen. The load applied to the specimen was calculated from the strain gauge signal of the output bar. Deformation of the specimen was recorded using a high speed camera (PHOTRON[TM] ultima APX) and the strain induced was derived from this visual data.
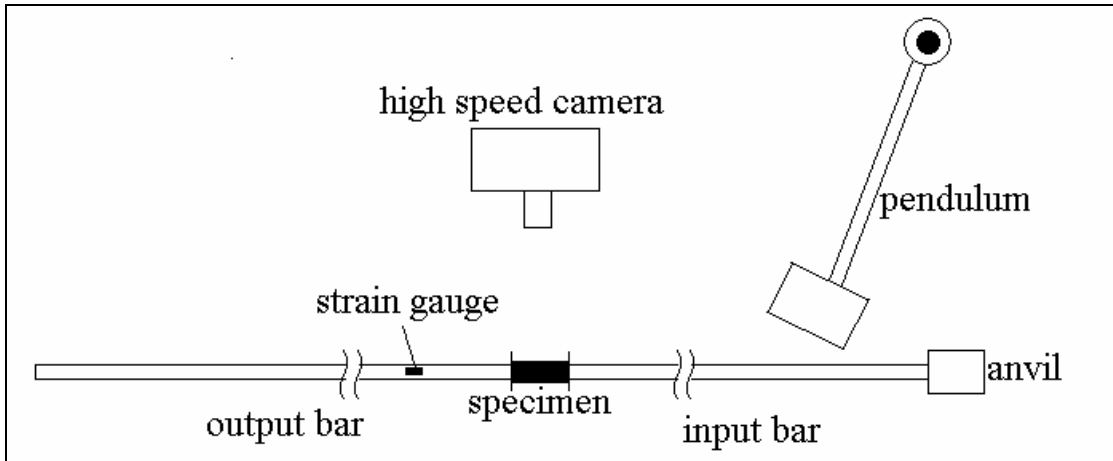
Fig. 3.7 Split Hopkinson bar arrangement

The tests yielded dynamic engineering stress-strain data and a typical stress-strain curve for foam is shown in Fig. 3.8. The initial part of the curve (up to a strain of about 0.008) shows a slightly nonlinear increase (note that the stress in the specimen is not yet uniform during this early phase and hence the data may not be accurate – see [59]). Neglecting this initial phase, the curve shows that the foam has an essentially linear initial response followed by some nonlinearity before fracture. This is similar to its behaviour under quasi-static loading.
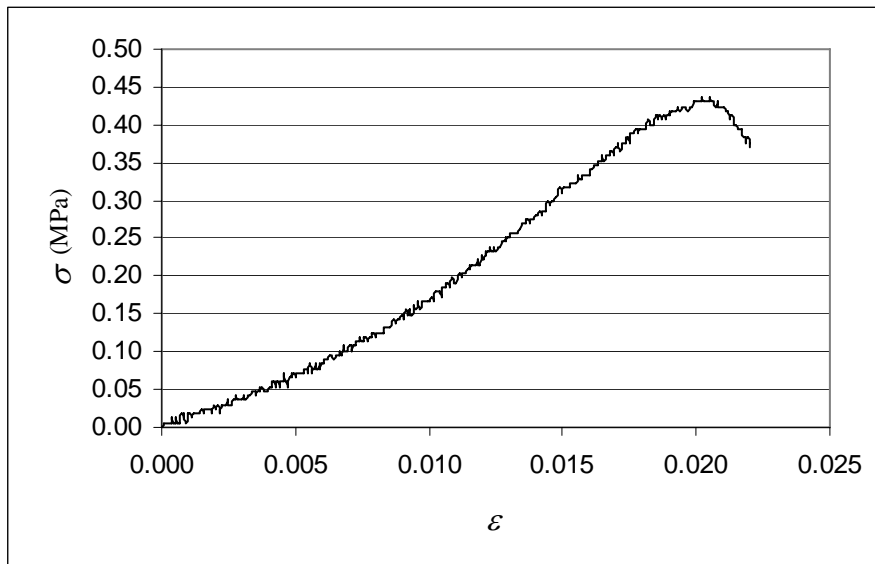
Fig. 3.8 Typical stress-strain curve

The stress-strain curves were then converted into tensile stiffness and strength data. Fig. 3.9 shows stiffness as a function of strain rate while Fig. 3.10 shows

strength as a function of strain rate. Data from quasi-static tensile tests performed using the Instron® (model 5500) universal testing machine are included for comparison with responses at low strain rates.
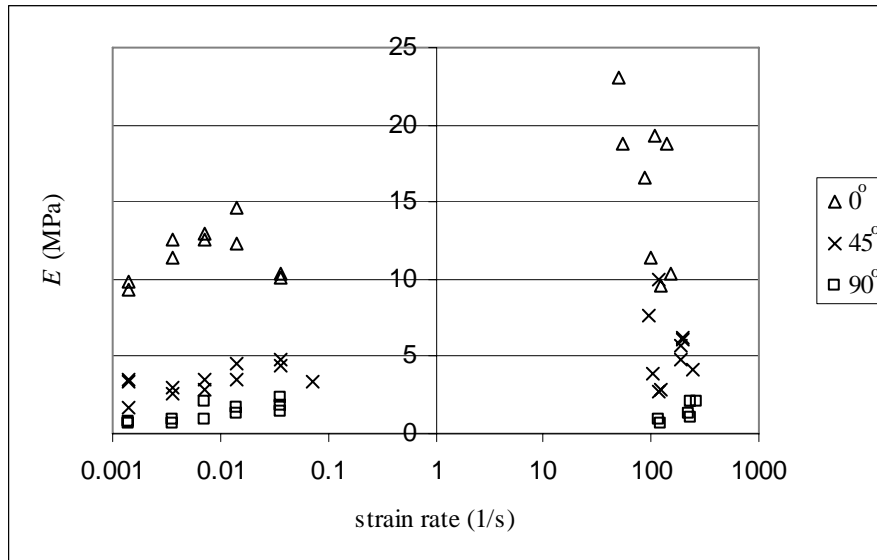
Fig. 3.9 Stiffness
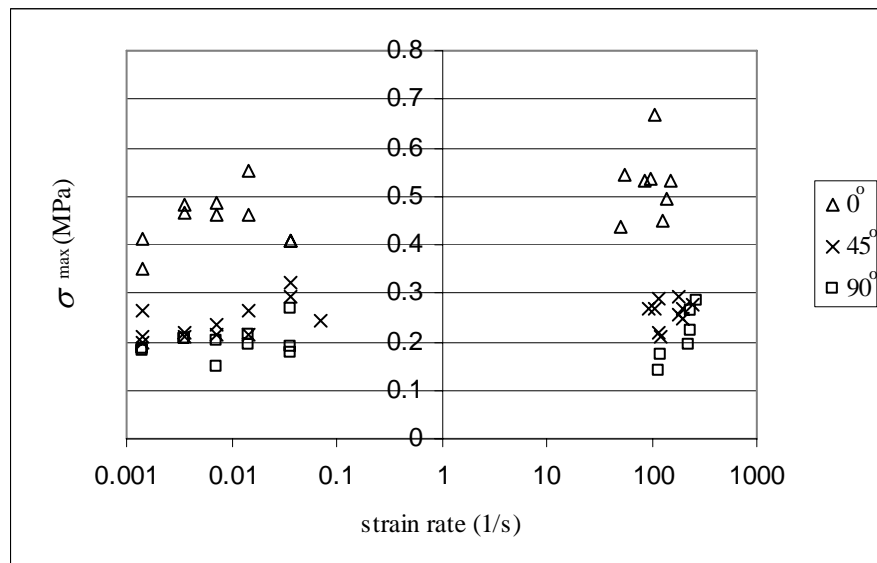
Fig. 3.10 Tensile strength

As with the data from quasi-static tensile tests, the foam also displayed anisotropy in mechanical properties for dynamic loading – the stiffness and strength depend on loading direction. Again, the foams are stiffest in their rise direction (0°) and the stiffness decreases with angle with the rise direction. Minimum stiffness corresponds to loading in the transverse direction. With regards to strength, this is also

highest in the foam rise direction and decreases with alignment to the transverse direction, where it is lowest. The reasons for these are the same as those for quasi-static tests (Section 3.2.) Figs. 3.9 and 3.10 appear to indicate no obvious dependence of tensile strength and stiffness on strain rate. The strength at low strain rates (e.g. less than 0.1/s) does not show any significant difference with that at higher strain rates (higher than 10/s). The stiffness corresponding to these two ranges do not show any notable difference as well. Although the glass transition temperature of rigid polyurethane is 200-250K [2], the foam exhibits insignificant rate sensitivity probably because it is loaded in tension; it is relatively brittle and hence fracture occurs before any rate sensitivity becomes apparent.

3.4 Micro CT imaging of rigid polyurethane foam cells

As described in Chapter 2, the cell structure within a foam plays an important role in determining its mechanical properties. Micro CT scanning of foam cells was therefore performed to study the cell structure. Micro CT scan was performed on rigid polyurethane foam samples using a SkyScan™-1076 machine with a resolution of $18 \mu m$; this resulted in two-dimensional images of the sample cross-sections, which were then converted to three-dimensional images using software (CTAN). Fig. 3.11 shows images of cells obtained from CT scanning and they resemble an elongated tetrakaidecahedron cell model shown in Fig. 3.12. Both the actual cells and the model have:

- horizontal faces at the upper and lower ends

- slanted faces adjacent to upper and lower faces

- vertical faces at the sides

This probably arises because during the foaming process, the foam bubbles generated tend towards the minimum surface energy conditions [40] and the energy criteria

stated in Plateau's law [39]. Tetrakaidecahedra, as suggested by Zhu et al. [40] and Warren and Kraynik [39], are the only polyhedra that can fill space (arranged in three dimensions) and that approximately satisfy both energy criteria. This is consistent with Patel and Finnie's [33] suggestion that cells in actual foam are similar to pentagonal dodecahedra and tetrakaidecahedra.
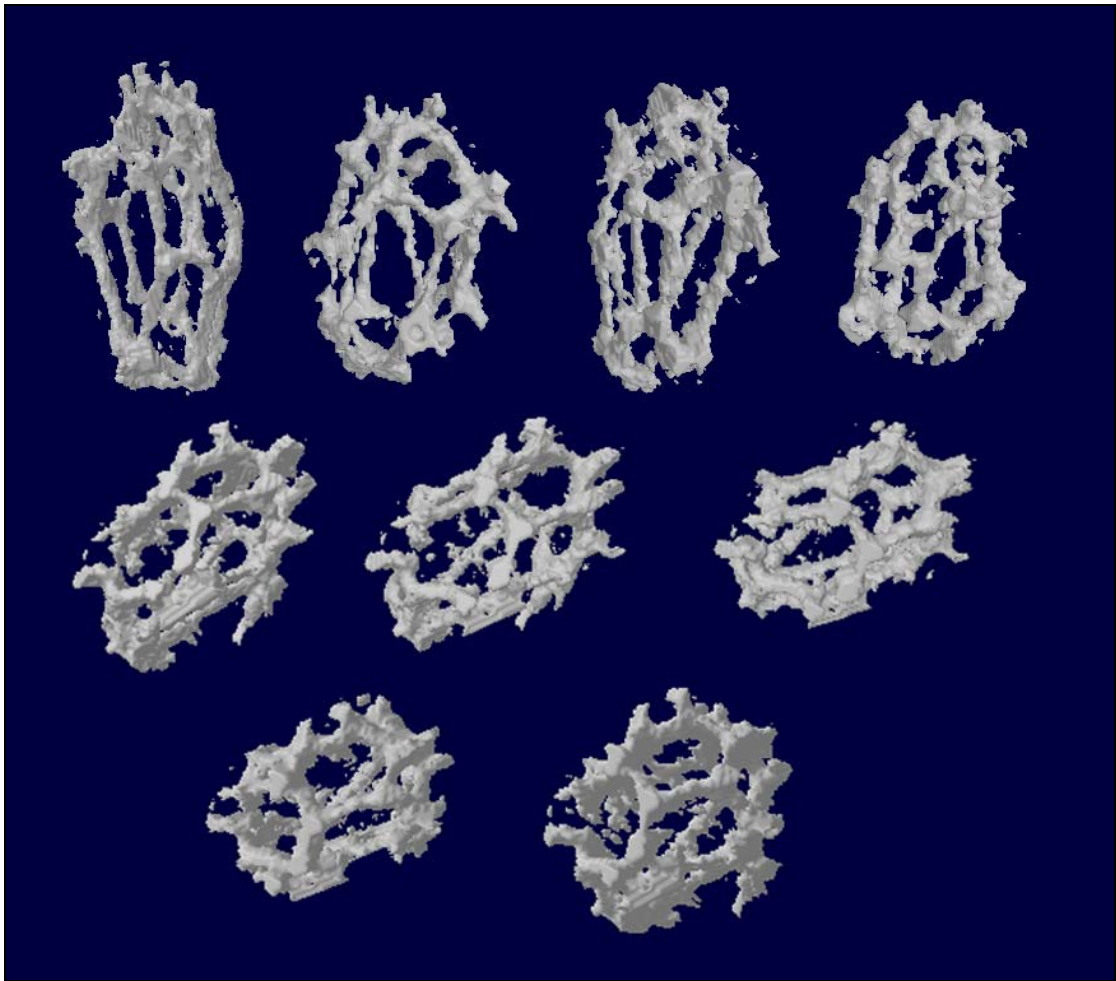
Fig. 3.11 3-D images of cell structure
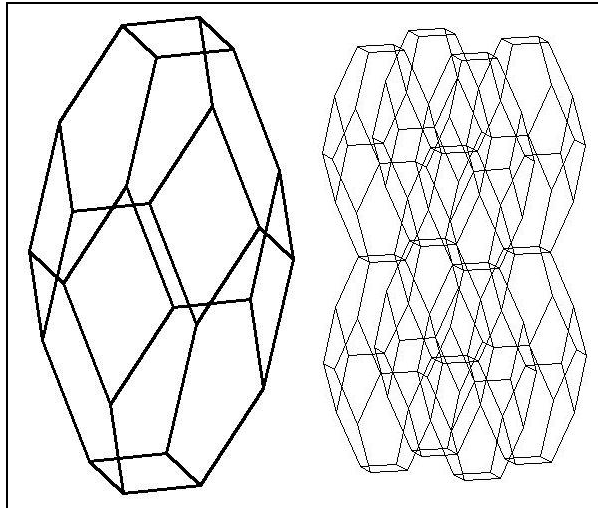
Fig. 3.12 Elongated tetrakaidecahedron cell model

3.5 Microscopic observation of cell struts

In addition to microscopic observations of foam cells using CT scanning, microscopic observations were made on foam struts that define the cell edges. This was undertaken to examine the shape and size of their cross-sections. For this purpose, specimens cut from the foam blocks were examined using an optical microscope set to a magnification of 1000X or 1500X and photographic images were taken.
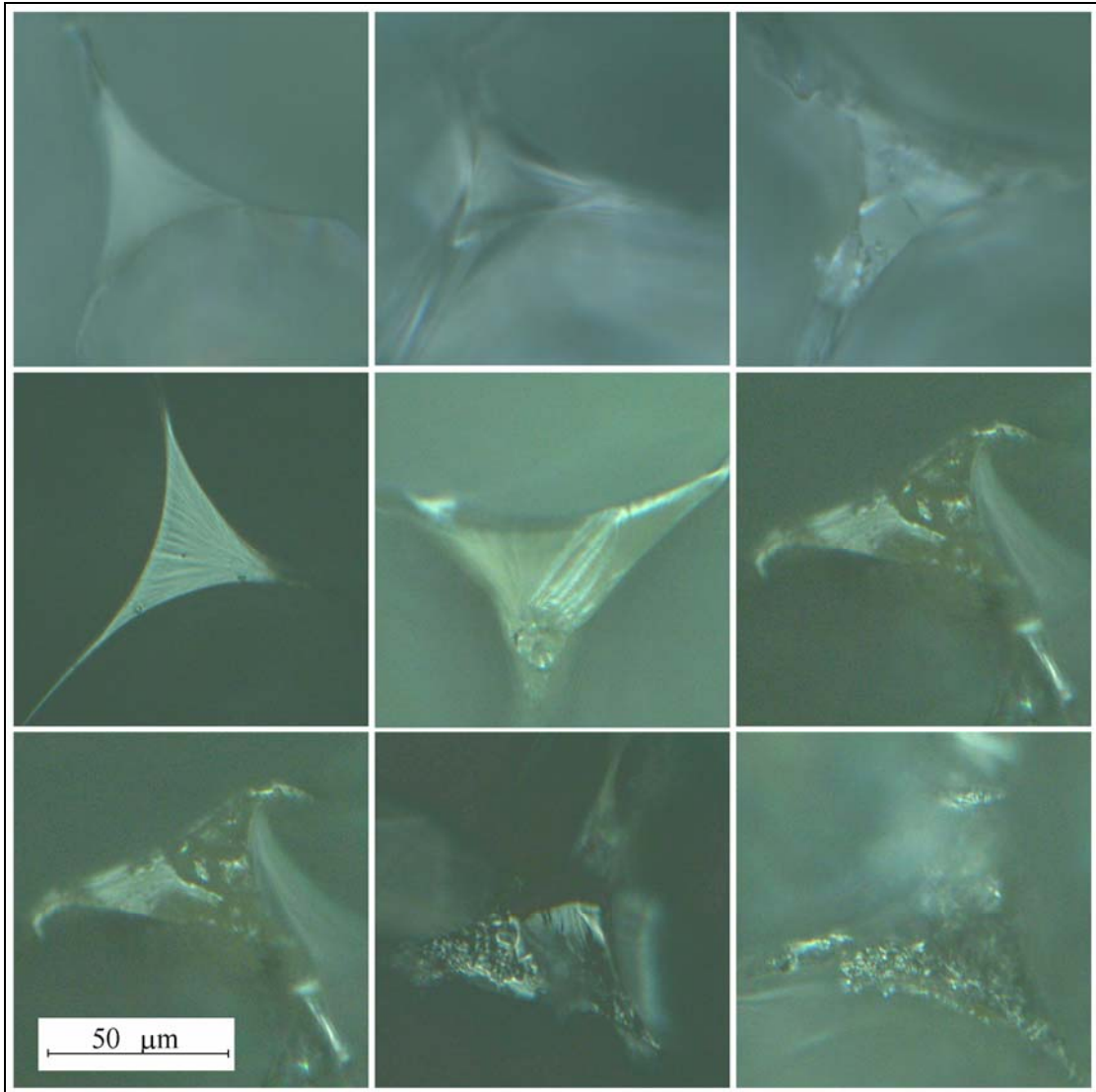
Fig. 3.13 Cross-sections of cell struts in rigid polyurethane foam (foam B; $\rho = 29.5\,\text{kg}/\text{m}^3$)

Fig. 3.13 shows several typical images of cross-sections of cell struts in rigid polyurethane foam. They indicate that the cross-sections is similar in shape to that of the Plateau border [1] geometry shown in Fig. 3.14, which is defined by three circular arcs that touch each other. This is consistent with Plateau's law [1] that proposes that soap bubble surfaces always meet in threes and do so at an angle of 120°, forming an edge called a Plateau border. The same phenomenon is likely to occur in the foaming process in fabricating rigid polyurethane foam, whereby adjacent bubbles in the foam adjust to a stable configuration as the polyurethane hardens (cures). Thus, a Plateau

border shape is assumed by the struts as the material sets. Zhu et al. [40] also observed Plateau border shapes in the cross-sections of struts in foam cells.

To measure the size of these cross-sections, an inscribed circle of radius r was drawn for each image (see Fig. 3.14), and a sample of taking a measurement is shown in Fig. 3.15. The relationship between the inscribed radius r and the outer dimension R, shown in Fig. 3.14, is

$$R = \frac{r}{\sqrt{3}\left(\dfrac{2}{\sqrt{3}} - 1\right)}$$

(3.1)

The average results from these measurements are presented in Table 3.2

Table 3.2 Average dimensions of rigid polyurethane foam struts

	$\rho\left(\text{kg}/\text{mm}^3\right)$	$R\left(\mu\text{m}\right)$
Foam A	23.3	49
Foam B	29.5	51.4
Foam C	35.2	59

Fig. 3.14 also suggests that the thickness of membranes that constitute cell walls is much smaller than the thickness of the struts. Hence, the presence of membranes has minimal influence of the mechanical properties of the foam, which is mainly governed by the response of the struts. This is because the very thin cell walls can easily be broken, folded, or buckled under load [30].
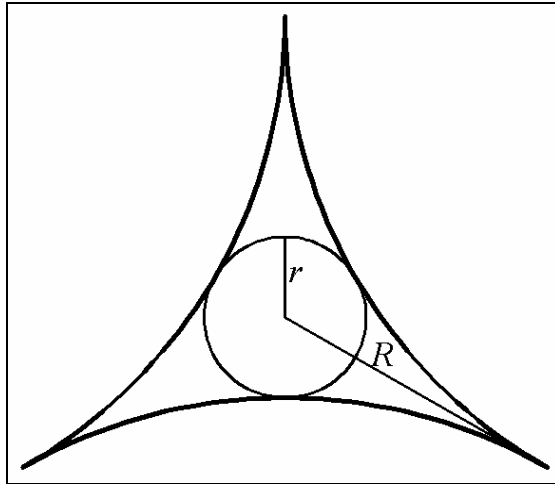
Fig. 3.14 Plateau border
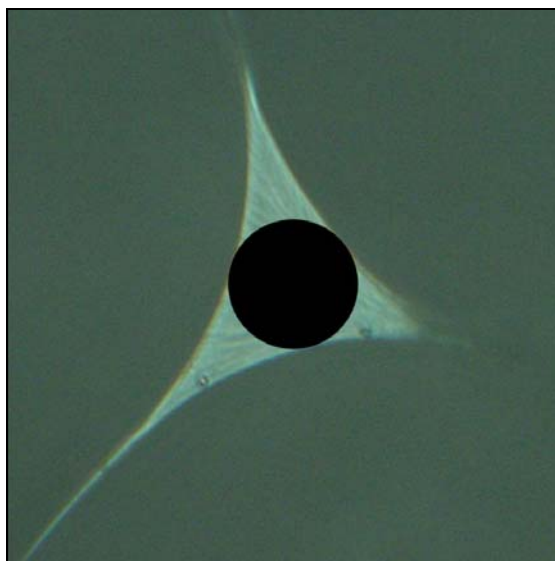
Fig. 3.15 Size measurement

3.6 Microscopic observation of deformation and failure of polyurethane foam

Microscopic observations of foam were carried out to study the nature of its internal structure, as well as its response under tensile and compressive loading. Cuboid specimens cut from foam B ($\rho = 29.5\,\mathrm{kg/m^3}$) were placed under a microscope and loaded using a screw-driven jig (see Fig. 3.16). During the tests, images were recorded using a high speed camera, resulting in photographic sequences of deformation in the cells. Several modes of loading were carried out, i.e. tension and

compression along the foam rise direction (0°), the transverse direction (90°) and 45° to the rise and transverse directions.
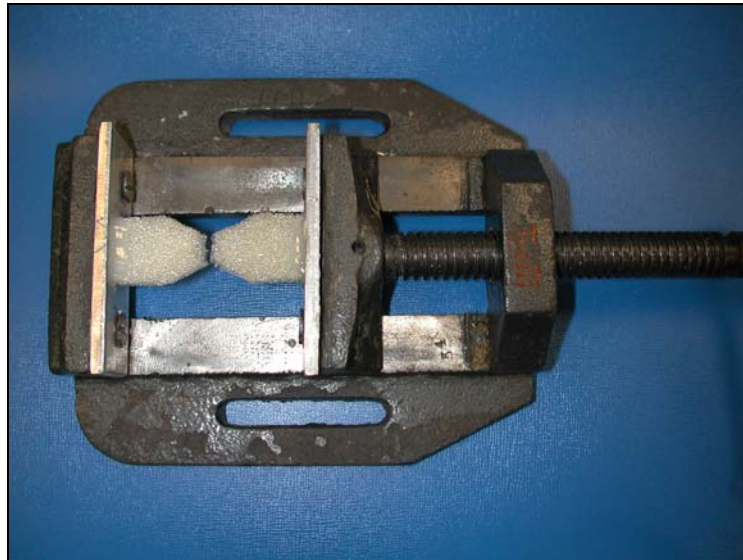
Fig. 3.16 Foam specimen loaded using screw driven jig

3.6.1   Tensile response

Figs. 3.17 and 3.18 show foam behaviour under tension along the rise direction (0°), Figs. 3.19 and 3.20 depict tension along the transverse direction (90°) and Figs. 3.21 and 3.22 illustrate tension along the 45° direction. The pictures indicate that the deformation mechanisms in cells comprise bending and stretching of cell walls and struts, with bending being dominant. Bending can be identified from the change in angle between struts at their interconnections. Several reports – e.g. Ko [28], Gibson et al. [21], Triantafillou et al. [8], Gibson and Ashby [2, 20], Huber and Gibson [26], Maiti et al. [31] and Zhu et al. [40, 41] – have also stated that bending of cell struts is the primary deformation mechanism in foam. It is also evident from the pictures that fracture occurs by crack propagation through struts and cell wall membranes, perpendicular to the loading direction.
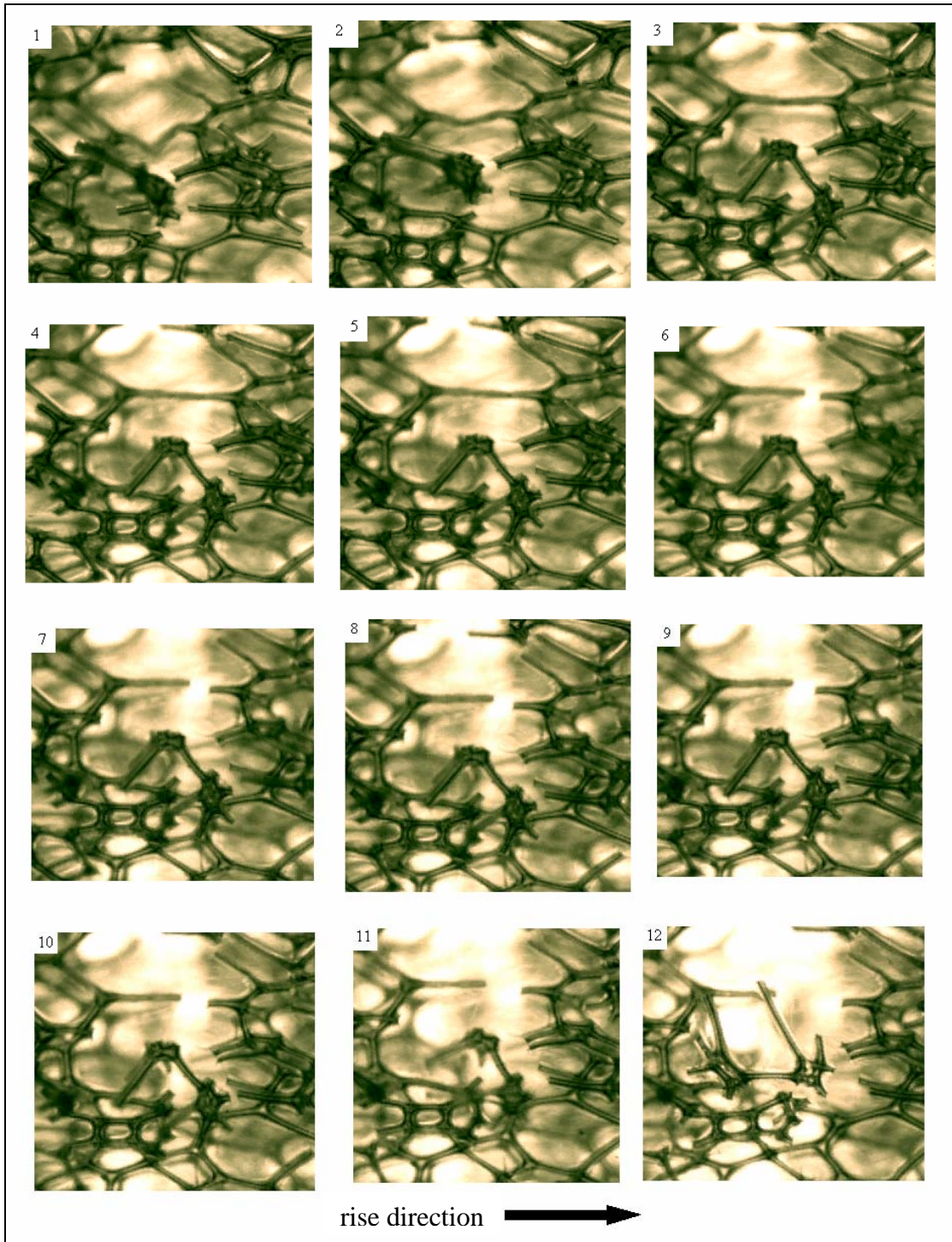
Fig. 3.17 Micrographs of fracture propagation for tension along the foam rise direction
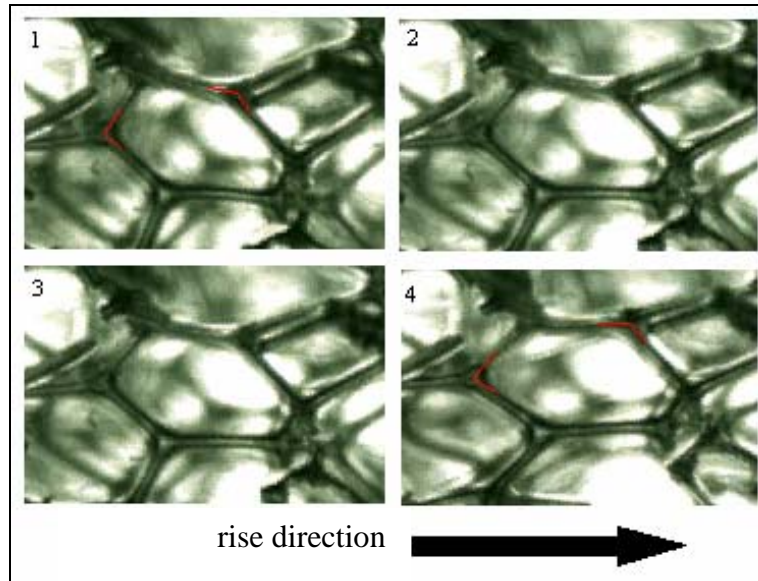
Fig. 3.18 Micrographs of cell deformation for tension along the foam rise direction
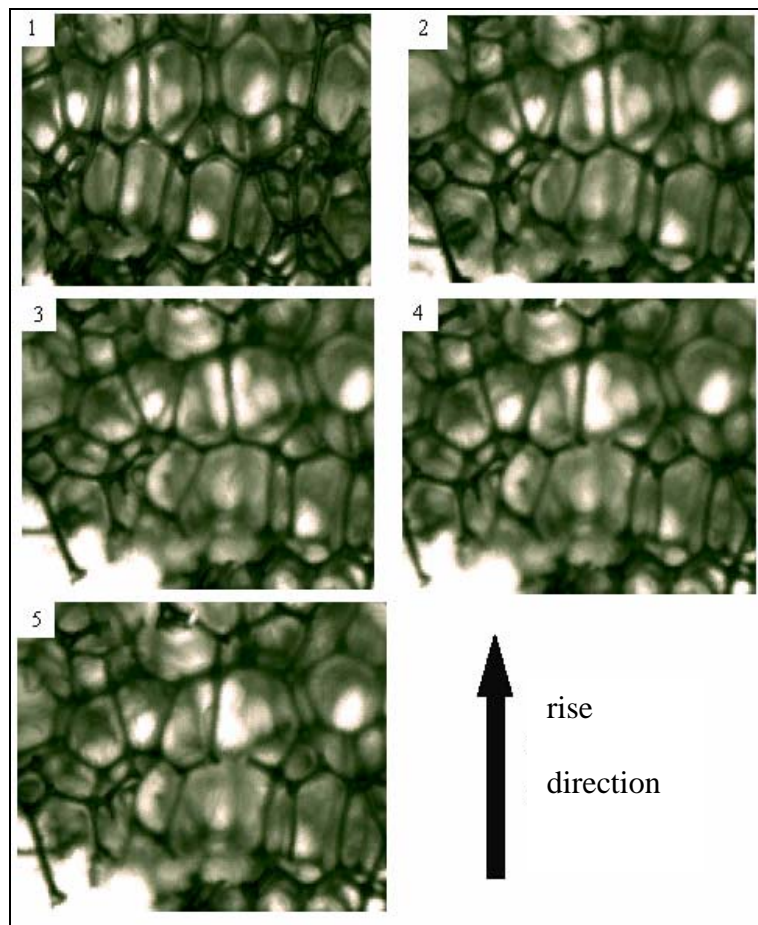
Fig. 3.19 Micrographs of fracture propagation for tension along the transverse direction
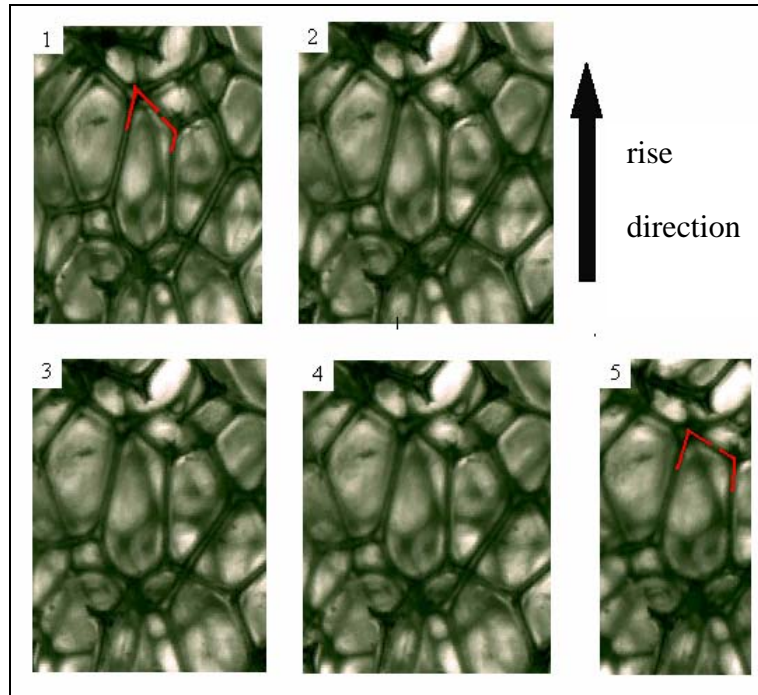
Fig. 3.20 Micrographs of cell deformation for tension along the transverse direction
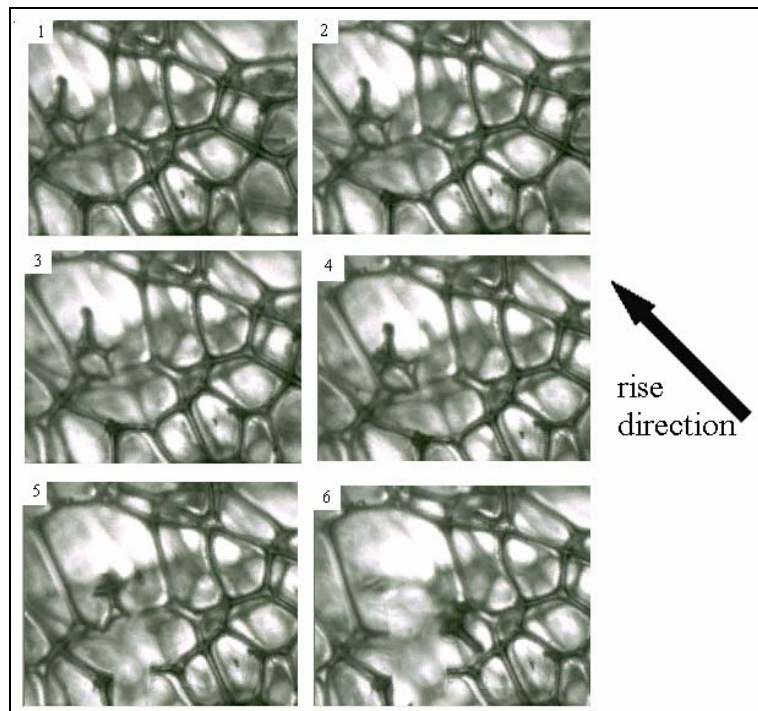
Fig. 3.21 Micrographs of fracture for tension along the 45° to the foam rise direction
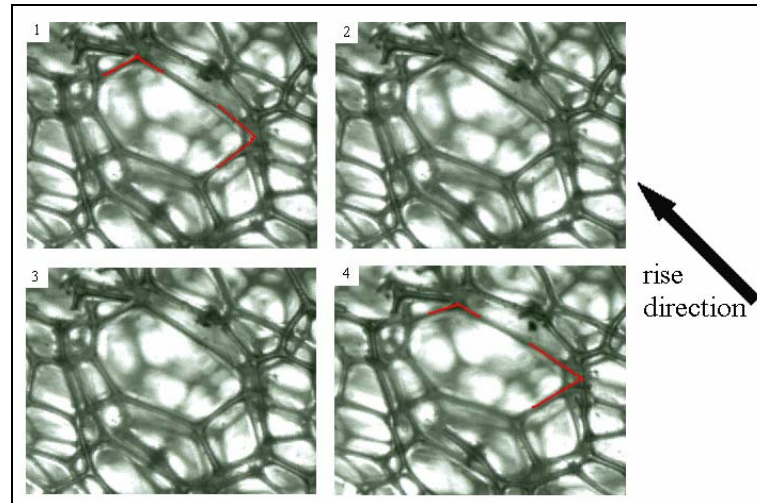
Fig. 3.22 Micrographs of cell deformation for tension along the 45° to the foam rise direction

3.6.2　Compressive response

Fig. 3.23 shows the deformation in cells for compression along the rise direction (0°), while Fig. 3.24 shows the response for compression in the transverse direction (90°). Fig. 3.25 depicts the response for compression along the 45° direction. These pictures demonstrate that deformation initiates via bending and contraction of struts, followed primarily by buckling of compressed struts or plastic bending of struts. The bending and shortening of struts, with bending as the main mechanism, correspond to linear elastic deformation, while the buckling and plastic deformation of the struts are associated with inelastic behaviour in plateau phase of the stress-strain response.

Note that during deformation, the segments of the struts at their interconnections do not exhibit much bending. This implies that deformation occurs away from these end segments because the portions near the interconnections are stiffer and the struts are thicker there. Moreover, the membranes attached to these intersections are also thicker and thus contribute to the bending resistance (see Fig. 3.26). The length of these rigid portions were measured and Fig. 3.27 shows some of these measurements. The average length of the rigid segment is 48.6 μm or about 95 % of the average outer dimension of the strut cross-section R (see Section 3.5)

43
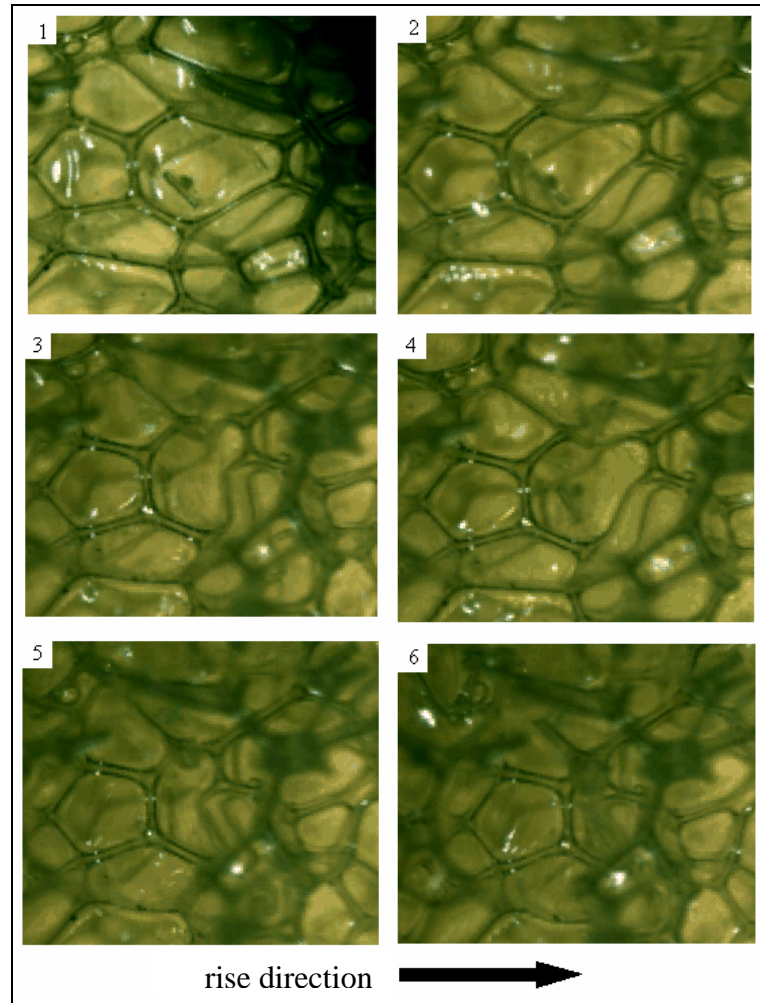
Fig. 3.23 Micrographs of cell deformation for compression along the foam rise direction
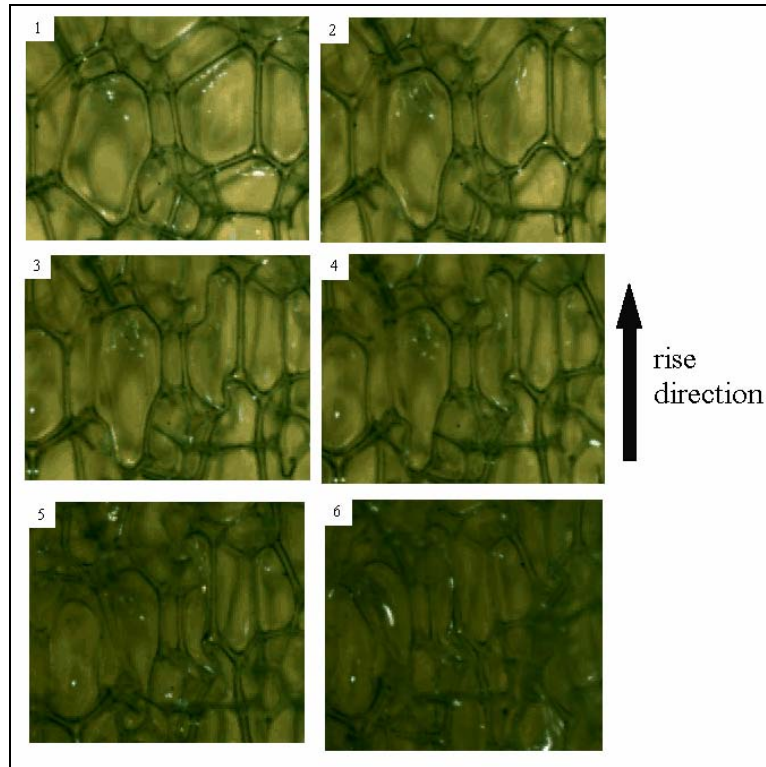
Fig. 3.24 Micrographs of cell deformation for compression along the transverse direction
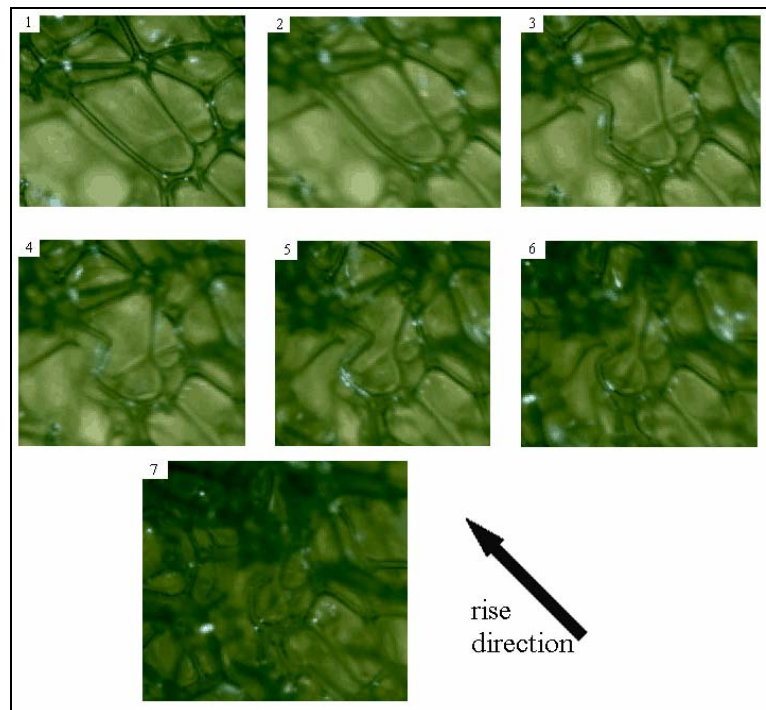
Fig. 3.25 Micrographs of cell deformation for compression in the 45° to the foam rise direction
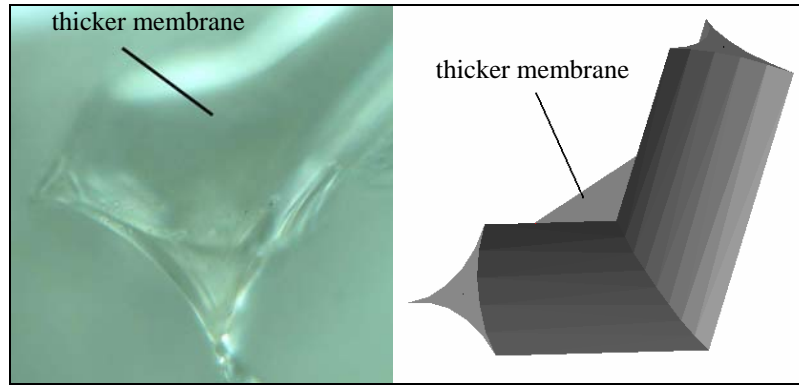
Fig. 3.26 Thick membrane at struts interconnection
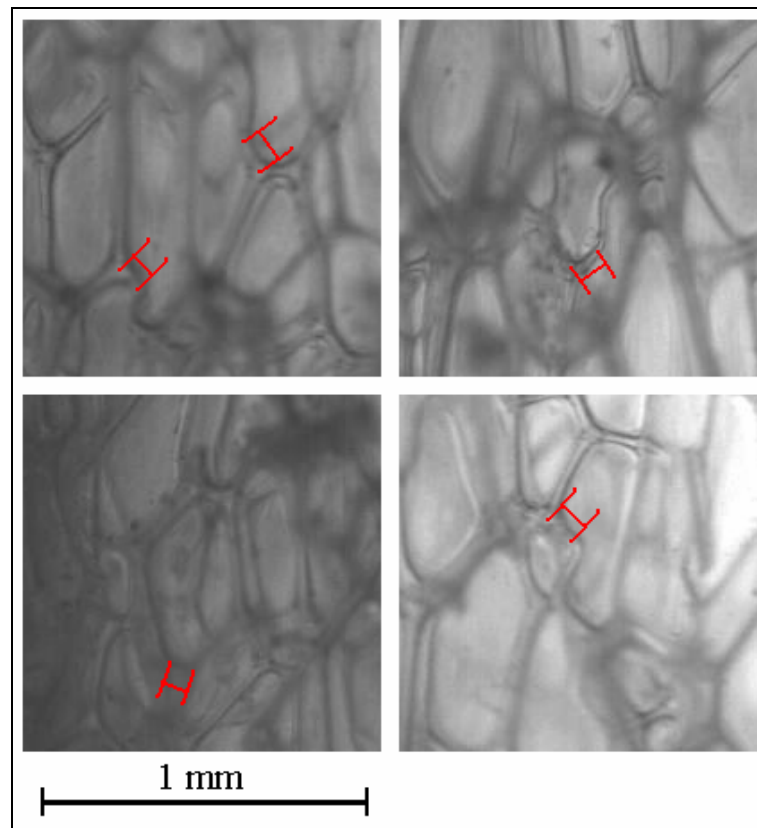
Fig. 3.27 Measurements of rigid strut segments

3.7 Mechanical properties of solid polyurethane

Other than the cell structure, the material properties of the solid material in the struts and walls also determine the mechanical properties of the foam. Several mechanical tests were therefore performed on solid polyurethane specimens to obtain their mechanical properties – i.e. stiffness and tensile strength. The tests included compression, tension and three-point bending. Solid polyurethane was made by mixing the polyurethane resin with the hardener and curing it inside a closed tube to

prevent foaming. The resulting samples were essentially solid, but not entirely homogeneous, because there was still a small amount of gas produced that could not be totally expelled. Nevertheless, the samples showed a good degree of homogeneity near the wall of the container. Consequently, the central portion was cored out to yield tubular samples with an average density of around 1200 kg/m^3; this is consistent with published values of the density of solid polyurethane [2]. The solid polyurethane samples were then prepared for compression, tension, and three point bending tests.

- For compression tests – Tubular samples were cut to an appropriate length and strain gauges were attached to the sides; Fig. 3.28 shows one of the specimens. The specimens were then loaded in compression using a Shimadzu (model AG-25TB) universal testing machine.

Fig. 3.28 Compression specimen

- For tensile tests – Tubular solid polyurethane samples were split lengthwise and cut into dog-bone shaped specimens. The ends of the specimens were glued onto aluminium plates to facilitate gripping. Strain gauges were then attached to the specimens; Fig. 3.29 shows one of the specimens. The specimens were then loaded using an Instron® (model 5500) universal testing machine.
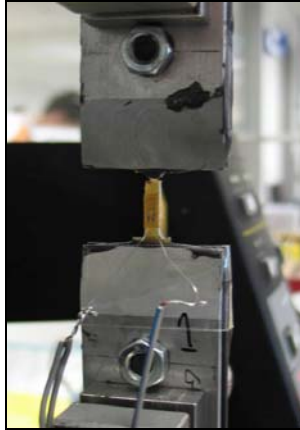
Fig. 3.29 Tension specimen

- For three-point bending tests – Rectangular specimens were cut out from the solid tubular polyurethane sample. The specimens were then loaded transversely using the Instron® universal testing machine with a special jig to facilitate three-point bending; Fig. 3.30 shows one of the specimens being tested.
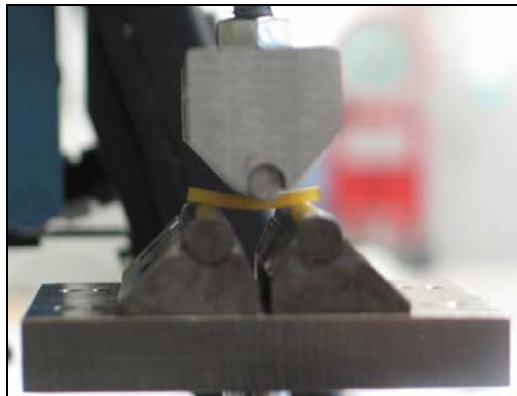
Fig. 3.30 Three point bending test

Two specimens were subjected to elastic compression, and each specimen was loaded three times. Results from the compression tests are presented in form of engineering stress-strain curves. Figs. 3.31 and 3.32 show the stress-strain response for loading and unloading of Specimens 1 and 2. Overlapping of the loading and unloading curves indicates elasticity and the behaviour appears linear. The initial parts of the curve ($\varepsilon < 0.002$ for Specimen 1 and $\varepsilon < 0.002$ for Specimen 2) are not linear probably because contact between the loading plates and the specimens were not perfect.
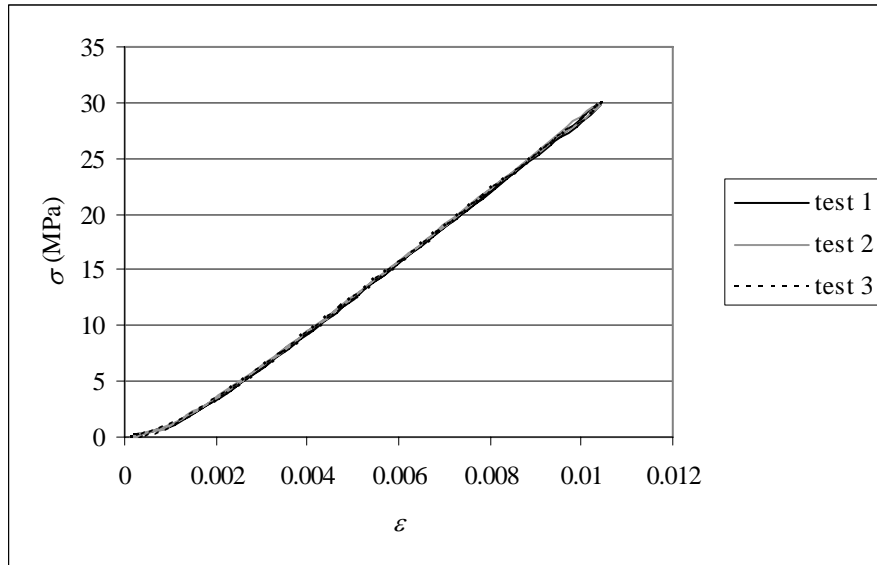
Fig. 3.31 Compression stress-strain curve for Specimen 1
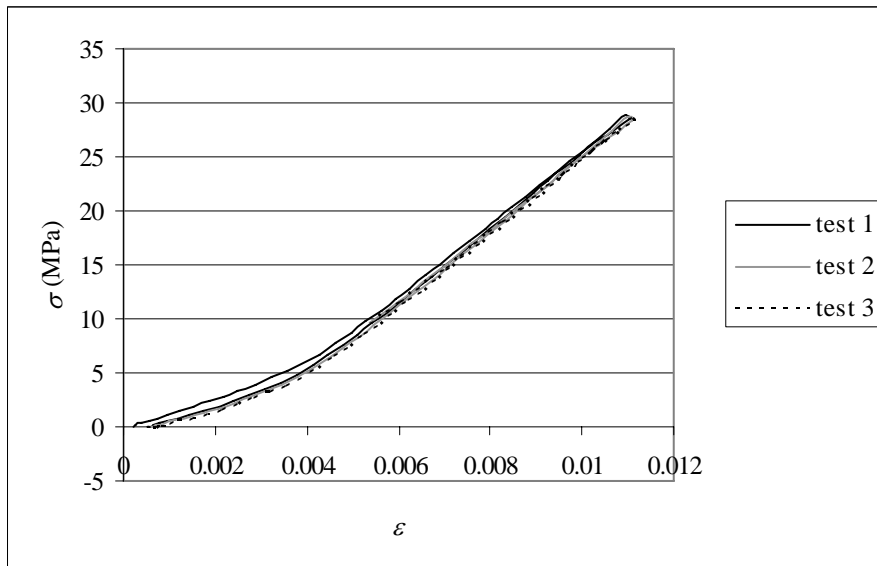
Fig. 3.32 Compression stress-strain curve for Specimen 2

The stiffness of solid polyurethane calculated from the stress-strain curve is shown in Table 3.3. Specimens 1 and 2 show a difference in their stiffness; on average, Specimen 1 has a stiffness of 3.175 MPa, while that of specimen 2 is 3.365 MPa. This difference is relatively small and some variation is expected because the solid polyurethane produced for the fabrication of test specimens was not perfectly homogeneous. Even though no gassing agent was used in making these specimens, the reaction between the polyurethane resin and hardener did generate some small bubbles which remained trapped inside the specimens. Moreover, the mechanical

properties of polymers also depend on the molecular polymer-chain alignment, ageing and oxidation which are not easy to control [2]. The average stiffness of the two specimens is 3.365 MPa.

Table 3.3 Stiffness from compression tests

Specimen 1 (MPa)	Specimen 2 (MPa)
3.169	3.411
3.175	3.309
3.180	3.375

The results from the three-point bending tests are in the form of load-displacement curves. Figs. 3.33 – 3.35 show the results obtained from these tests. In order to obtain the stress-strain curve corresponding to this mode of loading, finite element simulations of the tests were performed using ABAQUS. Structural model having similar dimensions with the three-point bend specimens were established using 100 linear Timoshenko beam elements available in ABAQUS-Standard (B21). The structure was loaded transversely, as shown schematically in Fig. 3.36. Bilinear elastic-plastic material properties were assumed and adjusted to obtain responses similar to the actual specimens in terms of load-displacement curves shown in Figs. 3.33-3.35. It was found that the mechanical properties of solid polyurethane could be approximated by an isotropic elastic-plastic material model with a bilinear stress-strain response. Table 3.4 shows the stiffness and the yield strength determined from results based on comparing FEM simulations and test data.
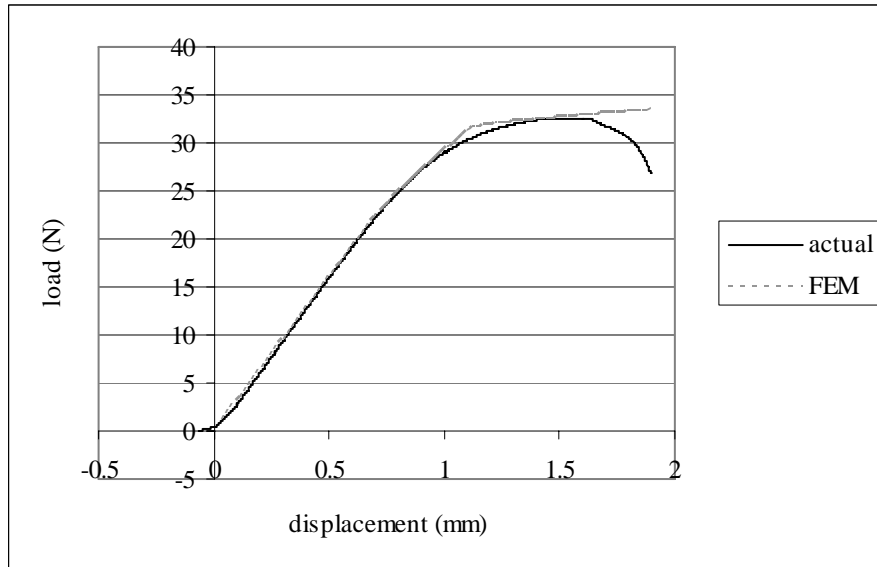
Fig. 3.33 Load-displacement curve for three-point bending test of Specimen 1
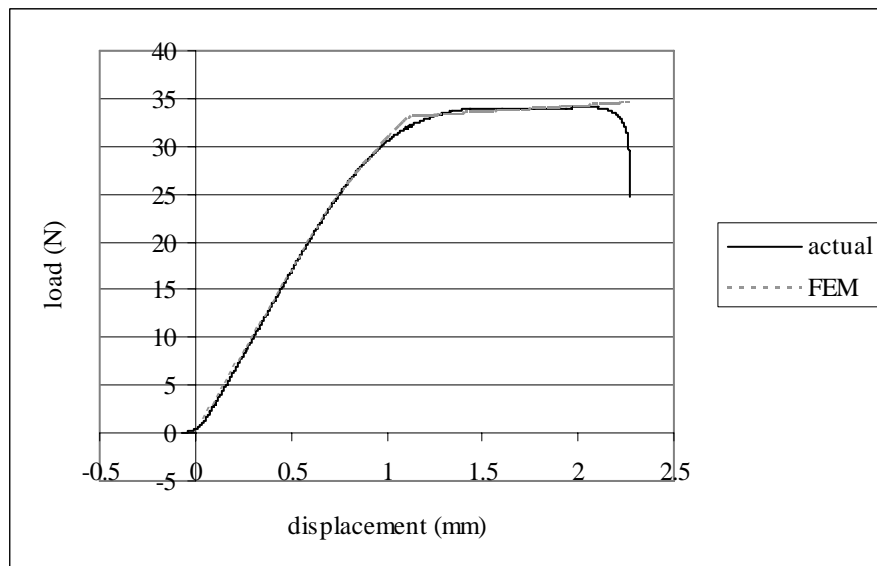
Fig. 3.34 Load-displacement curve for three-point bending test of Specimen 2
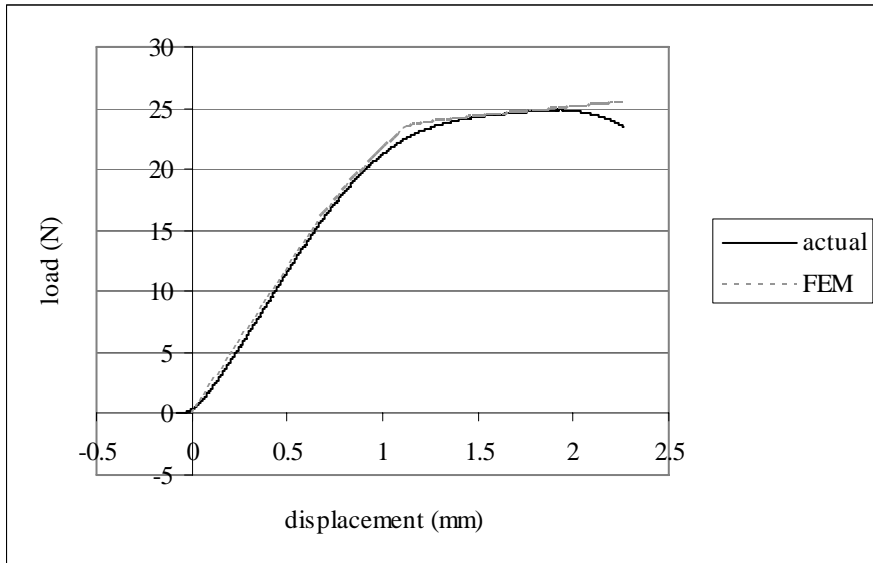
Fig. 3.35 Load-displacement curve for three-point bending test of Specimen 3
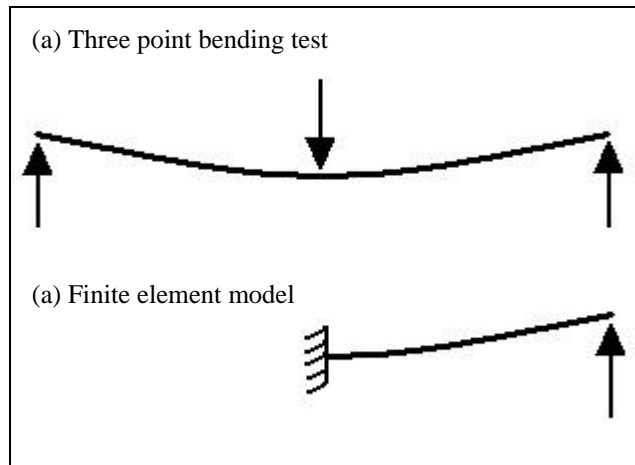
Fig. 3.36 Three-point bending test and its finite element model

Table 3.4 Stiffness and yield strength from three point bending tests

	Dimension: length ; width ; thickness (mm)	Stiffness (MPa)	Yield strength (MPa)	Tensile strength (MPa)
Specimen1	17.93 ; 3.29 ; 2.23	2610	68	73
Specimen2	17.93 ; 2.89 ; 2.4	2520	70	72
Specimen3	17.93 ; 1.99 ; 2.48	2340	67.50	74
Average		2490	68.5	73

As with compression tests, engineering stress-strain curves were obtained from tension tests. Fig. 3.37 shows the results, whereby the curve is initially approximately linear, followed by some non-linearity before fracture. The curves for the three specimens show little scatter in term of their initial linear slope (i.e. the stiffness), but shows significant scatter in terms of the fracture strain. This is due to the lack of

perfect homogeinity of the specimens, whereby the gas bubbles inside the specimens introduce stress concentration during the tests and hence affects the fracture properties. These curves were used to calculate the stiffness and the yield strength of the specimens. The stiffness was obtained from the slope of the linear portion of the curve, while the yield strength was obtained using a 0.002 offset strain line from the linear response and tensile the strength was derived from the maximum stress attained.
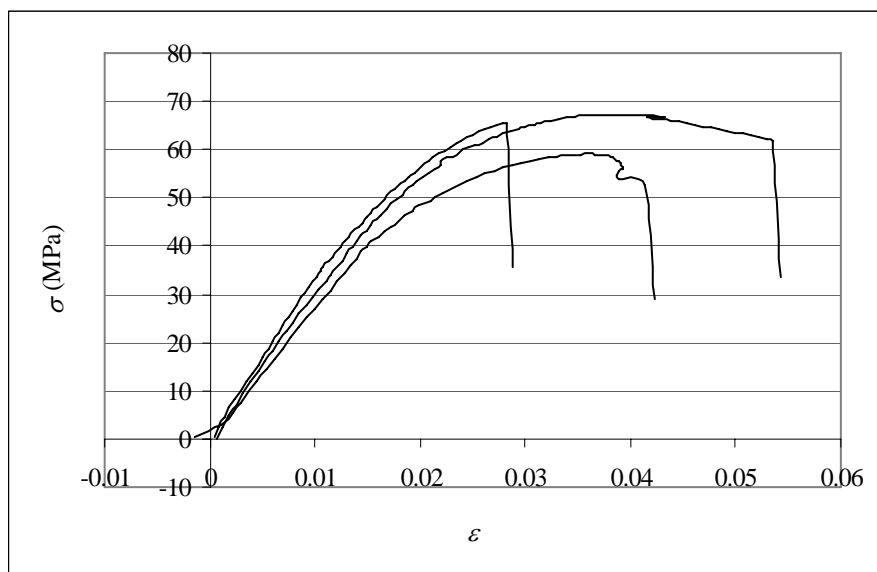
Fig. 3.37 Stress-strain curves from tension tests
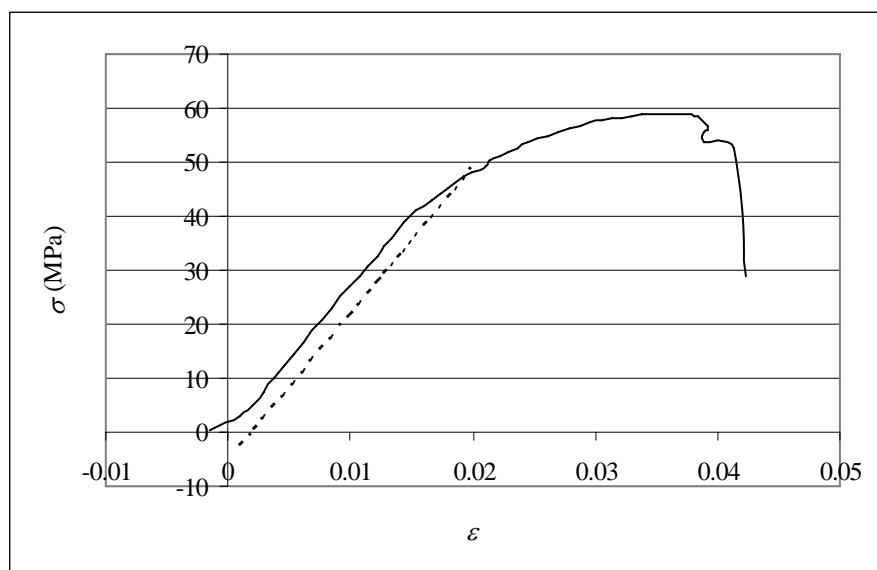
Fig. 3.38 Determination of yield strength

Table 3.5 Mechanical properties from tensile tests

	Stiffness (MPa)	Yield Strength (MPa)	Tensile Strength (MPa)	Fracture strain
Specimen 1	2718	48	59	0.041
Specimen 2	2952	54	67	0.054
Specimen 3	3387	50	66	0.028
Average	3019	51	64	0.041

Table 3.5 shows the stiffness, yield strength, tensile strength, and failure strain values derived from tensile tests on solid polyurethane. Although there is scatter in the data, the variation is smaller than that from bending tests. The data from tensile tests are more consistent, especially for the stiffness, the yield strength and the tensile strength. Thus, this data is used in subsequent development of a cell model in this investigation.

3.8 Summary

The mechanical properties of rigid polyurethane foam were investigated by performing tensile tests on foam samples. The influence of loading direction, foam density, and cell anisotropy on these mechanical properties was examined. Results show that foam stiffness and strength decrease with angle between the loading and the foam rise direction. This arises from the orientation of the struts in cells that make them harder to bend for loading in rise direction. Moreover, more struts are required to be broken to initiate failure for loading in the rise direction, making the foam stronger in this direction. The results also show that foam stiffness and strength increase with density, and that anisotropy in the mechanical properties increases with anisotropy in cell geometry.

Microscopic observations of the cross-section of cell struts show that they have a shape similar to that of a Plateau border [1]. This is probably because cell formation during the foaming process follows Plateau's law [1] that relates minimum energy with a stable structure. Microscopic observation of polyurethane foam loaded under

tension and compression show that the main mechanism governing foam deformation is the bending of cell struts and walls; other researchers [2, 8, 20, 21, 26, 28, 31, 40, 41] have also reported similar findings. The images also reveal that the portions of the struts near their interconnections with other struts are stiffer and do not flex during deformation, because the thickness of these portions are relatively larger and their deformation is constrained by thicker membranes at the interconnections. They also show that fracture in the foams occurs by crack propagation through struts and cell wall membranes, perpendicular to the loading direction

Micro CT scan images show that the shape of polyurethane foam cells bears a high degree of resemblance to an elongated tetrakaidecahedron, probably because a tetrakaidecahedron is a stable polyhedral geometry when the minimum surface energy and the energy criteria defined in Plateau's law [1] are considered [39, 40].

Compression, three-point bending, and tensile tests were performed on solid polyurethane to obtain the stiffness, yield strength and tensile strength properties. These data will be used in the development of a cell model for foam. The experimental data exhibited some scatter because the solid polyurethane samples were not completely homogeneous, as some tiny gas bubbles generated from reaction between the polyurethane resin and the hardener were still trapped inside. Nevertheless the data obtained is considered valid for the formulation of foam models in the following chapters.

Chapter 4   Analytical Model of Idealized Cell

This chapter describes the development of idealized cell models for the rigid polyurethane foam studied. Simplified cell assemblies comprising identical cells are established to facilitate analysis and derive the essential load-deformation characteristics of foam. Variations to the model will be examined in Chapter 5. Two analytical open cell models are proposed – a rhombic dodecahedron and a tetrakaidecahedron. Both are open celled even though the actual rigid polyurethane foam has closed cells, because the membranes that make up the walls are very thin compared to the thickness of the cell struts and corners; hence, the foam behaves as if it is open celled [26, 30] (see Section 3.5). These two geometries are selected because both of them can be assembled in three dimensions to fill space. Small deformation analysis based on linear elastic-brittle fracture material behaviour will be developed. This is aimed at obtaining expressions to define the mechanical properties of foam such as stiffness, tensile strength, and Poisson's ratio.

4.1   Rhombic dodecahedron cell model

Fig. 4.1 shows an elongated rhombic dodecahedron open cell (i.e. polyhedron comprising twelve parallelograms). The cell model is elongated in the z-direction, corresponding to the foam rise direction, in order to incorporate the geometric anisotropy observed in actual foam cells. This model can be assembled such that it fills space in three dimensions, forming a structure that consists of cells positioned along an elongated FCC lattice, as shown in Fig. 4.2. The foam properties based on this cell model – i.e. density, stiffness, Poisson's ratio, and tensile strength – will be derived and discussed. For this analysis, the following definitions and assumptions are made:

56

- The lengths $\hat{L}$ of the struts at the edges of each rhombic dodecahedron are the same.

- The geometric anisotropy ratio, i.e. the ratio between the cell dimension in the rise direction to that in the transverse direction, can be defined by $\tan\theta$ where θ is shown in Fig. 4.5 (see Figs. 4.3-4.5).

- The struts have a constant cross-sectional area A and a constant second moment of area I, such that

$$C_1 = \frac{I}{A^2}$$

(4.1)

- The maximum distance from the surface of the strut to its centroidal axis is R and the relationship between R and A is

$$C_2 = \frac{R}{\sqrt{A}}$$

(4.2)

- The struts are assumed to be made of an isotropic linear elastic material with stiffness E_s and tensile fracture stress $\sigma_{\max s}$.

- The struts follow the Bernoulli-Euler beam theory when they deform.

- Failure of the model is assumed to occur when any location in a strut attains the tensile fracture stress $\sigma_{\max s}$.
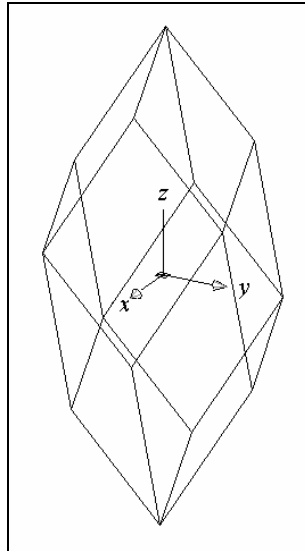
Fig. 4.1 Elongated rhombic dodecahedron cell
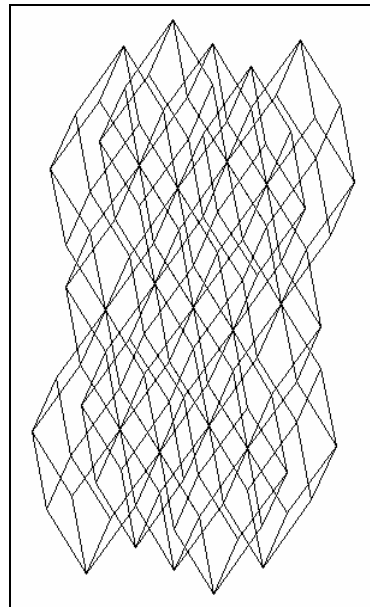
Fig. 4.2 Elongated FCC structure made from rhombic dodecahedron cells

4.1.1 Relative density

The length of the struts in the cell model is assumed to be much longer than the size of the vertices; hence, the volume of the struts can be approximated by taking the total length of the struts multiplied by their cross-section area. By using the repeating unit shown in Figs. 4.3-4.5, the foam relative density, i.e. ratio of the overall foam density (ρ) to the density of the solid material in the cell struts and walls (ρ_s), can be defined.

$$\frac{\rho}{\rho_s} = \frac{4LA\sqrt{\cos^2\theta + 1}}{\dfrac{(4L\cos\theta)^2}{2}2L\sin\theta}$$

(4.3)

$$\Rightarrow \frac{\rho}{\rho_s} = \frac{\sqrt{\cos^2\theta + 1}}{4\sin\theta\cos^2\theta}\frac{A}{L^2}$$

(4.4)

4.1.2 Mechanical properties in the z-direction

The z-direction is the direction of cell elongation in this model, which corresponds to the foam rise direction in actual foam. To derive the elastic stiffness and the Poisson's ratios for this cell model in the z-direction, an analysis of structural deformation for loading in this direction is performed. From symmetry and similarity, the analysis can be simplified such that only the fundamental repeating unit (shown in bold lines in Fig. 4.3) is considered. Symmetry of this repeating unit with its neighbours will be considered in imposing boundary conditions. More detailed views are shown in Figs. 4.4 and 4.5, which depict three-dimensional and two-dimensional views respectively. Fig. 4.5 also defines the geometrical quantities used in the analysis.
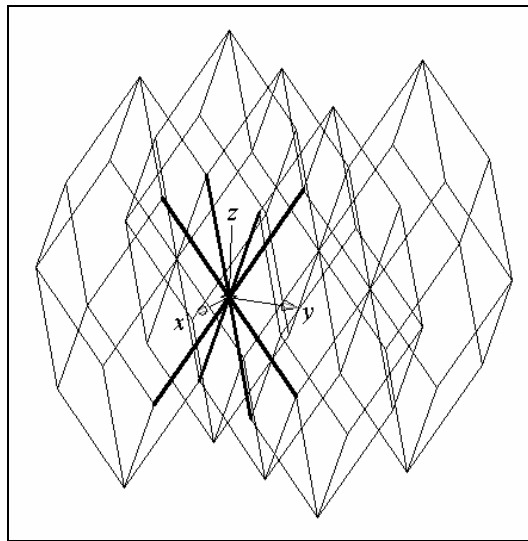
Fig. 4.3 Repeating unit for the analysis of an elongated rhombic dodecahedron cell loaded in the z-direction
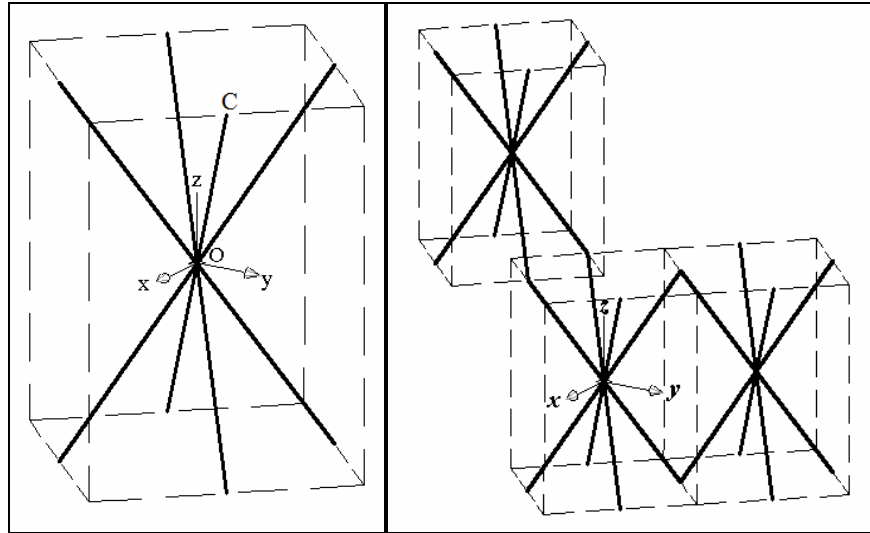
Fig. 4.4 Three-dimensional view of repeating unit in the analysis of an elongated rhombic dodecahedron cell loaded in the *z*-direction
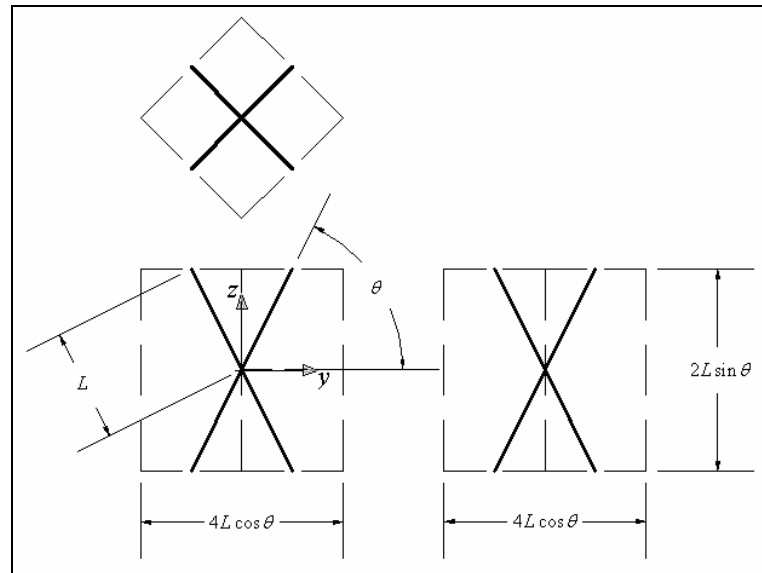
Fig. 4.5 Two-dimensional view of repeating unit in the analysis of an elongated rhombic dodecahedron cell loaded in the *z*-direction

Taking into consideration similarity and symmetry, the analysis can be further simplified to the analysis of just one of the struts – e.g. OC – and then applying it to other similar struts (Fig. 4.4). Fig. 4.6(a) and (b) show respectively, a 3-dimensional view of OC and its projection onto the plane ODCB. For the purpose of analysis, the angle α is defined as a parameter. It can be seen from Fig. 4.6(a) that the geometric quantities $L, \hat{L}, \theta$, and α are interrelated via the following:

$$\tan \alpha = \frac{1}{\sqrt{2}} \tan \theta$$

$$(4.5)$$

$$\sin \alpha = \frac{\sin \theta}{\sqrt{\cos^2 \theta + 1}}$$

$$(4.6)$$

$$\cos \alpha = \frac{\sqrt{2} \cos \theta}{\sqrt{\cos^2 \theta + 1}}$$

$$(4.7)$$

$$\hat{L} = L\sqrt{\cos^2 \theta + 1}$$

$$(4.8)$$
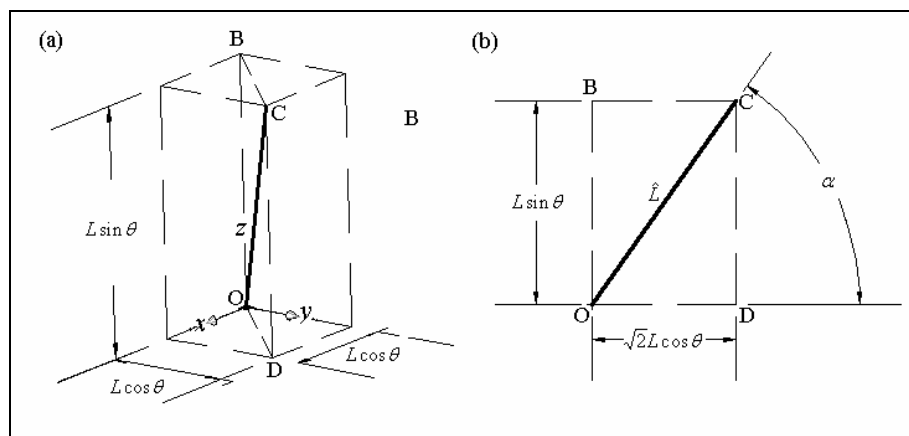
Fig. 4.6 Strut OC
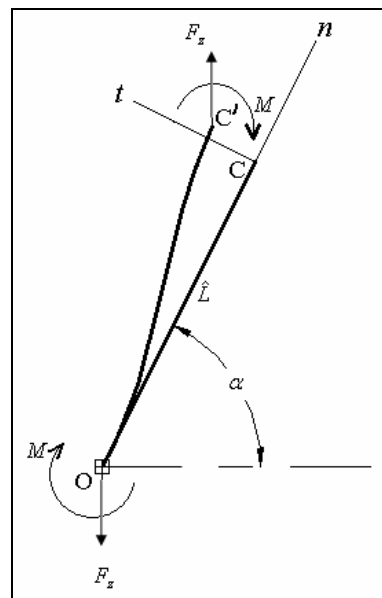
Fig. 4.7 Deformation of strut OC in plane OBCD

For convenience, analysis of the deformation of strut OC can be done with respect to the plane ODCB (see Figs. 4.6 and 4.7) and then expressed in terms of the

Cartesian space defined by the coordinates *xyz*. When the rhombic dodecahedron structure is loaded in the *z*-direction, point C moves upwards and left to point C' (Fig. 4.7). Note that there is no force in the horizontal planes (i.e. parallel to the *xy*-plane) because the struts are free to move in the *x* and *y* directions. Because of symmetry about the line CD (Fig. 4.6) with another strut in the adjacent repeating unit, the slope of the strut at point C with respect to the plane ODCB does not change during deformation, i.e. the slope remains equal to α with respect to the *xy*-plane. Hence, the bending moment *M* in the strut at point C is related to the vertical force F_z at that cross-section by

$$\frac{F_z \hat{L}^2 \cos \alpha}{2 E_s I} - \frac{ML}{E_s I} = 0$$

(4.9)

$$\Rightarrow M = \frac{F_z \hat{L} \cos \alpha}{2}$$

(4.10)

Thus, the respective displacements of point C in the axial (*n*) and transverse (*t*) directions are

$$u_n = \frac{\hat{L}}{AE_s} F_z \sin \alpha$$

(4.11)

and

$$u_t = \frac{F_z \hat{L}^3 \cos \alpha}{3 E_s I} - \frac{ML^2}{2 E_s I}$$

$$= \frac{F_z \hat{L}^3 \cos \alpha}{3 E_s I} - \frac{F_z L \cos \alpha}{2} \frac{L^2}{2 E_s I}$$

$$= \frac{F_z \hat{L}^3 \cos \alpha}{12 E_s I}$$

(4.12)

$$\Rightarrow u_t = \frac{\hat{L}^3}{12 E_s I} F_z \cos \alpha$$

(4.13)

These displacements can be related to the deformation of the repeating units in the x, y and z-directions by using the geometrical relationships inferred from Figs. 4.6 and 4.7, and considering symmetry and similarity of the struts in Fig. 4.4 . The results are:

$$\delta_x = \delta_y = \frac{2}{\sqrt{2}}\left(u_n \cos\alpha - u_t \sin\alpha\right)$$

$$= \left(\frac{\hat{L}}{AE_s} - \frac{\hat{L}^3}{12E_sI}\right)\sqrt{2}F_z \sin\alpha\cos\alpha$$

$$\tag{4.14}$$

$$\delta_z = 2\left(u_n \sin\alpha + u_t \cos\alpha\right)$$

$$= \left(\frac{\hat{L}}{AE_s}\sin^2\alpha + \frac{\hat{L}^3}{12E_sI}\cos^2\alpha\right)2F_z$$

$$\tag{4.15}$$

Substituting Eqs. (4.5)-(4.8) into Eqs. (4.14) and (4.15) replacing $\hat{L}$ and α by L and θ:

$$\delta_x = \delta_y = \left(\frac{L\sqrt{\cos^2\theta+1}}{AE_s} - \frac{\left(L\sqrt{\cos^2\theta+1}\right)^3}{12E_sI}\right)\sqrt{2}F_z \frac{\sin\theta}{\sqrt{\cos^2\theta+1}}\frac{\sqrt{2}\cos\theta}{\sqrt{\cos^2\theta+1}}$$

$$= \left(\frac{L}{AE_s} - \frac{L^3}{12E_sI}\left(\cos^2\theta+1\right)\right)\frac{2\sin\theta\cos\theta}{\sqrt{\cos^2\theta+1}}F_z$$

$$\tag{4.16}$$

$$\delta_z = \left(\frac{L\sqrt{\cos^2\theta+1}}{AE_s}\sin^2\theta + \frac{\left(L\sqrt{\cos^2\theta+1}\right)^3}{12E_sI}2\cos^2\theta\right)\frac{2}{\cos^2\theta+1}F_z$$

$$= \left(\frac{L}{AE_s}\sin^2\theta + \frac{L^3}{6E_sI}\left(\cos^2\theta+1\right)\cos^2\theta\right)\frac{2}{\sqrt{\cos^2\theta+1}}F_z$$

$$\tag{4.17}$$

Consequently, the strains are obtained by dividing the deformation by the initial lengths.

$$\varepsilon_{xx} = \varepsilon_{yy} = \frac{\delta_x}{2L\cos\theta}$$

$$= \left(\frac{1}{AE_s} - \frac{L^2}{12E_sI}\left(\cos^2\theta+1\right)\right)\frac{\sin\theta}{\sqrt{\cos^2\theta+1}}F_z$$

$$\tag{4.18}$$

$$\varepsilon_{zz} = \frac{\delta_z}{2L\sin\theta}$$

$$= \left(\frac{1}{AE_s}\sin^2\theta + \frac{L^2}{6E_s I}\left(\cos^2\theta + 1\right)\cos^2\theta \right) \frac{1}{\sin\theta\sqrt{\cos^2\theta + 1}} F_z$$

(4.19)

The stress in the z-direction is given by the ratio of the applied force $4F_z$ to the area A_z over which it acts

$$\sigma_{zz} = \frac{4F_z}{A_z} = \frac{F_z}{2L^2\cos^2\theta}$$

(4.20)

The stiffness in the z-direction is obtained by dividing the stress by the strain in the z-direction, while the Poisson's ratios are obtained from the ratios between the appropriate strains.

$$E_{zz} = \frac{\sigma_{zz}}{\varepsilon_{zz}} = \frac{E_s}{\left(\dfrac{2\sin\theta\cos^2\theta}{\sqrt{\cos^2\theta + 1}}\dfrac{L^2}{A} + \dfrac{\cos^4\theta\sqrt{\cos^2\theta + 1}}{3\sin\theta}\dfrac{L^4}{I} \right)}$$

(4.21)

$$\upsilon_{zx} = \upsilon_{zy} = -\frac{\varepsilon_{xx}}{\varepsilon_{zz}} = -\frac{\varepsilon_{yy}}{\varepsilon_{zz}} - \frac{\left(\dfrac{1}{A} - \dfrac{\left(\cos^2\theta + 1\right)}{12}\dfrac{L^2}{I} \right)\sin^2\theta}{\left(\sin^2\theta\dfrac{1}{A} + \dfrac{\left(\cos^2\theta + 1\right)\cos^2\theta}{6}\dfrac{L^2}{I} \right)}$$

(4.22)

For foams with a low overall density, the term $\dfrac{L^2}{A} = \dfrac{4\sin\theta\cos^2\theta}{\sqrt{\cos^2\theta + 1}}\dfrac{\rho}{\rho_s}$ is much smaller

than $\dfrac{L^4}{I}$ because L is much larger than the dimensions of the cross-section of the cell struts; hence, the elastic stiffness and the Poisson's ratios can be approximated by

$$E_{zz} \approx \frac{3\sin\theta}{\cos^4\theta\sqrt{\cos^2\theta + 1}}\frac{E_s I}{L^4}$$

(4.23)

$$\upsilon_{zx} = \upsilon_{zy} \approx \frac{1}{2}\tan^2\theta$$

(4.24)

The stiffness and the Poisson's ratios can also be defined in terms of the relative density (ratio between the overall density of the foam to that of the solid material in the cells) by substituting Eqs. (4.1) and (4.4) into Eqs. (4.21) and (4.22). The results are:

$$E_{zz} = \frac{E}{\left(\dfrac{1}{2} \dfrac{\rho_s}{\rho} + \dfrac{\left(\cos^2\theta + 1\right)^{3/2}}{48\sin^3\theta} \dfrac{1}{C_1} \left(\dfrac{\rho_s}{\rho}\right)^2 \right)}$$

(4.25)

$$\upsilon_{xz} = \upsilon_{yz} = -\frac{\varepsilon_{xx}}{\varepsilon_{zz}} = -\frac{\left(\sin^2\theta - \dfrac{\sin\theta\left(\cos^2\theta + 1\right)^{3/2}}{48\cos^2\theta} \dfrac{1}{C_1}\left(\dfrac{\rho_s}{\rho}\right) \right)}{\left(\sin^2\theta + \dfrac{\left(\cos^2\theta + 1\right)^{3/2}}{24\sin\theta} \dfrac{1}{C_1}\left(\dfrac{\rho_s}{\rho}\right) \right)}$$

(4.26)
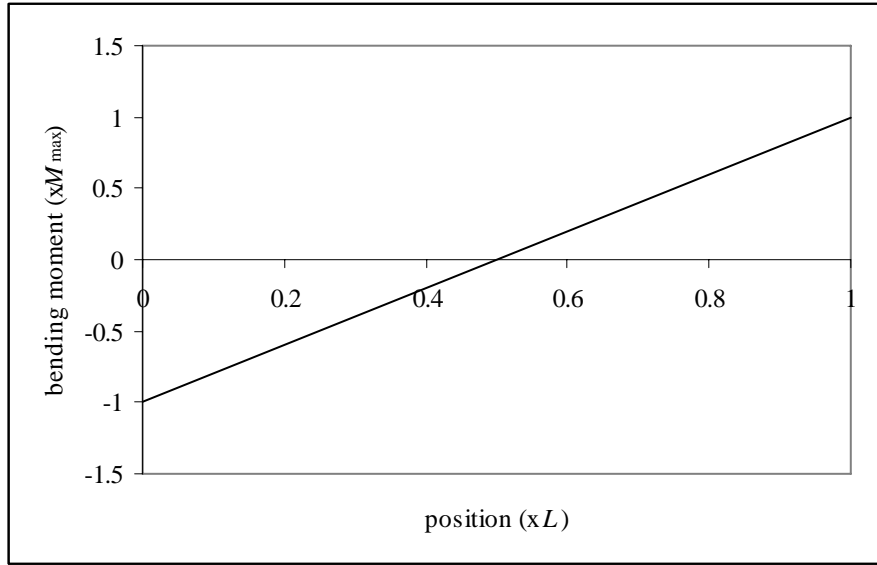
Fig. 4.8 Bending moment distribution along strut OC

The tensile strength of this cell model in the z-direction can also be derived using the repeating unit shown in Figs. 4.3-4.5. Again, the analysis is simplified by considering the failure of one strut, as shown in Fig. 4.6. It can be seen that the maximum normal stress in a strut is attained at the outer surface at both ends because the bending moment is highest there (note that the bending moment along a beam loaded as shown in Fig. 4.7 varies linearly with distance from its ends, as shown in

Fig. 4.8; the maximum bending moment thus occurs at both ends). The stress at these points can be derived by considering a combination of the axial force and the bending moment.

$$\sigma = \frac{F_z \sin\alpha}{A} + \frac{M\,R}{I}$$

(4.27)

Substitution of Eq. (4.10) into (4.27) and equating the stress σ to the failure stress $\sigma_{\max s}$ yields

$$\sigma_{\max s} = \left(\frac{\sin\alpha}{A} + \frac{\hat{L}\,R\cos\alpha}{2I} \right) F_z$$

(4.28)

$\hat{L}$ and α are replaced by L and θ by using Eqs. (4.5)-(4.8):

$$\sigma_{\max s} = \left(\frac{\sin\theta}{\sqrt{\cos^2\theta + 1}} \frac{1}{A} + \frac{\cos\theta}{\sqrt{2}} \frac{L\,R}{I} \right) F_z$$

(4.29)

Finally, by substituting Eq. (4.20), which defines the overall stress, into (4.29), the tensile strength in the z-direction is defined by

$$\sigma_{z\max} = \frac{\sigma_{\max s}}{\left(\dfrac{2\sin\theta\cos^2\theta}{\sqrt{\cos^2\theta + 1}} \dfrac{L^2}{A} + \sqrt{2}\cos^3\theta \dfrac{L^3 R}{I} \right)}$$

(4.30)

Eqs. (4.30) can also be expressed in terms of the relative density by substituting Eqs. (4.1)-(4.4) into it.

$$\sigma_{z\max} = \frac{\sigma_{\max s}}{\dfrac{1}{2}\dfrac{\rho_s}{\rho} + \dfrac{\left(\cos^2\theta + 1\right)^{3/4}}{4\sqrt{2}\left(\sin\theta\right)^{3/2}} \dfrac{C_2}{C_1}\left(\dfrac{\rho_s}{\rho}\right)^{3/2}}$$

(4.31)

4.1.3 Mechanical properties in the *y*-direction

The *y*-direction is the transverse direction for this cell model, which corresponds to the direction perpendicular to the rise direction in actual foam. In order to derive the stiffness and the Poisson's ratios for the *y*-direction, loading of the cell in this

66

direction is analysed. As with loading in the *z*-direction, the analysis of loading in the *y*-direction can also be reduced to the analysis of a single repeating unit, as shown in bold lines in Fig. 4.9. Figs. 4.10 and 4.11 show respectively, more detailed three-dimensional and two-dimensional views of the unit. Although the repeating unit looks the same as that used for the analysis of loading in the *z*-direction, this unit cell is extracted in a different way to simplify the analysis (see Fig. 4.10).
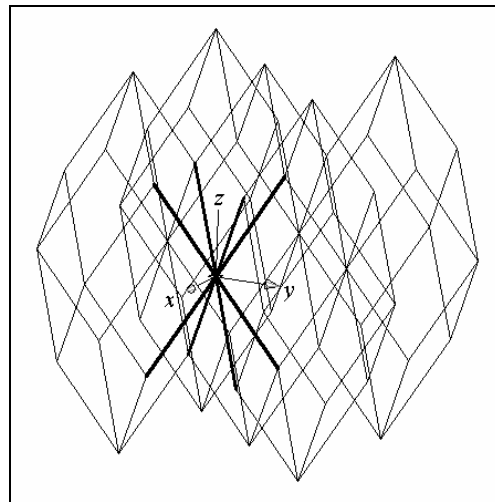
Fig. 4.9 Repeating unit for the analysis of an elongated rhombic dodecahedron cell loaded in the *y*-direction
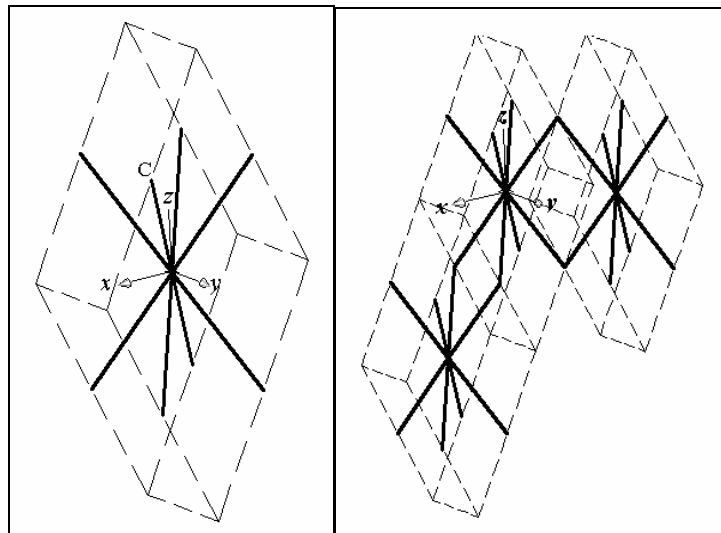
Fig. 4.10 Three-dimensional view of repeating unit for analysis of an elongated rhombic dodecahedron cell loaded in *y*-direction
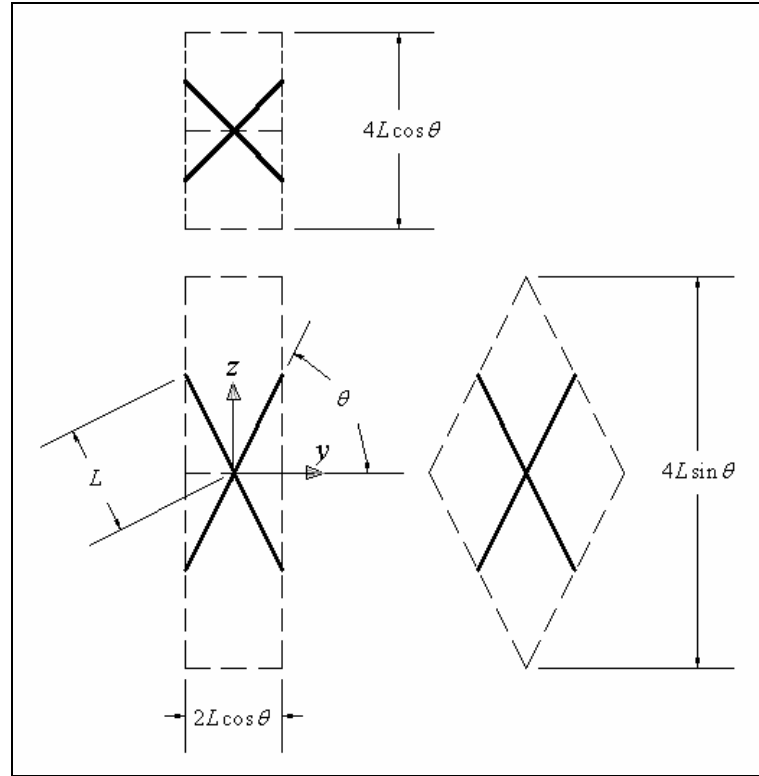
Fig. 4.11 Two-dimensional view of repeating unit for analysis of an elongated
rhombic dodecahedron cell loaded in the *y*-direction

This analysis can also be further simplified to the analysis of one strut – i.e. OC – and then applying it to the other struts. Fig. 4.12(a) and (b) show respectively, the strut OC in a 3-dimensional view and its projection onto the plane OGCH. For the purpose of analysis, an angle β is defined, as illustrated in Fig. 4.12, which also shows that the geometric parameters L, $\hat{L}$, θ, and β are related by

$$\tan \beta = \cos \theta$$

(4.32)

$$\sin \beta = \frac{\cos \theta}{\sqrt{\cos^2 \theta + 1}}$$

(4.33)

$$\cos \beta = \frac{1}{\sqrt{\cos^2 \theta + 1}}$$

(4.34)

$$\hat{L} = L\sqrt{\cos^2 \theta + 1}$$

(4.35)
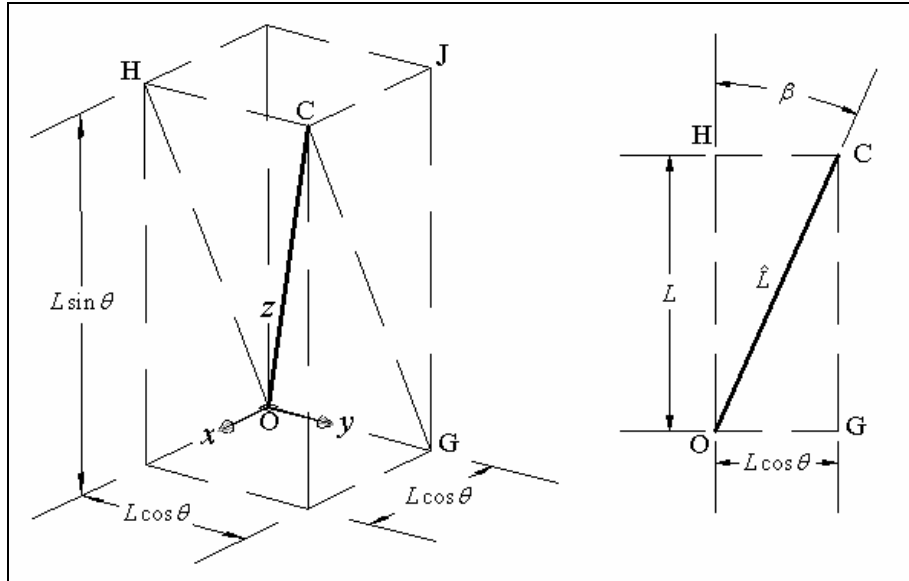
Fig. 4.12 Strut OC
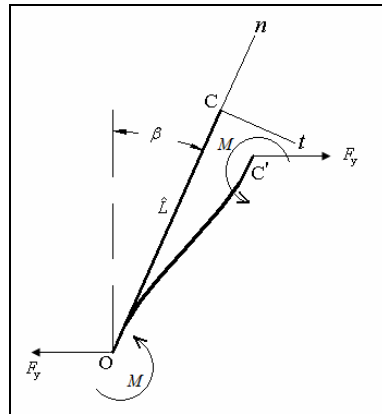
Fig. 4.13 Deformation of strut OC in plane OGCH

Analysis of the deformation of strut OC can be done with respect to the plane OGCH (see Figs. 4.12 and 4.13) and then relating it to the x, y and z coordinate axes. When the rhombic dodecahedron is loaded in the y-direction, point C moves to point C' (see Fig. 4.13). Note that there is no force in the xz-plane because the struts are free to move in the x and z direction. Because of symmetry about the line CG (Fig. 4.13) with another strut in the adjacent repeating unit, the slope of the strut at point C with respect to the plane OGCH does not change during the deformation, i.e. the slope remains equal to β with respect to the xz-plane. Thus, the relationship between the bending moment M and the horizontal force F_y at point C is given by

69

$$\frac{F_y \hat{L}^2 \cos \beta}{2E_s I} - \frac{ML}{E_s I} = 0$$

(4.36)

$$\Rightarrow M = \frac{F_y \hat{L} \cos \beta}{2}$$

(4.37)

Hence, the displacements of point C in the axial (n) and transverse (t) directions are respectively,

$$u_n = \frac{\hat{L}}{AE_s} F_y \sin \beta$$

(4.38)

and

$$u_t = \frac{F_y \hat{L}^3 \cos \beta}{3E_s I} - \frac{ML^2}{2E_s I}$$
$$= \frac{F_y \hat{L}^3 \cos \beta}{3E_s I} - \frac{F_z L \cos \beta}{2} \frac{L^2}{2E_s I}$$
$$= \frac{F_y \hat{L}^3 \cos \beta}{12E_s I}$$

(4.39)

$$\Rightarrow u_t = \frac{\hat{L}^3}{12E_s I} F_y \cos \beta$$

(4.40)

These displacements can be related to the deformation of the repeating unit in the x, y and z directions by determining the change in length of the repeating unit projected onto those axes. The results are

$$\delta_x = 2(u_n \cos \alpha - u_t \sin \alpha) \cos \theta$$
$$= \left(\frac{\hat{L}}{AE_s} - \frac{\hat{L}^3}{12E_s I} \right) 2F_y \sin \beta \cos \beta \cos \theta$$

(4.41)

$$\delta_y = 2(u_n \sin \beta + u_t \cos \beta)$$
$$= \left(\frac{\hat{L}}{AE_s} \sin^2 \beta + \frac{\hat{L}^3}{12E_s I} \cos^2 \beta \right) 2F_y$$

(4.42)

$$\delta_z = 2(u_n \cos\beta - u_t \sin\beta)\sin\theta$$

$$= \left(\frac{\hat{L}}{AE_s} - \frac{\hat{L}^3}{12E_sI}\right)2F_y \sin\beta\cos\beta\sin\theta$$

(4.43)

Replacing all $\hat{L}$ and β with L and θ by using Eqs. (4.32)-(4.35):

$$\delta_x = \left(\frac{L\sqrt{\cos^2\theta+1}}{AE_s} - \frac{\left(L\sqrt{\cos^2\theta+1}\right)^3}{12E_sI}\right)\frac{\cos^2\theta}{\cos^2\theta+1}2F_y$$

$$= \left(\frac{L}{AE_s} - \frac{L^3}{12E_sI}\left(\cos^2\theta+1\right)\right)\frac{\cos^2\theta}{\sqrt{\cos^2\theta+1}}2F_y$$

(4.44)

$$\delta_y = \left(\frac{L\sqrt{\cos^2\theta+1}}{AE_s}\frac{\cos^2\theta}{\cos^2\theta+1} + \frac{\left(L\sqrt{\cos^2\theta+1}\right)^3}{12E_sI}\frac{1}{\cos^2\theta+1}\right)2F_y$$

$$= \left(\frac{L}{AE_s}\cos^2\theta + \frac{L^3}{12E_sI}\left(\cos^2\theta+1\right)\right)\frac{2}{\sqrt{\cos^2\theta+1}}F_y$$

(4.45)

$$\delta_z = \left(\frac{L\sqrt{\cos^2\theta+1}}{AE_s} - \frac{\left(L\sqrt{\cos^2\theta+1}\right)^3}{12E_sI}\right)\frac{\sin\theta\cos\theta}{\cos^2\theta+1}2F_y$$

$$= \left(\frac{L}{AE_s} - \frac{L^3}{12E_sI}\left(\cos^2\theta+1\right)\right)\frac{\sin\theta\cos\theta}{\sqrt{\cos^2\theta+1}}2F_y$$

(4.46)

Hence, the strains can be obtained by dividing the deformations by the appropriate initial lengths.

$$\varepsilon_{xx} = \frac{\delta_x}{2L\cos\theta} = \left(\frac{1}{AE_s} - \frac{L^2}{12E_sI}\left(\cos^2\theta+1\right)\right)\frac{\cos\theta}{\sqrt{\cos^2\theta+1}}F_y$$

(4.47)

$$\varepsilon_{yy} = \frac{\delta_y}{2L\cos\theta} = \left(\frac{1}{AE_s}\cos^2\theta + \frac{L^2}{12E_sI}\left(\cos^2\theta+1\right)\right)\frac{1}{\cos\theta\sqrt{\cos^2\theta+1}}F_y$$

(4.48)

$$\varepsilon_{zz} = \frac{\delta_z}{2L\sin\theta} = \left(\frac{1}{AE_s} - \frac{L^2}{12E_sI}\left(\cos^2\theta+1\right)\right)\frac{\cos\theta}{\sqrt{\cos^2\theta+1}}F_y$$

(4.49)

The stress in the y-direction is

$$\sigma_{yy} = \frac{4F_y}{A_y} = \frac{F_y}{2L^2 \sin\theta\cos\theta}$$

(4.50)

The stiffness and the Poisson's ratios can then be obtained from considering the stress and strains in the respective directions using Eqs. (4.47)-(4.50)

$$E_{yy} = \frac{\sigma_{yy}}{\varepsilon_{yy}} = \frac{E_s}{\left(\dfrac{2\sin\theta\cos^2\theta}{\sqrt{\cos^2\theta+1}}\dfrac{L^2}{A} + \dfrac{\sin\theta\sqrt{\cos^2\theta+1}}{6}\dfrac{L^4}{I} \right)}$$

(4.51)

$$\upsilon_{yx} = -\frac{\varepsilon_{xx}}{\varepsilon_{yy}} = -\frac{\left(\dfrac{1}{A} - \dfrac{\left(\cos^2\theta+1\right)}{12}\dfrac{L^2}{I} \right)\cos^2\theta}{\left(\cos^2\theta\dfrac{1}{A} + \dfrac{\left(\cos^2\theta+1\right)}{12}\dfrac{L^2}{I} \right)}$$

(4.52)

$$\upsilon_{yz} = -\frac{\varepsilon_{zz}}{\varepsilon_{yy}} = -\frac{\left(\dfrac{1}{A} - \dfrac{\left(\cos^2\theta+1\right)}{12}\dfrac{L^2}{I} \right)\cos^2\theta}{\left(\cos^2\theta\dfrac{1}{A} + \dfrac{\left(\cos^2\theta+1\right)}{12}\dfrac{L^2}{I} \right)}$$

(4.53)

As highlighted, for foams with a low density, the term $\dfrac{L^2}{A} = \dfrac{4\sin\theta\cos^2\theta}{\sqrt{\cos^2\theta+1}}\dfrac{\rho}{\rho_s}$ is much smaller than $\dfrac{L^4}{I}$; hence, the stiffness and Poisson's ratios can be approximated by

$$E_{yy} \approx \frac{6}{\sin\theta\sqrt{\cos^2\theta+1}}\frac{E_s I}{L^4}$$

(4.54)

$$\upsilon_{yx} \approx \cos^2\theta$$

(4.55)

$$\upsilon_{yz} \approx \cos^2\theta$$

(4.56)

Eqs. (4.51)-(4.54) can be expressed in terms of the relative density by substituting Eqs. (4.1)-(4.4) into them, resulting in:

$$E_{yy} = \frac{E_s}{\left(\dfrac{1}{2}\dfrac{\rho_s}{\rho} + \dfrac{\left(\cos^2\theta+1\right)^{3/2}}{96\sin\theta\cos^4\theta}\dfrac{1}{C_1}\left(\dfrac{\rho_s}{\rho}\right)^2 \right)}$$

(4.57)

$$\upsilon_{yx} = -\frac{\varepsilon_{xx}}{\varepsilon_{yy}} = -\frac{\left(\cos^2\theta - \dfrac{\left(\cos^2\theta+1\right)^{3/2}}{48\sin\theta}\dfrac{1}{C_1}\left(\dfrac{\rho_s}{\rho}\right)\right)}{\left(\cos^2\theta + \dfrac{\left(\cos^2\theta+1\right)^{3/2}}{48\sin\theta\cos^2\theta}\dfrac{1}{C_1}\left(\dfrac{\rho_s}{\rho}\right)\right)}$$

(4.58)

$$\upsilon_{yz} = -\frac{\varepsilon_{zz}}{\varepsilon_{yy}} = -\frac{\left(\cos^2\theta - \dfrac{\left(\cos^2\theta+1\right)^{3/2}}{48\sin\theta}\dfrac{1}{C_1}\left(\dfrac{\rho_s}{\rho}\right)\right)}{\left(\cos^2\theta + \dfrac{\left(\cos^2\theta+1\right)^{3/2}}{48\sin\theta\cos^2\theta}\dfrac{1}{C_1}\left(\dfrac{\rho_s}{\rho}\right)\right)}$$

(4.59)

The repeating unit shown in Figs. 4.9-4.11 can also be used to analyse the tensile strength for loading in the *y*-direction. As with the analysis of the stiffness and the Poisson's ratios, determination of the tensile strength can be simplified by considering one strut, as shown in Fig. 4.12. Following the same approach for the tensile strength in the *z*-direction, the maximum stress in the strut also occurs at the outer surface at both ends; its value being:

$$\sigma = \frac{F_y \sin\beta}{A} + \frac{M\,R}{I}$$

(4.60)

Substituting Eq. (4.37) into (4.60) and equating the stress σ to the tensile failure stress $\sigma_{\max s}$:

$$\sigma_{\max s} = \left(\frac{\sin\beta}{A} + \frac{\hat{L}\,R\cos\beta}{2I}\right)F_y$$

(4.61)

Eliminating $\hat{L}$ and β using Eqs. (4.32)-(4.35) results in

$$\sigma_{\max s} = \left(\frac{\cos\theta}{\sqrt{\cos^2\theta+1}}\frac{1}{A} + \frac{L\,R}{2I}\right)F_y$$

(4.62)

Finally by substituting Eq. (4.50), which defines the overall stress, into Eq. (4.62), the tensile strength in the *z*-direction is given by

$$\sigma_{y\max} = \frac{\sigma_{\max s}}{\left(\dfrac{2\sin\theta\cos^2\theta}{\sqrt{\cos^2\theta+1}}\dfrac{L^2}{A}+\sin\theta\cos\theta\dfrac{L^3 R}{I}\right)}$$

(4.63)

Eq. (4.63) can also be written in terms of the relative density by using Eqs. (4.1)-(4.4).

$$\sigma_{y\max} = \frac{\sigma_{\max s}}{\dfrac{1}{2}\dfrac{\rho_s}{\rho}+\dfrac{\left(\cos^2\theta+1\right)^{3/4}}{8\sqrt{\sin\theta}\cos^2\theta}\dfrac{C_2}{C_1}\left(\dfrac{\rho_s}{\rho}\right)^{3/2}}$$

(4.64)

4.1.4 Correction for rigid strut segments

It was highlighted in Section 3.6 that the strut segments adjoining the interconnection (cell corner) with adjacent struts do not exhibit noticeable bending during deformation. This shortening of the effective flexural length of the struts influences the mechanical properties of the foam. Thus, the equations derived in Sections 4.1.2 and 4.1.3 that define the deformation of the rhombic dodecahedron cell should be modified to incorporate the influence of these rigid strut segments. This modified model will be referred to as the "semi-flexible strut model".

As discussed in Section 3.6, shortening of the effective flexural length of the struts occurs because the struts are larger near their interconnections. Thus, in this study, the length of the rigid portion of each strut is assumed to be determined by the cross-sectional dimension R, which is the maximum distance from the surface of the strut to its centroidal axis. Based on this, the strut segment of length d immediately adjoining the interconnection with neighbouring struts is assumed to be rigid (they do not stretch nor flex) during cell deformation, where d is related to R by

$$d = C_3 R$$

(4.65)

The foam stiffness, Poisson's ratios and tensile strengths based on this cell model then take on the following expressions:

$$E_{zz} = \frac{\sigma_{zz}}{\varepsilon_{zz}} = \frac{E_s}{\left(\dfrac{2\sin\theta\cos^2\theta}{\sqrt{\cos^2\theta+1}} \dfrac{(L-2d)L}{A} + \dfrac{\cos^4\theta\sqrt{\cos^2\theta+1}}{3\sin\theta} \dfrac{(L-2d)^3 L}{I} \right)}$$

<div align="right">(4.66)</div>

$$E_{yy} = \frac{\sigma_{yy}}{\varepsilon_{yy}} = \frac{E_s}{\left(\dfrac{2\sin\theta\cos^2\theta}{\sqrt{\cos^2\theta+1}} \dfrac{(L-2d)L}{A} + \dfrac{2\sin\theta\sqrt{\cos^2\theta+1}}{12} \dfrac{(L-2d)^3 L}{I} \right)}$$

<div align="right">(4.67)</div>

$$\upsilon_{zx} = \upsilon_{zy} = -\frac{\varepsilon_{xx}}{\varepsilon_{zz}} = -\frac{\left(\dfrac{(L-2d)}{A} - \dfrac{(\cos^2\theta+1)(L-2d)^3}{12\,I} \right)\sin^2\theta}{\left(\sin^2\theta\dfrac{(L-2d)}{A} + \dfrac{(\cos^2\theta+1)\cos^2\theta}{6} \dfrac{(L-2d)^3}{I} \right)}$$

<div align="right">(4.68)</div>

$$\upsilon_{yx} = -\frac{\varepsilon_{xx}}{\varepsilon_{yy}} = -\frac{\left(\dfrac{(L-2d)}{A} - \dfrac{(\cos^2\theta+1)(L-2d)^3}{12\,I} \right)\cos^2\theta}{\left(\cos^2\theta\dfrac{(L-2d)}{A} + \dfrac{(\cos^2\theta+1)(L-2d)^3}{12\,I} \right)}$$

<div align="right">(4.69)</div>

$$\upsilon_{yz} = -\frac{\varepsilon_{zz}}{\varepsilon_{yy}} = -\frac{\left(\dfrac{(L-2d)}{A} - \dfrac{(\cos^2\theta+1)(L-2d)^3}{12\,I} \right)\cos^2\theta}{\left(\cos^2\theta\dfrac{(L-2d)}{A} + \dfrac{(\cos^2\theta+1)(L-2d)^3}{12\,I} \right)}$$

<div align="right">(4.70)</div>

$$\sigma_{z\max} = \frac{\sigma_{\max s}}{\left(\dfrac{2\sin\theta\cos^2\theta}{\sqrt{\cos^2\theta+1}} \dfrac{L^2}{A} + \sqrt{2}\cos^3\theta\dfrac{(L-2d)L^2 R}{I} \right)}$$

<div align="right">(4.71)</div>

$$\sigma_{y\max} = \frac{\sigma_{\max s}}{\left(\dfrac{2\sin\theta\cos^2\theta}{\sqrt{\cos^2\theta+1}} \dfrac{L^2}{A} + \sin\theta\cos\theta\dfrac{(L-2d)L^2 R}{I} \right)}$$

<div align="right">(4.72)</div>

Denoting X_1 as the fraction of the strut that deforms; i.e.

$$X_1 = \left(1 - \frac{2d}{L} \right) = \left(1 - \frac{4\sqrt{\sin\theta}\cos\theta}{(\cos^2\theta+1)^{1/4}} C_2 C_3 \sqrt{\frac{\rho}{\rho_s}} \right)$$

<div align="right">(4.73)</div>

Eqs. (4.66)-(4.72) can also be expressed in terms of the relative density by substituting Eqs. (4.1)-(4.4) and (4.65) into them; thus:

$$E_{zz} = \frac{E_s}{\left(X_1 \frac{1}{2} \frac{\rho_s}{\rho} + X_1^{\ 3} \frac{\left(\cos^2 \theta + 1\right)^{3/2}}{48 \sin^3 \theta} \frac{1}{C_1} \left(\frac{\rho_s}{\rho}\right)^2 \right)}$$

(4.74)

$$E_{yy} = \frac{E_s}{\left(X_1 \frac{\rho_s}{\rho} + X_1^{\ 3} \frac{\left(\cos^2 \theta + 1\right)^{3/2}}{96 \sin \theta \cos^4 \theta} \frac{1}{C_1} \left(\frac{\rho_s}{\rho}\right)^2 \right)}$$

(4.75)

$$\upsilon_{zx} = \upsilon_{zy} == -\frac{\left(X_1 \sin^2 \theta - X_1^{\ 3} \frac{\sin \theta \left(\cos^2 \theta + 1\right)^{3/2}}{48 \cos^2 \theta} \frac{1}{C_1} \left(\frac{\rho_s}{\rho}\right) \right)}{\left(X_1 \sin^2 \theta + X_1^{\ 3} \frac{\left(\cos^2 \theta + 1\right)^{3/2}}{24 \sin \theta} \frac{1}{C_1} \left(\frac{\rho_s}{\rho}\right) \right)}$$

(4.76)

$$\upsilon_{yx} = -\frac{\varepsilon_{xx}}{\varepsilon_{yy}} = -\frac{\left(X_1 \cos^2 \theta - X_1^{\ 3} \frac{\left(\cos^2 \theta + 1\right)^{3/2}}{48 \sin \theta} \frac{1}{C_1} \left(\frac{\rho_s}{\rho}\right) \right)}{\left(X_1 \cos^2 \theta + X_1^{\ 3} \frac{\left(\cos^2 \theta + 1\right)^{3/2}}{48 \sin \theta \cos^2 \theta} \frac{1}{C_1} \left(\frac{\rho_s}{\rho}\right) \right)}$$

(4.77)

$$\upsilon_{yz} = -\frac{\varepsilon_{zz}}{\varepsilon_{yy}} = -\frac{\left(X_1 \cos^2 \theta - X_1^{\ 3} \frac{\left(\cos^2 \theta + 1\right)^{3/2}}{48 \sin \theta} \frac{1}{C_1} \left(\frac{\rho_s}{\rho}\right) \right)}{\left(X_1 \cos^2 \theta + X_1^{\ 3} \frac{\left(\cos^2 \theta + 1\right)^{3/2}}{48 \sin \theta \cos^2 \theta} \frac{1}{C_1} \left(\frac{\rho_s}{\rho}\right) \right)}$$

(4.78)

$$\sigma_{z \max} = \frac{\sigma_{\max s}}{\frac{1}{2} \frac{\rho_s}{\rho} + X_1 \frac{\left(\cos^2 \theta + 1\right)^{3/4}}{4\sqrt{2}\left(\sin \theta\right)^{3/2}} \frac{C_2}{C_1} \left(\frac{\rho_s}{\rho}\right)^{3/2}}$$

(4.79)

$$\sigma_{y \max} = \frac{\sigma_{\max s}}{\frac{1}{2} \frac{\rho_s}{\rho} + X_1 \frac{\left(\cos^2 \theta + 1\right)^{3/4}}{8\sqrt{\sin \theta} \cos^2 \theta} \frac{C_2}{C_1} \left(\frac{\rho_s}{\rho}\right)^{3/2}}$$

(4.80)

4.2   Tetrakaidecahedron cell model

The preceding section described an elongated rhombic dodecahedron cell model. Another polyhedron that can be assembled in three-dimensions is the tetrakaidecahedron, which has hexagonal and square faces, and can be arranged in a BCC lattice to fill space. Zhu et al. [40] and Warren and Kraynik [22] have analysed an isotropic tetrakaidecahedron open cell model in terms of its elastic properties and asserted that a tetrakaidecahedron is the only polyhedron that can be assembled in three dimensions to fill space and satisfy approximately the surface energy criterion and Plateau's law [1]. Tetrakaidecahedra are also similar to cells in actual foam [33]. Zhu et al. [40] and Warren and Kraynik [22] showed that the mechanical properties of their model are approximately isotropic; hence, it cannot be used to describe the foam in the present study.

As with the rhombic dodecahedron cell model, the tetrakaidecahedron model is elongated in the z-direction (see Fig. 4.14) to facilitate investigation of the actual foam cells which are larger in the foam rise direction. The elongated tetrakaidecahedron cells can be packed in an elongated BCC lattice, as shown in Fig. 4.15.
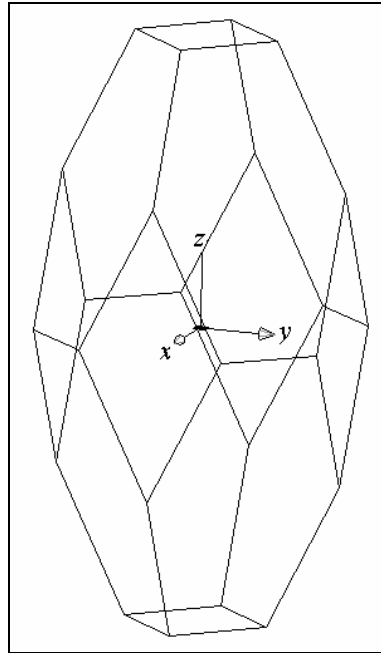
Fig. 4.14 Elongated tetrakaidecahedral cell

The following definitions and assumptions are made in deriving foam density, stiffness, Poisson's ratio and tensile strength based on this model:

- The length of struts other than those that lie on horizontal planes (parallel to the *xy*-plane) is *L*.

- The geometric anisotropy ratio, i.e. the ratio between the cell length in the rise direction to that in the transverse direction, can be described by $\tan\theta$, where θ is defined in Fig. 4.18 (see Figs. 4.16-4.18).

- The struts lying on horizontal planes have the same length *l* related to *L* by

$$l = L\sqrt{2}\cos\theta$$

(4.81)

- The struts have a constant cross-sectional area *A* and a constant cross-sectional second moment of area *I*; relationship between *I* and *A* being

$$C_1 = \frac{I}{A^2}$$

(4.82)

- The maximum distance from the surface of a strut to its centroidal axis is *R* and the relationship between *R* and *A* is

78

$$C_2 = \frac{R}{\sqrt{A}}$$

<div align="right">(4.83)</div>

- The struts are assumed to be made from an isotropic material with elastic stiffness E_s and tensile fracture stress $\sigma_{\max s}$.

- The struts follow Bernoulli-Euler beam theory when they deform.

- Failure occurs when any location in a strut attains the tensile fracture stress $\sigma_{\max s}$.
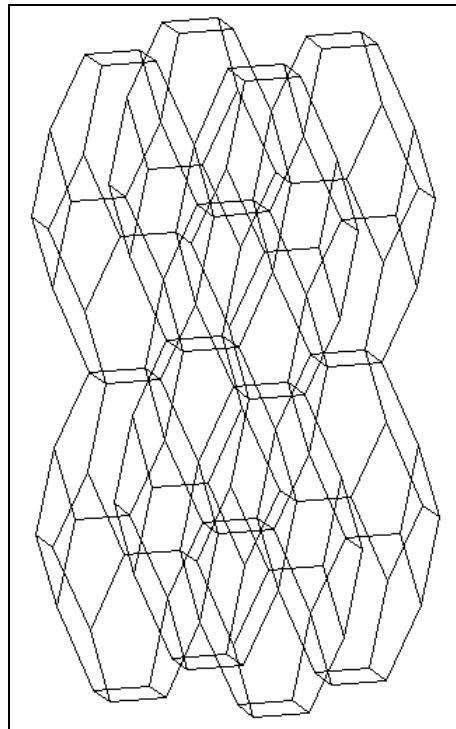
Fig. 4.15 Elongated BCC structure made from tetrakaidecahedron cells

4.2.1 Relative density

As with the rhombic dodecahedron cell, the lengths of the struts in this model are assumed to be much larger than the size of the cell vertices. Thus, the relative density of the foam based on the repeating unit shown in Figs. 4.16-4.18 can be approximated by considering the strut lengths.

$$\frac{\rho}{\rho_s} = \frac{4LA + 2\sqrt{2}LA\cos\theta}{\dfrac{(4L\cos\theta)^2}{2}2L\sin\theta}$$

<div align="right">(4.84)</div>

$$\Rightarrow \frac{\rho}{\rho_s} = \frac{2+\sqrt{2}\cos\theta}{8\sin\theta\cos^2\theta}\frac{A}{L^2}$$

<div align="right">(4.85)</div>

4.2.2 Mechanical properties in the *z*-direction

As with the rhombic dodecahedron model, the *z*-direction is also the direction of cell elongation for this model, which corresponds to the foam rise direction in actual foam. An analysis of structural deformation for loading in the *z*-direction is performed to derive the elastic stiffness and the Poisson's ratios of this cell model for this direction. The analysis is simplified such that it only considers the fundamental repeating unit (shown in bold lines in Fig. 4.16) due to symmetry and similarity. Figs. 4.17 and 4.18 show respectively, the three-dimensional and two-dimensional view of the unit. The geometrical quantities used in the analysis are defined in Fig. 4.18.
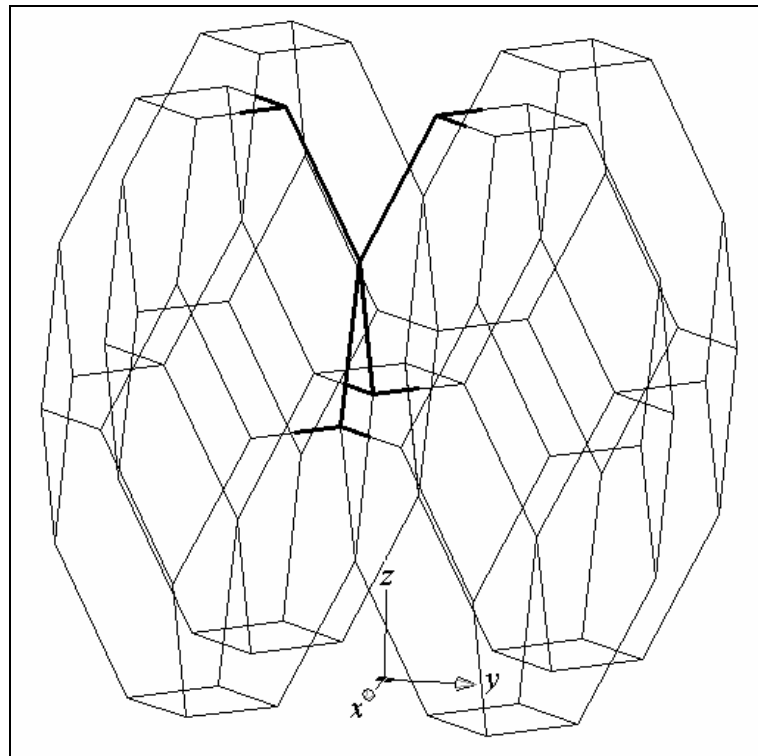
Fig. 4.16 Repeating unit for the analysis of an elongated tetrakaidecahedron cell loaded in the *z*-direction
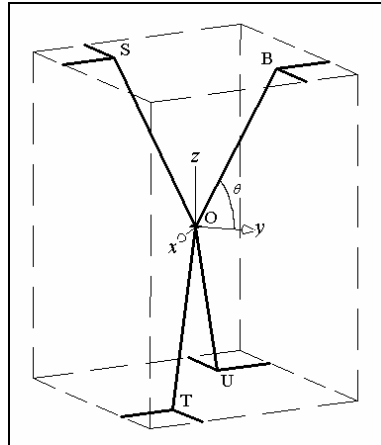
Fig. 4.17 Three-dimensional view of repeating unit in the analysis of an elongated tetrakaidecahedron cell loaded in the z-direction
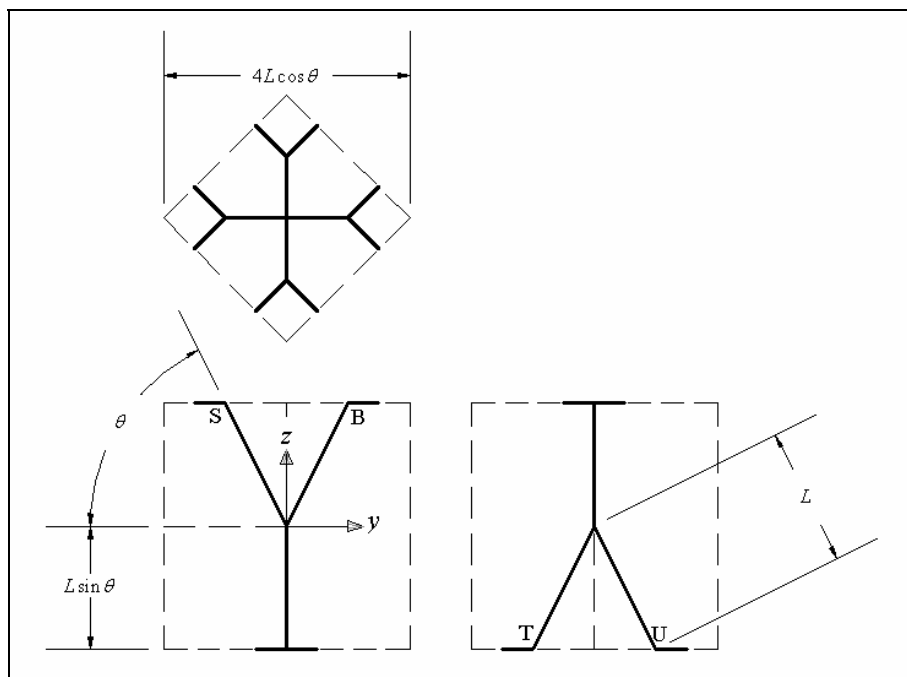
Fig. 4.18 Two-dimensional view of repeating unit for the analysis of an elongated tetrakaidecahedron cell loaded in the z-direction

Because there is no loading in the horizontal planes (i.e. planes parallel to the xy-plane), all the struts lying on the horizontal planes do not deform. Hence, the analysis can be simplified to just analyzing struts OB, OS, OT and OU (Fig. 4.17). Taking into consideration similarity and symmetry of these struts, the analysis can be further reduced to an analysis of just one of the struts – e.g. OB – and then applying it to the others (see Fig. 4.19).
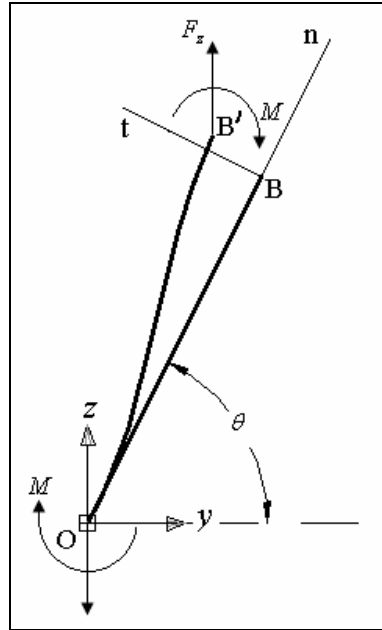
Fig. 4.19 Deformation of strut OB

Fig. 4.19 shows strut OB in the yz-plane. When the tetrakaidecahedron structure is loaded in the z-direction, point B moves upwards and left to point B', but due to symmetry along the z-direction, the slope of the strut at point B does not change. Consequently, the bending moment M and vertical force F_z at point B are related by

$$\frac{F_z L^2 \cos\theta}{2E_s I} - \frac{ML}{E_s I} = 0$$

(4.86)

$$\Rightarrow M = \frac{F_z L \cos\theta}{2}$$

(4.87)

Hence, the displacements of point B in the axial (n) and transverse (t) directions are:

$$u_n = \frac{L}{AE_s} F_z \sin\theta$$

(4.88)

$$u_t = \frac{F_z L^3 \cos\theta}{3E_s I} - \frac{ML^2}{2E_s I}$$

$$= \frac{F_z L^3 \cos\theta}{3E_s I} - \frac{F_z L \cos\theta}{2}\frac{L^2}{2E_s I}$$

(4.89)

$$\Rightarrow u_t = \frac{L^3}{12E_s I} F_z \cos\theta$$

(4.90)

82

These displacements can be related to the deformation of the repeating unit in the x, y and z-directions by projecting them onto the corresponding axes and considering the symmetry and similarities of the units as shown in Fig. 4.17. The results are:

$$\delta_x = \delta_y = 2(u_n \cos\theta - u_t \sin\theta)$$
$$= 2\left(\frac{L}{AE_s} - \frac{L^3}{12E_s I}\right)F_z \sin\theta \cos\theta$$

(4.91)

$$\delta_z = 2(u_n \sin\theta + u_t \cos\theta)$$
$$= 2\left(\frac{L}{AE_s}\sin^2\theta + \frac{L^3}{12E_s I}\cos^2\theta\right)F_z$$

(4.92)

The strains are obtained by dividing the deformation by the initial lengths.

$$\varepsilon_{xx} = \varepsilon_{yy} = \frac{\delta_x}{4L\cos\theta}$$
$$= \left(\frac{1}{2AE_s} - \frac{L^2}{24E_s I}\right)F_z \sin\theta$$

(4.93)

$$\varepsilon_{zz} = \frac{\delta_z}{2L\sin\theta}$$
$$= \left(\frac{1}{AE_s}\sin\theta + \frac{L^2}{12E_s I}\frac{\cos^2\theta}{\sin\theta}\right)F_z$$

(4.94)

The stress in the z-direction is obtained by dividing the applied force $2F_z$ by the area A_z over which it acts.

$$\sigma_{zz} = \frac{2F_z}{A_z} = \frac{F_z}{4L^2 \cos^2\theta}$$

(4.95)

The stiffness and the Poisson's ratios of this model can then be found by dividing the stress by the strain in the z-direction, and taking the ratio between the appropriate strains:

$$E_{zz} = \frac{\sigma_{zz}}{\varepsilon_{zz}} = \frac{E_s}{\left(4\sin\theta\cos^2\theta\frac{L^2}{A} + \frac{\cos^4\theta}{3\sin\theta}\frac{L^4}{I}\right)}$$

(4.96)

$$v_{zx} = v_{zy} = -\frac{\varepsilon_{xx}}{\varepsilon_{zz}} = -\frac{\varepsilon_{yy}}{\varepsilon_{zz}} = -\frac{\left(\dfrac{1}{2A} - \dfrac{L^2}{24I}\right)\sin\theta}{\left(\sin\theta\dfrac{1}{A} + \dfrac{\cos^2\theta}{12\sin\theta}\dfrac{L^2}{I}\right)}$$

(4.97)

As highlighted in the rhombic dodecahedron model, the term $\dfrac{L^2}{A}$ is much smaller

than $\dfrac{L^4}{I}$ for low density foams because L is much larger than the lateral dimensions

of the strut cross-section; hence, the stiffness and the Poisson's ratios can be

approximated by

$$E_{zz} = \frac{3\sin\theta}{\cos^4\theta}\frac{E_s I}{L^4}$$

(4.98)

$$v_{zx} = v_{zy} \approx \frac{1}{2}\tan^2\theta$$

(4.99)

Eqs. (4.96) and (4.97) can also be expressed in terms of the relative density by

substituting Eqs. (4.82) and (4.85) into them.

$$E_{zz} = \frac{E_s}{\left[\left(1 + \dfrac{\cos\theta}{\sqrt{2}}\right)\left(\dfrac{\rho_s}{\rho}\right) + \left(\dfrac{(2+\sqrt{2}\cos\theta)^2}{192\sin^3\theta}\right)\dfrac{1}{C_1}\left(\dfrac{\rho_s}{\rho}\right)^2\right]}$$

(4.100)

$$v_{zx} = v_{zy} = -\frac{\varepsilon_{xx}}{\varepsilon_{zz}} = -\frac{\left(\dfrac{\sin\theta}{2} - \left(\dfrac{2+\sqrt{2}\cos\theta}{192\cos^2\theta}\right)\dfrac{1}{C_1}\left(\dfrac{\rho_s}{\rho}\right)\right)}{\left(\sin\theta + \left(\dfrac{2+\sqrt{2}\cos\theta}{96\sin^2\theta}\right)\dfrac{1}{C_1}\left(\dfrac{\rho_s}{\rho}\right)\right)}$$

(4.101)

The tensile strength of this cell model in the z-direction can be derived from the

repeating unit shown in Figs. 4.16-4.18. The analysis is simplified by considering the

failure of one strut, as shown in Fig. 4.19. As with the rhombic dodecahedron model,

the maximum normal stress in a strut is attained at its outer surface at both ends of the

struts and its value is obtained by considering a combination of the axial force and bending moment.

$$\sigma = \frac{F_z \sin \theta}{A} + \frac{M R}{I}$$

(4.102)

Substitution of Eq. (4.87) into Eq. (4.102) and equating the stress σ to the failure stress $\sigma_{\max s}$ yields:

$$\sigma_{\max s} = \left(\frac{\sin \theta}{A} + \frac{L R \cos \theta}{2I} \right) F_z$$

(4.103)

Finally, by substituting Eq. (4.95), which defines the overall stress, into Eq. (4.102), the tensile strength in the z-direction is defined.

$$\sigma_{z \max} = \frac{\sigma_{\max s}}{4 \sin \theta \cos^2 \theta \dfrac{L^2}{A} + 2 \cos^3 \theta \dfrac{L^3 R}{I}}$$

(4.104)

Eq. (4.104) can also be expressed in terms of the relative density by incorporating Eqs. (4.82), (4.83), and (4.85) into it.

$$\sigma_{z \max} = \frac{\sigma_{\max s}}{\left(1 + \dfrac{\cos \theta}{\sqrt{2}} \right) \left(\dfrac{\rho_s}{\rho} \right) + \left(\dfrac{2 + \sqrt{2} \cos \theta}{\sin \theta} \right)^{3/2} \dfrac{C_2}{8\sqrt{2}C_1} \left(\dfrac{\rho_s}{\rho} \right)^{3/2}}$$

(4.105)

4.2.3   Mechanical properties in the *y*-direction

As with the analysis of the rhombic dodecahedron cell model, the *y*-direction for the tetrakaidecahedron cell model corresponds to the transverse direction for actual foam. In order to derive the stiffness and the Poisson's ratios in the *y*-direction, loading of the cell in this direction is analysed. As with loading in the *z*-direction, the analysis of loading in the *y*-direction can also be reduced to the analysis of the single repeating unit shown in bold lines in Fig. 4.20. The deformation of struts lying in planes parallel to the vertical *xz*-plane need not be considered because there is no

force in those planes. This analysis is further simplified to an analysis of two struts – one lying in the horizontal *xy*-plane and one in the *yz*-plane (see Figs. 4.21 and 4.22). Thus, the analysis of the mechanical properties of this cell model in the *y*-direction is performed in two parts – an analysis of a strut in the vertical *yz*-plane and one in the *xy*-plane, followed by a combination of the two.

In this analysis, it is assumed that a force $2F$ is pulling the repeating units in the *y*-direction; hence, each strut has to sustain a load of F. The overall stress in the *y*-direction can then be expressed as

$$\sigma_{yy} = \frac{2F_y}{A_x} = \frac{F_y}{4L^2 \sin\theta \cos\theta}$$

(4.106)
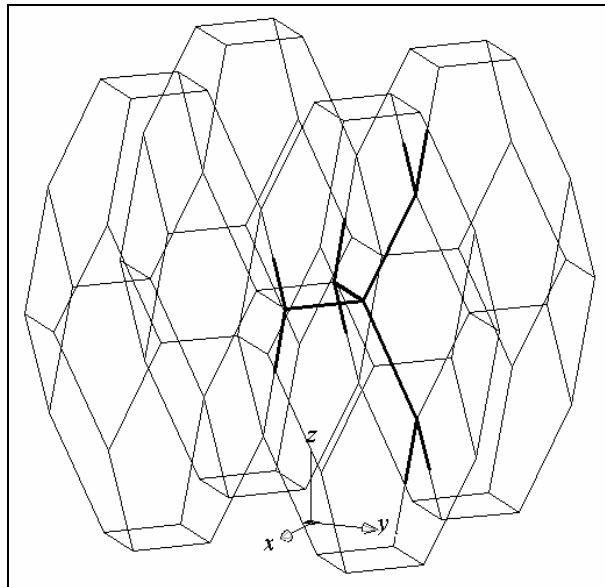
Fig. 4.20 Repeating unit for the analysis of an elongated tetrakaidecahedron cell loaded in the *y*-direction
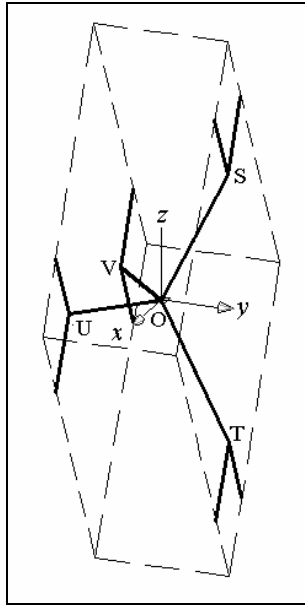
Fig. 4.21 Three-dimensional view of repeating unit for the analysis of an elongated tetrakaidecahedron cell loaded in the *y*-direction
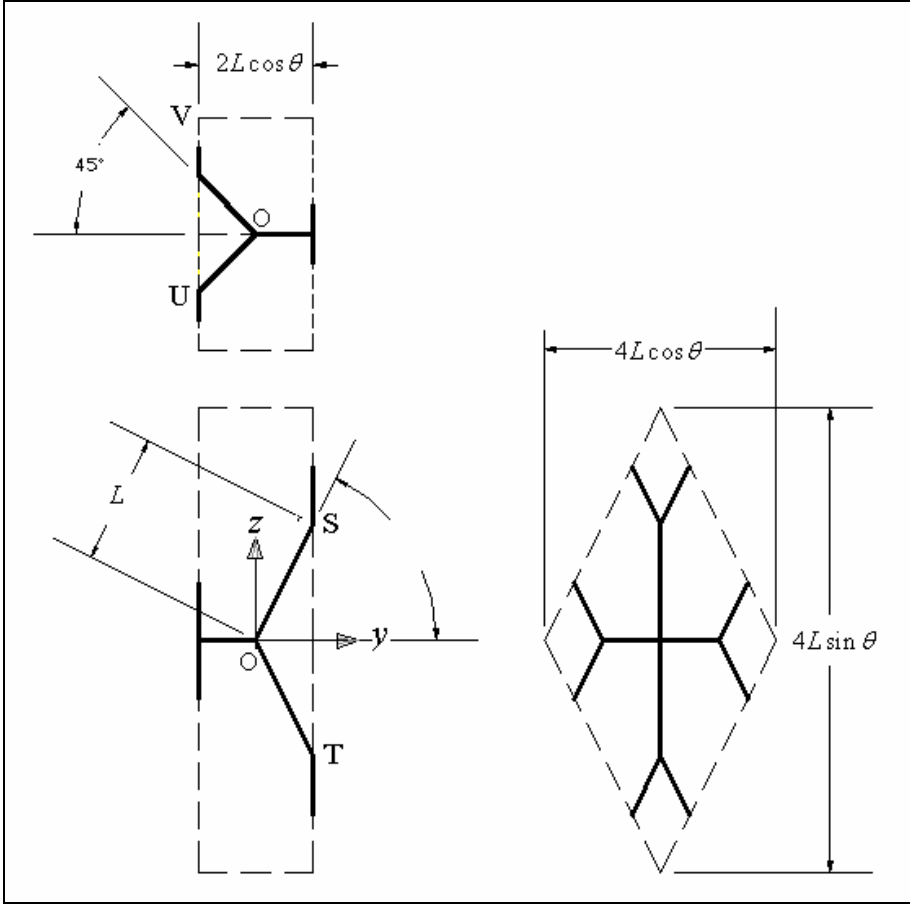
Fig. 4.22 Two-dimensional view of repeating unit used for the analysis of elongated tetrakaidecahedron cell loaded in the *y*-direction

Analysis of struts in the vertical *yz*-plane
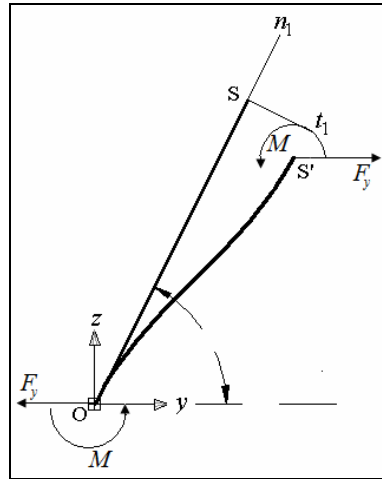
Fig. 4.23 Deformation of strut OS

Arising from symmetry, the analysis of struts lying in the *yz*-plane can be further simplified to an analysis of just one strut – e.g. OS (Figs. 4.21 and 4.22) – and then applying it to other similar struts. When the tetrakaidecahedron structure is loaded in the *y*-direction, Fig. 4.23 shows that point S moves in the axial (n_1) and transverse (t_1) directions. However, the slope of the strut at point F does not change due to symmetry with another repeating unit in the *y*-direction. Thus, the bending moment M and the horizontal force F_y at point S are related by

$$\frac{F_y L^2 \sin\theta}{2E_s I} - \frac{ML}{E_s I} = 0$$

(4.107)

$$\Rightarrow M = \frac{F_y L \sin\theta}{2}$$

(4.108)

The displacements of point S in the axial (n_1) and transverse (t_1) directions are:

$$u_{n1} = \frac{L}{AE_s} F_y \cos\theta$$

(4.109)

$$u_{t1} = \frac{F_y L^3 \sin\theta}{3E_s I} - \frac{ML^2}{2E_s I}$$

$$= \frac{F_y L^3 \sin\theta}{3E_s I} - \frac{F_y L \sin\theta}{2} \frac{L^2}{2E_s I}$$

(4.110)

$$\Rightarrow u_{t1} = \frac{L^3}{12E_s I} F_y \sin\theta$$

(4.111)

Therefore, the displacement of point S in the y and z-directions can be obtained by projecting them onto these axes.

$$\delta_{y1} = u_{n1} \cos\theta + u_{t1} \sin\theta$$

$$= \left(\frac{L}{AE_s} \cos^2\theta + \frac{L^3}{12E_s I} \sin^2\theta \right) F_y$$

(4.112)

$$\delta_{z1} = u_{n1} \sin\theta - u_{t1} \cos\theta$$

$$= \left(\frac{L}{AE_s} - \frac{L^3}{12E_s I} \right) F_y \sin\theta \cos\theta$$

(4.113)

Strut OF in Fig. 4.23 can also be used to determine the tensile strength of this cell model, governed by failure of struts in the vertical yz-plane. The maximum stress occurs at the outer surface of strut OS at both ends, where the bending moment is highest, and its value being:

$$\sigma = \frac{F_y \cos\theta}{A} + \frac{M}{I}\frac{R}{}$$

(4.114)

Substitution of Eq. (4.108) into Eq. (4.114) and equating the stress σ to the tensile failure stress $\sigma_{max\,s}$ yields

$$\sigma_{max\,s} = \left(\frac{\cos\theta}{A} + \frac{L\,R\sin\theta}{2I} \right) F_y$$

(4.115)

Finally, by incorporating Eq.(4.106) for stress in the y-direction into Eq. (4.115), the tensile strength in the y-direction is given by.

$$\sigma_{y\,max1} = \frac{\sigma_{max\,s}}{4\sin\theta\cos^2\theta\dfrac{L^2}{A} + 2\sin^2\theta\cos\theta\dfrac{L^3 R}{I}}$$

(4.116)

Eq. (4.116) can also be expressed in terms of the relative density by using Eqs. (4.82),

(4.83) and (4.85).

$$\sigma_{y\,max1} = \frac{\sigma_{max\,s}}{\left(1+\dfrac{\cos\theta}{\sqrt{2}}\right)\left(\dfrac{\rho_s}{\rho}\right) + \dfrac{\sqrt{\sin\theta}\left(2+\sqrt{2}\cos\theta\right)^{3/2}}{8\sqrt{2}\,\cos^2\theta}\dfrac{C_2}{C_1}\left(\dfrac{\rho_s}{\rho}\right)^{3/2}}$$

(4.117)

Analysis of struts in the *xy*-plane
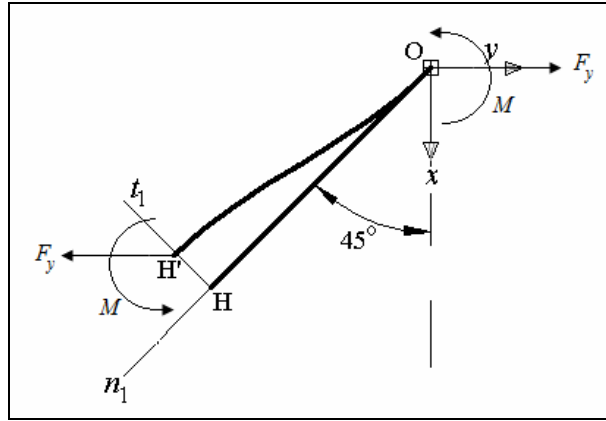
Fig. 4.24 Deformation of strut OH

As with the analysis of struts in the *yz*-plane, the analysis for struts lying in the

xy-plane can also be simplified to the analysis of one strut – e.g. OH – as shown in

Fig. 4.24. When the tetrakaidecahedron structure is loaded in the *y*-direction, point H

moves in the axial (n_2) and transverse (t_2) directions. However, the slope of the strut at

point H does not change due to repeating symmetry in the *y*-direction. Consequently

the bending moment M and the horizontal force F_y at point A are related by

$$\frac{\dfrac{F_y}{\sqrt{2}}\left(\sqrt{2}L\cos\theta\right)^2}{2E_s I} - \frac{M\left(\sqrt{2}L\cos\theta\right)}{E_s I} = 0$$

(4.118)

$$\Rightarrow M = \frac{F_y L\cos\theta}{2}$$

(4.119)

The displacements of point H in the axial (n_2) and transverse (t_2) directions are:

$$u_{n2} = \frac{\sqrt{2}L\cos\theta}{AE_s}\frac{1}{\sqrt{2}}F_y = \frac{F_y L\cos\theta}{AE_s}$$

(4.120)

$$u_{t2} = \frac{\frac{F_y}{\sqrt{2}}\left(\sqrt{2}L\cos\theta\right)^3}{3E_s I} - \frac{M\left(\sqrt{2}L\cos\theta\right)^2}{2E_s I}$$

$$= \frac{2F_y L^3 \cos^3\theta}{3E_s I} - \frac{F_y L\cos\theta}{2}\frac{\left(\sqrt{2}L\cos\theta\right)^2}{2E_s I}$$

(4.121)

$$u_{t2} = \frac{L^3 \cos^3\theta}{6E_s I}F_y$$

(4.122)

Therefore, the displacements of point H in the x and y-directions are

$$\delta_{x2} = \frac{1}{\sqrt{2}}\left(u_{n2} - u_{t2}\right)$$

$$= \left(\frac{L}{\sqrt{2}AE_s}\cos\theta - \frac{\sqrt{2}L^3}{12E_s I}\cos^3\theta\right)F_y$$

(4.123)

$$\delta_{y2} = \frac{1}{\sqrt{2}}\left(u_{n2} + u_{t2}\right)$$

$$= \left(\frac{L}{\sqrt{2}AE_s}\cos\theta + \frac{\sqrt{2}L^3}{12E_s I}\cos^3\theta\right)F_y$$

(4.124)

Strut OH can also be used to ascertain the tensile strength in the y-direction, which corresponds to the failure of struts in the xy-plane. Following the previous analysis, the maximum stress in this strut is

$$\sigma = \frac{F_y}{\sqrt{2}A} + \frac{M\,R}{I}$$

(4.125)

Substitution of Eq. (4.118) into Eq. (4.125) and equating the stress σ to the failure stress $\sigma_{max\,s}$ yields:

$$\sigma_{max\,s} = \left(\frac{1}{\sqrt{2}A} + \frac{L\,R\cos\theta}{2I}\right)F_y$$

(4.126)

Finally by using Eq. (4.106), which describes the overall stress in the y-direction, in the preceding expression, the tensile strength in the y-direction is defined by.

$$\sigma_{y\max 2} = \frac{\sigma_{\max s}}{2\sqrt{2}\sin\theta\cos\theta\dfrac{L^2}{A} + 2\sin\theta\cos^2\theta\dfrac{L^3 r}{I}}$$

(4.127)

Eq. (4.127) can also be expressed in terms of the relative density by substituting Eqs. (4.82), (4.83) and (4.85) into it.

$$\sigma_{y\max 2} = \frac{\sigma_{\max s}}{\left(\dfrac{1}{\sqrt{2}\cos\theta} + \dfrac{1}{2}\right)\left(\dfrac{\rho_s}{\rho}\right) + \dfrac{\left(2+\sqrt{2}\cos\theta\right)^{3/2}}{8\sqrt{2}\sin\theta\cos\theta}\dfrac{C_2}{C_1}\left(\dfrac{\rho_s}{\rho}\right)^{3/2}}$$

(4.128)

Summary

The total deformation of the tetrakaidecahedron cell model in the x, y and z-directions is obtained by combining the deformation of the struts in the vertical yz and horizontal xy-planes.

$$\delta_x = 2\delta_{x2} = 2\left(\frac{L}{\sqrt{2}AE_s}\cos\theta - \frac{\sqrt{2}L^3}{12E_s I}\cos^3\theta\right)F_x$$

(4.129)

$$\delta_y = \delta_{y1} + \delta_{y2}$$
$$= \left(\frac{L}{AE_s}\cos^2\theta + \frac{L^3}{12E_s I}\sin^2\theta\right)F_y + \left(\frac{L}{\sqrt{2}AE_s}\cos\theta + \frac{\sqrt{2}L^3}{12E_s I}\cos^3\theta\right)F_y$$

(4.130)

$$\delta_y = \left\{\left(\cos^2\theta + \frac{1}{\sqrt{2}}\cos\theta\right)\frac{L}{AE_s} + \left(\sin^2\theta + \sqrt{2}\cos^3\theta\right)\frac{L^3}{12E_s I}\right\}F_y$$

(4.131)

$$\delta_z = 2\delta_{z1} = 2\left(\frac{L}{AE_s} - \frac{L^3}{12E_s I}\right)F_x\sin\theta\cos\theta$$

(4.132)

The strains are then calculated by dividing the deformations by their corresponding initial lengths.

$$\varepsilon_{yy} = \frac{\delta_y}{2L\cos\theta} = \left\{\left(\cos\theta + \frac{1}{\sqrt{2}}\right)\frac{1}{2AE_s} + \left(\frac{\sin^2\theta}{\cos\theta} + \sqrt{2}\cos^2\theta\right)\frac{L^2}{24E_s I}\right\}F_y$$

(4.133)

92

$$\varepsilon_{xx} = \frac{\delta_x}{4L\cos\theta} = \left(\frac{\sqrt{2}}{4AE_s} - \cos^2\theta\frac{\sqrt{2}L^2}{24E_sI}\right)F_y$$

(4.134)

$$\varepsilon_{zz} = \frac{\delta_z}{4L\sin\theta} = \left(\cos\theta\frac{1}{2AE_s} - \cos\theta\frac{L^2}{24E_sI}\right)F_y$$

(4.135)

Thus, the stiffness is given by the ratio of the tensile stress σ_{yy} (Eq. (4.106)) to the corresponding strain ε_{yy} (Eq. (4.115))

$$E_{yy} = \frac{\sigma_{yy}}{\varepsilon_{yy}} = \frac{E_s}{\left(2\sin\theta\cos^2\theta + \sqrt{2}\sin\theta\cos\theta\right)\dfrac{L^2}{A} + \left(\sin^3\theta + \sqrt{2}\sin\theta\cos^3\theta\right)\dfrac{L^4}{6I}}$$

(4.136)

The Poisson's ratios are derived by taking the ratio of the appropriate strains.

$$\upsilon_{yx} = -\frac{\varepsilon_{xx}}{\varepsilon_{yy}} = -\frac{\left(\dfrac{1}{\sqrt{2}A} - \dfrac{\cos^2\theta}{6\sqrt{2}}\dfrac{L^2}{I}\right)}{\left(\cos\theta + \dfrac{1}{\sqrt{2}}\right)\dfrac{1}{A} + \left(\dfrac{\sin^2\theta}{\cos\theta} + \sqrt{2}\cos^2\theta\right)\dfrac{L^2}{12I}}$$

(4.137)

$$\upsilon_{yz} = -\frac{\varepsilon_{zz}}{\varepsilon_{yy}} = -\frac{\left(\dfrac{1}{A} - \dfrac{L^2}{12I}\right)\cos\theta}{\left(\cos\theta + \dfrac{1}{\sqrt{2}}\right)\dfrac{1}{A} + \left(\dfrac{\sin^2\theta}{\cos\theta} + \sqrt{2}\cos^2\theta\right)\dfrac{L^2}{12I}}$$

(4.138)

Eqs. (4.136)-(4.138) can also be expressed in terms of the relative density by substituting Eqs. (4.82), (4.83) and (4.85) into them.

$$E_{yy} = \frac{E_s}{\left(2 + \dfrac{\sqrt{2}}{\cos\theta}\right)\left(2 + \sqrt{2}\cos\theta\right)\dfrac{1}{8}\left(\dfrac{\rho_s}{\rho}\right) + \left(\dfrac{\sin\theta}{\cos^4\theta} + \dfrac{\sqrt{2}}{\sin\theta\cos\theta}\right)\left(2 + \sqrt{2}\cos\theta\right)^2\dfrac{1}{384C_1}\left(\dfrac{\rho_s}{\rho}\right)^2}$$

(4.139)

$$\upsilon_{yx} = -\frac{\varepsilon_{xx}}{\varepsilon_{yy}} = -\frac{\left(\dfrac{1}{\sqrt{2}} - \left(\dfrac{\sqrt{2}+\cos\theta}{48\sin\theta}\right)\dfrac{1}{C_1}\left(\dfrac{\rho_s}{\rho}\right)\right)}{\left(\cos\theta + \dfrac{1}{\sqrt{2}}\right) + \left(\dfrac{\sin^2\theta}{\cos\theta} + \sqrt{2}\cos^2\theta\right)\left(\dfrac{2 + \sqrt{2}\cos\theta}{96\sin\theta\cos^2\theta}\right)\dfrac{1}{C_1}\left(\dfrac{\rho_s}{\rho}\right)}$$

(4.140)

$$\upsilon_{yz} = -\frac{\varepsilon_{zz}}{\varepsilon_{yy}} = -\frac{\left(\cos\theta - \left(\dfrac{2+\sqrt{2}\cos\theta}{96\sin\theta\cos\theta}\right)\dfrac{1}{C_1}\left(\dfrac{\rho_s}{\rho}\right)\right)}{\left(\cos\theta + \dfrac{1}{\sqrt{2}}\right) + \left(\dfrac{\sin^2\theta}{\cos\theta} + \sqrt{2}\cos^2\theta\right)\left(\dfrac{2+\sqrt{2}\cos\theta}{96\sin\theta\cos^2\theta}\right)\dfrac{1}{C_1}\left(\dfrac{\rho_s}{\rho}\right)}$$

(4.141)

The overall tensile strength is determined by comparing Eqs. (4.116) and (4.129), which describe the tensile strength corresponding to failure of struts in the *yz* and *xy*-planes, respectively. The struts in the *yz*-plane are more vulnerable than the struts in the *xy*-plane, i.e. $\sigma_{y\max 1} \le \sigma_{y\max 2}$, if the geometric anisotropy ratio $\tan\theta \ge 1$. For foams with a low density, the ratio between the two failure stresses can be approximated by:

$$\frac{\sigma_{y\max 2}}{\sigma_{y\max 1}} \approx \tan\theta$$

(4.142)

Hence, the overall tensile strength of this model is governed by the failure of struts in the vertical *yz*-plane.

$$\sigma_{y\max} = \sigma_{y\max 1} = \frac{\sigma_{\max s}}{4\sin\theta\cos^2\theta\dfrac{L^2}{A} + 2\sin^2\theta\cos\theta\dfrac{L^3 R}{I}}$$

(4.143)

$$\sigma_{y\max} = \frac{\sigma_{\max s}}{\left(1 + \dfrac{\cos\theta}{\sqrt{2}}\right)\left(\dfrac{\rho_s}{\rho}\right) + \dfrac{\sqrt{\sin\theta}\left(2+\sqrt{2}\cos\theta\right)^{3/2}}{8\sqrt{2}\,\cos^2\theta}\dfrac{C_2}{C_1}\left(\dfrac{\rho_s}{\rho}\right)^{3/2}}$$

(4.144)

4.2.4   Correction for rigid strut segments

As with the rhombic dodecahedron cell model, the equations defining the mechanical properties of the tetrakaidecahedron model derived in Sections 4.2.2 and 4.2.3 should be modified to include the influence of rigid segments at the ends of each strut. Following the rhombic dodecahedron model, this modified model will also be referred to as the "semi-flexible strut model". Similar assumptions are used, i.e. strut

segments of length d adjacent to the interconnection with neighbouring struts do not deform during cell deformation, where d is related to R by

$$d = C_3 R$$

(4.145)

Consequently, the foam stiffness, Poisson's ratio and tensile strengths based on this cell model are modified to:

$$E_{zz} = \frac{\sigma_{zz}}{\varepsilon_z} = \frac{E_s}{\left(4\sin\theta\cos^2\theta \frac{(L-2d)L}{A} + \frac{\cos^4\theta}{3\sin\theta} \frac{(L-2d)^3 L}{I} \right)}$$

(4.146)

$$E_{yy} = \frac{\sigma_{yy}}{\varepsilon_{yy}}$$

$$= \frac{E_s}{\left(2\sin\theta\cos^2\theta(L-2d) + \sin\theta\left(\sqrt{2}\,L\cos\theta - 2d\right) \right)\frac{L}{A} + \left(\sin^3\theta(L-2d)^3 + \frac{\sin\theta}{2}\left(\sqrt{2}\,L\cos\theta - 2d\right)^3 \right)\frac{L}{6I}}$$

(4.147)

$$\upsilon_{zx} = \upsilon_{zy} = -\frac{\varepsilon_{xx}}{\varepsilon_{zz}} = -\frac{\left(\frac{(L-2d)}{2A} - \frac{(L-2d)^3}{24I} \right)\sin\theta}{\left(\sin\theta\frac{(L-2d)}{A} + \frac{\cos^2\theta}{12\sin\theta} \frac{(L-2d)^3}{I} \right)}$$

(4.148)

$$\upsilon_{yx} = -\frac{\varepsilon_{xx}}{\varepsilon_{yy}} = -\frac{\left(\frac{\left(\sqrt{2}\,L\cos\theta - 2d\right)}{2A\cos\theta} - \frac{\left(\sqrt{2}\,L\cos\theta - 2d\right)^3}{24\cos\theta} \frac{1}{I} \right)}{\left(\cos\theta(L-2d) + \frac{\left(\sqrt{2}\,L\cos\theta - 2d\right)}{2\cos\theta} \right)\frac{1}{A} + \left(\frac{\sin^2\theta}{\cos\theta}(L-2d)^3 + \frac{\left(\sqrt{2}\,L\cos\theta - 2d\right)^3}{2\cos\theta} \right)\frac{1}{12I}}$$

(4.149)

$$\upsilon_{yz} = -\frac{\varepsilon_{zz}}{\varepsilon_{yy}} = -\frac{\left(\frac{(L-2d)}{A} - \frac{(L-2d)^3}{12I} \right)\cos\theta}{\left(\cos\theta(L-2d) + \frac{\left(\sqrt{2}L\cos\theta - 2d\right)}{2\cos\theta} \right)\frac{1}{A} + \left(\frac{\sin^2\theta}{\cos\theta}(L-2d)^3 + \frac{\left(\sqrt{2}L\cos\theta - 2d\right)^3}{2\cos\theta} \right)\frac{1}{12I}}$$

(4.150)

$$\sigma_{z\max} = \frac{\sigma_{\max s}}{4\sin\theta\cos^2\theta \frac{L^2}{A} + 2\cos^3\theta \frac{(L-2d)L^2 r}{I}}$$

(4.151)

$$\sigma_{y\max} = \frac{\sigma_{\max s}}{4\sin\theta\cos^2\theta \frac{L^2}{A} + 2\sin^2\theta\cos\theta \frac{(L-2d)L^2 r}{I}}$$

(4.152)

95

These expressions can also be written in terms of the relative density by substituting Eqs. (4.82)-(4.86) and (4.145) into them, thus:

$$E_{zz} = \frac{E}{\left[\left(1 - X_2\right)\left(1 + \frac{\cos\theta}{\sqrt{2}}\right)\left(\frac{\rho_s}{\rho}\right) + \left(1 - X_2\right)^3 \frac{\left(2 + \sqrt{2}\cos\theta\right)^2}{192\sin^3\theta} \frac{1}{C_1}\left(\frac{\rho_s}{\rho}\right)^2 \right]}$$

(4.153)

$$E_{yy} = \frac{E_s}{\left(2\left(1 - X_2\right) + \frac{\sqrt{2}}{\cos\theta}\left(1 - \frac{X_2}{\sqrt{2}\cos\theta}\right)\right)\left(2 + \sqrt{2}\cos\theta\right)\frac{1}{8}\left(\frac{\rho_s}{\rho}\right) + \left(\frac{\sin\theta}{\cos^4\theta}\left(1 - X_2\right)^3 + \frac{\sqrt{2}\left(1 - \frac{X_2}{\sqrt{2}\cos\theta}\right)^3}{\sin\theta\cos\theta}\right)\left(2 + \sqrt{2}\cos\theta\right)^2 \frac{1}{384 C_1}\left(\frac{\rho_s}{\rho}\right)^2}$$

(4.154)

$$\upsilon_{zx} = \upsilon_{zy} = -\frac{\varepsilon_{xx}}{\varepsilon_{zz}} = -\frac{\left(\left(1 - X_2\right)\frac{\sin\theta}{2} - \left(1 - X_2\right)^3\left(\frac{2 + \sqrt{2}\cos\theta}{192\cos^2\theta}\right)\frac{1}{C_1}\left(\frac{\rho_s}{\rho}\right)\right)}{\left(\left(1 - X_2\right)\sin\theta + \left(1 - X_2\right)^3\left(\frac{2 + \sqrt{2}\cos\theta}{96\sin^2\theta}\right)\frac{1}{C_1}\left(\frac{\rho_s}{\rho}\right)\right)}$$

(4.155)

$$\upsilon_{yx} = -\frac{\varepsilon_{xx}}{\varepsilon_{yy}} = -\frac{\left(\frac{1}{\sqrt{2}}\left(1 - \frac{X_2}{\sqrt{2}\cos\theta}\right) - \left(1 - \frac{X_2}{\sqrt{2}\cos\theta}\right)^3\left(\frac{\sqrt{2} + \cos\theta}{48\sin\theta}\right)\frac{1}{C_1}\left(\frac{\rho_s}{\rho}\right)\right)}{\left(\cos\theta\left(1 - X_2\right) + \frac{1}{\sqrt{2}}\left(1 - \frac{X_2}{\sqrt{2}\cos\theta}\right)\right) + \left(\frac{\sin^2\theta}{\cos\theta}\left(1 - X_2\right)^3 + \sqrt{2}\cos^2\theta\left(1 - \frac{X_2}{\sqrt{2}\cos\theta}\right)^3\right)\left(\frac{2 + \sqrt{2}\cos\theta}{96\sin\theta\cos^3\theta}\right)\frac{1}{C_1}\left(\frac{\rho_s}{\rho}\right)}$$

(4.156)

$$\upsilon_{yz} = -\frac{\varepsilon_{zz}}{\varepsilon_{yy}} = -\frac{\left(\cos\theta\left(1 - X_2\right) - \left(1 - X_2\right)^3\left(\frac{2 + \sqrt{2}\cos\theta}{96\sin\theta\cos\theta}\right)\frac{1}{C_1}\left(\frac{\rho_s}{\rho}\right)\right)}{\left(\cos\theta\left(1 - X_2\right) + \frac{1}{\sqrt{2}}\left(1 - \frac{X_2}{\sqrt{2}\cos\theta}\right)\right) + \left(\frac{\sin^2\theta}{\cos\theta}\left(1 - X_2\right)^3 + \sqrt{2}\cos^2\theta\left(1 - \frac{X_2}{\sqrt{2}\cos\theta}\right)^3\right)\left(\frac{2 + \sqrt{2}\cos\theta}{96\sin\theta\cos^3\theta}\right)\frac{1}{C_1}\left(\frac{\rho_s}{\rho}\right)}$$

(4.157)

$$\sigma_{z\,max} = \frac{\sigma_{max}}{\left(1 + \frac{\cos\theta}{\sqrt{2}}\right)\left(\frac{\rho_s}{\rho}\right) + \left(1 - X_2\right)\left(\frac{2 + \sqrt{2}\cos\theta}{\sin\theta}\right)^{3/2} \frac{C_2}{8\sqrt{2}C_1}\left(\frac{\rho_s}{\rho}\right)^{3/2}}$$

(4.158)

$$\sigma_{y\,max} = \frac{\sigma_{max}}{\left(1 + \frac{\cos\theta}{\sqrt{2}}\right)\left(\frac{\rho_s}{\rho}\right) + \left(1 - X_2\right)\frac{\sqrt{\sin\theta}\left(2 + \sqrt{2}\cos\theta\right)^{3/2}}{8\sqrt{2}\cos^2\theta} \frac{C_2}{C_1}\left(\frac{\rho_s}{\rho}\right)^{3/2}}$$

(4.159)

where

$$X_2 = \left(\frac{2d}{L}\right) = \left(2C_2 C_3 \sqrt{\frac{8\sin\theta\cos^2\theta}{2 + \sqrt{2}\cos\theta}}\sqrt{\frac{\rho}{\rho_s}}\right)$$

(4.160)

denotes the fraction of strut that that is rigid.

4.3 Constants C_1, C_2 and C_3

As suggested in Section 3.5, the cross-section of the struts in rigid polyurethane foam is similar in shape to the Plateau border [1] shown in Fig. 4.25. Thus, the model developed will adopt the Plateau border as the shape of the strut cross-section. Based on this, the constants C_1 and C_2 defined in Sections 4.1 and 4.2 can be determined.

$$C_1 = \frac{20\sqrt{3} - 11\pi}{6\left(2\sqrt{3} - \pi\right)^2} \approx 0.1338$$

(4.161)

$$C_2 = \frac{1}{\sqrt{3\sqrt{3} - 1.5\pi}} \approx 1.4378$$

(4.162)

The value of C_2 is calculated based on the maximum distance R from the centroid of the Plateau border (Fig. 4.25). Failure however might not occur at that point; it depends on the direction and orientation of the strut cross-section relative to the applied bending moment. To account for this variation, C_2 should be determined by using the average maximum distance $\overline{R}$ from the centroid of the Plateau border, thus:

$$C_2 = \frac{1}{\sqrt{3\sqrt{3} - 1.5\pi}} \times \frac{\overline{R}}{R} = \frac{1}{\sqrt{3\sqrt{3} - 1.5\pi}} \frac{\int_0^{\frac{\pi}{3}} \cos\theta \, d\theta}{\frac{\pi}{3}}$$

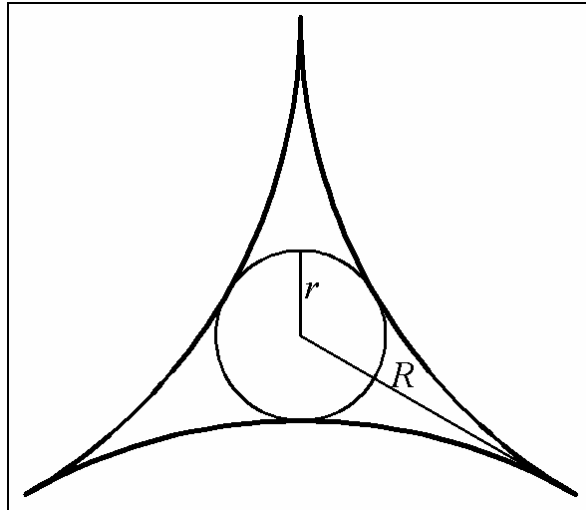$$C_2 = \frac{1}{\sqrt{3\sqrt{3} - 1.5\pi}} \times \frac{3\sqrt{3}}{2\pi} \approx 1.189$$

(4.163)

Fig. 4.25 Plateau border

C_3, which is the ratio of the rigid strut segment lengths to the maximum distance of the strut surface from the centroidal axis of the cross-section, is determined from experimental observations of the size of the struts and the length of the rigid segments at the vertices of the cells inside actual foam (see Sections 3.5 and 3.6). This showed that on average $C_3 = 0.95$. However, because C_2 is determined by using the average maximum distance ($\overline{R}$) from the cross-section centroidal axes, C_3 also has to be based on this average distance so that the length of the rigid segments and the area of the strut cross-section are still related by

$$d = C_2 C_3 \sqrt{A}$$

(4.164)

Hence, C_3 becomes:

$$C_3 = \frac{2\pi}{3\sqrt{3}} \times 0.95 \approx 1.149$$

(4.165)

The constants C_1, C_2 and C_3 and the data derived from the experiments discussed in Chapter 3 facilitate calculation of the mechanical properties of foam based on the models. Parametric studies and comparison of these models with actual foam can then be performed; this will be discussed in Section 4.4.

4.4　Results and discussion

4.4.1　Cell geometry and parametric studies

Fig. 4.26 shows an elongated rhombic dodecahedron and an elongated tetrakaidecahedron cell, while Fig. 4.27 shows cells in actual foam. The figures indicate that the geometry of the rhombic dodecahedron cell model has some distinct differences with the cells in rigid polyurethane foam. Actual cells have slanted faces adjacent to the upper and lower ends, vertical faces on the sides and horizontal faces at the top and bottom; the rhombic dodecahedron cell model only has slanted faces and pointed apices at the top and bottom. On the other hand, as highlighted in Section 3.4, an elongated tetrakaidecahedron cell displays great similarity with actual foam cells, much better than that of a rhombic dodecahedron cell.

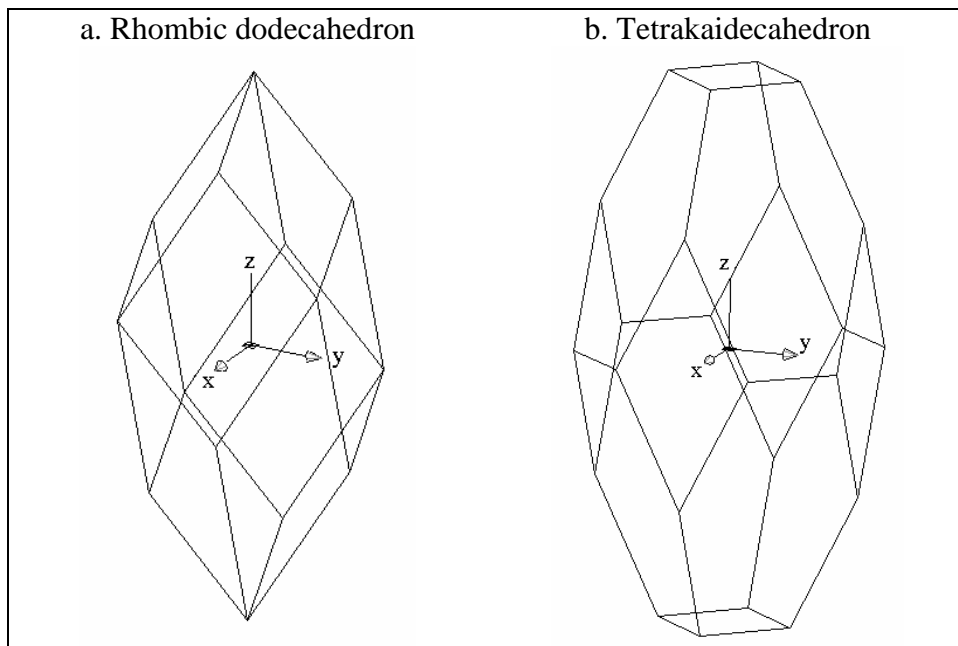

a. Rhombic dodecahedron　　　　b. Tetrakaidecahedron

Fig. 4.26 Elongated rhombic dodecahedron and tetrakaidecahedron cells
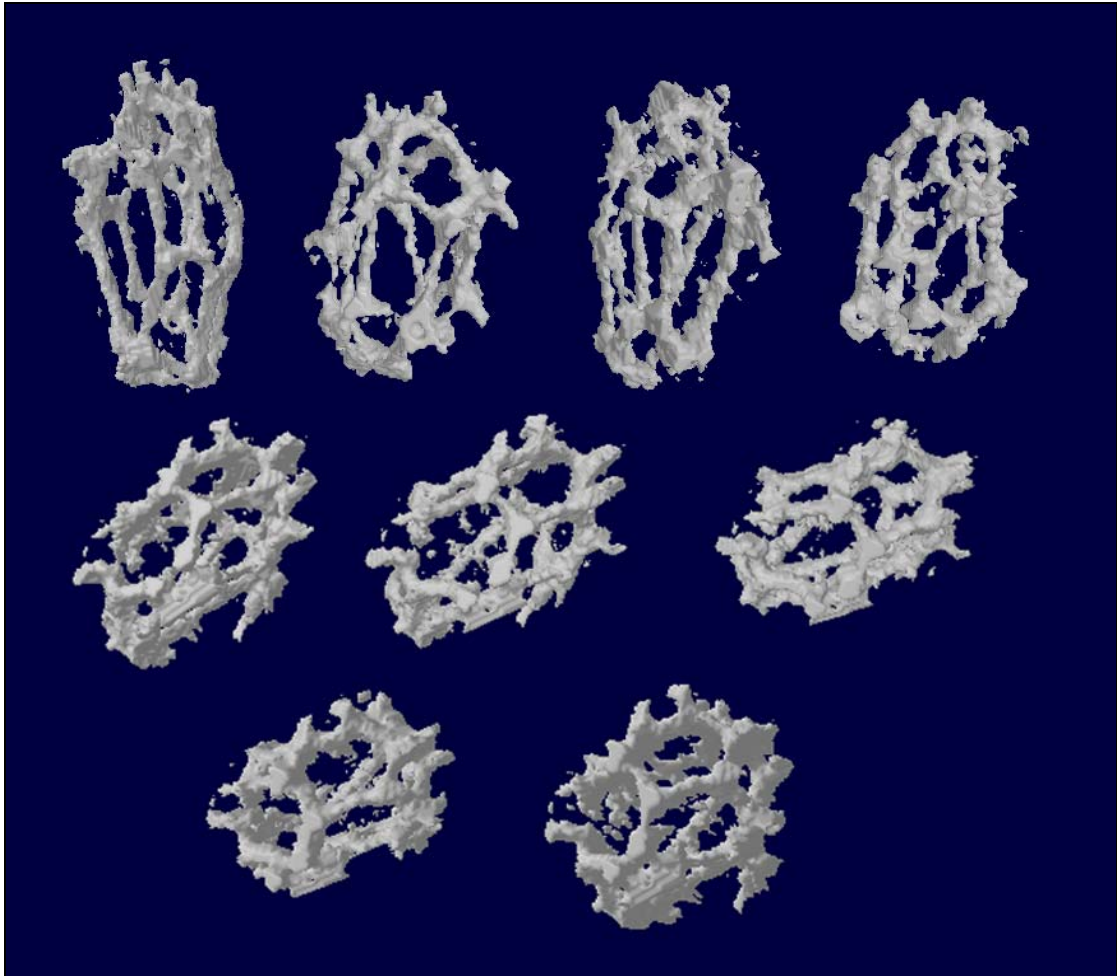
Fig. 4.27 Actual foam cell

The mechanical properties of an idealized foam model based on rhombic dodecahedron and tetrakaidecahedron cells in term of its stiffness, Poisson's ratios and tensile strength can be determined by using the equations derived in Sections 4.1-4.3. The parameters required are the elastic stiffness (E_s) and tensile strength $(\sigma_{\max s})$ of the solid material that constitutes the struts, the relative density of the foam $\left(\dfrac{\rho}{\rho_s}\right)$ and the geometric anisotropy ratio of the cells $(\tan\theta)$. A parametric study was undertaken by varying these parameters to analyse their influence on the overall mechanical properties of foam based on these models.

Stiffness

The stiffness of foam predicted by the rhombic dodecahedron cell model can be calculated using the following equations defined in Sections 4.1:

- Neglecting the correction for rigid segments at the strut ends (fully flexible struts)

  o The stiffness in the rise direction is given by

$$E_{zz} = \frac{E_s}{\left(\dfrac{1}{2}\dfrac{\rho_s}{\rho} + \dfrac{\left(\cos^2\theta + 1\right)^{3/2}}{48\sin^3\theta}\dfrac{1}{C_1}\left(\dfrac{\rho_s}{\rho}\right)^2 \right)}$$

(4.166)

  o The stiffness in the transverse direction is

$$E_{yy} = \frac{E_s}{\left(\dfrac{1}{2}\dfrac{\rho_s}{\rho} + \dfrac{\left(\cos^2\theta + 1\right)^{3/2}}{96\sin\theta\cos^4\theta}\dfrac{1}{C_1}\left(\dfrac{\rho_s}{\rho}\right)^2 \right)}$$

(4.167)

- Considering the correction for rigid segments at the strut ends (semi-flexible struts)

  o The stiffness in the rise direction is

$$E_{zz} = \frac{E_s}{\left(X_1\dfrac{1}{2}\dfrac{\rho_s}{\rho} + X_1^3\dfrac{\left(\cos^2\theta + 1\right)^{3/2}}{48\sin^3\theta}\dfrac{1}{C_1}\left(\dfrac{\rho_s}{\rho}\right)^2 \right)}$$

(4.168)

  o The stiffness in the transverse direction is

$$E_{yy} = \frac{E_s}{\left(X_1\dfrac{\rho_s}{\rho} + X_1^3\dfrac{\left(\cos^2\theta + 1\right)^{3/2}}{96\sin\theta\cos^4\theta}\dfrac{1}{C_1}\left(\dfrac{\rho_s}{\rho}\right)^2 \right)}$$

(4.169)

where

$$X_1 = \left(1 - \frac{4\sqrt{\sin\theta}\cos\theta}{\left(\cos^2\theta + 1\right)^{1/4}}C_2 C_3\sqrt{\frac{\rho}{\rho_s}} \right)$$

(4.170)

The stiffness of foam predicted by the tetrakaidecahedron cell model derived in Section 4.2 are given by:

- For fully flexible struts

  o The stiffness in the rise direction is

$$E_{zz} = \frac{E_s}{\left[\left(1 + \frac{\cos\theta}{\sqrt{2}}\right)\left(\frac{\rho_s}{\rho}\right) + \left(\frac{\left(2 + \sqrt{2}\cos\theta\right)^2}{192\sin^3\theta}\right)\frac{1}{C_1}\left(\frac{\rho_s}{\rho}\right)^2\right]}$$

(4.171)

  o The stiffness in the transverse direction is

$$E_{yy} = \frac{E_s}{\left(2 + \frac{\sqrt{2}}{\cos\theta}\right)\left(2 + \sqrt{2}\cos\theta\right)\frac{1}{8}\left(\frac{\rho_s}{\rho}\right) + \left(\frac{\sin\theta}{\cos^4\theta} + \frac{\sqrt{2}}{\sin\theta\cos\theta}\right)\left(2 + \sqrt{2}\cos\theta\right)^2\frac{1}{384 C_1}\left(\frac{\rho_s}{\rho}\right)^2}$$

(4.172)

- For semi-flexible struts

  o The stiffness in the rise direction is

$$E_{zz} = \frac{E}{\left[\left(1 - X_2\right)\left(1 + \frac{\cos\theta}{\sqrt{2}}\right)\left(\frac{\rho_s}{\rho}\right) + \left(1 - X_2\right)^3 \frac{\left(2 + \sqrt{2}\cos\theta\right)^2}{192\sin^3\theta}\frac{1}{C_1}\left(\frac{\rho_s}{\rho}\right)^2\right]}$$

(4.173)

  o The stiffness in the transverse direction is

$$E_{yy} = \frac{E_s}{\left(2(1 - X_2) + \frac{\sqrt{2}}{\cos\theta}\left(1 - \frac{X_2}{\sqrt{2}\cos\theta}\right)\right)\left(2 + \sqrt{2}\cos\theta\right)\frac{1}{8}\left(\frac{\rho_s}{\rho}\right) + \left(\frac{\sin\theta}{\cos^4\theta}\left(1 - X_2\right)^3 + \frac{\sqrt{2}\left(1 - \frac{X_2}{\sqrt{2}\cos\theta}\right)^3}{\sin\theta\cos\theta}\right)\left(2 + \sqrt{2}\cos\theta\right)^2\frac{1}{384 C_1}\left(\frac{\rho_s}{\rho}\right)^2}$$

(4.174)

where

$$X_2 = \left(2 C_2 C_3 \sqrt{\frac{8\sin\theta\cos^2\theta}{2 + \sqrt{2}\cos\theta}}\sqrt{\frac{\rho}{\rho_s}}\right)$$

(4.175)

(Differences arising from consideration of rigid strut segment will be highlighted later.)

Note that all the expressions have the terms $\left(\dfrac{\rho_s}{\rho}\right)$ and $\left(\dfrac{\rho_s}{\rho}\right)^2$ in their denominators, which represent respectively the contribution from the axial force and the bending moment in the struts. For low density foams, $\left(\dfrac{\rho_s}{\rho}\right)^2$ is much larger than $\left(\dfrac{\rho_s}{\rho}\right)$ showing that the dominant deformation mechanism in foam is bending of the struts. This is consistent with the observations described in Section 3.6 as well as with results by some previous researchers [2, 8, 20, 21, 28, 33, 40, 41]. It is also worth noting that cell size does not affect foam stiffness, which depends only on the stiffness E_s of the solid strut material, the relative density $\left(\dfrac{\rho}{\rho_s}\right)$, the cell geometric anisotropy ratio $(\tan\theta)$, the strut cross-section shape represented by C_1 and C_2, and the length of the rigid strut segments represented by C_3.
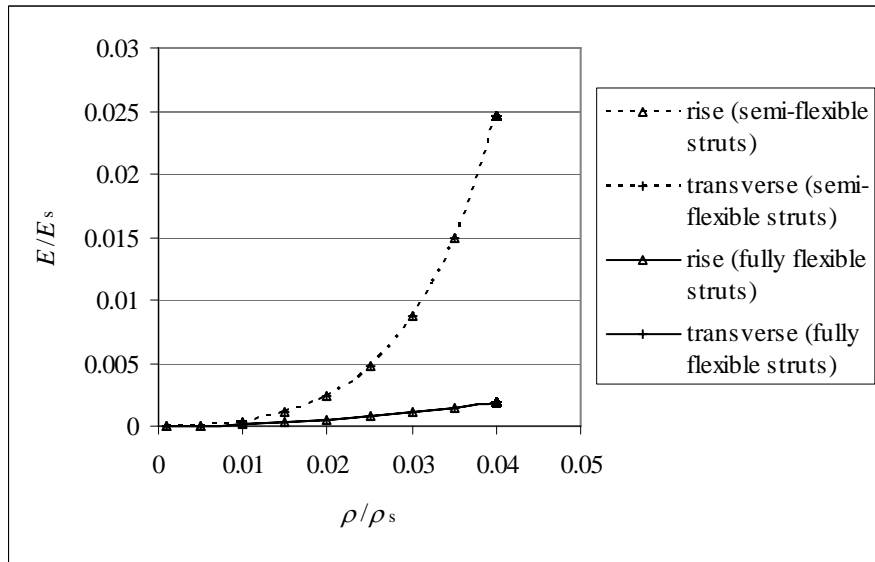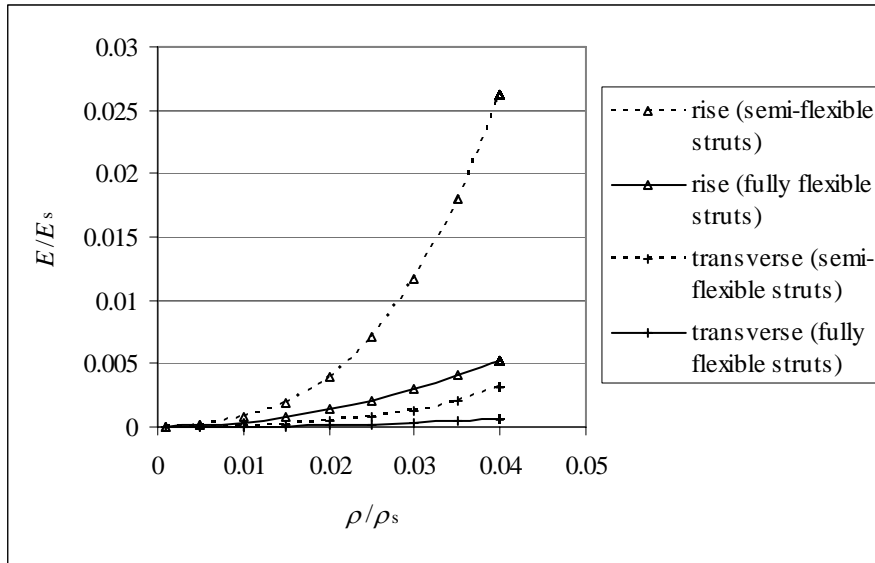

Fig. 4.28 Variation of foam stiffness with relative density based on an isotropic rhombic dodecahedron cell model
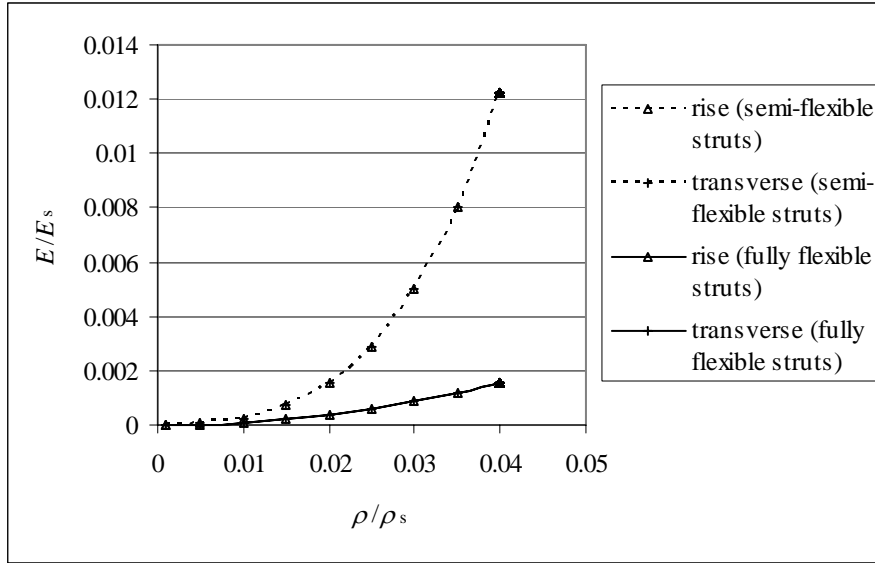
Fig. 4.29 Variation of foam stiffness with relative density based on an isotropic tetrakaidecahedron model

Figs. 4.28 and 4.29 show respectively the variation of foam stiffness with relative density based on an isotropic $(\tan\theta = 1)$ rhombic dodecahedron and an isotropic tetrakaidecahedron cell model. As expected, the stiffness in the foam rise direction is the same as that in the transverse direction because the models are isotropic. Another expected result is that the foam stiffness based on both cells with rigid strut segments (semi-flexible struts) is higher than that without this correction and this difference increases with density because the length of the rigid strut segments also increases with density.

Foam stiffness predicted by the models increases with relative density, as shown in Figs. 4.28 and 4.29. This is expected, as a higher density means that there is more solid material to bear the applied load, making the structure stiffer. The stiffness E of foam based on a cell model without rigid segment (fully flexible struts) can be approximated by a power law relationship in terms of the relative density.

$$\frac{E}{E_s} = C_f \left(\frac{\rho}{\rho_s}\right)^n$$

(4.176)

where E_s is the stiffness of the solid strut material, and ρ and ρ_s are respectively the densities of the foam and the solid strut material, and C_f and n are constants that are governed by the shape of the cells and the strut cross-section, as well as the deformation mechanism in the foam (bending and stretching of the struts). It turns out that $C_f = 1.175$ and $n = 1.99$ for the fully flexible rhombic dodecahedron cell model, while C_f and n for the fully flexible tetrakaidecahedron cell model are 0.893 and 1.98, respectively. This is similar to the values for the semi-empirical model by Gibson et al. [21], Triantafillou et al. [8] and Gibson and Ashby [2, 20], which had $C_f = 1$ and $n = 2$, but were not derived from any particular cell structure and strut cross-section. Hence, the proposed model has yielded the basis for the values of C_f and n, which the earlier researchers determined empirically from experimental results.

In contrast with the stiffness of cells without the correction for rigid strut segments, foam stiffness based on cells with rigid strut segments (Figs. 4.28 and 4.29) cannot be approximated using a power law equation of the form of Eq. (4.176) because introduction of the correction for rigid strut segments to the expressions for stiffness results in an additional term $\left(\dfrac{\rho_s}{\rho} \right)^m$ with different specific values of m. The values of the stiffness are also not similar to those of the semi-empirical model by Gibson et al. [21], Triantafillou et al. [8], Gibson and Ashby [2, 20] if the length of the rigid strut segments is significant compared to the length of cell struts (greater than 0.1 of the strut length). This is probably because the foams they studied in deriving their empirical equation have relatively short rigid strut segments compared to the strut length.

Fig. 4.30 Variation of foam stiffness with relative density based on an anisotropic rhombic dodecahedron cell model
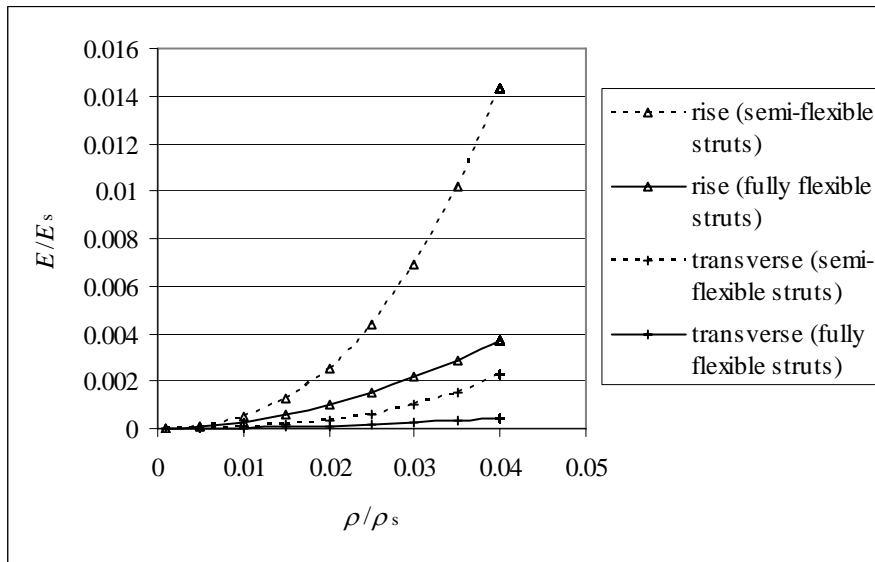

Fig. 4.31 Variation of foam stiffness with relative density based on an anisotropic tetrakaidecahedron cell model

Figs. 4.30 and 4.31 show respectively the variation of foam stiffness with relative density based on the anisotropic rhombic dodecahedron and the anisotropic tetrakaidecahedron cell model. The anisotropy ratio ($\tan\theta$) in this instance is taken as 2 and as with the isotropic models, the anisotropic models also yield a higher value of stiffness when the relative density is higher. The stiffness is greater in the foam rise direction because struts in the cells are more aligned in this direction, making them harder to bend when loaded in this direction but easier to bend when loaded

106

transversely. These trends are in agreement with the experimental results described in Section 3.2.
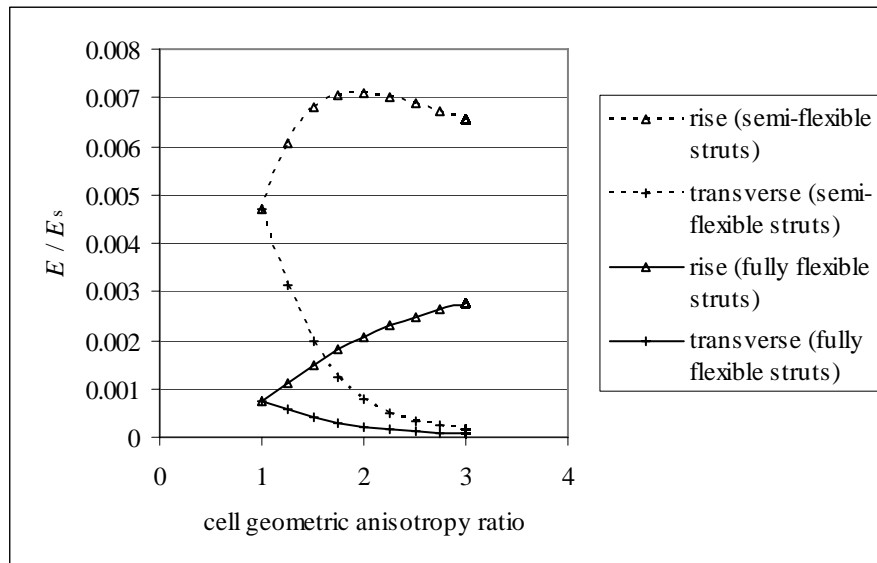
Fig. 4.32 Variation of foam stiffness with cell anisotropy based on a rhombic dodecahedron cell model
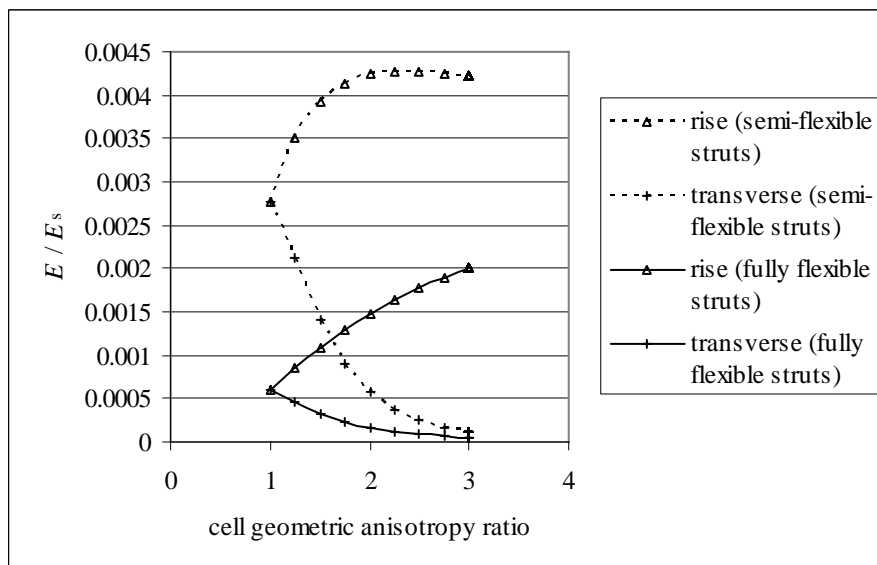
Fig. 4.33 Variation of foam stiffness with cell anisotropy based on a tetrakaidecahedron cell model

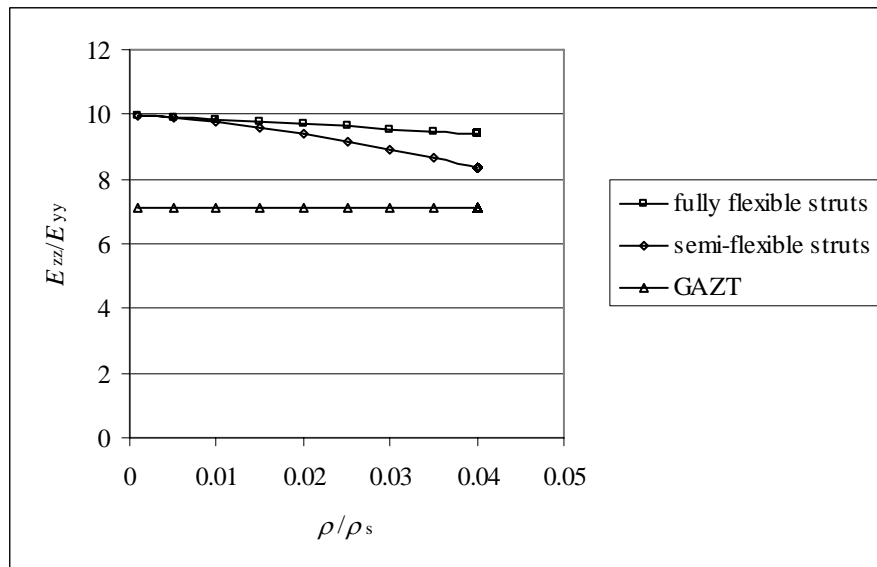Figs. 4.32 and 4.33 show respectively, the variation of stiffness with geometric cell anisotropy ratio for foam with a relative density $\left(\dfrac{\rho}{\rho_s} \right) = 0.0246$, based on a rhombic dodecahedron and a tetrakaidecahedron cell model. As the geometric anisotropy increases, the stiffnesses in the rise and transverse directions diverge,

107

resulting in an increase in the anisotropic stiffness ratio, as shown in Figs. 4.34 and 4.35. Figs. 4.32 and 4.33 also show that the stiffness in the rise direction increases with the geometric anisotropy ratio, but the rate of increase diminishes. In the case of rhombic dodecahedron cells with semi flexible struts, the stiffness actually decreases after a certain point. The elevation in stiffness is due mainly to the orientation of cell struts, whereby a higher anisotropy ratio implies that struts are more aligned towards the rise direction, making them harder to bend for loading in this direction. This enhancement of stiffness due to strut orientation is however reduced by the reduction in cross-sectional area of the struts due to a higher anisotropy ratio, as implied by Eqs. (4.4) and (4.85). The effect of a smaller cross-section ultimately dominates, resulting in the convex curves shown in Figs. 4.32 and 4.33. On the other hand, the stiffness in the transverse direction decreases with cell geometric anisotropy and this arises from the orientation of the struts as well as the decrease in the cross-sectional area as the cell geometric anisotropy increases. With a larger geometric anisotropy ratio, struts are more aligned towards the rise direction, making them easier to bend when the foam is loaded in the transverse direction, resulting in a lower stiffness.
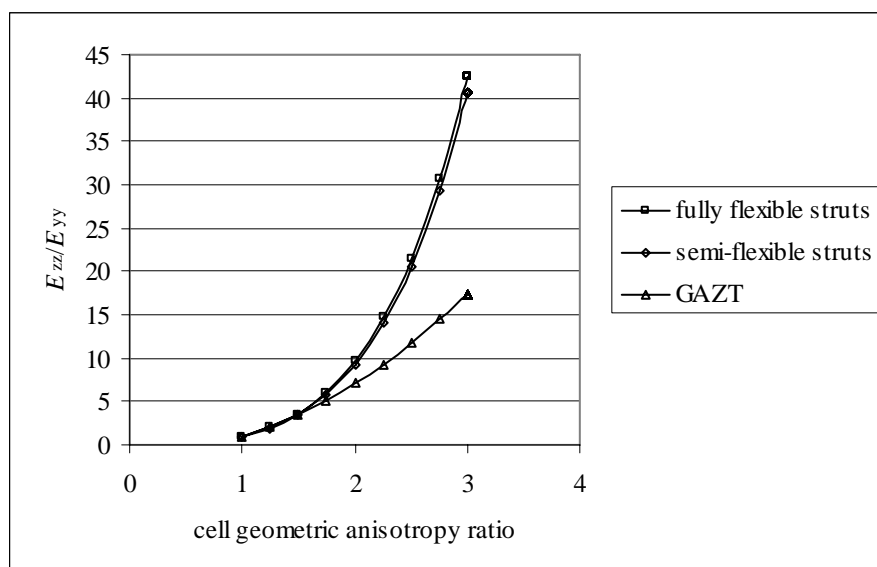
Fig. 4.34 Variation of anisotropy in foam stiffness with cell anisotropy based on a rhombic dodecahedron cell model
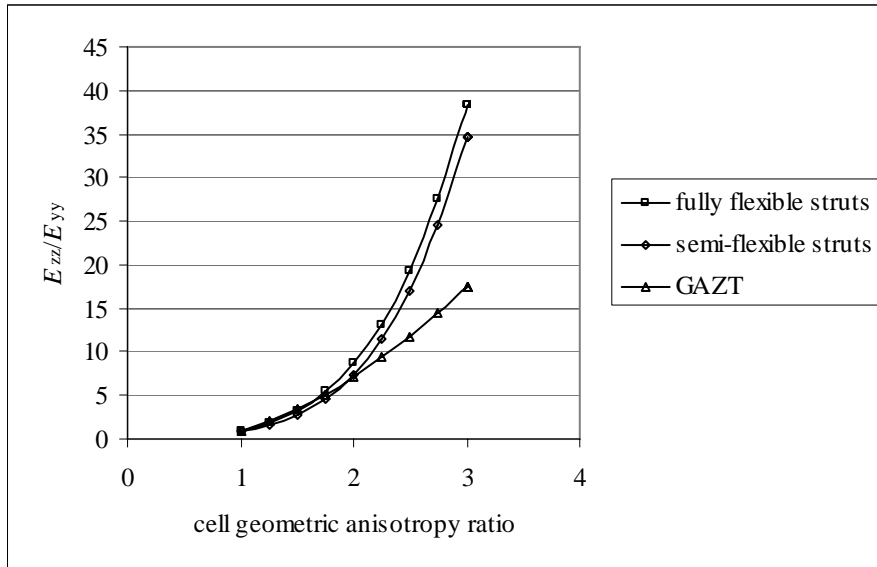
Fig. 4.35 Variation of anisotropy in foam stiffness with cell anisotropy based on a tetrakaidecahedron cell model

Fig. 4.36 Variation of anisotropy in foam stiffness with relative density based on a rhombic dodecahedron cell model
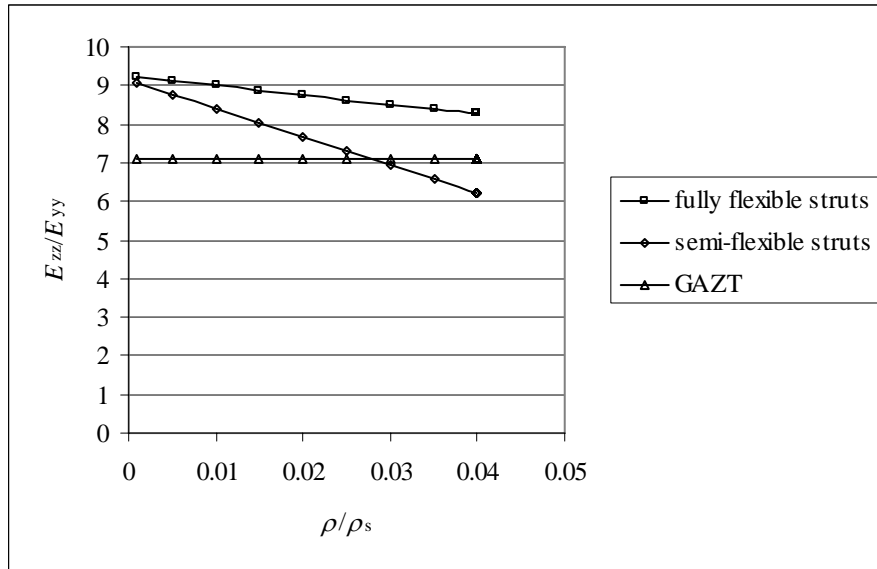
Fig. 4.37 Variation of anisotropy in foam stiffness with relative density based on a tetrakaidecahedron cell model

Figs. 4.34 and 4.35 depict respectively the variation of foam stiffness anisotropy ratio with geometric anisotropy for foam with a relative density $\left(\dfrac{\rho}{\rho_s}\right) = 0.0246$ based on a rhombic dodecahedron and a tetrakaidecahedron cell model, while Figs. 4.36 and 4.37 illustrate the variation of anisotropy in stiffness with relative density for foam with a geometric anisotropy ratio of $\tan\theta = 2$ based on the same two cell models. The graphs indicate that the influence of the relative density on the stiffness anisotropy ratio is relatively small compared to that of the cell geometric anisotropy (Fig. 4.35). This is similar to the prediction based on the cell model by Gibson et al. [21], Triantafillou et al. [8], Gibson and Ashby [2, 20], marked as GAZT, in the graphs. However, the present study gives higher values of the stiffness anisotropy ratio due to the difference in cell geometry with the GAZT model. Figs. 4.34 and 4.35 also show that cell models with and without correction for rigid strut segments predicts similar trends for the stiffness anisotropy ratio.

Tensile strength

The tensile strength of foam based on the models is governed by failure of the most vulnerable strut. The foam tensile strengths based on the rhombic dodecahedron cell model, as derived in Section 4.1, are:

- For fully flexible struts

  - Tensile strength in the rise direction

$$\sigma_{z\max} = \frac{\sigma_{\max s}}{\dfrac{1}{2}\dfrac{\rho_s}{\rho} + \dfrac{\left(\cos^2\theta + 1\right)^{3/4}}{4\sqrt{2}\left(\sin\theta\right)^{3/2}}\dfrac{C_2}{C_1}\left(\dfrac{\rho_s}{\rho}\right)^{3/2}}$$

(4.177)

  - Tensile strength in the transverse direction

$$\sigma_{y\max} = \frac{\sigma_{\max s}}{\dfrac{1}{2}\dfrac{\rho_s}{\rho} + \dfrac{\left(\cos^2\theta + 1\right)^{3/4}}{8\sqrt{\sin\theta}\cos^2\theta}\dfrac{C_2}{C_1}\left(\dfrac{\rho_s}{\rho}\right)^{3/2}}$$

(4.178)

- For semi-flexible struts

  - Tensile strength in the rise direction

$$\sigma_{z\max} = \frac{\sigma_{\max s}}{\dfrac{1}{2}\dfrac{\rho_s}{\rho} + X_1\dfrac{\left(\cos^2\theta + 1\right)^{3/4}}{4\sqrt{2}\left(\sin\theta\right)^{3/2}}\dfrac{C_2}{C_1}\left(\dfrac{\rho_s}{\rho}\right)^{3/2}}$$

(4.179)

  - Tensile strength in the transverse direction

$$\sigma_{y\max} = \frac{\sigma_{\max s}}{\dfrac{1}{2}\dfrac{\rho_s}{\rho} + X_1\dfrac{\left(\cos^2\theta + 1\right)^{3/4}}{8\sqrt{\sin\theta}\cos^2\theta}\dfrac{C_2}{C_1}\left(\dfrac{\rho_s}{\rho}\right)^{3/2}}$$

(4.180)

where

$$X_1 = \left(1 - \frac{4\sqrt{\sin\theta}\cos\theta}{\left(\cos^2\theta + 1\right)^{1/4}}C_2C_3\sqrt{\frac{\rho}{\rho_s}}\right)$$

(4.181)

Correspondingly, the expressions for foam tensile strengths based on the tetrakaidecahedron cell model, as derived in Section 4.2, are:

- For fully flexible struts

111

- Tensile strength in the rise direction

$$\sigma_{z\,max} = \frac{\sigma_{max\,s}}{\left(1 + \frac{\cos\theta}{\sqrt{2}}\right)\left(\frac{\rho_s}{\rho}\right) + \left(\frac{2 + \sqrt{2}\cos\theta}{\sin\theta}\right)^{\frac{3}{2}} \frac{C_2}{8\sqrt{2}C_1}\left(\frac{\rho_s}{\rho}\right)^{\frac{3}{2}}}$$

(4.182)

- Tensile strength in the transverse direction

$$\sigma_{y\,max} = \frac{\sigma_{max\,s}}{\left(1 + \frac{\cos\theta}{\sqrt{2}}\right)\left(\frac{\rho_s}{\rho}\right) + \frac{\sqrt{\sin\theta}\left(2 + \sqrt{2}\cos\theta\right)^{\frac{3}{2}}}{8\sqrt{2}\,\cos^2\theta}\frac{C_2}{C_1}\left(\frac{\rho_s}{\rho}\right)^{\frac{3}{2}}}$$

(4.183)

- For semi-flexible struts

  - Tensile strength in the rise direction

$$\sigma_{z\,max} = \frac{\sigma_{max}}{\left(1 + \frac{\cos\theta}{\sqrt{2}}\right)\left(\frac{\rho_s}{\rho}\right) + \left(1 - X_2\right)\left(\frac{2 + \sqrt{2}\cos\theta}{\sin\theta}\right)^{\frac{3}{2}} \frac{C_2}{8\sqrt{2}C_1}\left(\frac{\rho_s}{\rho}\right)^{\frac{3}{2}}}$$

(4.184)

  - Tensile strength in the transverse direction

$$\sigma_{y\,max} = \frac{\sigma_{max}}{\left(1 + \frac{\cos\theta}{\sqrt{2}}\right)\left(\frac{\rho_s}{\rho}\right) + \left(1 - X_2\right)\frac{\sqrt{\sin\theta}\left(2 + \sqrt{2}\cos\theta\right)^{\frac{3}{2}}}{8\sqrt{2}\,\cos^2\theta}\frac{C_2}{C_1}\left(\frac{\rho_s}{\rho}\right)^{\frac{3}{2}}}$$

(4.185)

where

$$X_2 = \left(2C_2C_3\sqrt{\frac{8\sin\theta\cos^2\theta}{2 + \sqrt{2}\cos\theta}}\sqrt{\frac{\rho}{\rho_s}}\right)$$

(4.186)

These expressions have the terms $\left(\frac{\rho_s}{\rho}\right)$ and $\left(\frac{\rho_s}{\rho}\right)^{\frac{3}{2}}$ in their denominators, and

they represent respectively the effects of axial stretching and bending of struts. For

low density foams, $\left(\frac{\rho_s}{\rho}\right)^{\frac{3}{2}}$ is much larger than $\left(\frac{\rho_s}{\rho}\right)$ indicating that the dominant

factor for tensile fracture in the foam is the bending of struts. As with the elastic

stiffness, the tensile strength is not influenced by the size of the cells; it is determined

112

by the tensile strength $\sigma_{\max s}$ of the cell strut material, the relative density $\left(\dfrac{\rho}{\rho_s}\right)$, cell

geometric anisotropy ratio $(\tan\theta)$, the shape of the strut cross-section represented by

C_1 and C_2, and the length of the rigid strut segments represented by C_3.
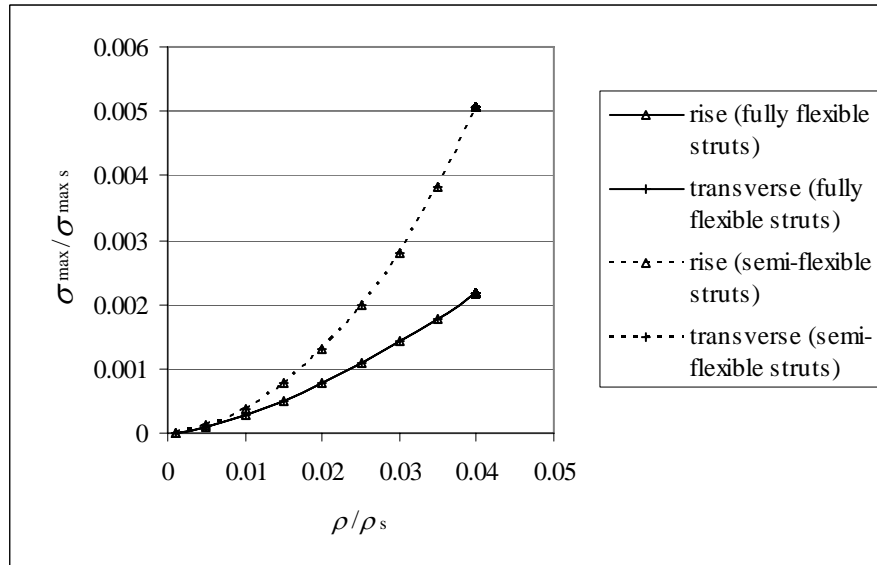
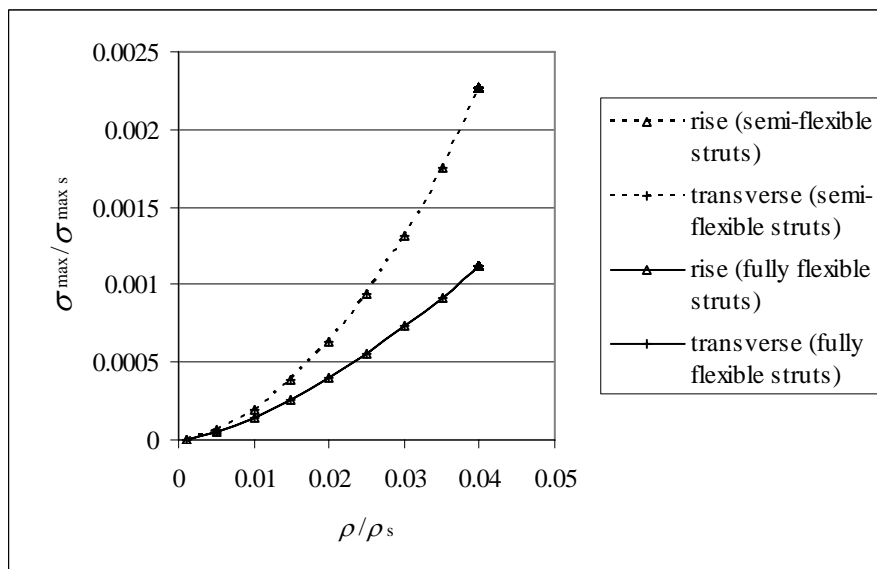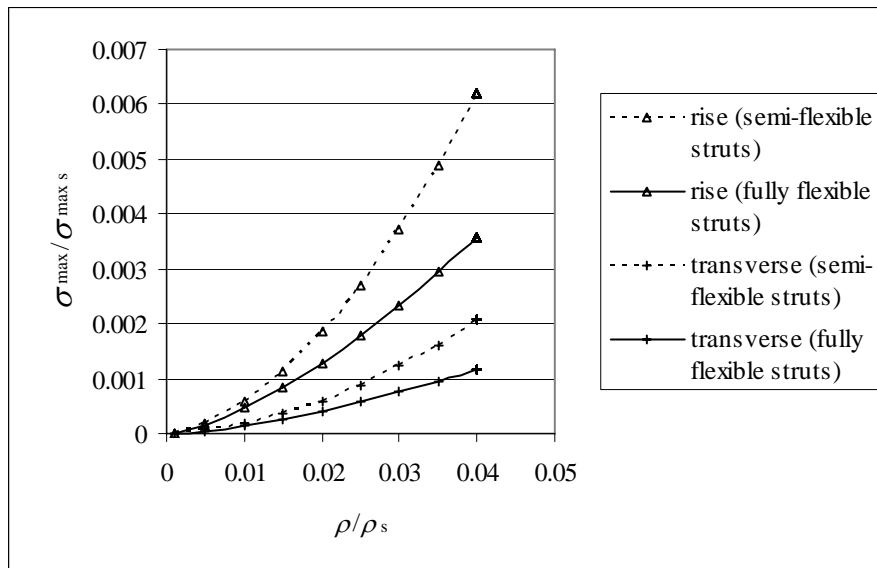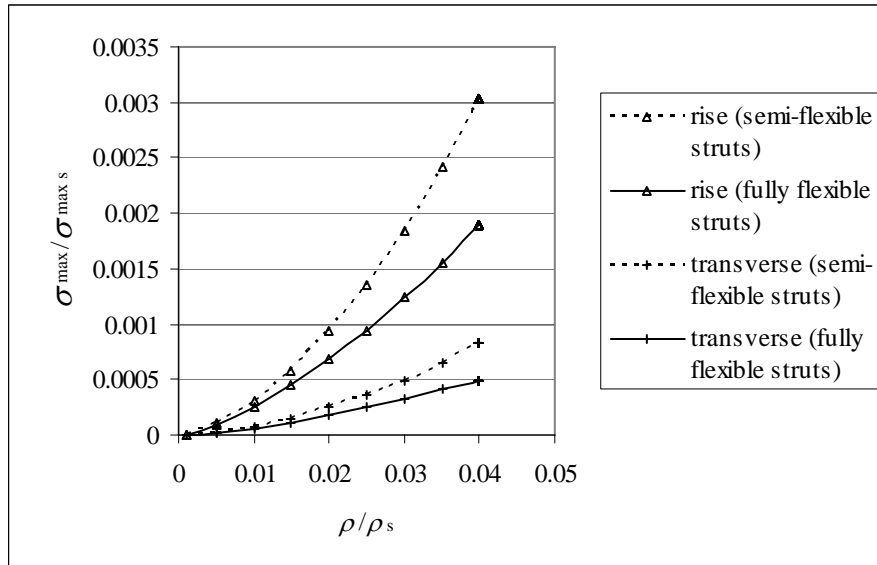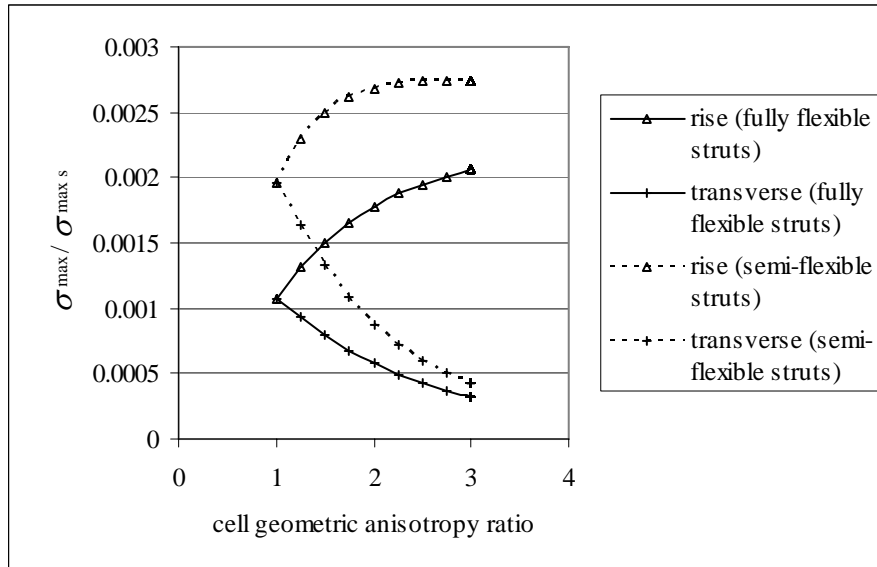Fig. 4.38 Variation of foam tensile strength with relative density based on a rhombic dodecahedron cell model
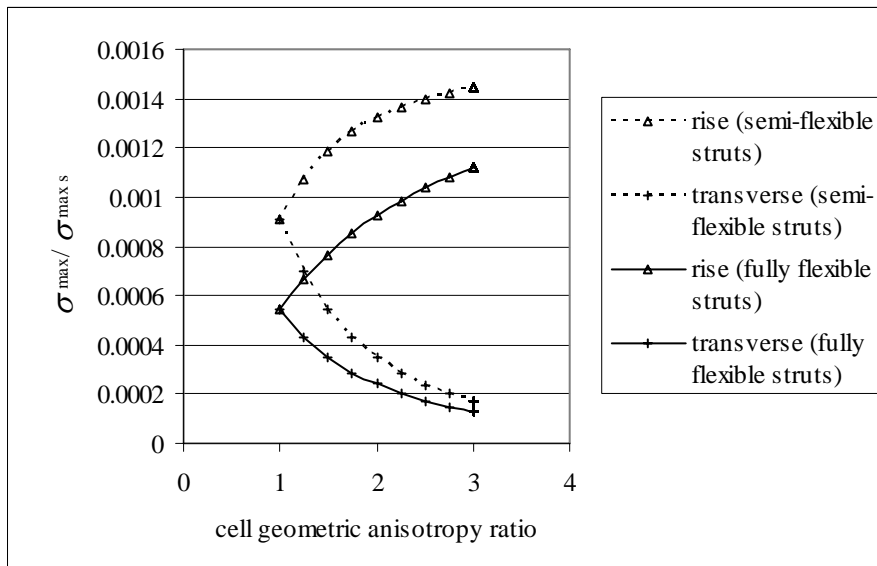

Fig. 4.39 Variation of foam tensile strength with relative density based on a tetrakaidecahedron cell model

Figs. 4.38 and 4.39 show respectively the variation of foam tensile strength with

relative density predicted by an isotropic $(\tan\theta = 1)$ rhombic dodecahedron and an

113

isotropic tetrakaidecahedron cell model. Coincidence of the strength values in the foam rise and transverse directions confirm isotropy. The tensile strength of the models incorporating the correction for rigid strut segments is higher than that of the model without this correction. This is because the deformable portion of the struts is reduced when their ends are considered rigid, thus changing the position of the maximum bending moment from the ends of the struts to the boundary between the rigid and the flexible portions, hence resulting in a higher strength.

Another similarity between foam strength and stiffness predicted by these models is that the tensile strength increases with relative density because more material is required to be broken at failure when the density is higher. The tensile strength $\sigma_{\max}$ of foam based on the fully flexible strut model can be approximated by

$$\frac{\sigma_{\max}}{\sigma_{\max s}} = C_f \left(\frac{\rho}{\rho_s} \right)^n$$

(4.187)

where $\sigma_{\max s}$ is the tensile strength the solid material in the cell struts, ρ and ρ_s are respectively the density of the foam and the solid strut material, and C_f and n are constants that are governed by the shape of the cells and the strut cross-section, as well as the mechanisms governing the failure (bending and stretching of struts). The values of the constants based on the fully flexible rhombic dodecahedron cells are $C_f = 0.265$ and $n = 1.493$, while those based on the fully flexible tetrakaidecahedron cells are $C_f = 0.135$ and $n = 1.489$. Gibson et al. [21], Triantafillou et al. [8] and Gibson and Ashby [2, 20] have expressed the tensile plastic collapse of foam, which is essentially similar to tensile fracture in this study, using the same expression, but with $C_f = 0.3$ and $n = 1.5$; however, the value of C_f in their model is determined using empirical data instead of an analytical solution. The values of n based on the

three models are close to each other because the main cause of failure in all the models is common – the bending of the struts. As with foam stiffness, the foam strength based on the cell models with the correction for rigid strut segments cannot be approximated by such a power law equation because the introduction of this correction makes the relationship between the strength and the density more complicated because of the additional term $\left(\dfrac{\rho_s}{\rho}\right)^m$ which has different specific values of m.
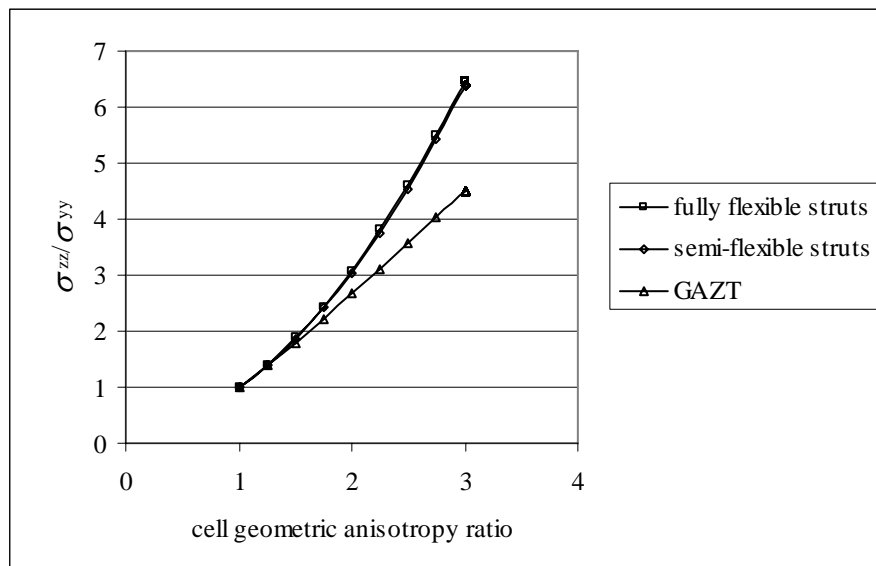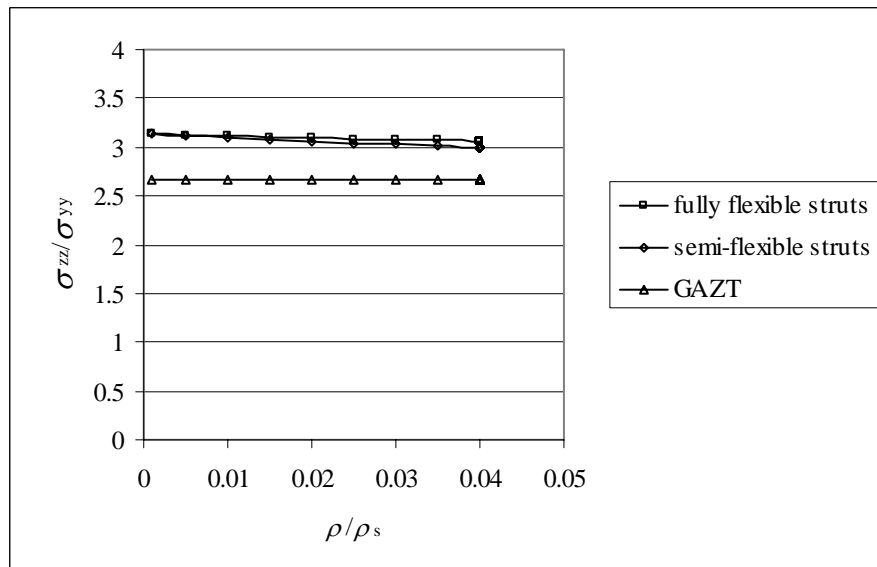

Fig. 4.40 Variation of foam tensile strength with relative density based on a rhombic dodecahedron cell model

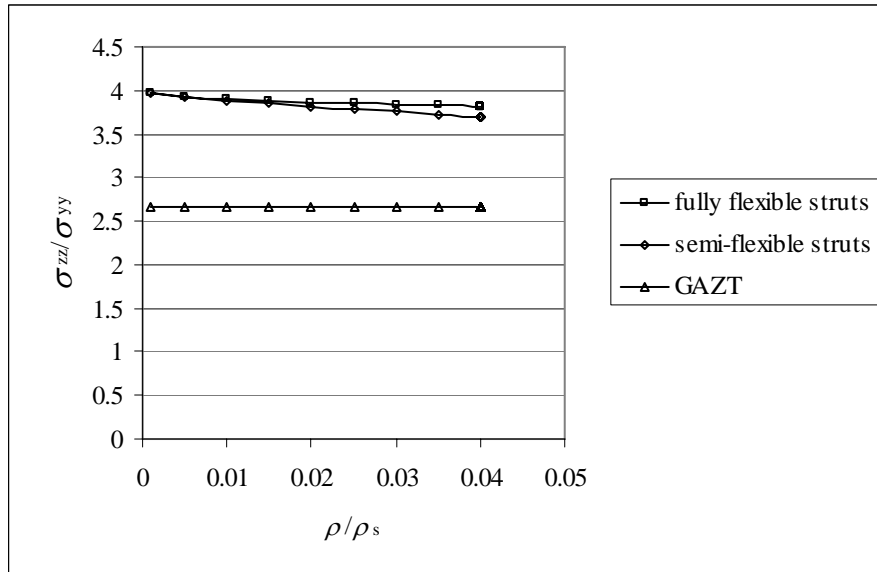Fig. 4.41 Variation of foam tensile strength with relative density based on a rhombic dodecahedron cell model

Figs. 4.40 and 4.41 show respectively the variation of foam tensile strength with relative density based on a rhombic dodecahedron and a tetrakaidecahedron cell model. The anisotropy ratio ($\tan\theta$) is 2, in this instance. The tensile strength exhibits a trend similar to that for foam stiffness (Figs. 4.34 and 4.35), i.e. it increases with foam density and is higher in the foam rise direction. This correlates with the experimental results described in Section 3.2. The tensile strength is lower in the transverse direction because struts are more aligned towards the rise direction, making them easier to bend for loading in the transverse direction and hence, easier to fail. Moreover, more struts need to be broken for loading in the rise direction, resulting in a higher strength in this direction.

116

Fig. 4.42 Variation of foam tensile strength with cell anisotropy based on a rhombic dodecahedron cell model

Fig. 4.43 Variation of foam tensile strength with cell anisotropy based on a tetrakaidecahedron cell model

Figs. 4.42 and 4.43 show respectively the variation of foam stiffness with cell geometric anisotropy ratio for foam with a relative density $\left(\dfrac{\rho}{\rho_s}\right) = 0.0246$, based on a rhombic dodecahedron and a tetrakaidecahedron cell model. As with stiffness, these graphs illustrate that the tensile strengths in the rise and transverse directions diverge, causing an increase in the tensile strength anisotropy ratio with geometric anisotropy, as shown in Figs. 4.44 and 4.45. Another expected similarity with stiffness is that

117

although the strength in the rise direction increases with the geometric anisotropy ratio, the rate of increase diminishes. In the same way, the strength in the transverse direction decreases with geometric anisotropy ratio. The reasons for this are also the orientation of the struts and the reduction in their cross-sectional area with greater cell anisotropy. The increase in cell geometric anisotropy ratio means that the struts are more aligned in the rise direction, thus making them harder to bend and stronger when loaded in that direction; however they bend more easily and are weaker when loaded in the transverse direction. The reduction in strut cross-sectional area when the cell anisotropy increases described by Eqs. (4.4) and (4.85), causes the rate of increase in strength in the rise direction to diminish.

Fig. 4.44 Variation of foam anisotropy in tensile strength with cell anisotropy based on a rhombic dodecahedron cell model
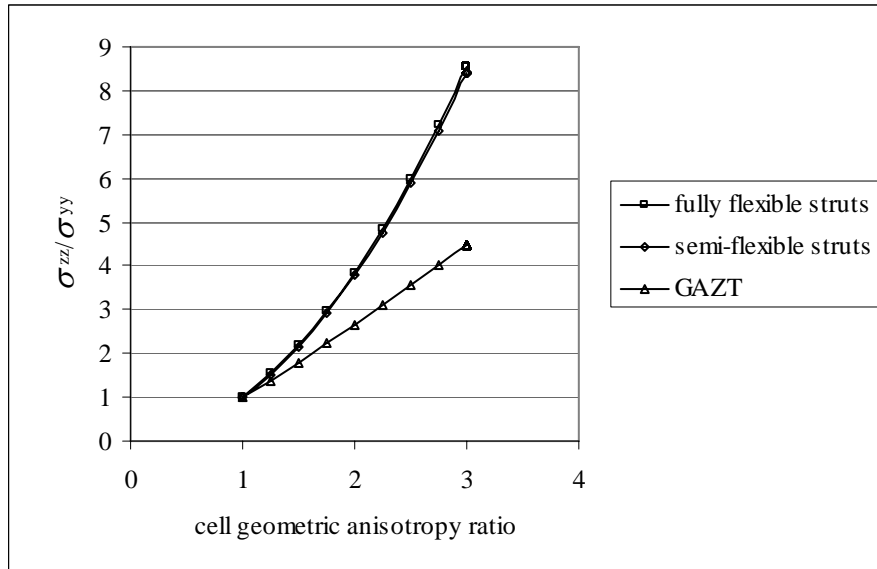
Fig. 4.45 Variation of foam anisotropy in tensile strength with cell anisotropy based on a tetrakaidecahedron cell model

Fig. 4.46 Variation of foam tensile strength anisotropy with relative density based on a rhombic dodecahedron cell model

119

Fig. 4.47 Variation of foam tensile strength anisotropy with relative density based on a tetrakaidecahedron cell model

Figs. 4.44 and 4.45 show respectively the variation of foam tensile strength anisotropy with geometric anisotropy for a foam with a relative density $\left(\dfrac{\rho}{\rho_s}\right) = 0.0246$, based on a rhombic dodecahedron and a tetrakaidecahedron cell model, while Figs. 4.46 and 4.47 show the variation of foam tensile strength anisotropy with relative density for foam with a cell geometric anisotropy ratio of $\tan\theta = 2$ for the same two cell models. As with stiffness, the graphs indicate that the influence of relative density on the anisotropic tensile strength ratio is relatively low and that anisotropy in foam strength is primarily dependent on cell geometric anisotropy. Gibson et al. [21], Triantafillou et al. [8], Gibson and Ashby [2, 20] found similar results, which are denoted by GAZT in the graphs. Figs. 4.44 and 4.45 also show that cell models with and without the correction for rigid strut segments exhibit similar behaviour in terms of their tensile strength anisotropy ratio. However, the values of the anisotropic tensile strength ratio based on the rhombic dodecahedron and tetrakaidecahedron cell models are higher than those based on the cubic cell model by Gibson et al. [21], Triantafillou et al. [8] and Gibson and Ashby [2], because different

assumptions were incorporated in determining the failure in the models – tensile failure of the models in the present study is assumed to occur when any strut fails, while failure in the GAZT model is assumed to occur at the average stress needed to break all loaded struts. The assumption made in the GAZT model mainly influences the strength in the transverse direction, whereby two types of struts with different lengths are deformed (Fig. 4.48). Based on their assumption, the overall tensile strength in the transverse direction is the average stress needed to break both types of struts; this is higher than the stress needed to break the longer struts which are more vulnerable. On the other hand, based on the assumption in the present study, the tensile strength of the foam is governed by the stress to break the most vulnerable struts. This is more reasonable because once the more vulnerable struts break, the overall strength of the foam is decreased.
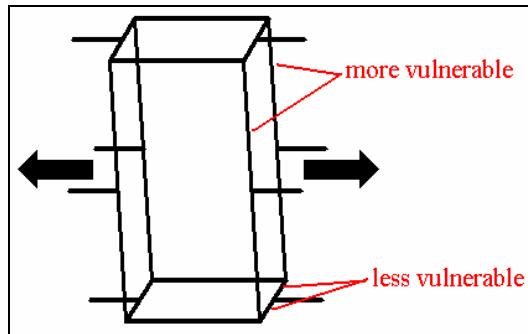
Fig. 4.48 Open celled cubic model (GAZT) loaded in the transverse direction

Poisson's ratio

The Poisson's ratios for foam based on a rhombic dodecahedron cell model can be calculated using the following expressions:

- For fully flexible struts

$$
\upsilon_{zx} = \upsilon_{zy} = -\frac{\varepsilon_{xx}}{\varepsilon_{zz}} = -\frac{\left(\sin^2\theta - \dfrac{\sin\theta \left(\cos^2\theta + 1 \right)^{3/2}}{48\cos^2\theta} \dfrac{1}{C_1} \left(\dfrac{\rho_s}{\rho} \right) \right)}{\left(\sin^2\theta + \dfrac{\left(\cos^2\theta + 1 \right)^{3/2}}{24\sin\theta} \dfrac{1}{C_1} \left(\dfrac{\rho_s}{\rho} \right) \right)}
$$

(4.188)

121

$$\upsilon_{yx} = -\frac{\varepsilon_{xx}}{\varepsilon_{yy}} = -\frac{\left(\cos^2\theta - \dfrac{(\cos^2\theta+1)^{3/2}}{48\sin\theta}\dfrac{1}{C_1}\left(\dfrac{\rho_s}{\rho}\right)\right)}{\left(\cos^2\theta + \dfrac{(\cos^2\theta+1)^{3/2}}{48\sin\theta\cos^2\theta}\dfrac{1}{C_1}\left(\dfrac{\rho_s}{\rho}\right)\right)}$$

(4.189)

$$\upsilon_{yz} = -\frac{\varepsilon_{zz}}{\varepsilon_{yy}} = -\frac{\left(\cos^2\theta - \dfrac{(\cos^2\theta+1)^{3/2}}{48\sin\theta}\dfrac{1}{C_1}\left(\dfrac{\rho_s}{\rho}\right)\right)}{\left(\cos^2\theta + \dfrac{(\cos^2\theta+1)^{3/2}}{48\sin\theta\cos^2\theta}\dfrac{1}{C_1}\left(\dfrac{\rho_s}{\rho}\right)\right)}$$

(4.190)

Note that z denotes the foam rise (cell elongation) direction

- For semi-flexible struts

$$\upsilon_{zx} = \upsilon_{zy} == -\frac{\left(X_1\sin^2\theta - X_1{}^3\dfrac{\sin\theta(\cos^2\theta+1)^{3/2}}{48\cos^2\theta}\dfrac{1}{C_1}\left(\dfrac{\rho_s}{\rho}\right)\right)}{\left(X_1\sin^2\theta + X_1{}^3\dfrac{(\cos^2\theta+1)^{3/2}}{24\sin\theta}\dfrac{1}{C_1}\left(\dfrac{\rho_s}{\rho}\right)\right)}$$

(4.191)

$$\upsilon_{yx} = -\frac{\varepsilon_{xx}}{\varepsilon_{yy}} = -\frac{\left(X_1\cos^2\theta - X_1{}^3\dfrac{(\cos^2\theta+1)^{3/2}}{48\sin\theta}\dfrac{1}{C_1}\left(\dfrac{\rho_s}{\rho}\right)\right)}{\left(X_1\cos^2\theta + X_1{}^3\dfrac{(\cos^2\theta+1)^{3/2}}{48\sin\theta\cos^2\theta}\dfrac{1}{C_1}\left(\dfrac{\rho_s}{\rho}\right)\right)}$$

(4.192)

$$\upsilon_{yz} = -\frac{\varepsilon_{zz}}{\varepsilon_{yy}} = -\frac{\left(X_1\cos^2\theta - X_1{}^3\dfrac{(\cos^2\theta+1)^{3/2}}{48\sin\theta}\dfrac{1}{C_1}\left(\dfrac{\rho_s}{\rho}\right)\right)}{\left(X_1\cos^2\theta + X_1{}^3\dfrac{(\cos^2\theta+1)^{3/2}}{48\sin\theta\cos^2\theta}\dfrac{1}{C_1}\left(\dfrac{\rho_s}{\rho}\right)\right)}$$

(4.193)

where

$$X_1 = \left(1 - \frac{4\sqrt{\sin\theta}\cos\theta}{(\cos^2\theta+1)^{1/4}}C_2 C_3\sqrt{\frac{\rho}{\rho_s}}\right)$$

(4.194)

While the Poisson's ratios for foam based on a tetrakaidecahedron cell are:

- For fully flexible struts

$$v_{zx} = v_{zy} = -\frac{\varepsilon_{xx}}{\varepsilon_{zz}} = -\frac{\left(\dfrac{\sin\theta}{2} - \left(\dfrac{2+\sqrt{2}\cos\theta}{192\cos^2\theta}\right)\dfrac{1}{C_1}\left(\dfrac{\rho_s}{\rho}\right)\right)}{\left(\sin\theta + \left(\dfrac{2+\sqrt{2}\cos\theta}{96\sin^2\theta}\right)\dfrac{1}{C_1}\left(\dfrac{\rho_s}{\rho}\right)\right)}$$

(4.195)

$$v_{yx} = -\frac{\varepsilon_{xx}}{\varepsilon_{yy}} = -\frac{\left(\dfrac{1}{\sqrt{2}} - \left(\dfrac{\sqrt{2}+\cos\theta}{48\sin\theta}\right)\dfrac{1}{C_1}\left(\dfrac{\rho_s}{\rho}\right)\right)}{\left(\dfrac{1}{\sqrt{2}}+\cos\theta\right) + \left(\dfrac{\sin^2\theta}{\cos\theta} + \sqrt{2}\cos^2\theta\right)\left(\dfrac{2+\sqrt{2}\cos\theta}{96\sin\theta\cos^2\theta}\right)\dfrac{1}{C_1}\left(\dfrac{\rho_s}{\rho}\right)}$$

(4.196)

$$v_{yz} = -\frac{\varepsilon_{zz}}{\varepsilon_{yy}} = -\frac{\left(\cos\theta - \left(\dfrac{2+\sqrt{2}\cos\theta}{96\sin\theta\cos\theta}\right)\dfrac{1}{C_1}\left(\dfrac{\rho_s}{\rho}\right)\right)}{\left(\dfrac{1}{\sqrt{2}}+\cos\theta\right) + \left(\dfrac{\sin^2\theta}{\cos\theta} + \sqrt{2}\cos^2\theta\right)\left(\dfrac{2+\sqrt{2}\cos\theta}{96\sin\theta\cos^2\theta}\right)\dfrac{1}{C_1}\left(\dfrac{\rho_s}{\rho}\right)}$$

(4.197)

- For semi-flexible struts

$$v_{zx} = v_{zy} = -\frac{\varepsilon_{xx}}{\varepsilon_{zz}} = -\frac{\left((1-X_2)\dfrac{\sin\theta}{2} - (1-X_2)^3\left(\dfrac{2+\sqrt{2}\cos\theta}{192\cos^2\theta}\right)\dfrac{1}{C_1}\left(\dfrac{\rho_s}{\rho}\right)\right)}{\left((1-X_2)\sin\theta + (1-X_2)^3\left(\dfrac{2+\sqrt{2}\cos\theta}{96\sin^2\theta}\right)\dfrac{1}{C_1}\left(\dfrac{\rho_s}{\rho}\right)\right)}$$

(4.198)

$$v_{yx} = -\frac{\varepsilon_{xx}}{\varepsilon_{yy}} = -\frac{\left(\dfrac{1}{\sqrt{2}}\left(1-\dfrac{X_2}{\sqrt{2}\cos\theta}\right) - \left(1-\dfrac{X_2}{\sqrt{2}\cos\theta}\right)^3\left(\dfrac{\sqrt{2}+\cos\theta}{48\sin\theta}\right)\dfrac{1}{C_1}\left(\dfrac{\rho_s}{\rho}\right)\right)}{\left(\cos\theta(1-X_2)+\dfrac{1}{\sqrt{2}}\left(1-\dfrac{X_2}{\sqrt{2}\cos\theta}\right)\right) + \left(\dfrac{\sin^2\theta}{\cos\theta}(1-X_2)^3 + \sqrt{2}\cos^2\theta\left(1-\dfrac{X_2}{\sqrt{2}\cos\theta}\right)^3\right)\left(\dfrac{2+\sqrt{2}\cos\theta}{96\sin\theta\cos^3\theta}\right)\dfrac{1}{C_1}\left(\dfrac{\rho_s}{\rho}\right)}$$

(4.199)

$$v_{yz} = -\frac{\varepsilon_{zz}}{\varepsilon_{yy}} = -\frac{\left(\cos\theta(1-X_2) - (1-X_2)^3\left(\dfrac{2+\sqrt{2}\cos\theta}{96\sin\theta\cos\theta}\right)\dfrac{1}{C_1}\left(\dfrac{\rho_s}{\rho}\right)\right)}{\left(\cos\theta(1-X_2)+\dfrac{1}{\sqrt{2}}\left(1-\dfrac{X_2}{\sqrt{2}\cos\theta}\right)\right) + \left(\dfrac{\sin^2\theta}{\cos\theta}(1-X_2)^3 + \sqrt{2}\cos^2\theta\left(1-\dfrac{X_2}{\sqrt{2}\cos\theta}\right)^3\right)\left(\dfrac{2+\sqrt{2}\cos\theta}{96\sin\theta\cos^3\theta}\right)\dfrac{1}{C_1}\left(\dfrac{\rho_s}{\rho}\right)}$$

(4.200)

where

$$X_2 = \left(2C_2C_3\sqrt{\frac{8\sin\theta\cos^2\theta}{2+\sqrt{2}\cos\theta}}\sqrt{\frac{\rho}{\rho_s}}\right)$$

(4.201)

As with foam stiffness and strength, the Poisson's ratios based on these models are not influenced by cell size. All the expressions for the Poisson's ratios have two terms in their numerators and denominators; the first term does not contain the relative density $\left(\dfrac{\rho_s}{\rho}\right)$ while the second term does. The first term represents the influence of the axial force in the struts, while the second term captures the effect of bending in the struts. For low density foams, the term $\left(\dfrac{\rho_s}{\rho}\right)$ is large and hence, the second term in the numerator and denominator becomes dominant, showing that bending of the struts is the main mechanism governing the Poisson's ratios. If the axial force (first term) is neglected, the expressions simplify to:

- For the rhombic dodecahedron cell model

$$\upsilon_{zx} = \upsilon_{zy} \approx \frac{1}{2}\tan^2\theta$$

(4.202)

$$\upsilon_{yx} \approx \cos^2\theta$$

(4.203)

$$\upsilon_{yz} \approx \cos^2\theta$$

(4.204)

- For the tetrakaidecahedron cell model

$$\upsilon_{zx} = \upsilon_{zy} \approx \frac{1}{2}\tan^2\theta$$

(4.205)

$$\upsilon_{yx} \approx \frac{1}{\dfrac{\sin^2\theta}{\sqrt{2}\cos^3\theta}+1}$$

(4.206)

$$\upsilon_{yz} \approx \frac{1}{\tan^2\theta+\sqrt{2}\cos\theta}$$

(4.207)

Eqs. (4.202)-(4.207) show that for low density foams, the main factor determining the Poisson's ratio is the geometric anisotropy ratio defined by $\tan\theta$; the density of the foam, the shape of the strut cross section, the length of the rigid edge,

and the properties of the solid material do not have much influence. Gibson and Ashby [2] reported that the Poisson's ratios of a foam depend on the shape of its constituent cells rather than the properties of the solid material, but they did not explain how the Poisson's ratios vary with cell anisotropy. In fact, an analysis based on their open celled cubic model suggests that the Poisson's ratios for foam are zero and do not depend on cell anisotropy.
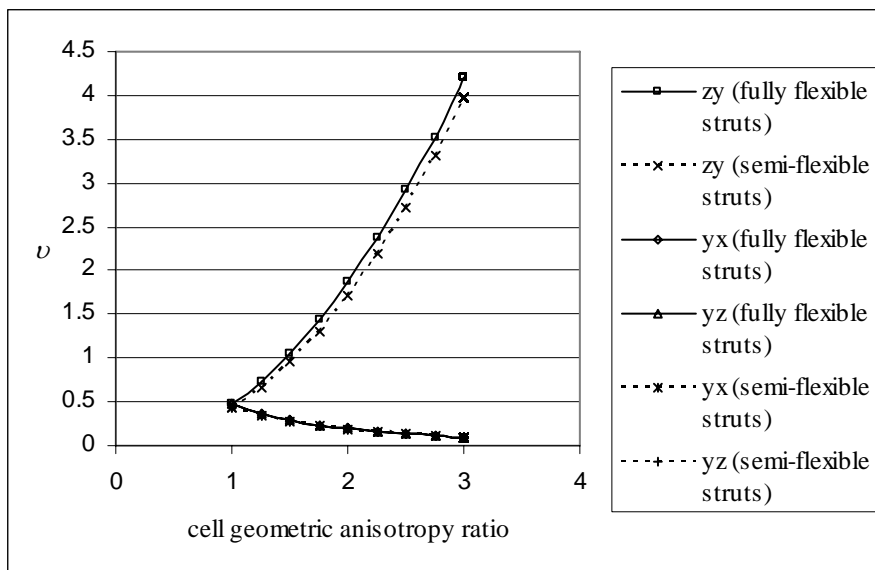
Fig. 4.49 Variation of Poisson's ratios with cell geometric anisotropy ratio for a rhombic dodecahedron cell model
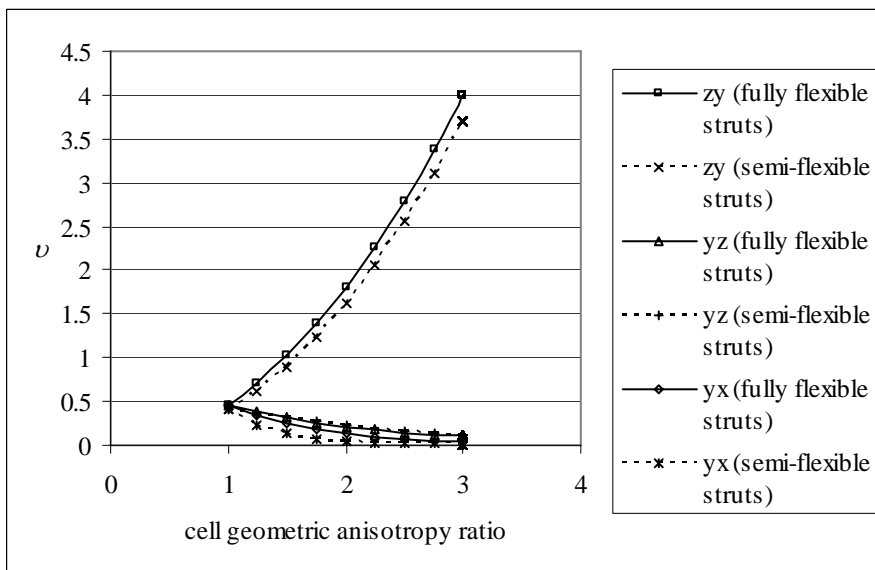
Fig. 4.50 Variation of Poisson's ratios with cell geometric anisotropy ratio for a tetrakaidecahedron cell model

Figs. 4.49 and 4.50 show the variation of the Poisson's ratios with cell geometric anisotropy ratio for a foam with a relative density of $\left(\dfrac{\rho}{\rho_s}\right) = 0.0246$, based respectively on a rhombic dodecahedron and a tetrakaidecahedron cell model. $\upsilon_{zy}\left(=\upsilon_{zx}\right)$ increases while υ_{yx} and υ_{yz} decrease with anisotropy because of the difference in strut orientation length, which can be accounted for as follows:

- The increase in $\upsilon_{zy}\left(=\upsilon_{zx}\right)$ with anisotropy can be explained by Fig. 4.51, which shows the deformation of repeating units in rhombic dodecahedron and tetrakaidecahedron cells, together with the projection of a deformed cell strut on the *yz*-plane when the cell is loaded in the *z*-direction (note that the *z*-direction corresponds to the foam rise/cell elongation direction). Fig. 4.51 shows that the ratio between foam deformation in the *y*-direction to that in the *z*-direction increases with cell anisotropy, resulting in a larger value of $\upsilon_{zy}\left(=\upsilon_{zx}\right)$.

3D cell deformation	Strut deformation in the *yz*-plane
rhombic dodecahedron	
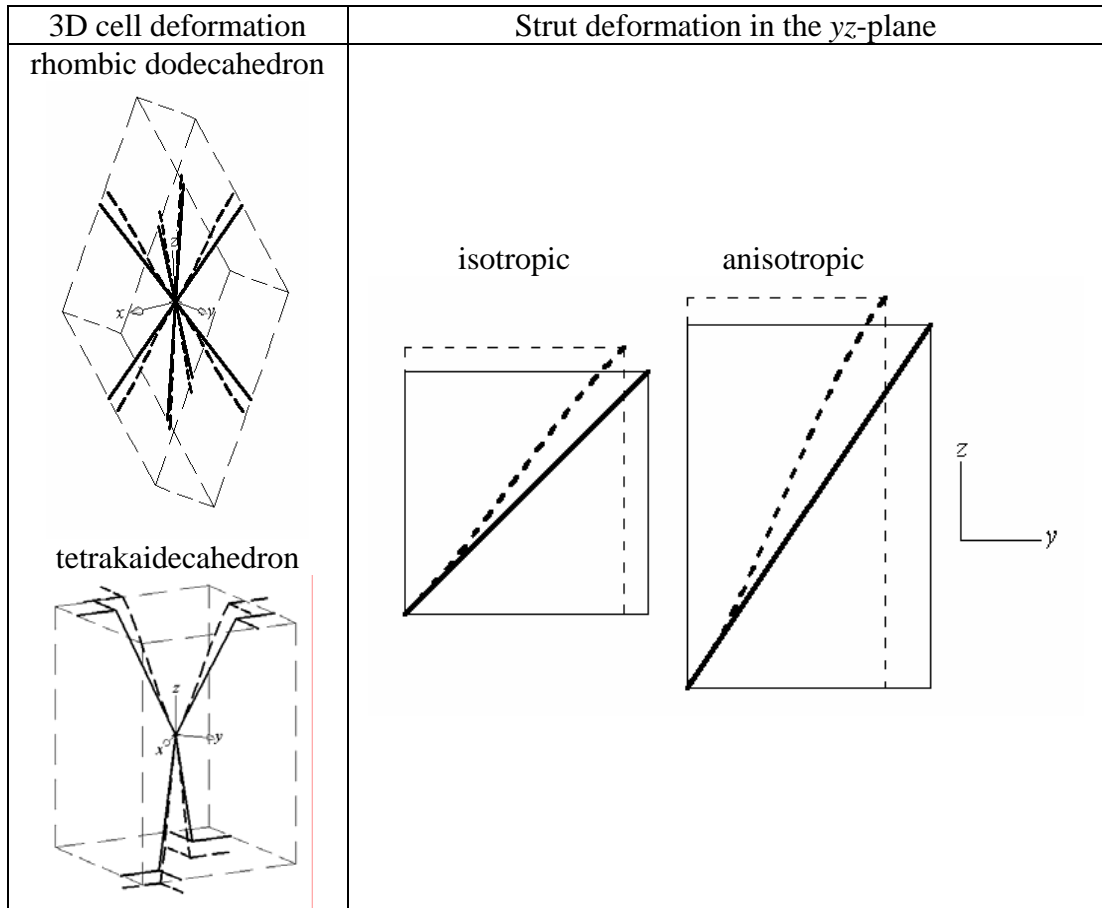
Fig. 4.51 Influence of cell anisotropy on $\upsilon_{zy}\left(=\upsilon_{zx}\right)$

- The influence of cell anisotropy on υ_{yx} for tetrakaidecahedron and rhombic dodecahedron cells can be explained using Figs. 4.52 and 4.53, respectively. Fig. 4.52 shows the deformation of the struts in a repeating unit of a tetrakaidecahedron cell, with respect to the *yz* and *xy*-planes when the cell is loaded in the *y*-direction. Note that the total deformation of the unit can be considered as the sum of four components – deformation of struts OS to OS' and OT to OT' in the *yz*-plane, as well as deformation of struts OU to OU' and OV to OV' in the *xy*-plane. For an elongated rhombic dodecahedron, the repeating cell unit has eight struts which are essentially identical, as shown Fig. 4.53. Hence, the deformation of a cell comprises the sum of the contributions from these struts. Fig. 4.53 shows that the deformation of each strut can be considered a sum of two

components – one in the *yz*-plane (for strut OC, deformation in the *yz*-plane causes point C to move to point C'') and the other in the *xy*-plane (deformation in the *xy*-plane moves point C'' to C'). Figs. 4.52 and 4.53 show that the total deformation of the cell in the *x*-direction does not change with cell anisotropy, while the deformation in the *y*-direction increases with anisotropy because the struts are more aligned towards the *z*-direction and hence are more compliant when loaded in the *y*-direction; this results in a lower value of υ_{yx}.
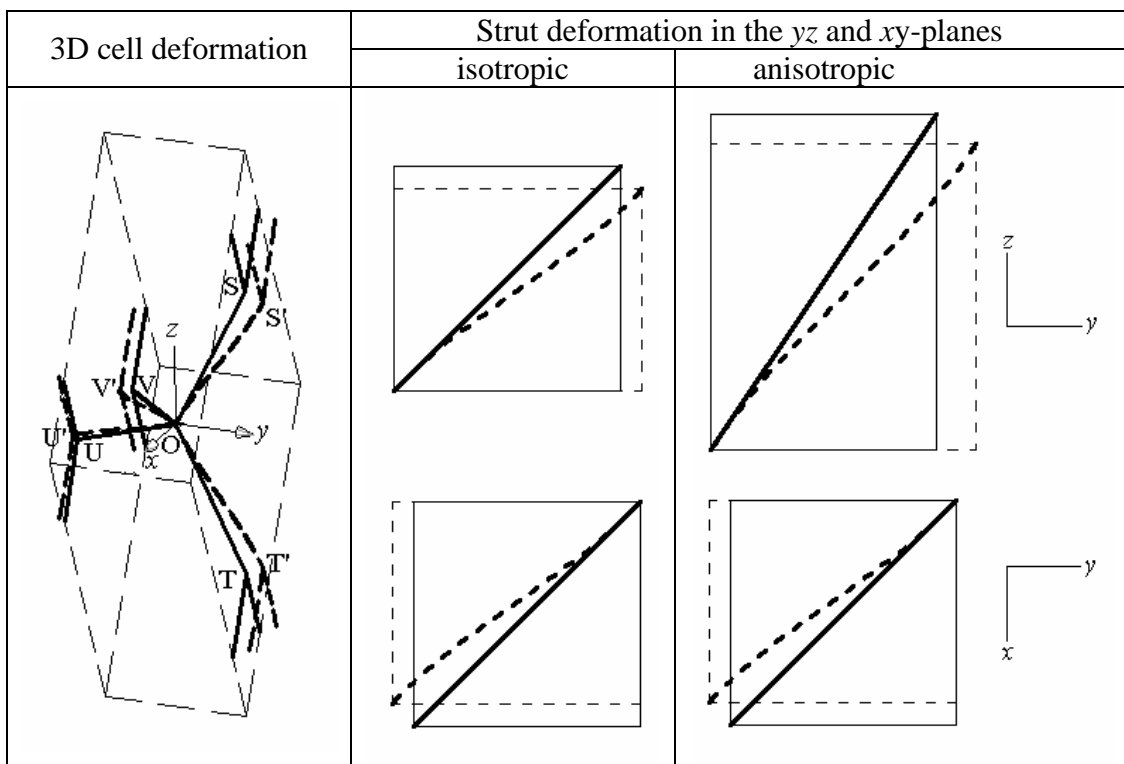
3D cell deformation	Strut deformation in the *yz* and *xy*-planes	
	isotropic	anisotropic

Fig. 4.52 Influence of cell anisotropy on υ_{yx} and υ_{yz} for tetrakaidecahedron cells

3D cell deformation	Strut deformation in the yz and xy-planes	
	isotropic	anisotropic
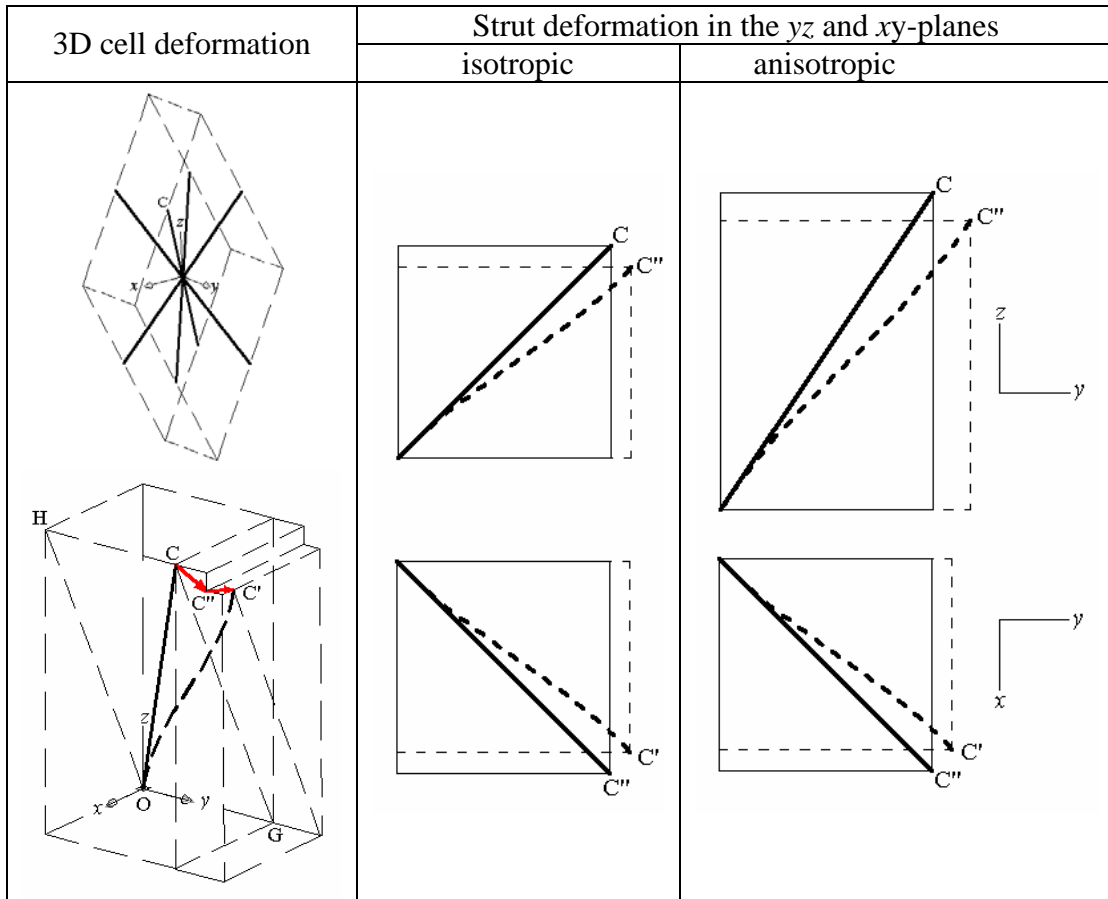
Fig. 4.53 Influence of cell anisotropy on υ_{yx} and υ_{yz} for rhombic dodecahedron cells

- Figs. 4.52 and 4.53 also illustrate the influence of cell anisotropy on υ_{yz}. The figures show that cell deformation in the y-direction increases with cell anisotropy because the struts become more compliant in that direction. Thus, the ratio between the deformation in the z-direction to that in the y-direction decreases with greater cell anisotropy, causing a decrease in υ_{yz}.

The Poisson's ratios for models with semi-flexible struts tend to be lower than those with fully-flexible struts because the axial elongation of struts in the semi-flexible strut model contributes proportionally more to the deformation of cell struts. The axial elongation of struts enlarges the foam cell in all directions, thus, decreasing the Poisson's ratios (Fig. 4.54). On the other hand, bending of the struts increases the cell dimension in one direction while decreasing it in another, causing an increase in

the Poisson's ratios (Fig. 4.54). This is because cell deformation associated with the bending of struts decreases more markedly with a longer rigid strut segment, compared to the reduction in stretching – deformation via bending decreases by the cube of the length of the rigid strut segments, while deformation via stretching decreases linearly – see Eqs. (4.68)-(4.70) and (4.148)-(4.150); the terms that contain the second moment of area I are associated with bending while those with the cross-sectional area A are linked to stretching. The difference between the semi-flexible strut model and the fully flexible strut model increases with density, because the length of the rigid strut segments in the semi-flexible strut model also increases with a higher density, as implied by Eqs. (4.73) and (4.160) (see Figs. 4.55 and 4.56). This trend applies to all the Poisson's ratios except for υ_{yz} for the tetrakaidecahedron cell model, because calculation of υ_{yz} for this model involves two types of struts (Fig. 4.52) and hence the mechanism cannot be simply described by Fig. 4.54. In this case, there are two competing effects that influences υ_{yz}:

- Mechanism that decreases υ_{yz} – As described previously, the greater contribution of strut elongation in the yz-plane to cell deformation because of longer rigid strut segments decreases υ_{yz}.

- Mechanism that increases υ_{yz} – For tetrakaidecahedron cells loaded in the y-direction, deformation in the z-direction arises only from the deformation of struts lying in the yz-plane – e.g. struts OS and OT in Fig. 4.52 – while deformation in the y-direction is due not only to the deformation of struts lying in the yz-plane, but also to that of struts in the xy-plane – e.g. struts OU and OV in Fig. 4.52. Because the struts in the xy-plane for anisotropic tetrakaidecahedron cells are shorter than those in the yz-plane, the compliance of these struts in the xy-plane

decreases more significantly when the rigid strut segments are longer, compared to the compliance of the struts in the *yz*-plane. This causes a greater decrease in cell deformation in the *y*-direction than in the *z*-direction when the length of the rigid strut segments increases, thus, resulting in an increase in υ_{yz}. This effect is more significant when the struts in the *yz*-plane are longer than the ones in the *xy*-plane, i.e. when the cell has a higher geometric anisotropy

Since the second effect is more prominent when the cell geometric anisotropy is higher, υ_{yz} for anisotropic tetrakaidecahedron cells with semi-flexible struts is larger than that for fully flexible struts when the cell geometric anisotropy ratio of the cells exceeds a threshold value (e.g. 1.33 in Fig. 4.50).
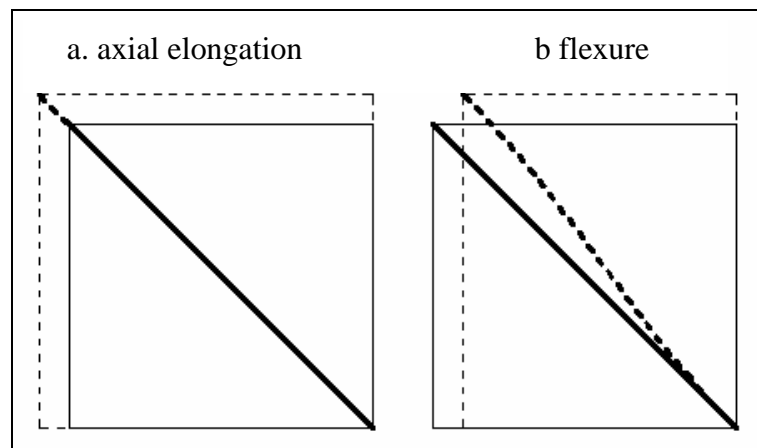
Fig. 4.54 Influence of axial elongation and flexure of struts on Poisson's ratio
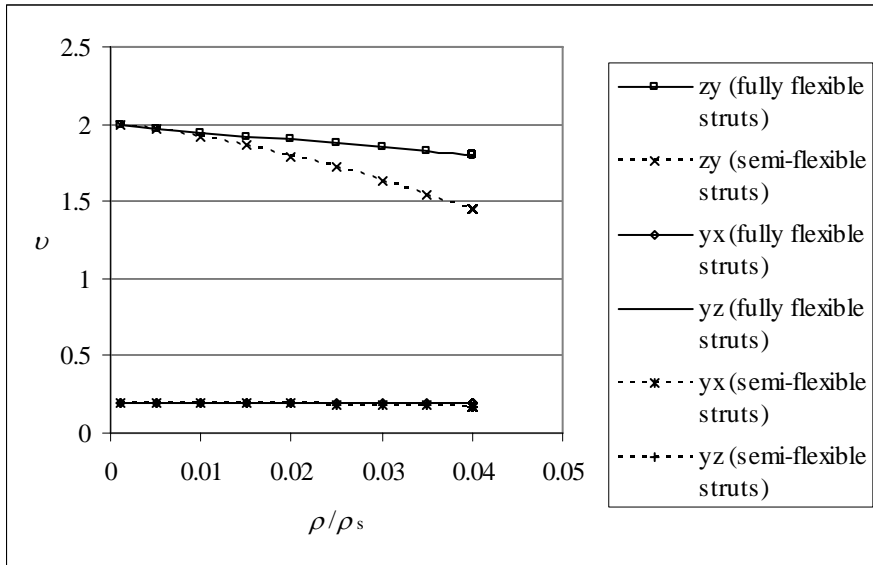
Fig. 4.55 Variation of Poisson's ratios with relative density for a rhombic dodecahedron cell model ($\tan\theta = 2$)
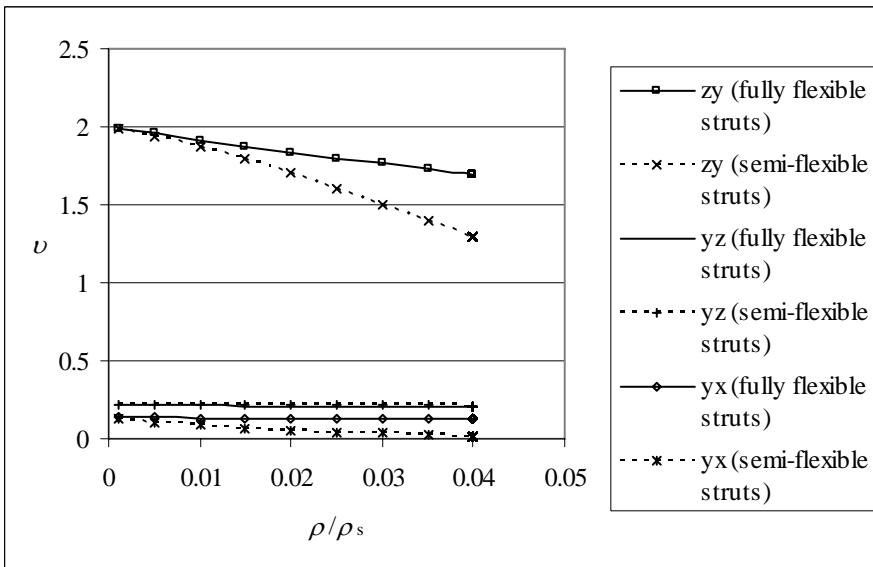
Fig. 4.56 Variation of Poisson's ratios with relative density for a tetrakaidecahedron cell model ($\tan\theta = 2$)

4.4.2 Comparison between model and actual foam

Figs. 4.57 and 4.58 show respectively comparisons between the stiffness of actual foam and that predicted by the rhombic dodecahedron and tetrakaidecahedron cell model. Figs. 4.59 and 4.60 show the normalized version of Figs. 4.57 and 4.58, whereby the predicted stiffnesses are divided by the stiffness of the actual foam. Experimental scatter in the stiffness of the actual foam is presented via the I-shaped bars. The cell models without the correction for rigid strut segments (fully flexible

strut model) predict lower stiffnesses than the actual foam. The tetrakaidecahedron cell model with the rigid strut segments (semi-flexible strut model) shows fairly good agreement with the actual foams, especially for foam B. This is because the shape of the actual cells is more similar to a tetrakaidecahedron than to a rhombic dodecahedron. This also confirms the significance of the rigid strut segments observed in the deformation of actual foams (see Chapter 3). The difference in stiffness predicted by the tetrakaidecahedron cell model with that of actual foam can be attributed to variations in the stiffness of the solid polyurethane material constituting the struts and membranes in actual foam. Moreover, Gibson and Ashby [2] asserted that the stiffness of the solid material in polymeric foams are rarely known with precision because it depends on "the degree of polymer-chain alignment, on chemical change brought about by the foaming agent and on gradual ageing and oxidation of the polymer".
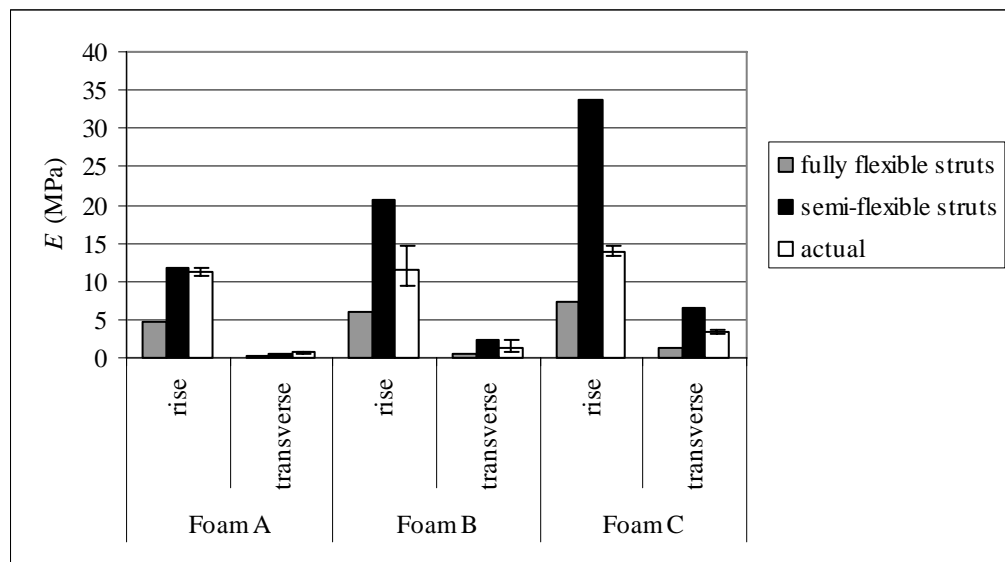
Fig. 4.57 Stiffness of actual foam and that based on a rhombic dodecahedron cell model
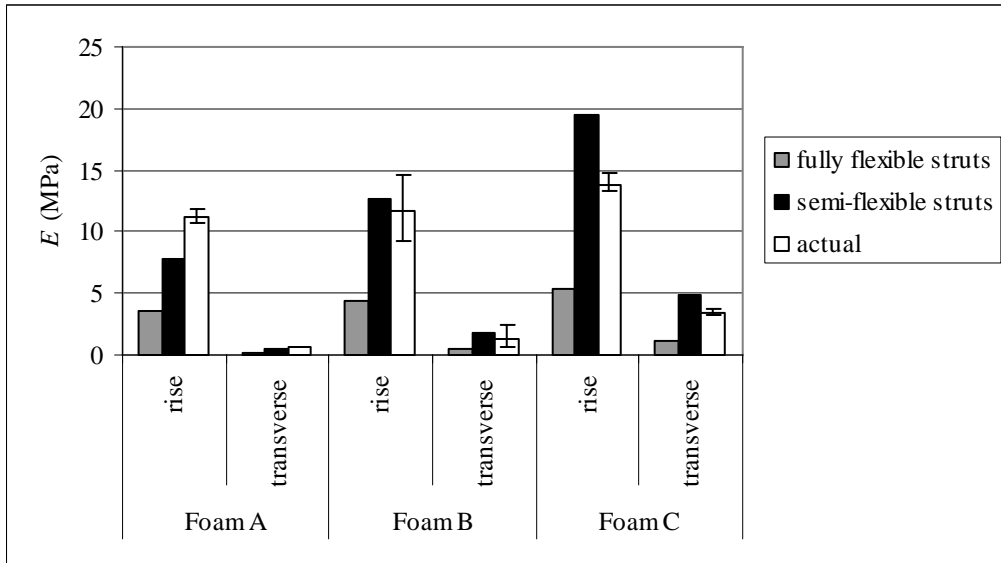
Fig. 4.58 Stiffness of actual foam and that based on a tetrakaidecahedron cell model
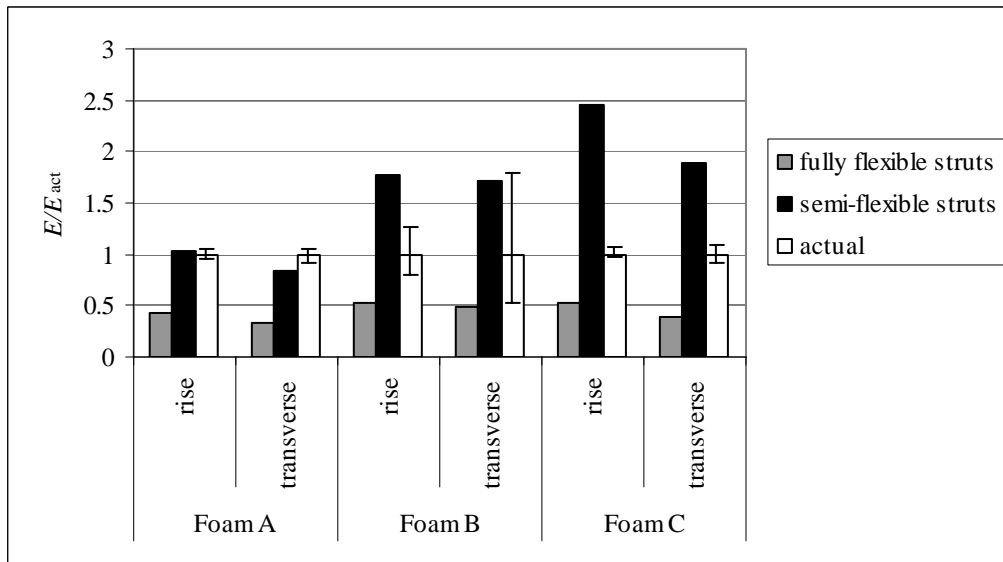
Fig. 4.59 Normalized stiffness of actual foam and that based on a rhombic dodecahedron cell model

134
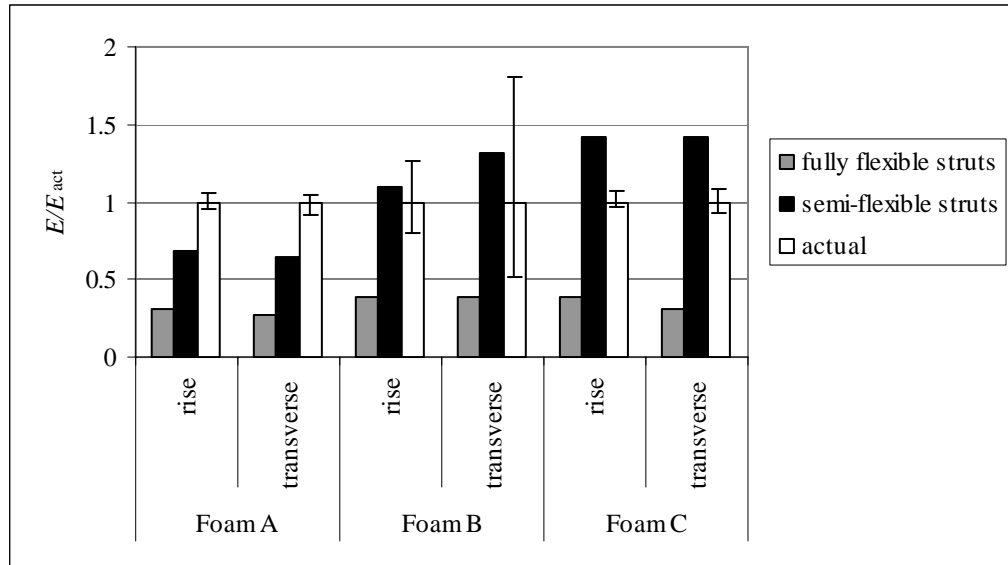
Fig. 4.60 Normalized stiffness of actual foam and that based on a tetrakaidecahedron cell model

The strength of actual foam and that predicted by the analytical models cannot be compared directly because the model assumes that the solid material has linear elastic mechanical and brittle fracture properties while actual foam exhibits some nonlinearity before fracture (see Section 3.7). The Poisson's ratios determined from the cell models are not compared because such data is difficult to obtain for actual foam.

4.4.3   Summary

This chapter described the development of an analytical cell model to define the mechanical behaviour of rigid polyurethane foam under tensile loading. Two open cell models were established and investigated – a rhombic dodecahedron cell and a tetrakaidecahedron cell. Both cell models can be arranged in three-dimensions to fill space and form a large structure. An open cell structure is assumed because even though actual rigid polyurethane foam has primarily closed cells, the membranes defining the walls are very thin compared to the size of the struts and vertices (see Section 3.5). Hence, the foam behaves as if it is open celled; such a perspective and approach have also been accepted and adopted by others [2, 30]. The mechanical

135

properties of the proposed models – tensile stiffness, Poisson's ratios and tensile strength – were derived analytically, resulting in expressions that relate the cell geometric anisotropy ratio, foam relative density, mechanical properties of the solid strut material and mechanical properties of foam to one another. The existence of rigid strut segments (see Chapter 3) was incorporated into the model.

A comparison of the geometry of the cell models with cells in actual foam shows that the tetrakaidecahedron cell has greater similarity than the rhombic dodecahedron cell. This is probably because a tetrakaidecahedron is a more stable geometry, based on satisfying minimum surface energy conditions as well as energy conditions stated in Plateau's law [1, 22, 40]. A study of the expressions describing the mechanical properties of foam shows that the bending of struts is the primary mechanism governing deformation and failure in low density foams. This is in line with observations on the deformation of actual foam discussed in Chapter 3, and with the findings of others [2, 8, 20, 21, 26, 28, 31, 40, 41]. The expressions for Poisson's ratios suggest that for low density foams, Poisson's ratio depends primarily on cell geometric anisotropy, indicating that the Poisson's effect arises from a structural geometry response rather than from material behaviour. As expected, the stiffness and strength of foam increase with relative density, because there is more solid material to sustain the load. Also, anisotropy in stiffness and strength increases with cell geometric anisotropy because of the change in the orientation of cell struts as the cells becomes more elongated in the rise direction.

For isotropic foam, a comparison between the stiffness predicted by both cell models without correction for rigid strut segments (fully flexible struts) with a semi-empirical model based on a open cubic cell proposed by Gibson et al. [21], Triantafillou et al. [8], Gibson and Ashby [2, 20] shows a strong agreement. This

136

demonstrates that the expressions developed in this study are able to provide an explanation for the numerical constants in the earlier semi-empirical models. The stiffness of foam predicted by the tetrakaidecahedron cell model with correction for rigid strut segments exhibits good agreement with actual foam. This is probably because the shapes of actual foam cells are similar to a tetrakaidecahedron cell. Moreover, the results show that inclusion of the correction for rigid strut segment is important in arriving at good correlation with experimental results. The foam strengths predicted by the two models developed in this study were not compared with that of actual foam because the assumption of linear elastic-brittle failure material for the cell struts is not totally applicable, as the polyurethane in actual foam exhibits some nonlinearity in its stress-strain response.

The cell models in this investigation are able to describe the mechanical behaviour of actual foam, especially in terms of the stiffness; moreover the idealized cell geometries are reasonably realistic because they are similar to those of cells in actual foam and the cells can be assembled together in three dimensions. However, these analytical models have only been utilized to describe the mechanical properties for two directions, i.e. the foam rise and transverse directions. The analytical equations defining the mechanical properties of these models derived are not amenable to describing the mechanical response of foam when loaded in other directions or loaded multi-axially as these situations are too complex. The tensile strength criterion established is also specific to linear elastic-brittle failure material and not fully applicable to the rigid polyurethane foam tested. Nevertheless, the analysis is still useful in demonstrating how the mechanical properties of foam relate to parameters such as foam density, cell anisotropy and the strength and stiffness of the strut material. Moreover, the expressions can be used to provide an estimate of the

137

mechanical properties of foam. These geometric cell models can be utilized to examine loading in directions other than the foam rise and transverse directions, to study multi-axial loading and cells made of non-linear material. These can be effected via finite element modelling and this is discussed in the following chapter.

Chapter 5   Finite Element Model

To augment the theoretical analysis described in Chapter 4, finite element modelling of a cellular structure based on tetrakaidecahedral cells was undertaken. The software ABAQUS-Explicit was used to facilitate a study of the effect of loading direction, the incorporation of non-linear mechanical behaviour of the solid cell material, as well as random variations in cell parameters. The FEM results are compared to those from experiments on actual foam, presented in Chapter 3.

5.1   Modelling of cells

Cellular structures comprising elongated tetrakaidecahedron open cells were modelled using linear Timoshenko beam elements (type B31) available in the explicit version of ABAQUS. This version of the code for transient dynamic analysis was employed although the simulation was for quasi-static loading, because ABAQUS-Standard, which is normally used to simulate quasi-static situations, does not accommodate material failure. The FE model consists of elongated tetrakaidecahedron cells packed together in an elongated BCC lattice (Fig. 5.1) and subjected to tension in five directions – rise (0°), transverse (90°), as well as 30°, 45° and 60° to the foam rise direction – for comparison with the experimental results in Section 3.2. These cell models were formulated to correspond to the three foam densities of the specimens described in Section 3.2. Values for the parameters in these models are presented in Table 5.1. Note that the strut cross-sectional dimension (R) based on this model is not exactly the same as that of the actual foam discussed in Section 3.5 because the shape of the cells in the actual foam are not exactly identical to tetrakaidecahedra and the cell sizes vary.
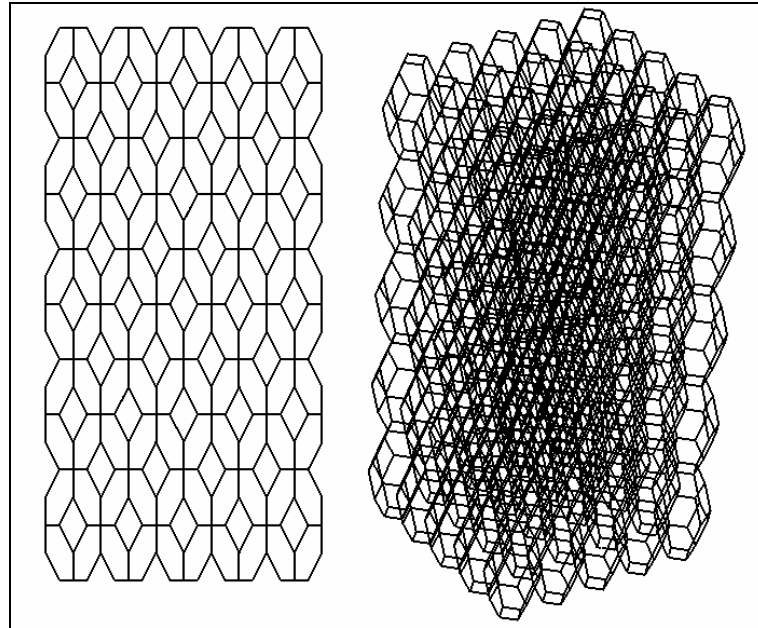
Fig. 5.1 Elongated tetrakaidecahedron cells packed together in an elongated BCC lattice

Table 5.1 Values of parameters in finite element cell models

	Foam A	Foam B	Foam C
Relative density $\left(\dfrac{\rho}{\rho_s}\right)$	0.0198	0.0246	0.0294
Cell size	1.0×0.4 mm	1.0×0.5 mm	0.9×0.53 mm
Geometric cell anisotropy ratio $(\tan\theta)$	2.5	2	1.7
Strut cross sectional area (A)	0.582×10^{-3} mm^2	1.045×10^{-3} mm^2	1.310×10^{-3} mm^2
2nd area moment of inertia of strut cross-section (I)	0.454×10^{-7} mm^4	1.460×10^{-7} mm^4	2.296×10^{-7} mm^4
Strut thickness (R) (see Fig. 3.14)	35 μm	46 μm	52 μm

The cross-section of the beam elements defining the flexible segment of the struts is a twelve pointed star comprising two components, as shown in Fig. 5.3. It has a total area A, a second moment of area I and the average distance $\overline{R}$ from its centroid to the point farthest away in its cross-section (see Section 4.3) which are equal to that for the Plateau border cross-section calculated (Table 5.1). A Plateau border was not employed as the cross-section because it only has three axes of symmetry; the beam elements would have been sensitive to orientation if they were defined using this

140

shape, especially with regard to fracture, thus making it necessary to define the orientation of each element. On the other hand, the twelve pointed star has 12 axes of symmetry and hence is much less sensitive to orientation. Consequently, the cross-sectional orientation of every strut does not have to be defined. Simpler cross-sections such as a circle and an annulus cannot yield the same cross-sectional area A and second moment of area I simultaneously as the Plateau border. The rigid segments at the strut ends have an annular circular cross-section with a much higher area and second moment of area than the flexible segments; this yields a higher rigidity. Five B31 beam elements were used to model the flexible segment of each strut. A larger number of elements was avoided to limit the cost of the simulation in terms of running time and computing resources. On the other hand, only one element was used for each rigid strut segment because its deformation is considered insignificant. Fig. 5.2 shows the elements in a tetrakaidecahedral cell model
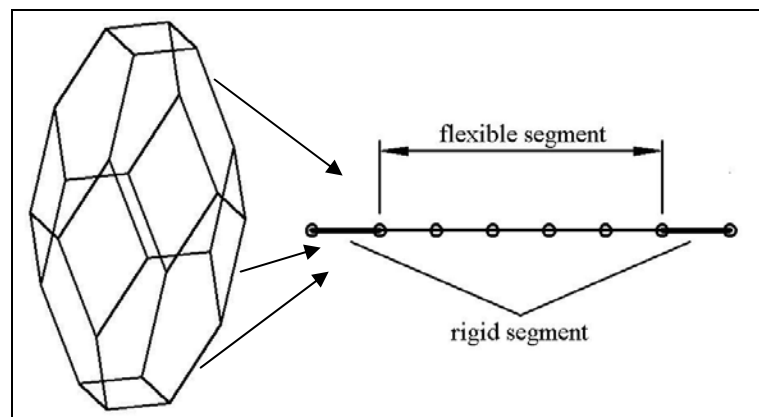
Fig. 5.2 Elements a tetrakaidecahedral cell model
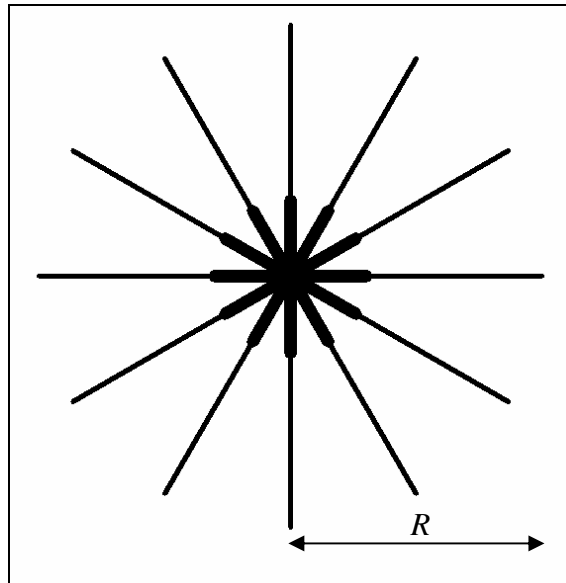
Fig. 5.3 Star shape for beam cross section

An isotropic material with a bilinear stress-strain relationship was selected for the struts. Fracture was defined using a shear failure option in ABAQUS-Explicit, whereby fracture is assumed to occur when the plastic strain at an element integration point attains a critical value (note that a fracture criterion based on stress and strain yields identical results because the stress state is uniaxial). The values of the parameters in the material model were derived from tests on solid polyurethane specimens (Section 3.7), i.e.:

- Stiffness $E = 3\,\text{GPa}$

- Density $\rho = 1200\,\text{kg}/\text{m}^3$

- Yield strength $\sigma_{ys} = 51\,\text{MPa}$

- Tensile fracture strength $\sigma_{\max} = 64\,\text{MPa}$

- Plastic strain at fracture $\varepsilon_{pl\,\max} = 0.02$

Loading of the cell assembly was prescribed through boundary conditions – defining a simple support at one side and imposing a constant velocity condition at the other (Fig. 5.5). Periodic boundary conditions were imposed on the models for loading in the rise and transverse directions by prescribing rotational constraints at the

boundaries. This makes the analysis essentially the same as modelling an assembly of infinite number of cells. Strain rates were limited to a maximum of 60/s to minimize non-uniformity of stress due to stress wave propagation within the structure. This facilitates approximation of quasi-static loading conditions (strain rates which are too low were also avoided to limit computational time). A localised area of weakness was introduced into the model to initiate failure. This was done by lowering the tensile strength of struts in a cell at the edge of the model (Fig. 5.4).
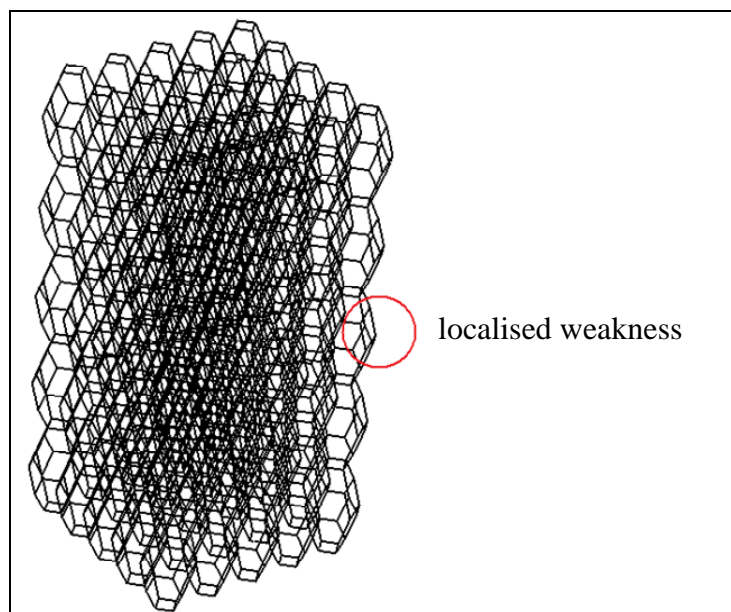
Fig. 5.4 Localised area of weakness in a finite element model
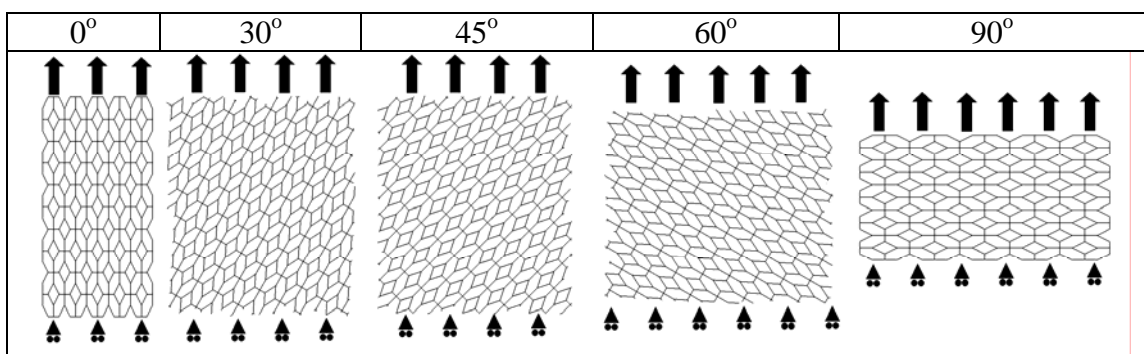
Fig. 5.5 Loading condition in the finite element model

5.2 Results and discussion

5.2.1 Response to tensile loading
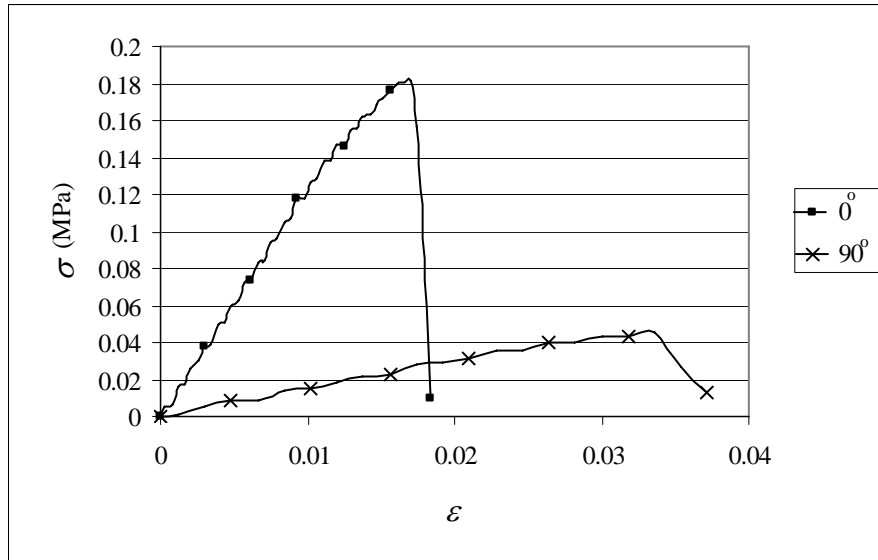
Fig. 5.6 Stress-strain curve for foam B ($\rho = 29.5 \, \text{kg}/\text{m}^3$; geometric anisotropy ratio = 2)

Fig. 5.6 shows the stress-strain curve for the model corresponding to foam B ($\rho = 29.5 \, \text{kg}/\text{m}^3$) loaded in the rise (0°) and transverse (90°) directions. The graph shows that as with the actual foam (Section 3.2), the stress-strain curves exhibit a linear response followed by a shorter phase of non-linearity before fracture. The figure also shows that the stiffness (i.e. gradient of the initial linear portion) and the tensile strength (maximum stress before fracture) are higher in the rise direction.

Unloaded, 2D view	Unloaded, isometric view	Failure initiation, 2D view	Failure initiation, isometric view
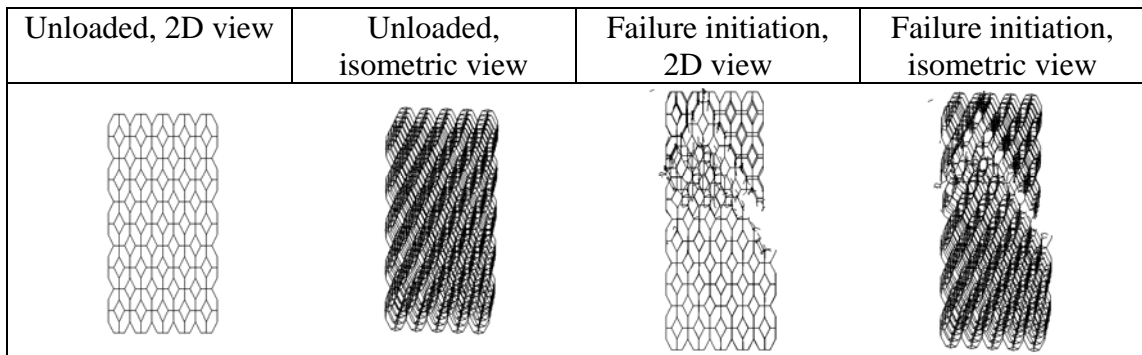
Fig. 5.7 Crack pattern for tension in the cell elongation/rise direction

Unloaded, 2D view	Unloaded, isometric view	Failure initiation, 2D view	Failure initiation, isometric view
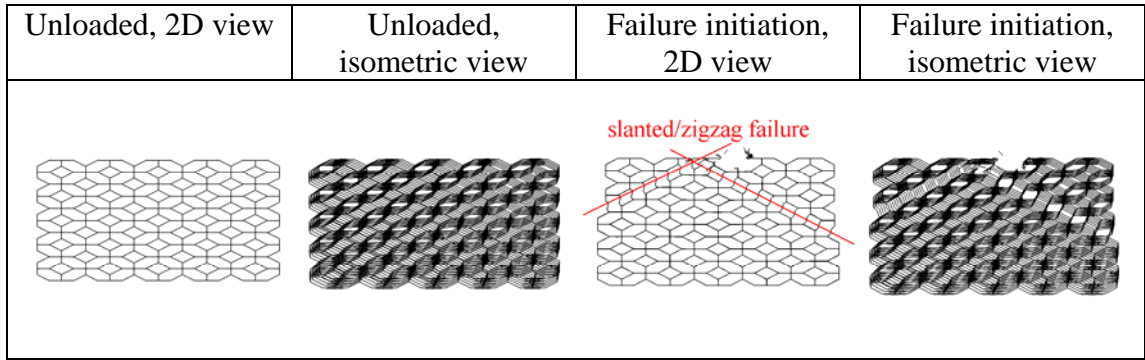
Fig. 5.8 Crack pattern for tension in the transverse direction

Figs. 5.7 and 5.8 show respectively, the response of the model corresponding to foam B for loading in the rise/elongation and transverse directions. The figures illustrate that the crack for loading in the transverse direction follows a slanted/zigzag pattern. This contrasts with the crack propagation in actual foam, whereby a crack propagates perpendicular to the direction of loading (see Figs. 3.17, 3.19 and 3.21 in Section 3.6.1). This phenomenon and its implications, particularly with regard to the fracture characteristics of the model, will be discussed in the next section.

5.2.2 Influence of cell wall membrane on crack propagation

Initial simulation results based on the proposed model (Fig. 5.6) showed an overestimation of the ratio of the tensile strength in the rise direction to that in the transverse direction for foam B ($\rho = 29.5 \, \text{kg}/\text{m}^3$; geometric anisotropy ratio = 2); the predicted anisotropy ratio was 4.05, while that of the actual foam was 1.95. It is also noted that the plastic collapse model for foam by Gibson et al. [21], Triantafillou et al. [8], and Gibson and Ashby [2, 20], which is essentially similar to the fracture model in this study, also overestimates this anisotropy ratio with a value of 2.6. An examination of how fracture develops in the models indicates that the behaviour differs somewhat from that in actual foam. In actual foam, the crack propagates sequentially through cell wall membranes and struts, resulting in crack propagation that is perpendicular to the loading direction (see Figs. 3.17, 3.19 and 3.21 in Section

145

3.6.1), while fracture predicted by the model occurs by failure of the most highly loaded struts without any accompanying crack propagation through membranes, resulting in a zigzag or slanted crack pattern, particularly for loading in the transverse direction (Figs. 5.7 and 5.8). In actuality, a crack which is initiated in a membrane facilitates continued crack propagation perpendicular to the direction of loading, thus driving the crack tip to the centre of the struts the membrane is connected to. On the other hand, cracking in the FEM models follows any direction that leads to vulnerable struts, i.e. struts that attain the highest stress. For loading in the transverse direction, two types of struts are loaded – struts lying in horizontal planes (planes that are parallel to the *xy*-plane) and struts lying in vertical planes (planes that are parallel to the *yz*-plane). These two types of struts have different lengths and orientations and thus they attain different stress levels when the foam is loaded in the transverse direction. According to the analysis in Section 4.2.3, the struts lying in the vertical planes attain a higher maximum stress than those lying in the horizontal planes and thus the struts in the vertical planes fail earlier – i.e. they are more vulnerable (see Fig. 5.9). This results in crack propagation that follows a zigzag or slanted pattern, cutting the struts lying in the vertical planes (Fig. 5.8). On the other hand, for loading in the rise direction, the struts that deform are of the same type and hence have the same vulnerability (Fig. 5.10).

FEM simulations were carried out using ABAQUS-Explicit to examine the influence of the presence of membranes on the direction of crack propagation. A single tetrakaidecahedron cell with beam elements (type B31) defining its edges and membrane elements (type S4R) for its walls was modelled to investigate loading in the rise and transverse directions. The size of the cell was 1 mm x 0.5 mm. Each strut was defined using 20 beam elements and the total number of membrane elements was

8800. The cross-section of the beam elements is assumed to be circular with a radius of 0.1 mm and the cell wall membranes were 0.001 mm thick. A linear elastic-brittle failure material model was assumed for the struts and cell wall membranes, and the failure of the elements was defined using a stress failure criterion whereby an element is assumed to fail whenever the hydrostatic stress value at its integration point attains a critical value. The following parameter values were used to define the material in the struts and walls.

- Stiffness $E = 1000 \, \text{GPa}$

- Density $\rho = 1000 \, \text{kg}/\text{m}^3$

- Tensile fracture strength $\sigma_{\text{max}} = 0.1 \, \text{MPa}$

Loading of the cell assembly was prescribed through boundary conditions – by defining a simple support at one side and imposing a constant velocity condition at the other.

Figs. 5.11 and 5.12 illustrate respectively, simulation results for loading in the rise and transverse directions. They show that crack propagation through the membranes tends to constrain the crack to cut struts that are perpendicular to loading direction, although these struts are less vulnerable according to the analysis in Sections 4.2.2 and 4.2.3. Fig. 5.12 shows that for loading in the transverse direction, cracks initiate from the slanted struts but continue to cut the struts lying in the horizontal planes (i.e. planes parallel to the *xy*-plane) resulting in a crack perpendicular to the loading direction. (Note that simulations for loading in the transverse direction were performed in two steps – the first step resulted in initiating failure of the membrane parallel to the rise direction, this was then followed by the second step whereby this membrane was deleted and failure in a strut was triggered by deleting an element at its centre, where the tip of the crack from the membrane met

147

the strut.). This indicates that the influence of crack propagation in the membrane has to be incorporated in the FEM model for foam. In this study, this is achieved by assuming that the strength of the struts that are broken during crack propagation is reduced by the crack that propagates through the membranes. Thus, the following assumptions are made.

- Loading in the transverse direction – the crack that propagates through the membranes tends to cut the struts lying in horizontal planes (Fig. 5.13); thus the strength of these struts is reduced so that they fail before the inclined struts do. From the analytical solution discussed in Section 4.2, the strut strength should be reduced by at least about $\left(\dfrac{1}{\tan \theta} \right)$ (see Eq. (4.142)) – i.e. the strength should be made smaller than the original strength divided by the cell geometric anisotropy ratio, to match the vulnerability of the inclined struts. Consequently, the tensile strength and yield strength of the material in struts lying in the horizontal planes are reduced by $\left(\dfrac{1}{\tan \theta} \right)$. (Note that failure of a strut occurs whenever an integration point in any element attains a critical plastic strain value corresponding to the tensile strength).

- Loading in the rise (cell elongation) direction – results from the single cell FEM analysis shows that the crack initiated in a membrane is likely to propagate to and cut the inclined struts. Thus, to be consistent with the modification for loading in the transverse direction, the strength of these struts is reduced by lowering both the tensile and yield strength of the material by $\left(\dfrac{1}{\tan \theta} \right)$.

- Loading 30°, 45°, and 60° to the rise direction – the crack is assumed to cut the inclined struts whenever the crack propagation perpendicular to the loading

148

direction, does not require it to cut struts which are parallel to the *xy*-plane (see Fig. 5.14). This results in cracks propagating through the inclined struts for all the loading directions considered in this study except for loading in the transverse direction. Hence, as with loading in the rise direction, the strength of the inclined struts for loading 30°, 45°, and 60° to the rise direction is also reduced by $\left(\dfrac{1}{\tan\theta}\right)$. FEM simulations were also performed to examine this assumption. A single tetrakaidecahedron cell, similar to the one used to examine loading in the rise and transverse directions, was stretched at 30°, 45°, 60°, and 82.5^o to the rise direction. Loading was imposed through a constant velocity boundary condition at the cell edges, so that the deformation resembles uniform extension in the loading direction. Figs. 5.15-5.18 show the results of the simulations and confirms the assumption made. These figures indicate that, for cells corresponding to foam B (cell anisotropy ratio = 2) loaded 30°, 45°, and 60° to the rise direction, the crack propagates through the inclined struts. On the other hand, for loading 82.5^o to the rise direction, the crack first intersects the inclined struts and then propagates through the membrane to meet the struts in the horizontal plane.
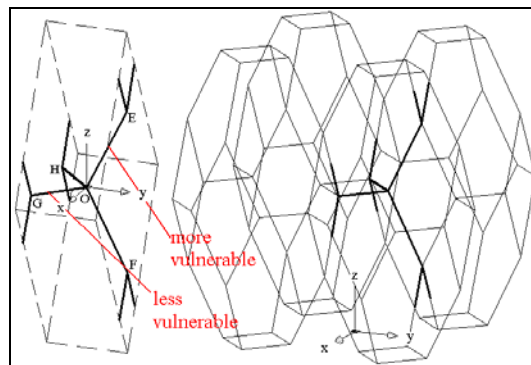
Fig. 5.9 Cell model loaded in the transverse (*y*) direction
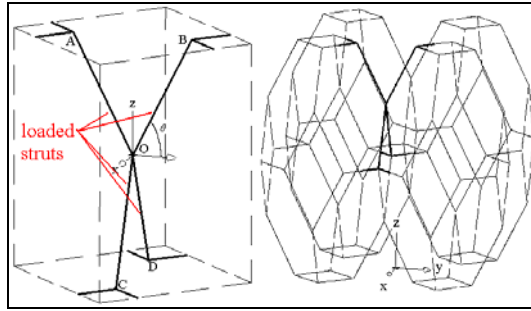
Fig. 5.10 Cell model loaded in the rise (*z*) direction
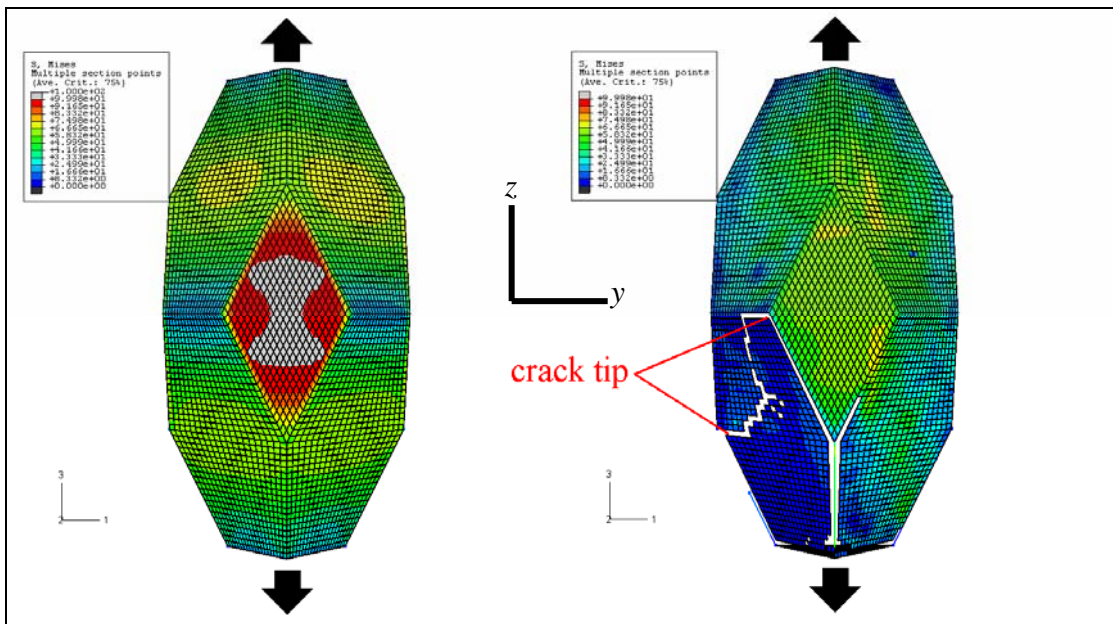
Fig. 5.11 Single cell loaded in the cell elongation (foam rise) direction
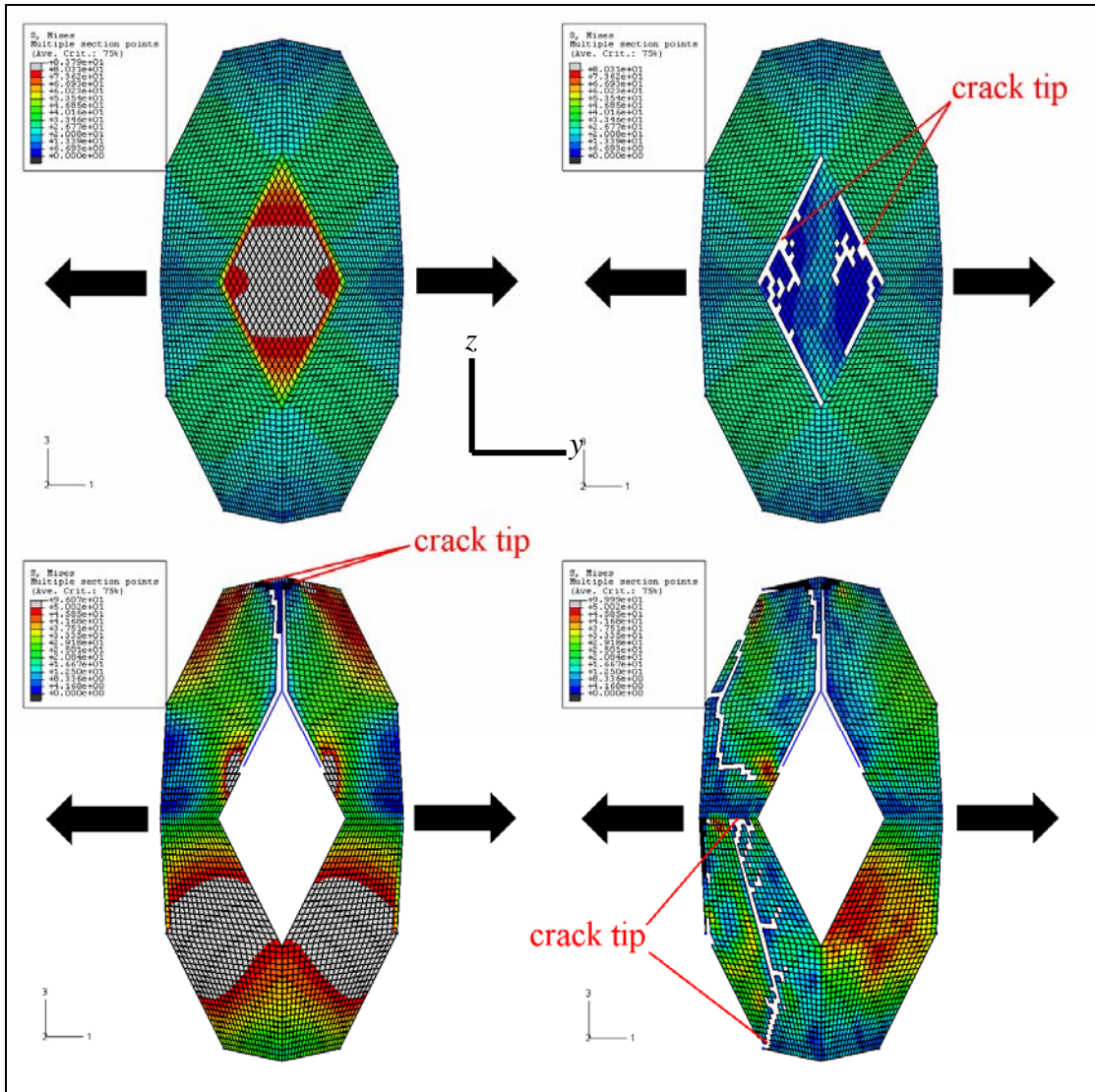
Fig. 5.12 Single cell loaded in the transverse direction
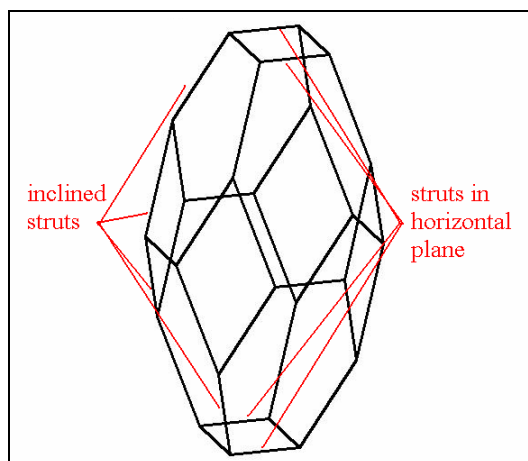
Fig. 5.13 Struts in a tetrakaidecahedron cell

151
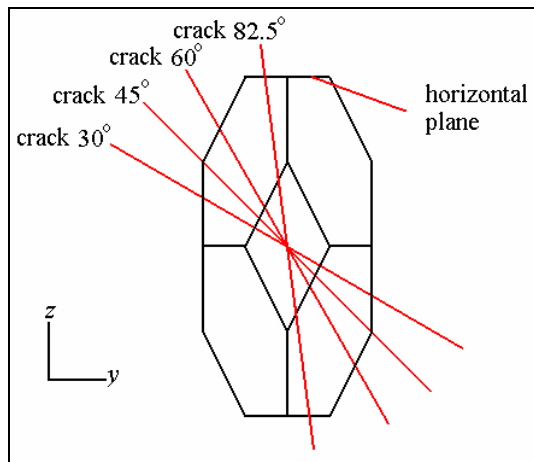
Fig. 5.14 Crack propagation for loading in the 30°, 45°, 60°, and 82.5^o directions
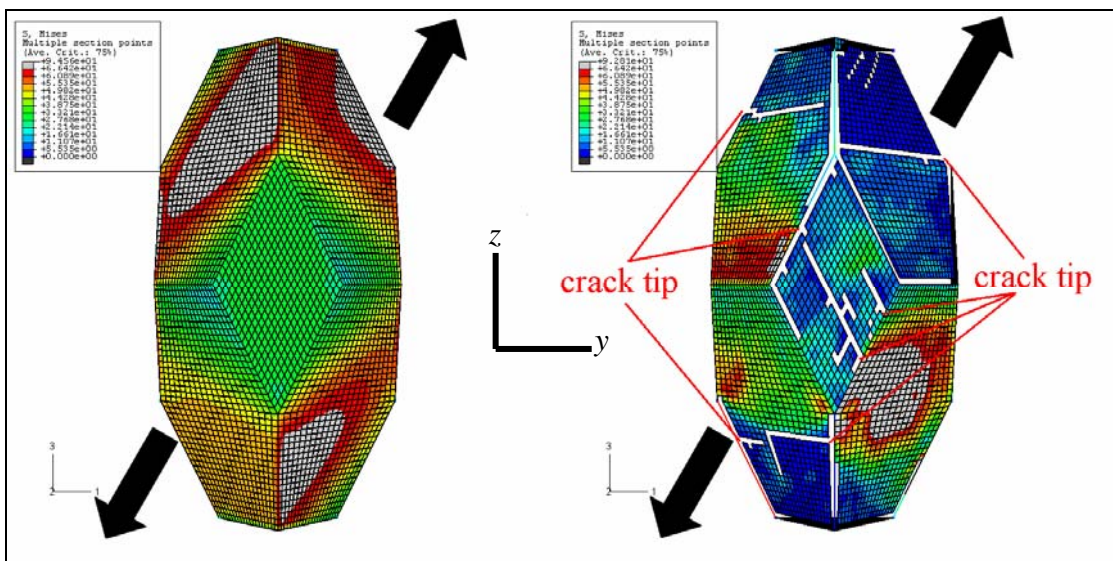
Fig. 5.15 Single cell loaded 30° to the cell elongation (foam rise) direction
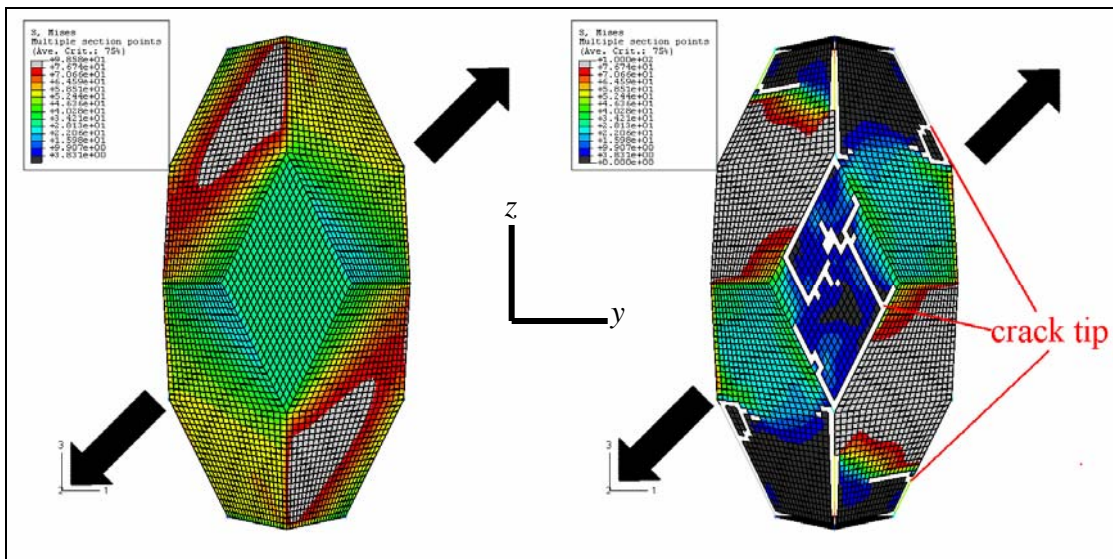
Fig. 5.16 Single cell loaded 45° to the cell elongation (foam rise) direction
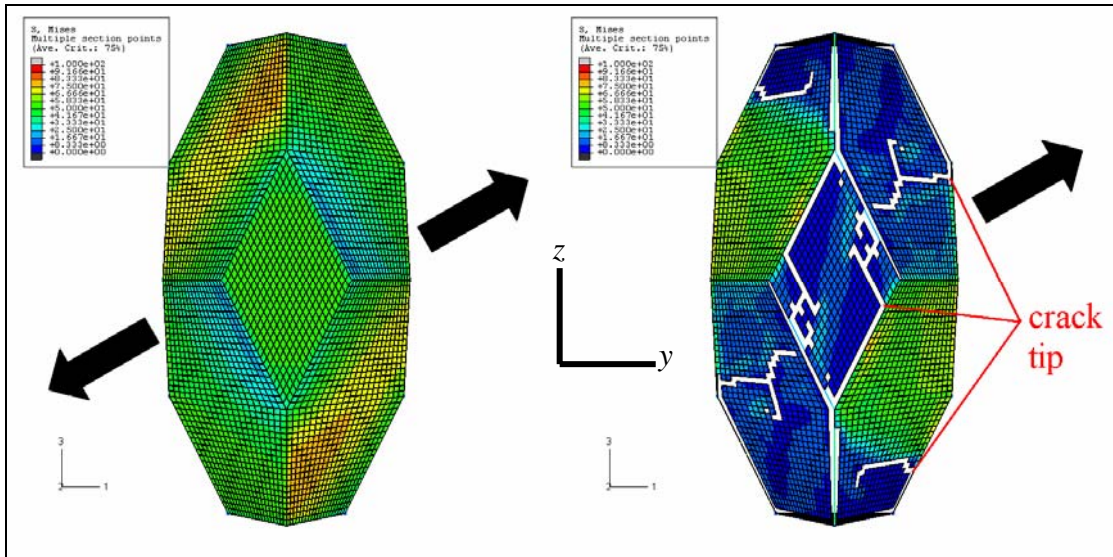
Fig. 5.17 Single cell loaded 60° to the cell elongation (foam rise) direction
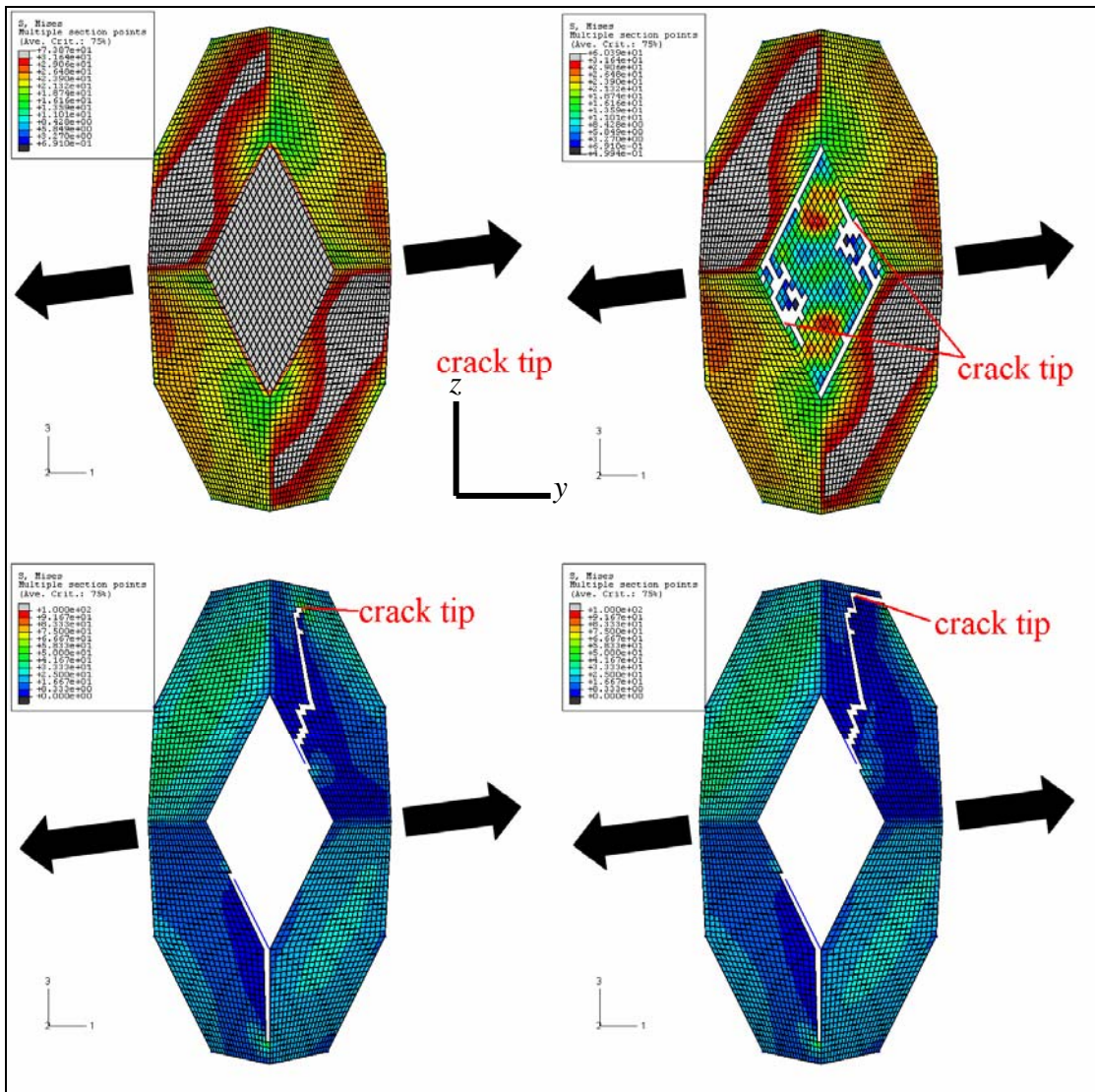
Fig. 5.18 Single cell loaded 82.5^o to the cell elongation (foam rise) direction

153

5.2.3 Response to tensile loading after modification

Figs. 5.19-5.21 show FE simulation results for cell assemblies corresponding to foams A, B, and C; they depict the foam structure initially load-free, then undergoing loading. The figures show that for loading in the transverse direction, the crack propagates in a direction approximately perpendicular to the line of load application, confirming that the correction incorporated to account for the influence of crack propagation in membranes results in correlation with experimental results (Figs. 3.17, 3.19 and 3.21). For loading in the rise direction as well as 30°, 45°, and 60° to this direction, the crack propagates generally perpendicular to the load direction with minor deviations in the middle

The FEM simulations are employed to generate stress-strain relationships for loading in the various directions; Figs. 5.22-5.24 show predicted stress-strain curves corresponding to foams A, B and C. They exhibit an initial linear response followed by a shorter non-linear phase before fracture. This is consistent with results from tests on actual foams presented in Chapter 3. As with the experimental data, the stiffness and strength predicted by FEM modelling are highest in the rise direction and decrease as the angle between the loading and rise directions increases. There are small oscillations in the stress-strain curves, especially for loading in the 30°, 45°, and 60° directions, because of premature failure in some struts at the loading boundaries due to variations in the load distribution among the struts. These oscillations appear noticeable because the number of cells in the model is relatively small and hence, the failure of individual struts causes oscillations in the stress-strain curve. The stress-strain curves for loading in the rise and transverse directions are much smoother because the loads are uniformly distributed among the struts at the loading boundaries and hence, early failure of struts at these edges does not occur. Note that the

boundaries where the loads are applied for loading in the rise and transverse directions consists of repeating cell surface which are regular, and thus the velocity boundary condition applied yields an evenly distributed load among the struts in that area.

Stiffness and tensile strength values were derived from the stress-strain curves – the stiffness was obtained from the gradient of the initial linear portion of the curve, while the strength correspond to the maximum stress attained before failure. Figs. 5.25-5.27 show comparisons between stiffness values from the FEM models with experimental data for foams A, B, and C. There is reasonably good agreement for foams B and C, but noticeable discrepancy for foam A, which exhibits a higher stiffness than the FEM model. This is probably because the stiffness of the cell strut material of foam A is higher than that in the model (the stiffness value in the model was based on tests on solid polyurethane samples, as discussed in Section 3.7). This might be because of a greater degree of polymer molecular chain alignment caused by cell stretching during the foaming process, as well as chemical changes due to the effect of a high gassing agent content [2].

Fig. 5.28 shows a comparison of the foam stiffness predicted by FEM and by the analytical solution; reasonable agreement is observed. The stiffness predicted by FEM simulation tends to be lower because the rigid strut segments in the FEM model are not fully rigid; they were simulated by making the cross-sectional area and the second moment of area much larger than the Plateau border. Moreover, a localised area of weakness was introduced in the FEM model by reducing the strength of some struts in a cell at the edge of the foam model. These struts thus yielded earlier than the others, decreasing the overall stiffness of the model.
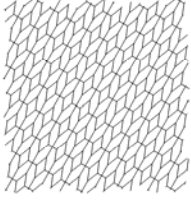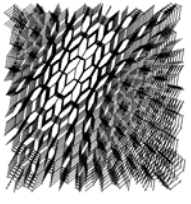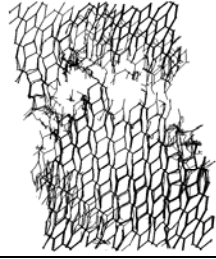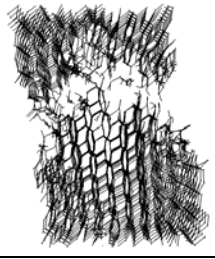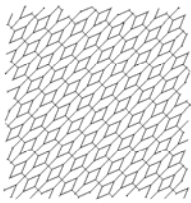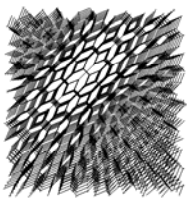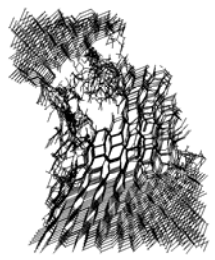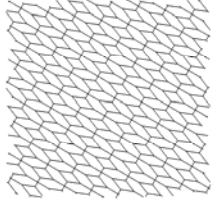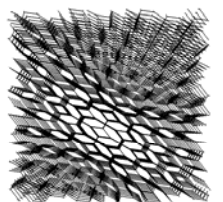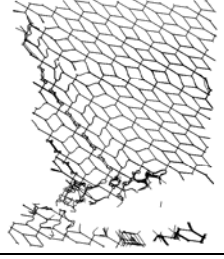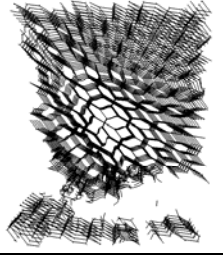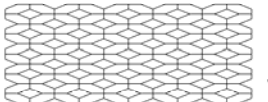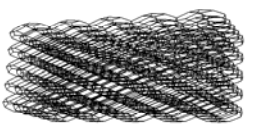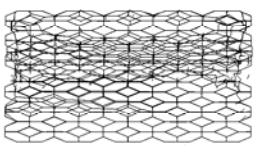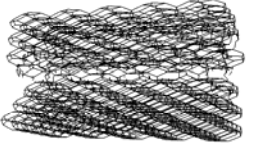
	Unloaded, 2D view	Unloaded, isometric view	Failure initiation, 2D view	Failure initiation, isometric view
0°				
30°				
45°				
60°				
90°				

Fig. 5.19 FEM simulation results for foam A ($\rho = 23.3\,\text{kg}/\text{m}^3$; geometric anisotropy ratio = 2.5)
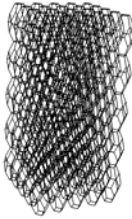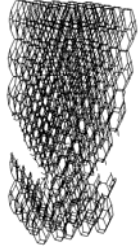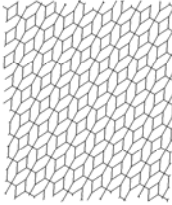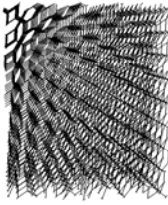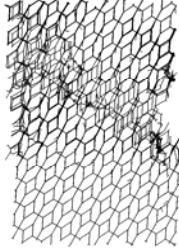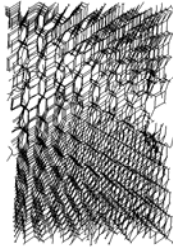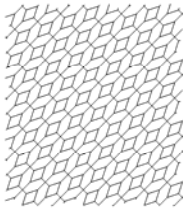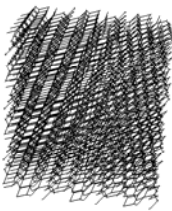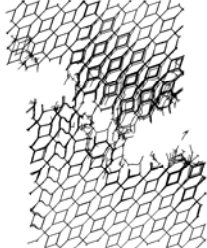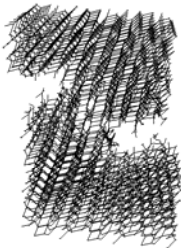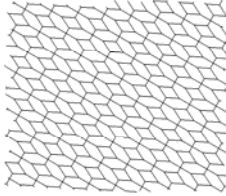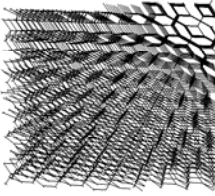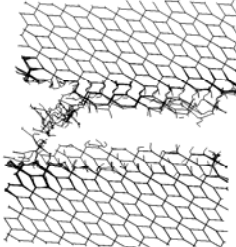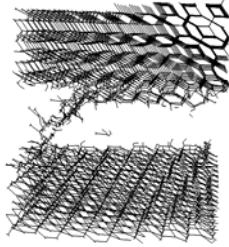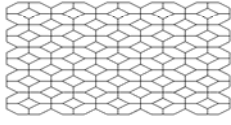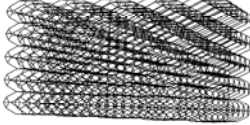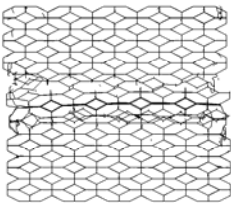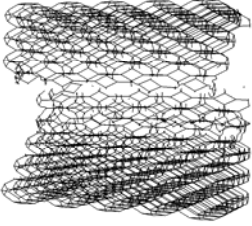
	Unloaded, 2D view	Unloaded, isometric view	Failure initiation, 2D view	Failure initiation, isometric view
0°				
30°				
45°				
60°				
90°				

Fig. 5.20 FEM simulation results for foam B ($\rho = 29.5\,\mathrm{kg}/\mathrm{m}^3$; geometric anisotropy ratio = 2)
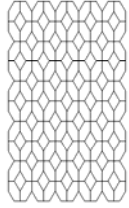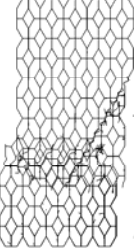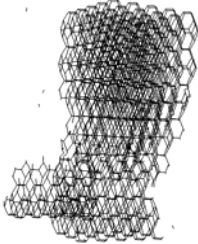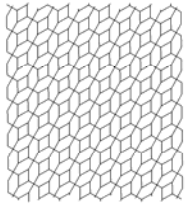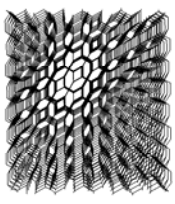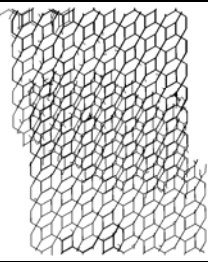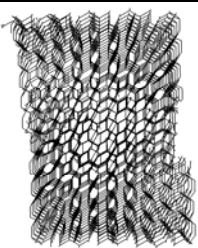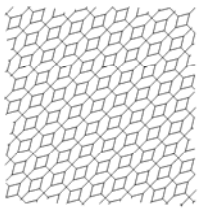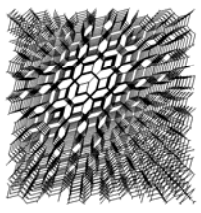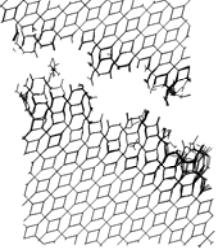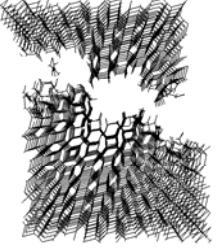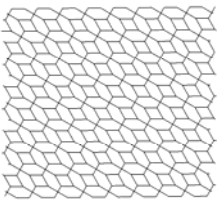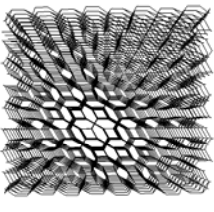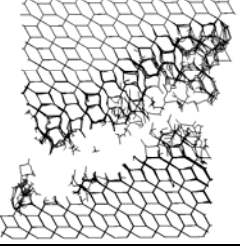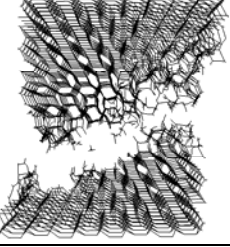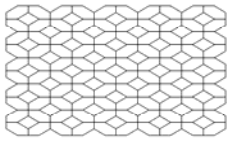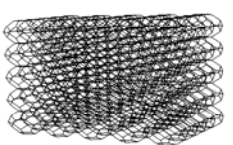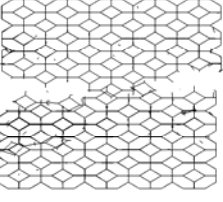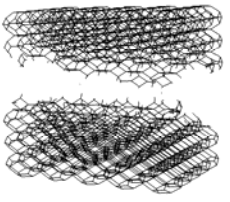
	Unloaded, 2D view	Unloaded, isometric view	Failure initiation, 2D view	Failure initiation, isometric view
0°				
30°				
45°				
60°				
90°				

Fig. 5.21 FEM simulation results for foam C ($\rho = 35.2\,\mathrm{kg}/\mathrm{m}^3$; geometric anisotropy ratio = 1.7)
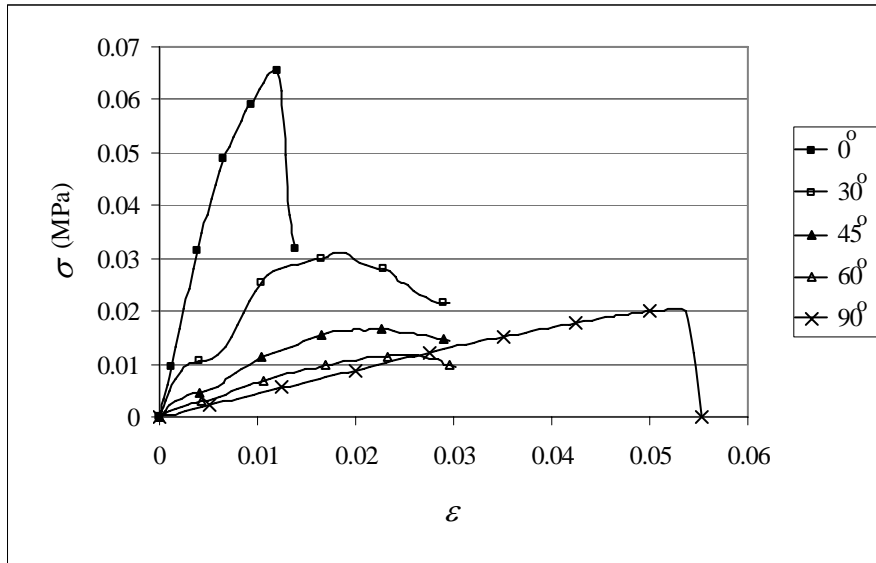
Fig. 5.22 Stress-strain curves for foam A ($\rho = 23.3 \, \text{kg/m}^3$; geometric anisotropy ratio = 2.5)
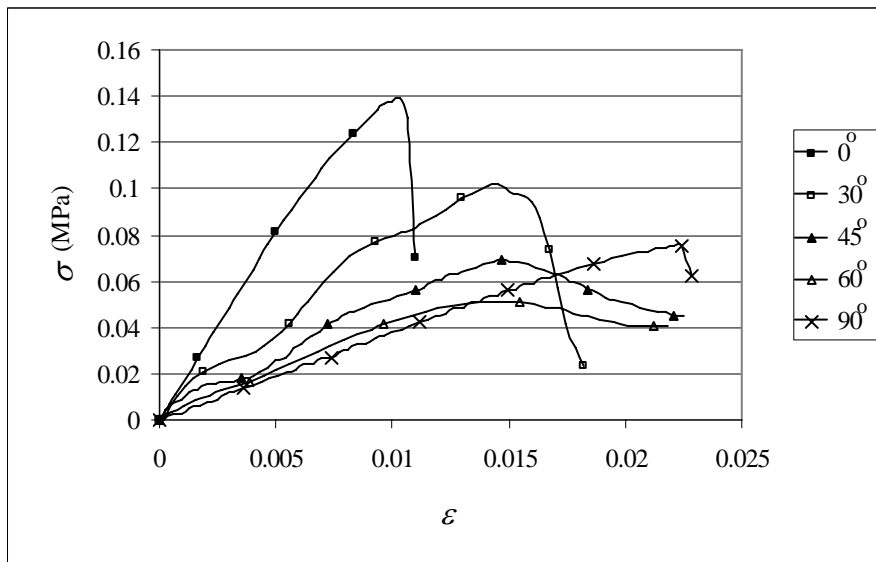

Fig. 5.23 Stress-strain curves for foam B ($\rho = 29.5 \, \text{kg/m}^3$; geometric anisotropy ratio = 2)

Fig. 5.24 Stress-strain curves for foam C ($\rho = 35.2\,\text{kg}/\text{m}^3$; geometric anisotropy ratio = 1.7)

Fig. 5.25 Stiffness of foam A ($\rho = 23.3\,\text{kg}/\text{m}^3$; geometric anisotropy ratio = 2.5)

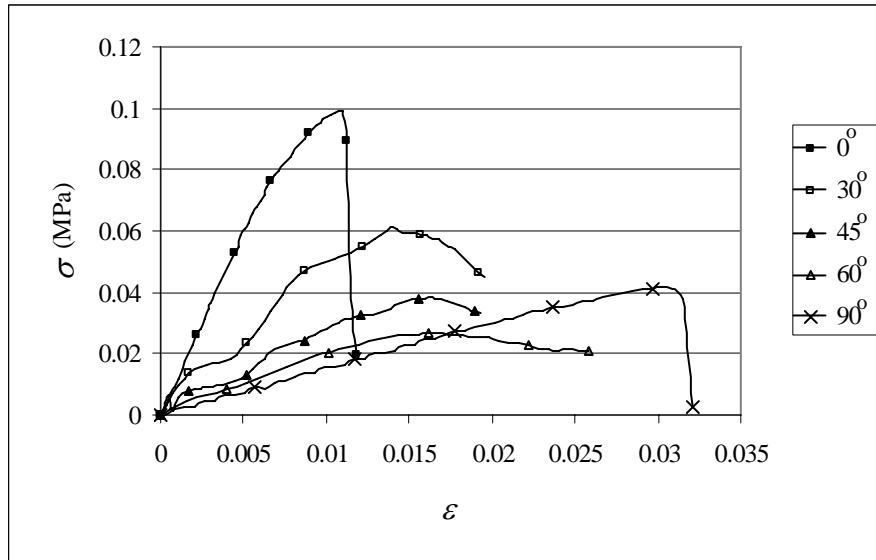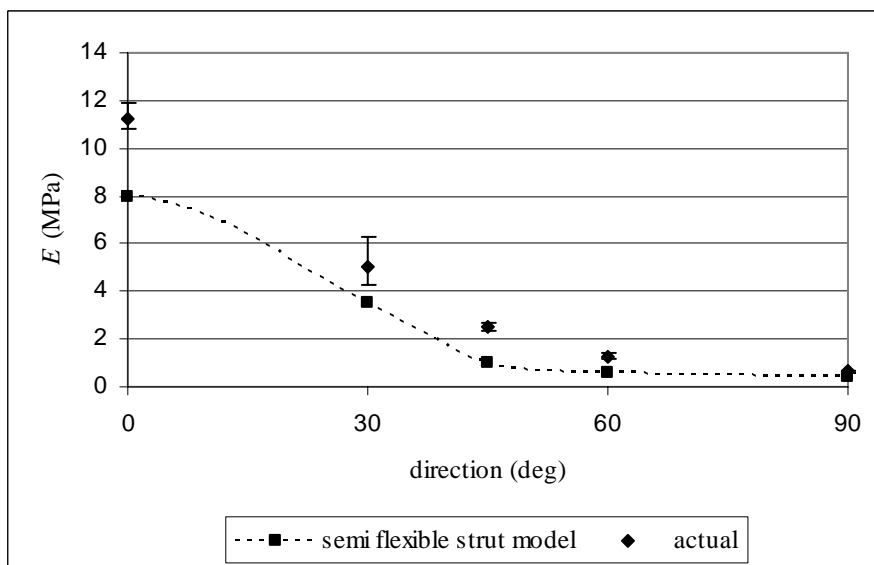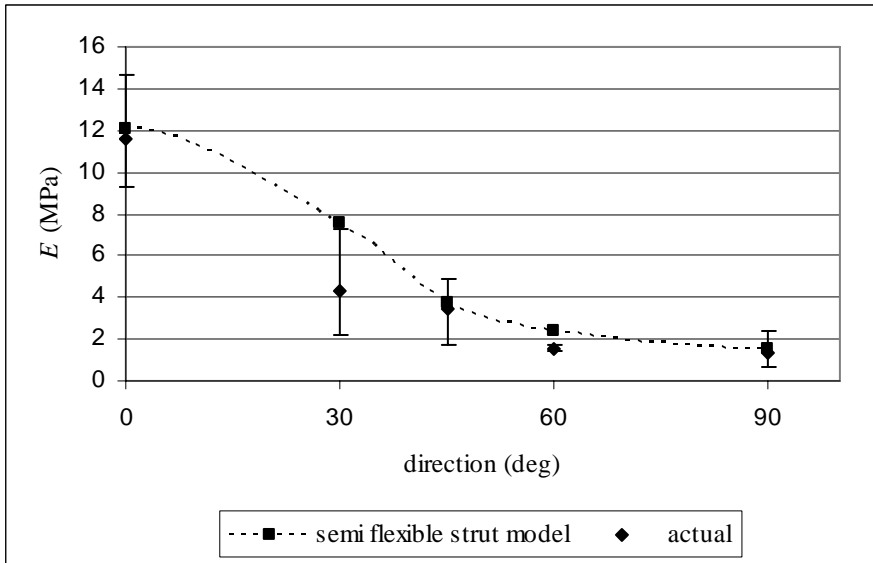Fig. 5.26 Stiffness of foam B ($\rho = 29.5 \, \text{kg}/\text{m}^3$; geometric anisotropy ratio = 2)
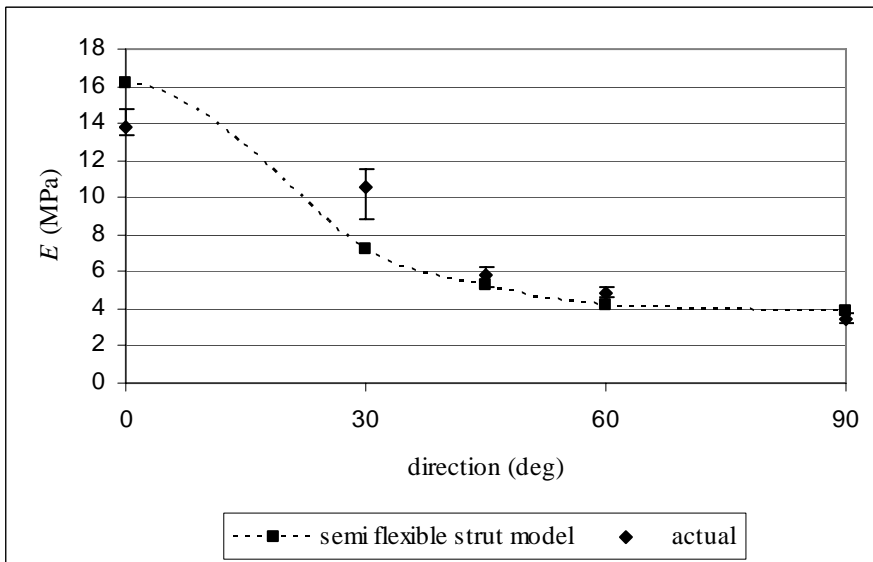

Fig. 5.27 Stiffness of foam C ($\rho = 35.2 \, \text{kg}/\text{m}^3$; geometric anisotropy ratio = 1.7)
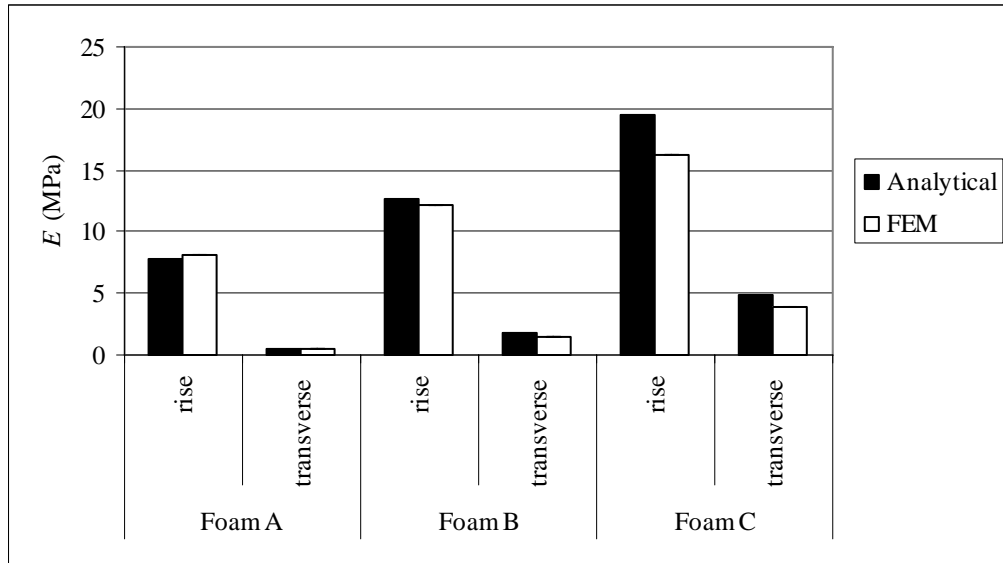
Fig. 5.28 Comparrison between stiffness predicted by FEM and analytical model

Figs. 5.29-5.31 show comparisons between the tensile strength predicted by the FEM model with actual values for foam A, B, and C. The models underestimate the actual tensile strength, probably because the yield and tensile strength data obtained from tests on solid polyurethane samples (Section 3.7) do not reflect fully the actual material in the cell struts because:

- The solid polyurethane specimens tested (Chapter 3) contain tiny bubbles that reduce the actual cross-sectional area and generate stress concentration; hence, the measured strength is lower.

- The stretching of polyurethane during the foaming process might align the molecular polymer chains preferentially, resulting in a higher strength compared to the solid polyurethane specimens, in which foaming was prevented.

- The gassing agent used to enhance foaming might have affected the property of the foams [2].

Nevertheless, when comparisons are made in terms of the normalized tensile strength, i.e. the tensile strength divided by the strength in the rise direction, agreement between the model and actual foam is quite good, as shown in Figs. 5.32-

5.34. This demonstrates that the adjustment of the strength of cell struts to take into account the influence of crack propagation in cell walls is valid and yields a closer correlation in terms of the anisotropic tensile strength ratio. This also indicates that although the thin cell wall membranes do not have much effect on foam stiffness [26, 30], they play an important part in determining its fracture characteristics by influencing the direction of fracture propagation. In contrast with actual foam, whereby the tensile strength decreases with angle between the loading and the rise directions, the tensile strength predicted by the FEM model for loading 60° to the rise direction is slightly lower than that in the transverse direction (Figs. 5.29-5.34). This is because different struts fail for loading in the two directions due to the adjustment of strut strength to incorporate the effect of crack propagation in cell walls – for loading 60° to the rise direction, the inclined struts in the FEM model fail, whereas for loading in the transverse direction, struts lying parallel to the horizontal xy-plane fail. Actual foams do not have cells with geometries exactly identical to the idealized FEM model and hence there is no abrupt change in the struts that fails; thus, the crack propagation direction and the tensile strength change gradually with loading direction.
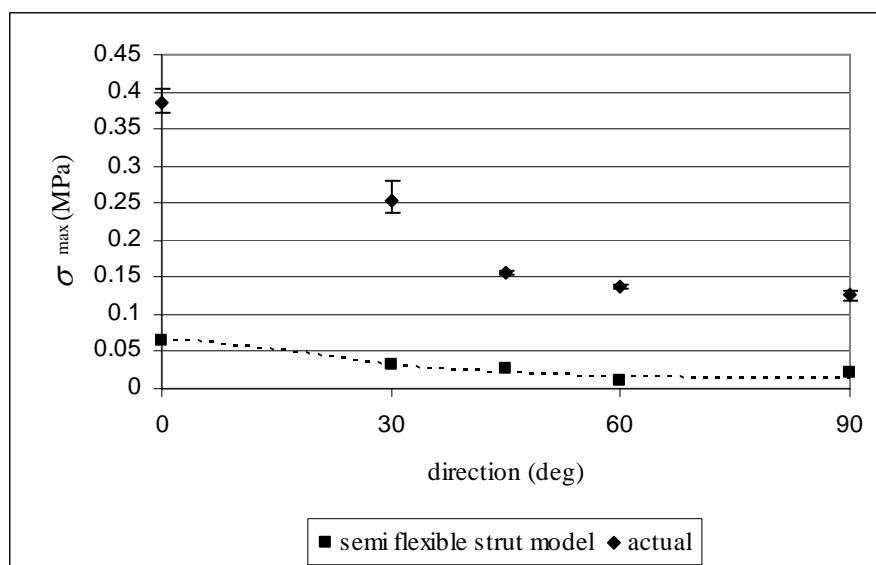
Fig. 5.29 Tensile strength for foam A ($\rho = 23.3 \text{kg}/\text{m}^3$; geometric anisotropy ratio = 2.5)
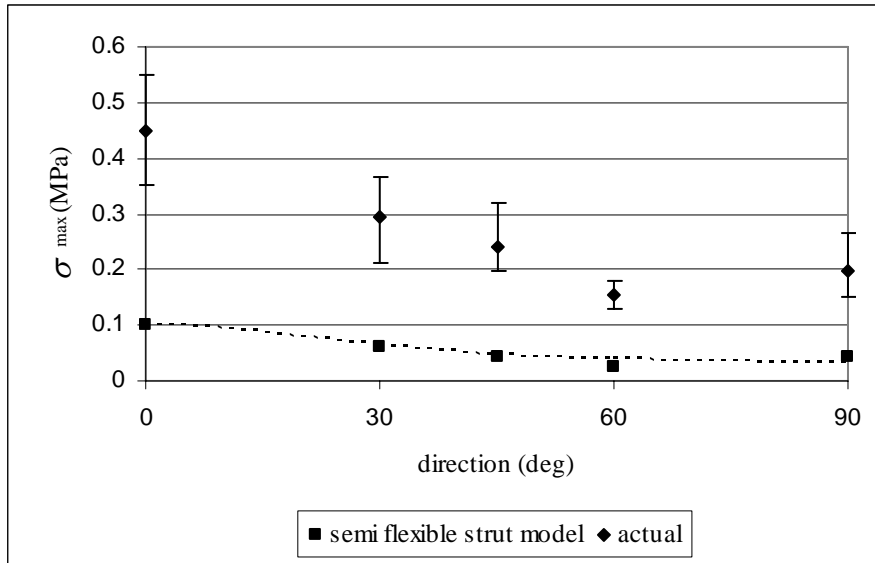
Fig. 5.30 Tensile strength for foam B ($\rho = 29.5\,\mathrm{kg}/\mathrm{m}^3$; geometric anisotropy ratio = 2)

Fig. 5.31 Tensile strength for foam C ($\rho = 35.2\,\mathrm{kg}/\mathrm{m}^3$; geometric anisotropy ratio = 1.7)

Fig. 5.32 Normalized tensile strength for foam A ($\rho = 23.3\,\mathrm{kg}/\mathrm{m}^3$; geometric anisotropy ratio = 2.5)
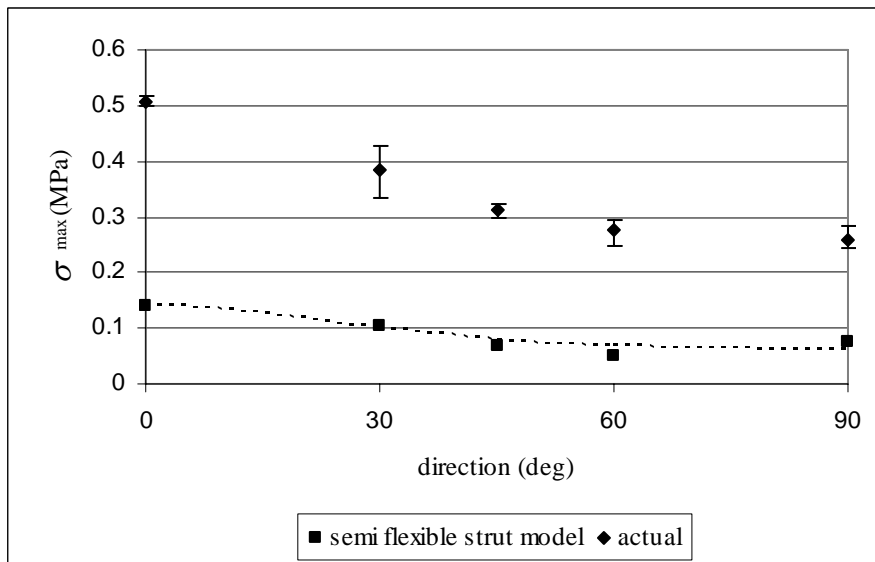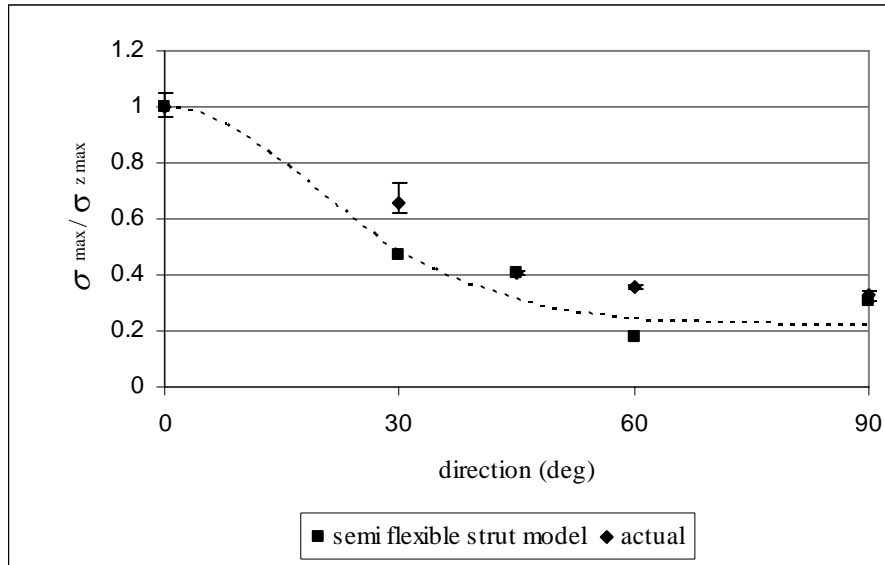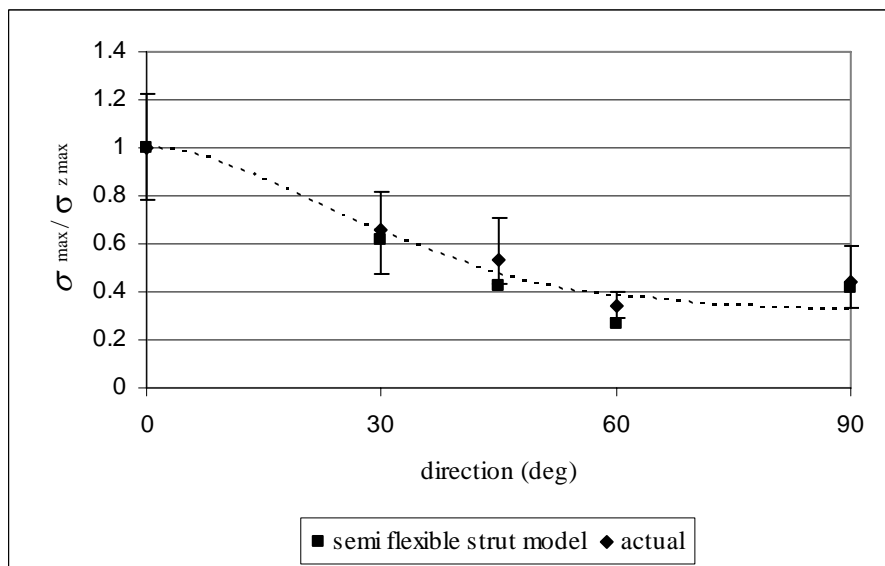

Fig. 5.33 Normalized tensile strength for foam B ($\rho = 29.5\,\mathrm{kg}/\mathrm{m}^3$; geometric anisotropy ratio = 2)
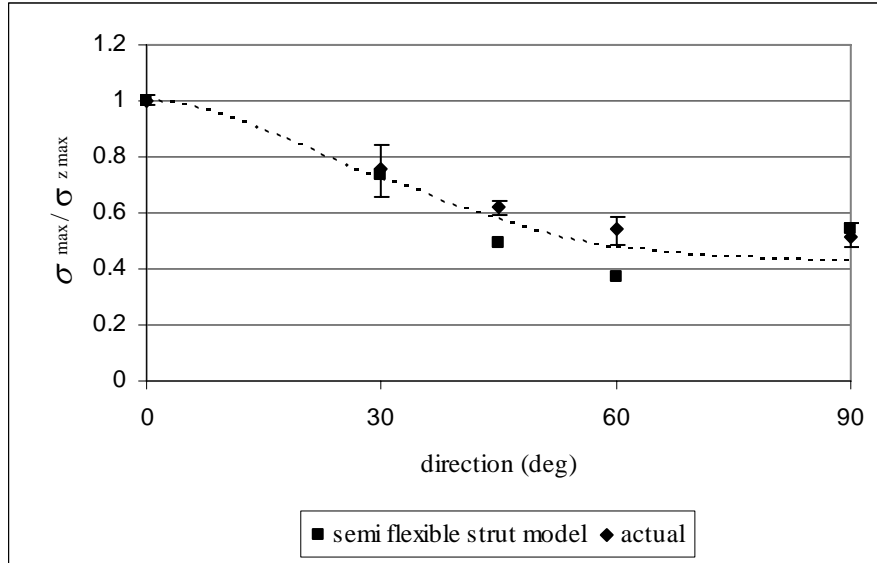
Fig. 5.34 Normalized tensile strength for foam C ($\rho = 35.2\,\mathrm{kg}/\mathrm{m}^3$; geometric anisotropy ratio = 1.7)

5.2.4 Influence of randomness in cell geometric anisotropy and shape

The influence of randomness in cell parameters on the mechanical behaviour of a tetrakaidecahedron cell assembly was examined using finite element simulation. Two modes of randomization were employed, i.e.

- Variation in cell geometric anisotropy – the four struts forming the edges of squares at the top and bottom of each tetrakaidecahedron cell were randomly moved in the rise (*z*-) direction, resulting in variations in cell geometric anisotropy of individual cells. These adjustments were limited so that the modified strut positions do not result in interpenetration between struts and the general shape of the tetrakaidecahedron is maintained. The following procedure was employed:

  o The coordinates of the nodes at the corners of the squares were modified using the following expression:

  $$z_{new} = z_{old} + \mathrm{rand}(-0.2375\,h\,,\,0.2375\,h)$$

  (5.1)

  where $\mathrm{rand}(a\,,\,b)$ is a random number that is evenly distributed between a and b, while h is the height of the original cell.

166

- o The coordinates of the other nodes were adjusted such that each strut remains straight and the length of the rigid segments is the same as that before the randomization process.

Fig. 5.35 shows a cell assembly incorporating this variation in cell geometric anisotropy. To facilitate the application of loading, the top and bottom surfaces of the model were not adjusted.

- Variations in the interconnections between struts – the position of each vertex or corner of a cell, where the struts are interconnected, was randomly adjusted in three dimensions. Again, these adjustments were limited so that the modified strut positions do not result in interpenetration between struts and the general shape of the tetrakaidecahedron is maintained. The following procedure was employed:

  - o The coordinates of the nodes at the vertices were modified via the following expressions:

$$x_{new} = x_{old} + \mathrm{rand}\left(-0.5\, x_{flex}\, , 0.2375\, x_{flex}\right)$$

(5.2)

$$y_{new} = y_{old} + \mathrm{rand}\left(-0.5\, y_{flex}\, , 0.2375\, y_{flex}\right)$$

(5.3)

$$z_{new} = z_{old} + \mathrm{rand}\left(-0.5\, z_{flex}\, , 0.2375\, z_{flex}\right)$$

(5.4)

where again, $\mathrm{rand}(a\, , b)$ is a random number evenly distributed between a and b, while x_{flex}, y_{flex}, and z_{flex} are the lengths of the flexible segment of the inclined struts in the original model projected onto the x, y, and z axes, respectively.

  - o The coordinates of the other nodes were adjusted such that each strut is straight and the length of the rigid segment remains the same as that before the randomization process.

As with the variation in cell geometric anisotropy ratio, no adjustments were made at the outer surfaces of the cell assembly. Fig. 5.36 shows a cellular structure corresponding to this mode of cell randomization.

These two modes of randomization were applied to the cell model corresponding to foam B ($\rho = 29.5 \, \text{kg}/\text{m}^3$).

Fig. 5.37 shows the response of the model with random cell variations, for loading in the rise and transverse directions. The direction of crack propagation is approximately perpendicular to the loading direction and does not exhibit any obvious zigzag path in the middle. The modified model exhibits better resemblance with the behaviour of actual foams compared to the original model which shows some unevenness in the fracture lines. This closer correlation is due to randomness in the strut lengths which causes variations in their strength. Thus the crack is not constrained to run at specific angles in order to cut particular struts, but can cause failure in any struts that is oriented close to the loading direction, resulting in a fracture line perpendicular to the loading direction.
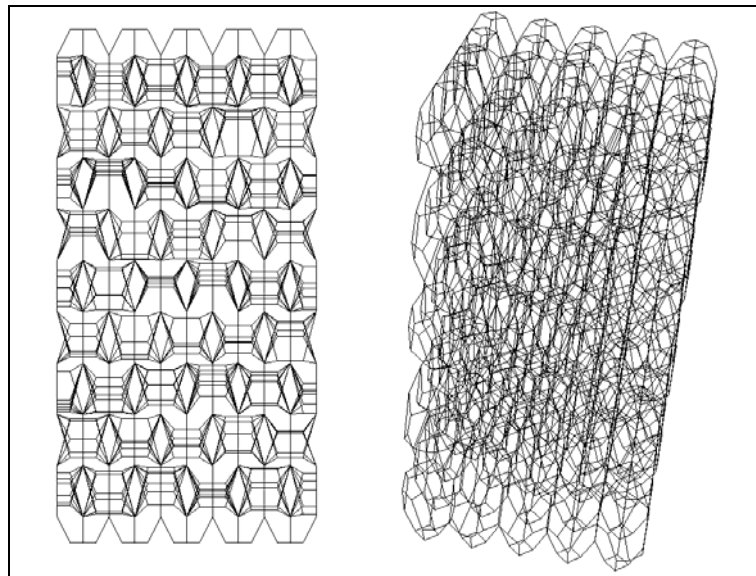

Fig. 5.35 Model with random variations in cell geometric anisotropy ratio
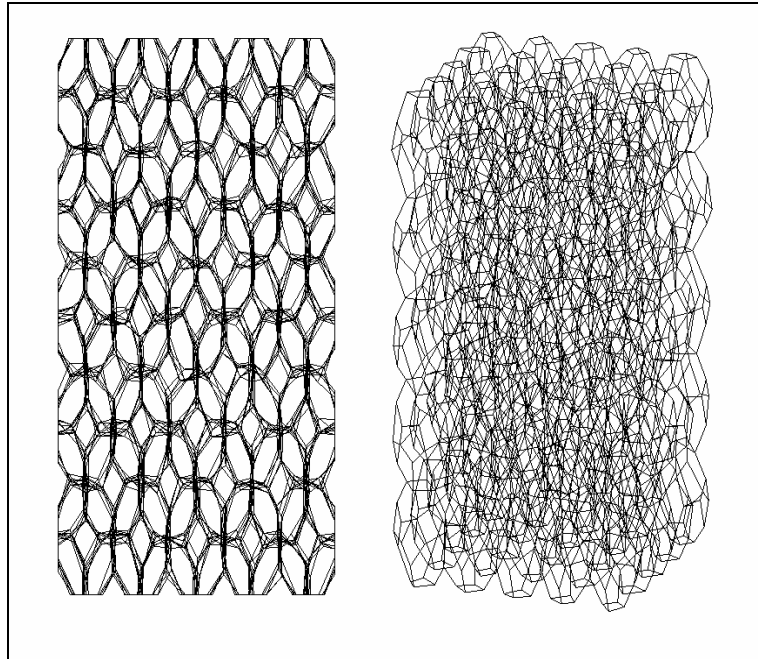
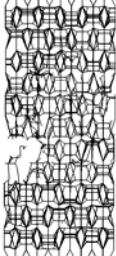Fig. 5.36 Model with random variations in cell vertex location
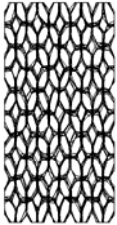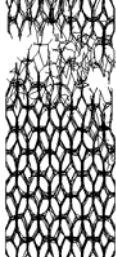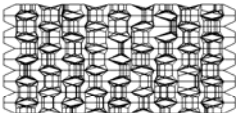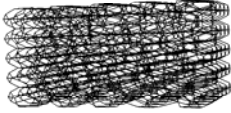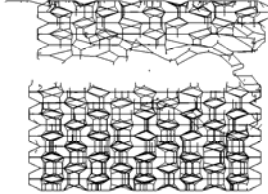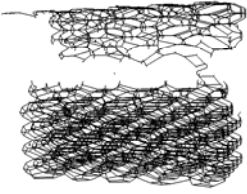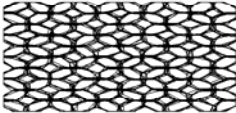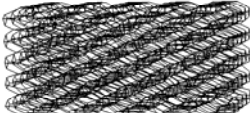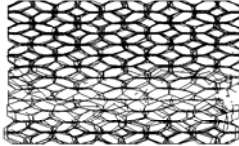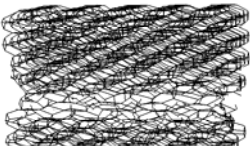
Unloaded, 2D view	Unloaded, isometric view	Failure initiation, 2D view	Failure initiation, isometric view
a. Model with variation in geometric anisotropy (loading in the rise direction)			
b. Model with variation in cell vertex location (loading in the rise direction)			
c. Model with variation in geometric anisotropy (loading in the transverse direction)			
d. Model with variation in cell vertex location (loading in the transverse direction)			

Fig. 5.37 Random cell model for loading in the rise and transverse directions

Figs. 5.38 and 5.39 show respectively comparisons between the original model and the ones with cell variations, in terms of the stress-strain response for loading in the rise and transverse directions. The figures show that the stiffness defined by the initial slope for loading in each direction remains approximately the same, but the tensile strength of the models with random cell variations tends to be lower than that

of the original model; Figs. 5.40 and 5.41 show respectively comparisons between the models in terms of their stiffness and tensile strength. The results indicate that the overall foam stiffness is independent of randomness in cells; however, foam strength is affected by such randomness. This is because the lengths and orientations of the struts in cells with random variations possess different vulnerabilities and hence, failure is determined by the weaker struts. This causes the overall tensile strength to be lower than that of the models with uniform cells.
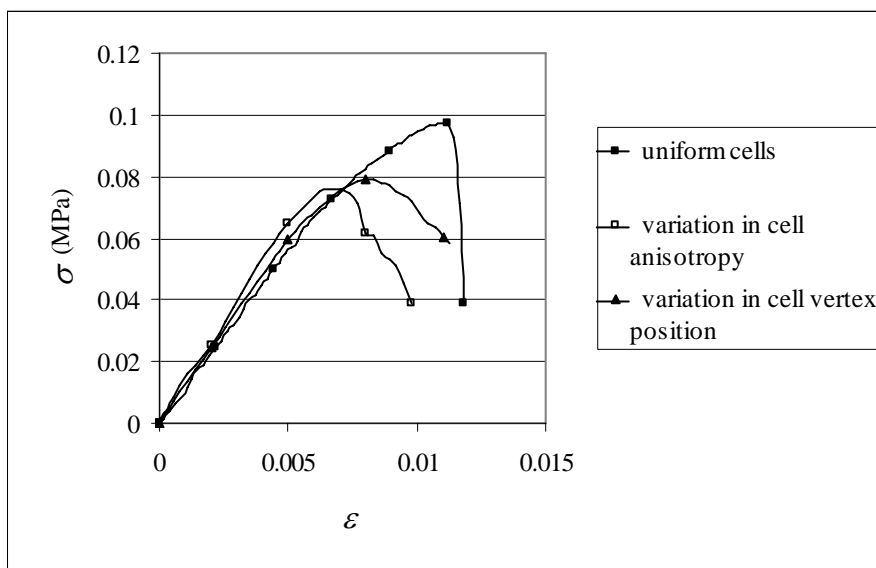
Fig. 5.38 Stress-strain curves for uniform and random cell models for loading in the rise direction
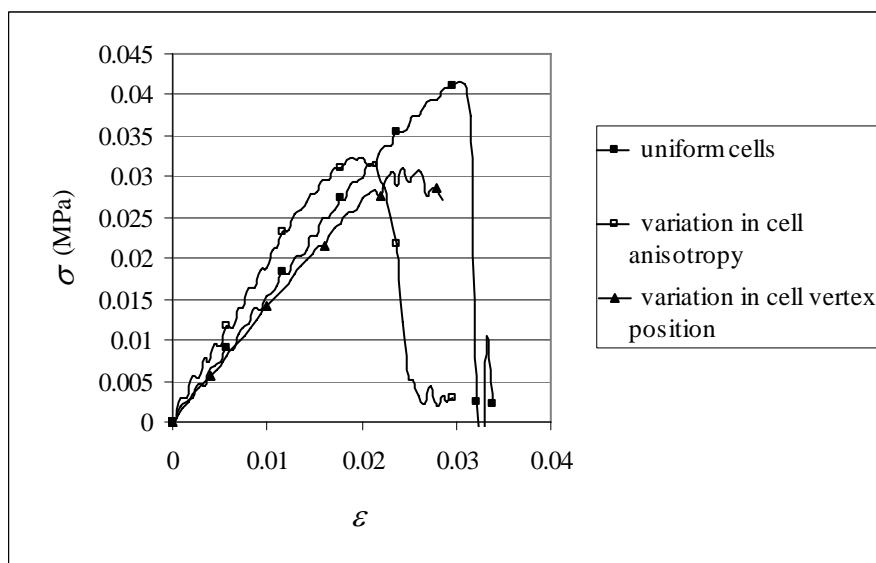
Fig. 5.39 Stress-strain curves for uniform and random cell models for loading in the transverse direction
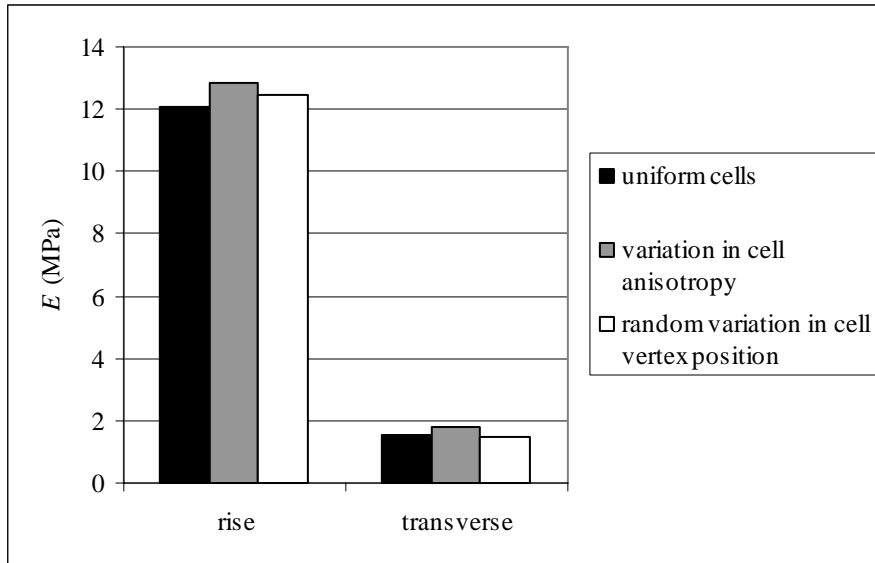
Fig. 5.40 Elastic stiffness of uniform and random cell models
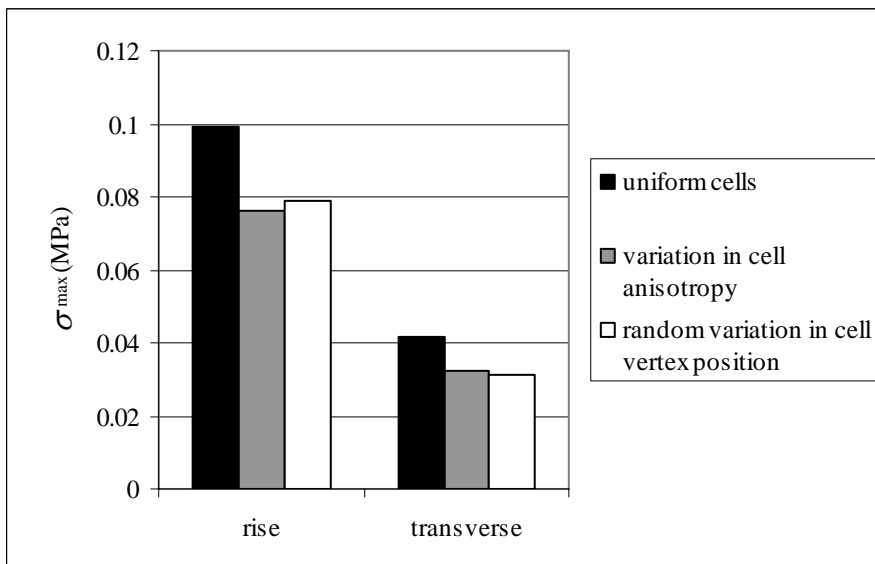
Fig. 5.41 Tensile strength of uniform and random cell models

5.3 Summary

Finite element simulations of foam behaviour based on tetrakaidecahedron cells were undertaken to examine foam stiffness and tensile strength for comparison with values from experimental tests. The modelling of cells was based on beam elements available in ABAQUS-Explicit and material properties derived from actual foam (Chapter 3). The model was loaded in the rise (0°) and transverse (90°) directions, as well as 30°, 45° and 60° to the rise direction. Models that do not consider the effect of crack propagation in cell membranes overestimate the strength anisotropy ratio of

actual foam. Subsequently, this influence was incorporated by reducing the strength of struts at locations where the cracks in the membranes meet them.

The stress-strain characteristics predicted by the models are similar to those of actual foam:

- There is an initial linear elastic response followed by some nonlinearity before fracture.

- The stiffness and strength are highest in the foam rise (cell elongation) direction and decrease with angle between the loading and the foam rise direction.

Foam stiffness predicted by the models displays generally good agreement with actual foams despite some discrepancies which arise because the stiffness of the strut material in the models may not be identical to that of the polyurethane in the struts and walls of actual foam cells. Although the model underestimates the tensile strength, there is good agreement in terms of values normalized with respect to the strength in the foam rise direction. As with the stiffness, the underestimation of foam tensile strength might be because the yield and tensile strengths defined in the models are not exactly the same as those of the polyurethane in actual foam cells. Agreement between the FEM model and the actual foam in terms of their normalized tensile strength shows that although cell membranes do not have much influence on the stiffness of closed cell foams with very thin cell walls such as rigid polyurethane foam [26, 30], they are significant in determining the tensile strength by influencing the direction of crack propagation.

An examination of the influence of randomness in cell parameters on stiffness and tensile strength indicate that crack propagation in FEM models with some degree of randomness in cells resembles that in actual foam more closely, whereby a crack propagates along a line perpendicular to the loading direction without any significant

deviation in path. This is because models with random cells have struts with a range of vulnerabilities to failure, thus the crack is not constrained to cut particular struts, but can cause failure in any struts that is oriented close to the loading direction, resulting in a fracture line perpendicular to the loading direction. Comparisons between the stiffness and tensile strength predicted by the uniform and random cell models show that the effect of variation in cell geometry on stiffness is negligible, but causes a noticeable decrease in foam strength. This is because tensile strength is governed by the weaker struts and the random cell models have a range of struts vulnerabilities compared to the uniform properties of the model with identical cells.

Chapter 6 Conclusions and Recommendations for future work

This study has focused on identifying and explaining the mechanical properties of rigid polyurethane foam under tensile loading, through an experimental investigation and the development of geometric cell models. Quasi-static and dynamic tensile loading in various directions on foam samples were undertaken to examine the influence of strain rate and loading direction on the mechanical properties of the foam studied. Observations using optical microscopy and micro-CT scanning were undertaken to examine the structure of foam cells, as well as their behaviour under tensile and compressive loads. The experimental investigation was accompanied by development of geometric models for the cells within the foam and these were studied both analytically and via finite element simulations.

6.1 Conclusions

Experimental tests and observations of the response of polyurethane foam specimens to tensile loading applied at various angles relative to the foam rise (cell elongation) direction were conducted to identify the overall mechanical properties as well as the behaviour of the cells within them. The results have yielded a fuller understanding of the structure of polyurethane foam and and its behaviour. The primary findings are as follows:

- The tensile strength and stiffness of the rigid polyurethane foams studied are highest in the foam rise (cell elongation) direction and decrease with angle between the loading and foam rise directions, indicating that the mechanical properties are anisotropic because of anisotropy in the cell geometry.

- The primary mechanism governing foam deformation is the bending of cell struts and walls. A significant observation is that a short segment at each end of a strut, where it is connected to neighbouring struts, essentially does not deform. This is because the strut cross-section there is larger and the interconnection with adjacent struts and cell membranes at these cell vertices restrict movement. The study has shown that this feature must be considered in developing geometric cell models for foam.

- Micro CT-scan images reveal that the cells in rigid polyurethane foam bear a reasonable resemblance with an elongated tetrakaidecahedron, while the cross-section of cell struts has a geometry similar to that of a Plateau border [1].

Two analytical models based on elongated rhombic dodecahedral and elongated tetrakaidecahedral cells were formulated to facilitate analysis of the mechanical properties of foam. The stiffness, tensile strength, and Poisson's ratio in the rise (cell elongation) and transverse directions were calculated and compared to actual foams. The presence of rigid strut segments near their ends, as observed in actual foam specimens, was taken into account in the analysis and shown to influence the results predicted by the models. A parametric study of the mechanical properties of foam based on the analytical models shows that:

- The elastic stiffness and strength of foam are not influenced by cell size; they are governed by density, geometric anisotropy of the cells, cell shape, strut cross-section geometry, as well as the length of the rigid strut segments.

- The bending of cell struts is the primary deformation mechanism in foams.

- Tensile strength and stiffness increase with density.

- Anisotropy of mechanical properties – tensile strength and stiffness – increases with anisotropy in the geometry of the constituent cells.

- The Poisson's ratio of a cellular structure is governed by the geometry of the internal structure and does not depend on the material it is made of.

A comparison between the cell models and actual foam shows that an elongated tetrakaidecahedron resembles the cells in actual foam more closely than a rhombic dodecahedron. Moreover, the prediction of foam stiffness based on elongated tetrakaidecahedron cells incorporating the correction for rigid strut segments agrees well with experimental results from tests on the foams studied. This shows that similarity between the idealized cell model geometry and the geometry of actual foam cells determines the effectiveness of a model in predicting actual foam behaviour. The analytical model enables identification of the influence of several parameters – overall foam density, cell anisotropy, stiffness and strength of the solid material in cell struts and walls – on the overall mechanical behaviour of a foam. Moreover, the model serves as a means to estimate mechanical property values of foam

Finite element simulations of foam behaviour based on elongated tetrakaidecahedron cells, were also undertaken to examine the mechanical properties for loading directions that were not amenable to analytical solution, and to facilitate incorporation of non-linear material properties and variations in cell geometry. The simulations yielded the following findings:

- Although cell membranes have little influence on the stiffness of closed cell foam with very thin cell walls, they play an important part in determining the tensile strength by influencing the direction of crack propagation. This must be taken into account in utilizing idealized cell geometries to model foam.

- The stiffness predicted by the tetrakaidecahedron cell model agrees quite well with values from tests on actual foam. Differences occur because stiffness values

obtained from tensile tests on solid polyurethane may not be identical to that of the polyurethane in the cell struts and walls of the foam specimens.

- The model underestimates the actual tensile strength for the different directions of loading; however, agreement is good when normalized tensile strength is considered (i.e. tensile strength normalized with respect to the tensile strength in the foam rise direction). As with foam stiffness, this underestimation is probably because the yield and tensile strength data obtained from tests on solid polyurethane specimens may not be exactly the same as that of the polyurethane in the actual foam. Close correlation between the model and actual foam behaviour in terms of normalized tensile strength shows that incorporation of the influence of crack propagation in cell wall membranes is justified and necessary.

- FEM modelling demonstrates that random variations in the geometry of individual cells do not exert a significant influence on the overall stiffness of foam, but decreases the predicted tensile strength.

Finite element simulations based on tetrakaidecahedron cells are able to model specific features of rigid polyurethane foam under tensile loading – i.e. stiffness and fracture characteristics. This method can be used for analysis of more complex problems in foam behaviour that are not amenable to analytical solution, such as inclusion of non-linear material properties, large deformation, variation of cell geometry, influence of cell membranes, etc; however, these may require extensive computational resource and time.

In essence, this study demonstrates that use of detailed experimental observation of the response of cellular material to formulate an idealized cell model, followed by subsequent finite element simulation, is an effective approach to understanding the

mechanical behaviour of foam. The cell model established in this study constitutes a basis for further development of constitutive models for foam

6.2 Recommendations for future work

This study has focused primarily on the mechanical behaviour of rigid polyurethane foam under tension and the development of idealized geometric cell models. This can be extended to examine other aspects of the mechanical behaviour of foam:

- The bulk and shear moduli can be analytically derived from the cell model. For this purpose, the method employed by Zhu et al. [40] for analyzing the bulk modulus and shear modulus for isotropic tetrakaidecahedron cells can be used as a basis, but has to be modified to incorporate cell anisotropy.

- The Poisson's ratio of foam can be measured and compared with values predicted by the model. A non-contact technique to measure strain could be used for this purpose, because the surfaces of polyurethane foam specimens are not flat and are easily deformed/crushed, making attachment of measurement devices difficult.

- Failure criteria based on the buckling of cell struts for foam under compression can be analysed using the cell model; Euler buckling analysis could be applied to cell struts.

- Compression involving large deformation and multi-axial loading can be examined to identify foam behaviour and to determine if the cell model proposed is able to represent the compressive response of actual foam. However, this requires non-linear deformation analysis; the method used by Zhu et al. [41] in analyzing high strain compression of an isotropic tetrakaidecahedron cell model could facilitate such a study. Numerical methods such as finite element modelling could also be employed; however, FEM simulation might be costly in terms of

179

computational time and resources as much longer simulation times would be needed to model large deformation and more elements are required for accurate results.

- The cell model can be examined for applicability to other types of foam with similar characteristics, i.e. open celled or closed celled with thin walls, such as flexible polyurethane foam, open celled aluminium foam, etc.

List of References

1.   Plateau, J., *Statique expérimentale et théorique des liquides soumis aux seules forces moléculaires*. 1873, Paris: Gauthier-Villars.

2.   Gibson, L.J. and M.F. Ashby, *Cellular Solids: Structure and Properties*. 2nd ed. 1997, Cambridge: Cambridge University Press.

3.   Deshpande, V.S. and N.A. Fleck, *Isotropic constitutive models for metallic foams.* Journal of the Mechanics and Physics of Solids, 2000. **48**(6-7): p. 1253-1283.

4.   Deshpande, V.S. and N.A. Fleck, *Multi-axial yield behaviour of polymer foams.* Acta Materialia, 2001. **49**(10): p. 1859-1866.

5.   Doyoyo, M. and T. Wierzbicki, *Experimental studies on the yield behavior of ductile and brittle aluminum foams.* International Journal of Plasticity, 2003. **19**(8): p. 1195-1214.

6.   Gdoutos, E.E., I.M. Daniel, and K.-A. Wang, *Failure of cellular foams under multiaxial loading.* Composites Part A: Applied Science and Manufacturing, 2002. **33**(2): p. 163-176.

7.   McIntyre, A. and G.E. Anderton, *Fracture properties of a rigid polyurethane foam over a range of densities.* Polymer, 1979. **20**(2): p. 247-253.

8.   Triantafillou, T.C., et al., *Failure Surfaces for Cellular Materials Under Multiaxial Loads. II. Comparison of Models With Experiment.* International Journal of Mechanical Sciences, 1989. **31**(9): p. 665-678.

9.   Zaslawsky, M., *Multiaxial-stress studies on rigid polyurethane foam.* Experimental Mechanics, 1973. **13**(2): p. 70-76.

10.   Zhang, J., et al., *Constitutive modeling of polymeric foam material subjected to dynamic crash loading.* International Journal of Impact Engineering, 1998. **21**(5): p. 369-386.

11.   Andrews, E.W., L.J. Gibson, and M.F. Ashby, *The creep of cellular solids.* Acta Materialia, 1999. **47**(10): p. 2853-2863.

12.   Chan, R. and M. Nakamura, *Mechanical properties of plastic foams.* Journal of Cellular Plastics, 1969. **5**: p. 112-118.

13.   Choi, J.B. and R.S. Lakes, *Analysis of elastic modulus of conventional foams and of re-entrant foam materials with a negative Poisson's ratio.* International Journal of Mechanical Sciences, 1995. **37**(1): p. 51-59.

14.   Christensen, R.M., *Mechanics of low density materials.* Journal of the Mechanics and Physics of Solids, 1986. **34**(6): p. 563-578.

15.   Cunningham, A., *Modulus anisotropy of low-density cellular plastics: an aggregate model.* Polymer, 1981. **22**(7): p. 882-885.

16.   Dement'ev, A.G. and O.G. Tarakanov, *Effect of cellular structure on the mechanical properties of plastic foams.* Mechanics of Composite Materials, 1970. **6**(4): p. 519-525.

17.   Dement'ev, A.G. and O.G. Tarakanov, *Model analysis of the cellular structure of plastic foams of the polyurethane type.* Mechanics of Composite Materials, 1970. **6**(5): p. 744-749.

18.   Gent, A.N. and A.G. Thomas, *The deformation of foamed elastic materials.* Journal of Applied Polymer Science, 1959. **1**(1): p. 107-113.

19.   Gent, A.N. and A.G. Thomas, *Mechanics of foamed elastic materials.* Rubber Chemistry and Technology, 1963. **36**(3): p. 597–610.

20. Gibson, L.J. and M.F. Ashby. *The Mechanics of Three-Dimensional Cellular Materials*. in *Proceedings of the Royal Society of London. Series A, Mathematical and Physical Sciences*. 1982: The Royal Society.

21. Gibson, L.J., et al., *Failure Surfaces for Cellular Materials Under Multiaxial Loads. I. Modelling.* International Journal of Mechanical Sciences, 1989. **31**(9): p. 635-663.

22. Warren, W.E. and A.M. Kraynik, *The linear elastic properties of open-cell foams.* Journal of Applied Mechanics, 1988. **55**(22): p. 341-346.

23. Grenestedt, J.L. and K. Tanaka, *Influence of cell shape variations on elastic stiffness of closed cell cellular solids.* Scripta Materialia, 1998. **40**(1): p. 71-77.

24. Grenestedt, J.L., *Effective elastic behavior of some models for perfect cellular solids.* International Journal of Solids and Structures, 1999. **36**(10): p. 1471-1501.

25. Huang, J.-S. and L.J. Gibson, *Creep of open-cell Voronoi foams.* Materials Science and Engineering A, 2003. **339**(1-2): p. 220-226.

26. Huber, A.T. and L.J. Gibson, *Anisotropy of foams.* Journal of Materials Science, 1988. **23**(8): p. 3031-3040.

27. Kanakkanatt, S.V., *Mechanical anisotropy of open-cell foams.* Journal of Cellular Plastics, 1973. **9**: p. 50-53.

28. Ko, W.L., *Deformations of foamed elastomers.* Journal of Cellular Plastics, 1965. **1**: p. 45-50.

29. Lederman, J.M., *The prediction of the tensile properties of flexible foams.* Journal of Applied Polymer Science, 1971. **15**(3): p. 693-703.

30.   Menges, G. and F. Knipschild, *Estimation of mechanical properties for rigid polyurethane foams.* Polymer Engineering & Science, 1975. **15**(8): p. 623-627.

31.   Maiti, S.K., L.J. Gibson, and M.F. Ashby, *Deformation and energy absorption diagrams for cellular solids.* Acta Metallurgica, 1984. **32**(11): p. 1963-1975.

32.   Mills, N.J. and H.X. Zhu, *The high strain compression of closed-cell polymer foams.* Journal of the Mechanics and Physics of Solids, 1999. **47**(3): p. 669-695.

33.   Patel, M.R. and I. Finnie, *Structural features and mechanical properties of rigid cellular plastics.* Journal of Materials, 1970. **5**(4): p. 909-932.

34.   Roberts, A.P. and E.J. Garboczi, *Elastic moduli of model random three-dimensional closed-cell cellular solids.* Acta Materialia, 2001. **49**(2): p. 189-197.

35.   Roberts, A.P. and E.J. Garboczi, *Elastic properties of model random three-dimensional open-cell solids.* Journal of the Mechanics and Physics of Solids, 2002. **50**(1): p. 33-55.

36.   Sahraoui, S., E. Mariez, and M. Etchessahar, *Linear elastic properties of anisotropic open-cell foams.* Journal of the Acoustical Society of America, 2001. **110**(1): p. 635-637.

37.   Simone, A.E. and L.J. Gibson, *Effects of solid distribution on the stiffness and strength of metallic foams.* Acta Materialia, 1998. **46**(6): p. 2139-2150.

38.   Wang, Y. and A.M. Cuitino, *Three-dimensional nonlinear open-cell foams with large deformations.* Journal of the Mechanics and Physics of Solids, 2000. **48**(5): p. 961-988.

39.   Warren, W.E. and A.M. Kraynik, *Linear elastic behavior of a low-density Kelvin foam with open cells.* Journal of Applied Mechanics, 1997. **64**(4): p. 787-794.

40.   Zhu, H.X., J.F. Knott, and N.J. Mills, *Analysis of the elastic properties of open-cell foams with tetrakaidecahedral cells.* Journal of the Mechanics and Physics of Solids, 1997. **45**(3): p. 319-325.

41.   Zhu, H.X., N.J. Mills, and J.F. Knott, *Analysis of the high strain compression of open-cell foams.* Journal of the Mechanics and Physics of Solids, 1997. **45**(11-12): p. 1875-1899.

42.   Zhu, H.X., J.R. Hobdell, and A.H. Windle, *Effects of cell irregularity on the elastic properties of open-cell foams.* Acta Materialia, 2000. **48**(20): p. 4893-4900.

43.   Zhu, H.X. and A.H. Windle, *Effects of cell irregularity on the high strain compression of open-cell foams.* Acta Materialia, 2002. **50**(5): p. 1041-1052.

44.   Ridha, M., V.P.W. Shim, and L.M. Yang. *An Elongated Tetrakaidecahedral Cell Model for Fracture in Rigid Polyurethane Foam.* in *Proceedings of The 6th International Conference on Fracture and Strength of Solids.* 2005.

45.   Ridha, M., V.P.W. Shim, and L.M. Yang. *An Elongated Tetrakaidecahedron Cell Idealization of the Microstructure of Rigid Polyurethane Foam.* in *Proceedings of JSME/ASME International Conference on Materials and Processing 2005 (The 13th JSME Material and Processing Conference).* 2005. Seattle, Washington, USA.

46.   Ridha, M., V.P.W. Shim, and L.M. Yang, *An Elongated Tetrakaidecahedral Cell Model for Fracture in Rigid Polyurethane Foam.* Key Engineering Materials, 2006. **306/308**(1): p. 43-48.

47.   Ehlers, W., H. Mullerschon, and O. Klar. *On the behaviour of aluminium foams under uniaxial and multiaxial loading*. in *the Conference on Metal Foams and Porous Metal Structures, MetForm 99, 14-16 June*. 1999. Bremen, Germany: MIT Verlag.

48.   Gioux, G., T.M. McCormack, and L.J. Gibson, *Failure of aluminum foams under multiaxial loads.* International Journal of Mechanical Sciences, 2000. **42**(6): p. 1097-1117.

49.   Hanssen, A.G., et al., *Validation of constitutive models applicable to aluminium foams.* International Journal of Mechanical Sciences, 2002. **44**(2): p. 359-406.

50.   Miller, R.E., *A continuum plasticity model for the constitutive and indentation behaviour of foamed metals.* International Journal of Mechanical Sciences, 2000. **42**(4): p. 729-754.

51.   Schreyer, H.L., Q.H. Zuo, and A.K. Maji, *Anisotropic Plasticity Model for Foams and Honeycombs.* Journal of engineering mechanics, 1994. **120**(9): p. 1913-1930.

52.   Banhart, J. and J. Baumeister, *Deformation characteristics of metal foams.* Journal of Materials Science, 1998. **33**(6): p. 1431-1440.

53.   Motz, C. and R. Pippan, *Deformation behaviour of closed-cell aluminium foams in tension.* Acta Materialia, 2001. **49**(13): p. 2463-2470.

54.   Zhang, J., et al., *Constitutive Modeling and Material Characterization of Polymeric Foams.* Journal of engineering materials and technology, 1997. **119**(3): p. 284-291.

55.   Tsai, S.W. and E.M. Wu, *A General Theory of Strength for Anisotropic Materials.* Journal of Composite Materials, 1971. **5**(1): p. 58-80.

56. McCullough, K.Y.G., N.A. Fleck, and M.F. Ashby, *Toughness of aluminium alloy foams.* Acta Materialia, 1999. **47**(8): p. 2331-2343.

57. Dawson, J.R. and J.B. Shortall, *The microstructure of rigid polyurethane foams.* Journal of Materials Science, 1982. **17**(1): p. 220-224.

58. Zhu, H.X. and N.J. Mills, *Modelling the creep of open-cell polymer foams.* Journal of the Mechanics and Physics of Solids, 1999. **47**(7): p. 1437-1457.

59. Yang, L.M. and V.P.W. Shim, *An analysis of stress uniformity in split Hopkinson bar test specimens.* International Journal of Impact Engineering, 2005. **31**(2): p. 129-150.

Appendix A: SPHB experiments data processing procedure
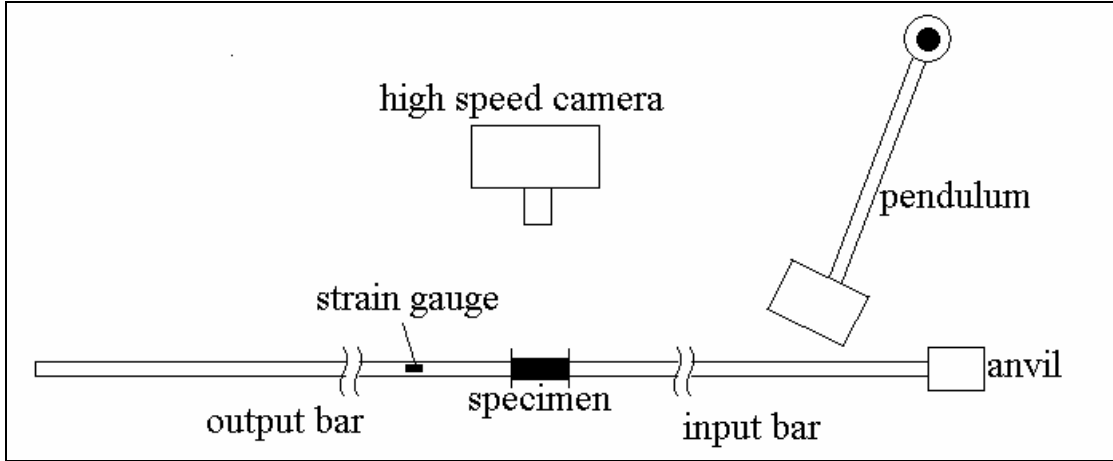
Fig. A.1 Split Hopkinson bar arrangement

Calculations for stress in SPHB specimens were performed using the following procedure.

- Strain-time data from the strain gauge on the output bar was obtained (see Fig. A.1)

- The data was then converted into stress imposed on the specimen using the following expression:

$$\sigma_s = \frac{A_s}{A_b} E_b \, \varepsilon_b$$

(A.1)

where σ_s is the stress in the specimen, A_s and A_b are respectively the cross-sectional areas of the specimen and the input/output bars, E_b is the stiffness of the bars, and ε_b is the strain in the output bar.

The strain in the specimen was calculated as follows.

- Two reference points were marked along the centre-line of the specimen (see Fig. A.2)

- The initial distance and subsequent relative displacement between the two points were obtained from high-speed photographs, using a PHOTRON™ ultima APX high-speed camera, operating at a framing rate of 30,000 frames per second.

- The specimen strain was then calculated by dividing the relative displacement by the initial distance between the two reference points.

- It was found that the variation of strain with time was essentially linear; hence, linear regression was employed to calculate the strain rate (see Fig. A.3). This strain rate was integrated to calculate the specimen strain corresponding to the stress data.
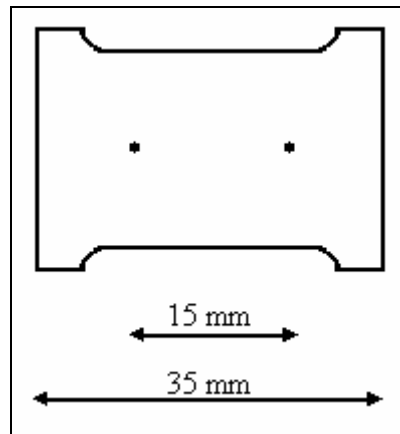
Fig. A.2 SPHB specimen with two reference points along the centre-line
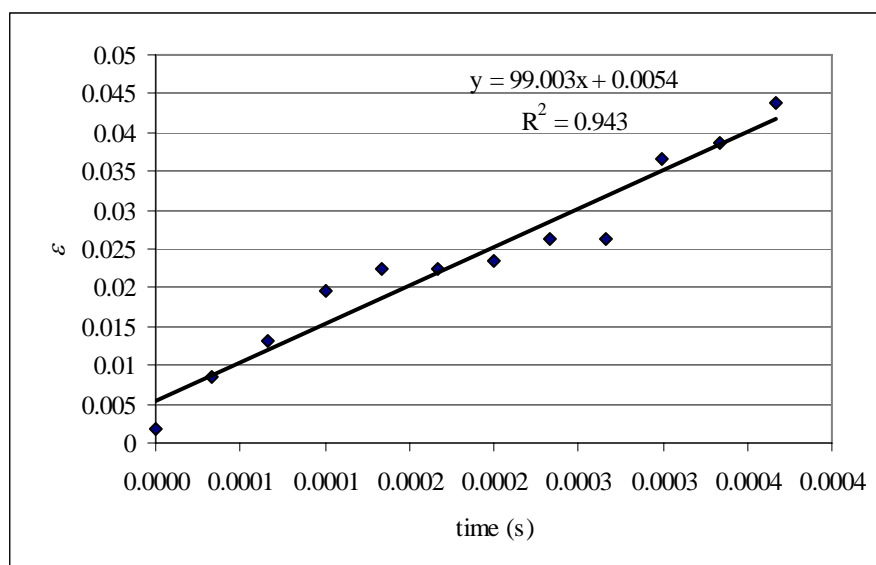
Fig. A.3 Example of strain-time data and application of linear regression

189

Appendix B: Figures and Tables

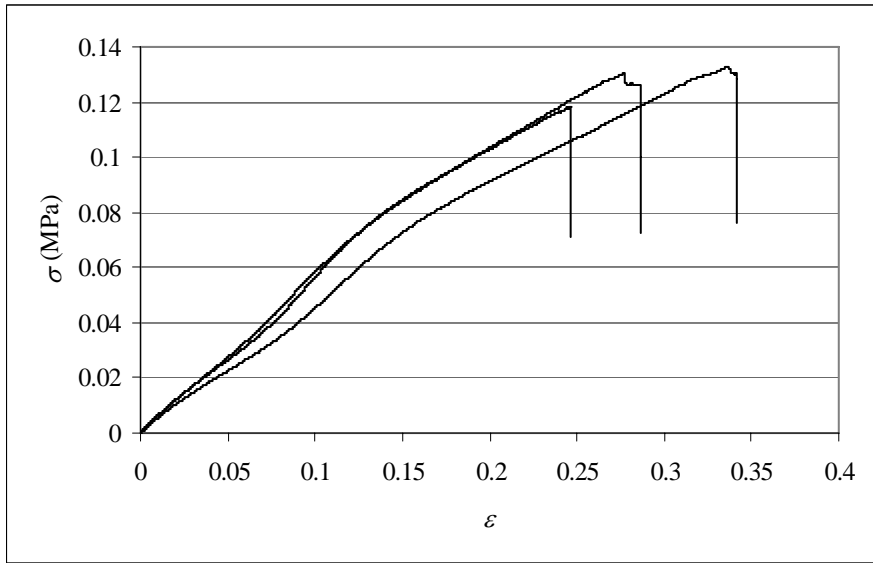Figs. B.1-B.15 show the results of quasi-static tensile tests on foams A, B and

C.
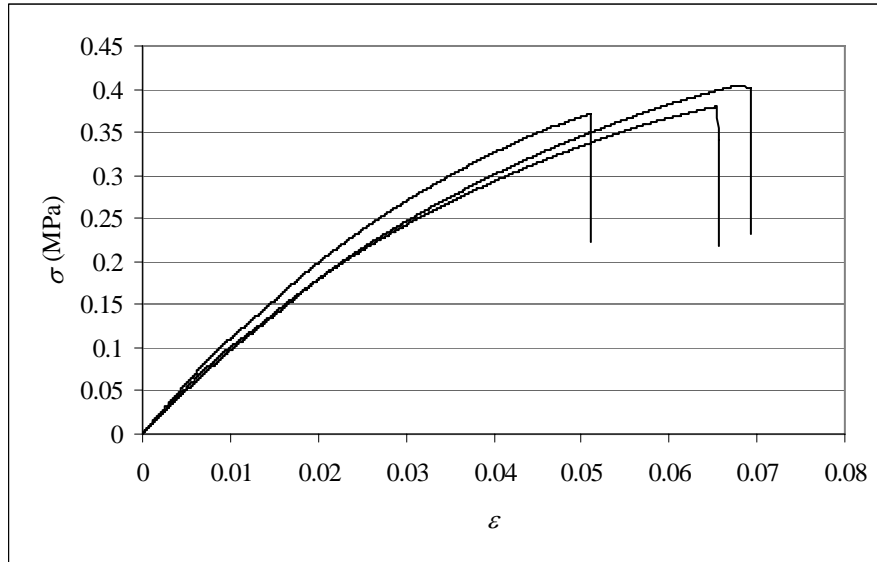
Fig. B.1 Stress-strain curves for loading in the rise direction (foam A
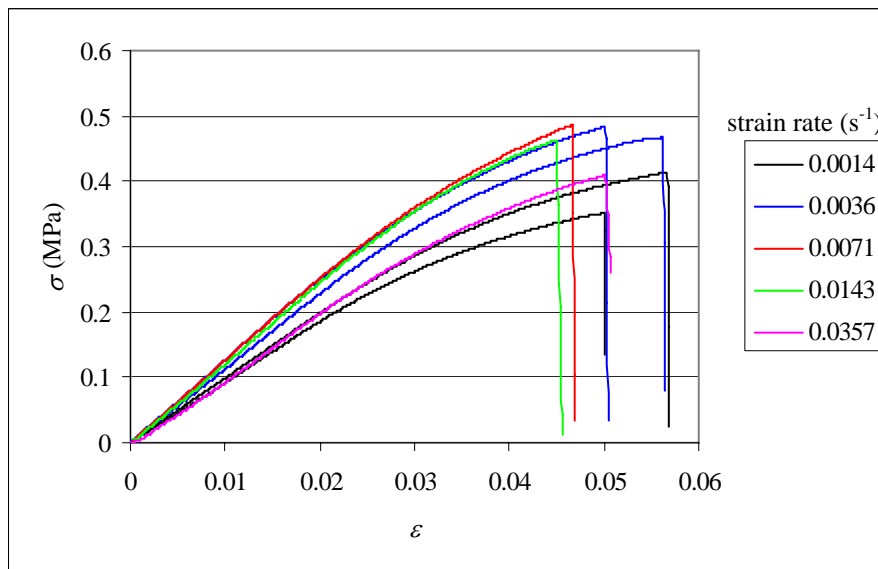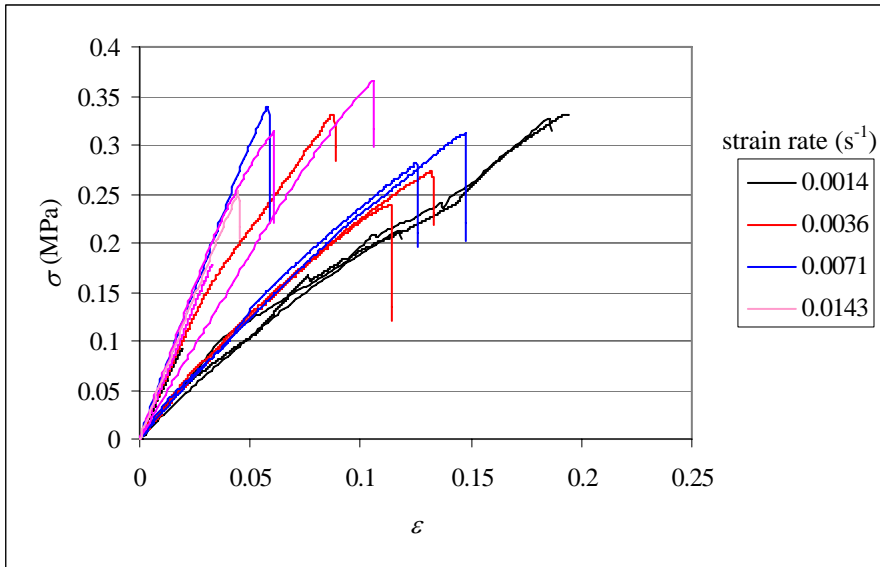$\rho = 23.3\,\text{kg}/\text{m}^3$; geometric anisotropy ratio = 2.5)
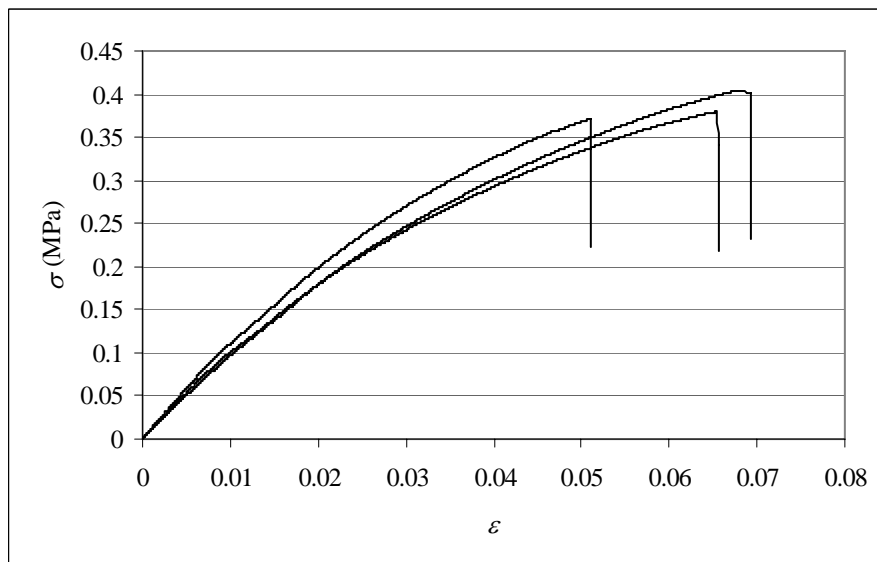
Fig. B.2 Stress-strain curves for loading 30° to the rise direction (foam A
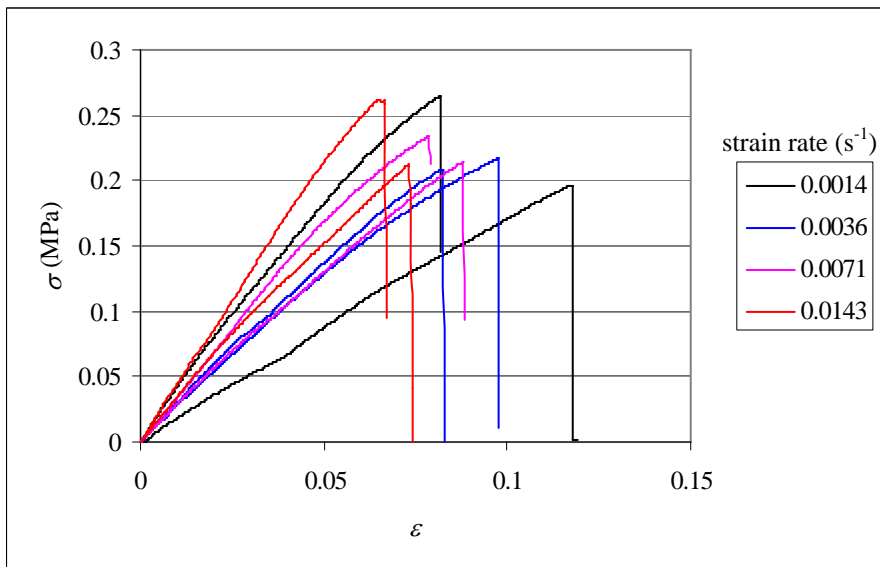$\rho = 23.3\,\text{kg}/\text{m}^3$; geometric anisotropy ratio = 2.5)
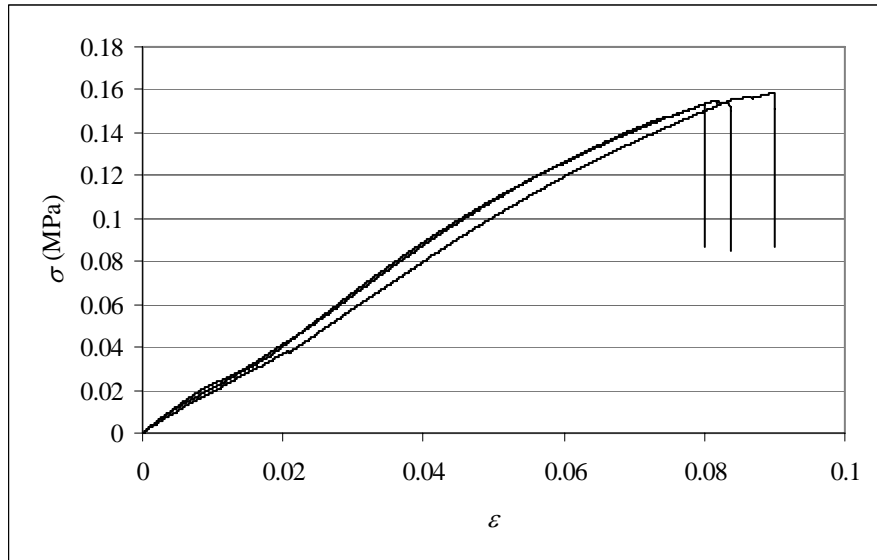
Fig. B.3 Stress-strain curves for loading 45° to the rise direction (foam A $\rho = 23.3 \text{kg}/\text{m}^3$; geometric anisotropy ratio = 2.5)
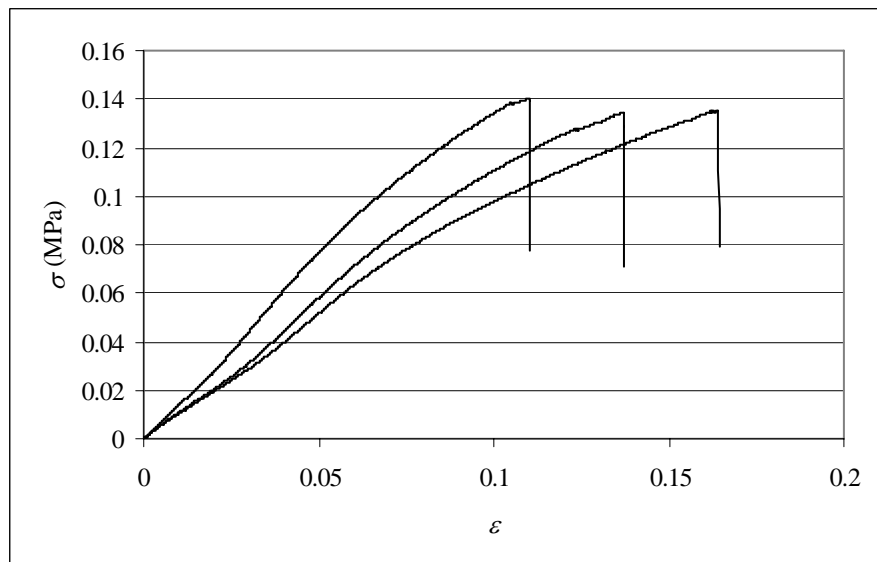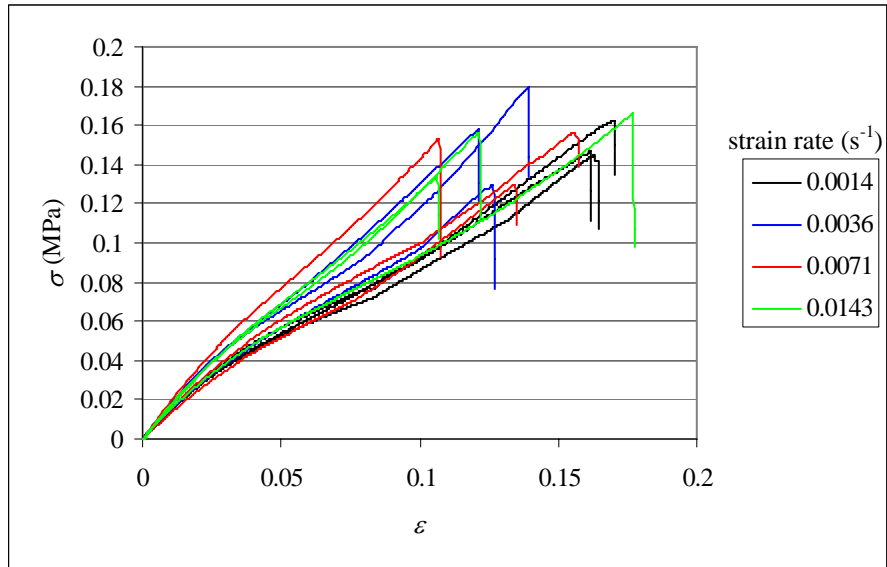

Fig. B.4 Stress-strain curves for loading 60° to the rise direction (foam A $\rho = 23.3 \text{kg}/\text{m}^3$; geometric anisotropy ratio = 2.5)

191

Fig. B.5 Stress-strain curves for loading in the transverse direction (foam A $\rho = 23.3\,\mathrm{kg/m^3}$; geometric anisotropy ratio = 2.5)

Fig. B.6 Stress-strain curves for loading in the rise direction (foam B $\rho = 29.5\,\mathrm{kg/m^3}$; geometric anisotropy ratio = 2)

Fig. B.7 Stress-strain curves for loading 30° to the rise direction (foam B $\rho = 29.5 \, \mathrm{kg/m^3}$; geometric anisotropy ratio = 2)

Fig. B.8 Stress-strain curves for loading 45° to the rise direction (foam B $\rho = 29.5 \, \mathrm{kg/m^3}$; geometric anisotropy ratio = 2)

Fig. B.9 Stress-strain curves for loading 60° to the rise direction (foam B $\rho = 29.5\,\mathrm{kg/m^3}$; geometric anisotropy ratio = 2)
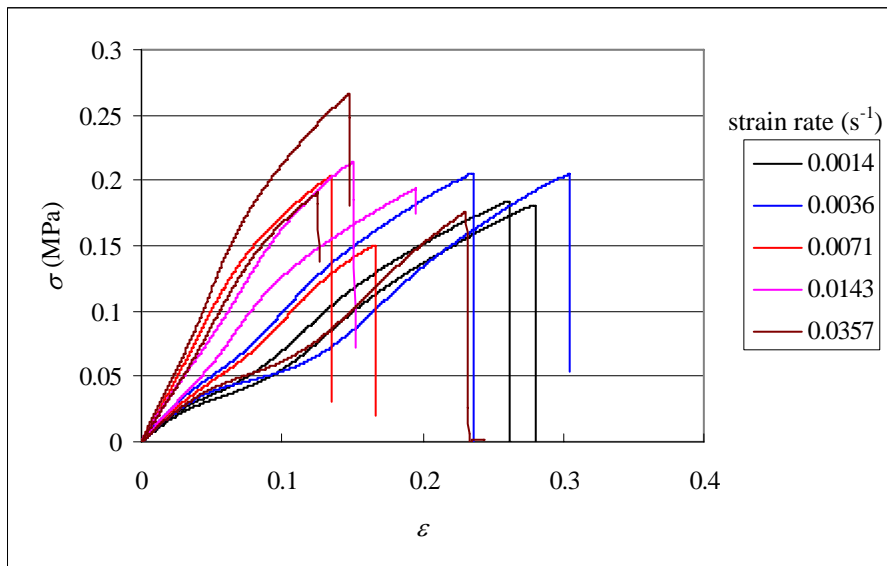

Fig. B.10 Stress-strain curves for loading in transverse direction (foam B $\rho = 29.5\,\mathrm{kg/m^3}$; geometric anisotropy ratio = 2)
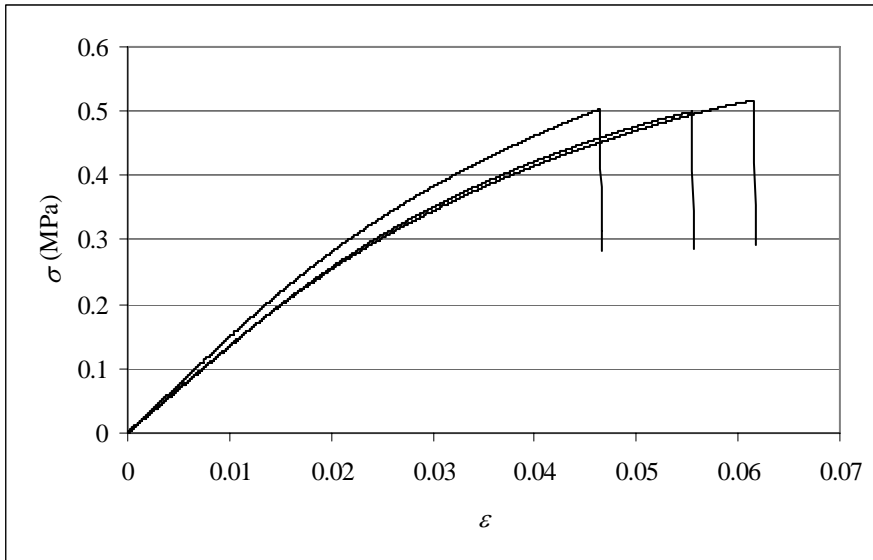
Fig. B.11 Stress-strain curves for loading in the rise direction (foam C
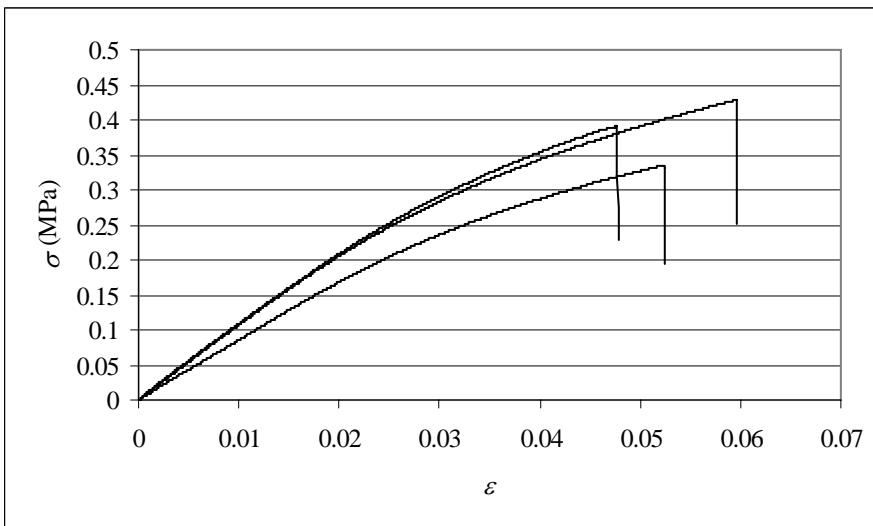$\rho = 35.2 \, \text{kg}/\text{m}^3$; geometric anisotropy ratio = 1.7)

Fig. B.12 Stress-strain curves for loading 30° to the rise direction (foam C
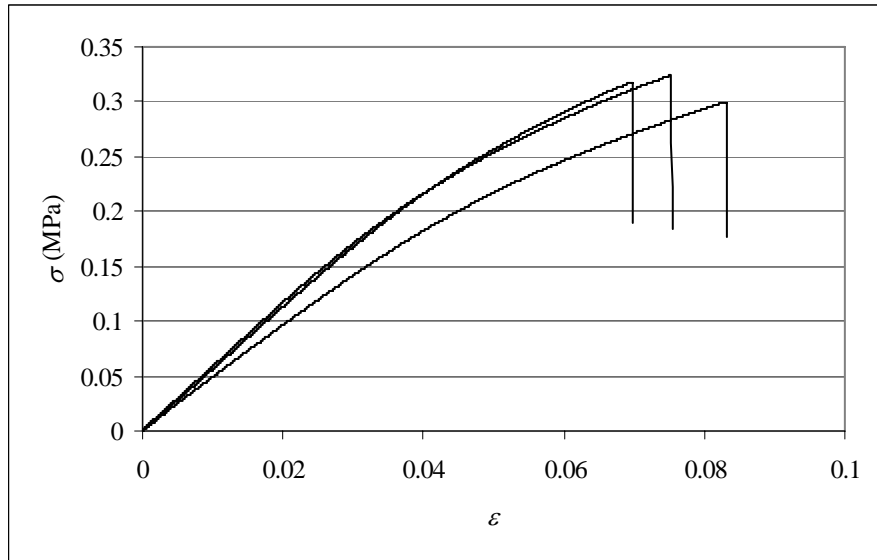$\rho = 35.2 \, \text{kg}/\text{m}^3$; geometric anisotropy ratio = 1.7)

Fig. B.13 Stress-strain curves for loading 45° to the rise direction (foam C $\rho = 35.2\,\mathrm{kg/m^3}$; geometric anisotropy ratio = 1.7)
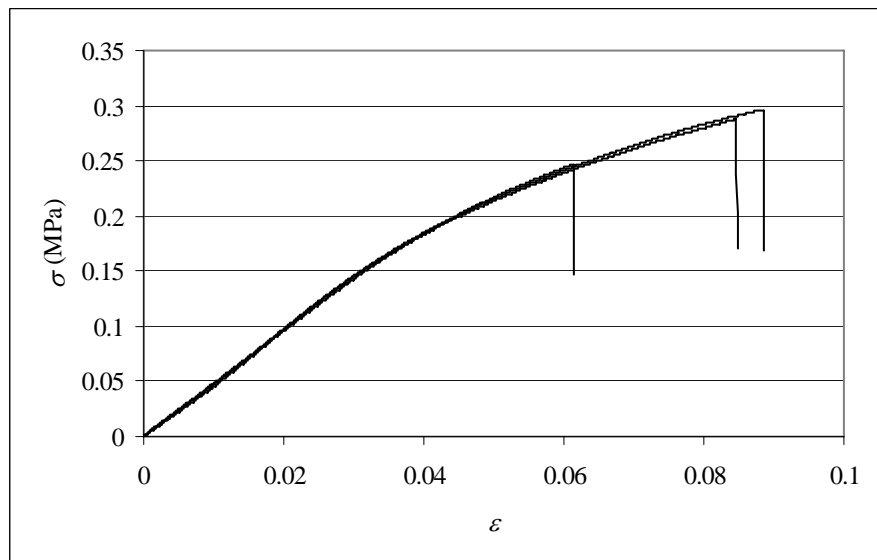

Fig. B.14 Stress-strain curves for loading 60° to the rise direction (foam C $\rho = 35.2\,\mathrm{kg/m^3}$; geometric anisotropy ratio = 1.7)
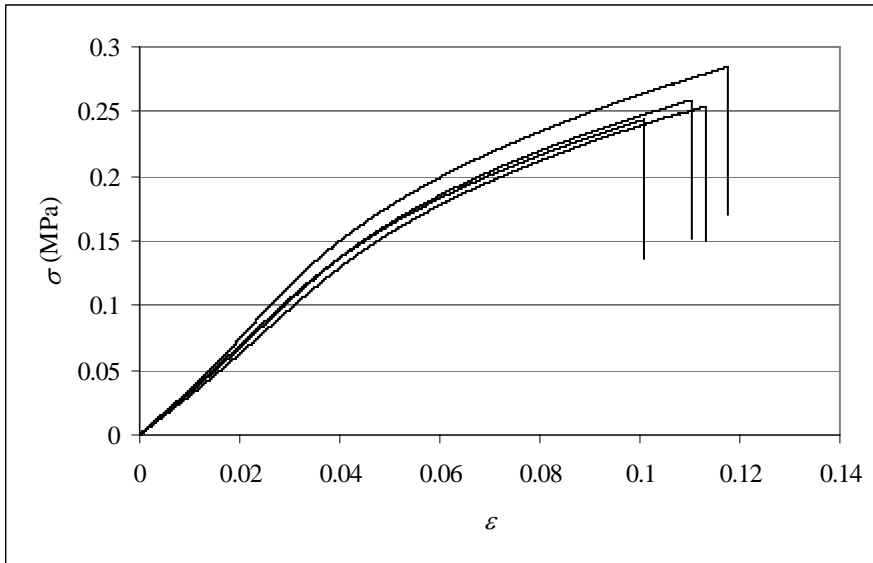
Fig. B.15 Stress-strain curves for loading in the transverse direction (foam C
$\rho = 35.2\,\mathrm{kg/m^3}$; geometric anisotropy ratio = 1.7)

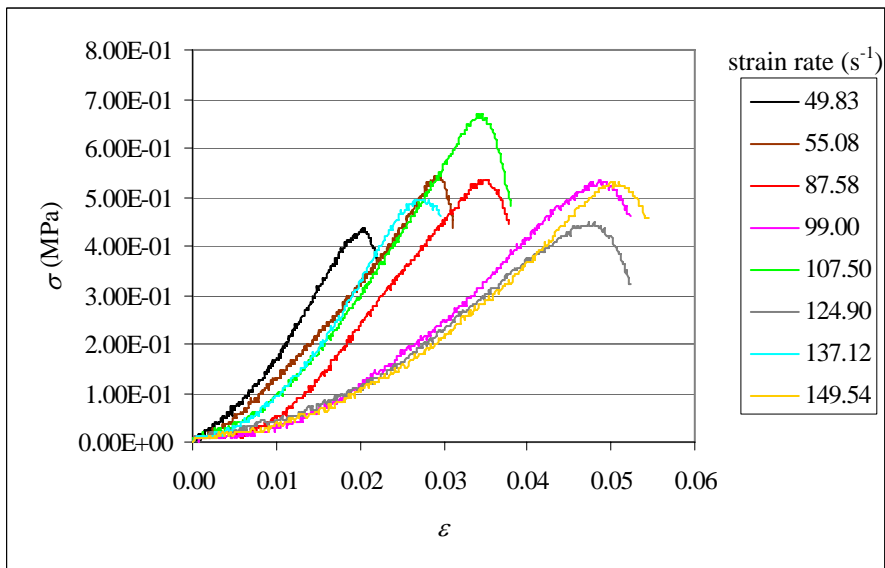Figs. B.16-B.18 show the stress-strain curves obtained from Split Hopkinson bar tests on foam B.

Fig. B.16 Stress-strain curves for loading in the rise direction (foam B
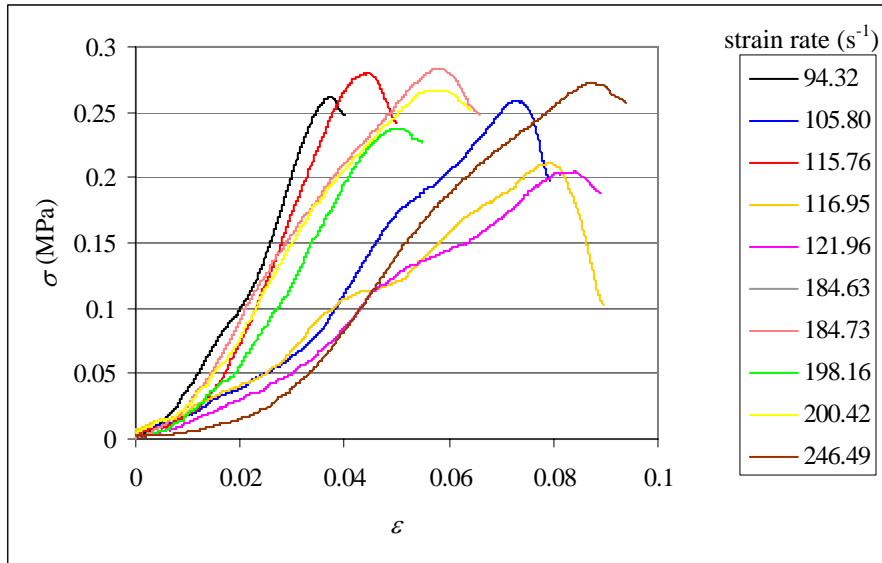$\rho = 29.5\,\mathrm{kg/m^3}$; geometric anisotropy ratio = 2)

Fig. B.17 Stress-strain curves for loading in the 45° direction (foam B $\rho = 29.5\,\mathrm{kg}/\mathrm{m}^3$; geometric anisotropy ratio = 2)
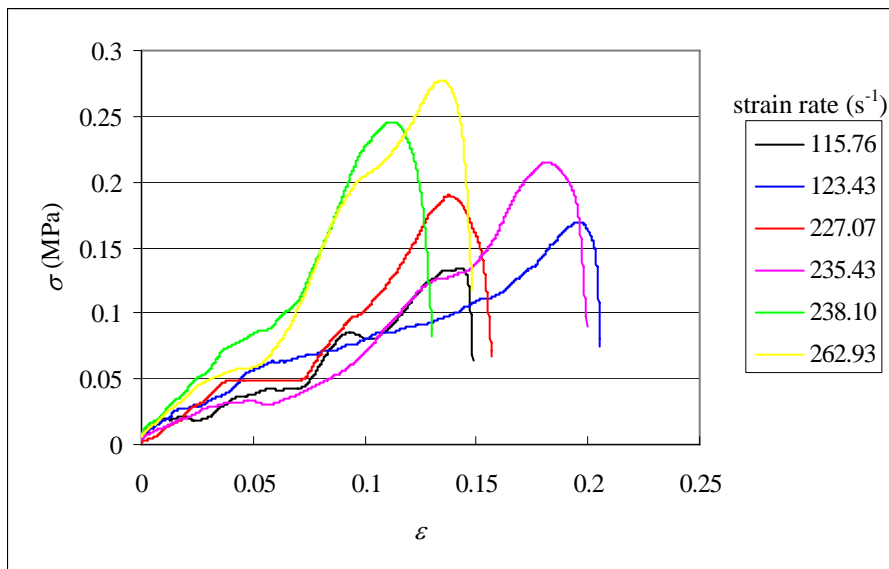

Fig. B.18 Stress-strain curves for loading in transverse direction (foam B $\rho = 29.5\,\mathrm{kg}/\mathrm{m}^3$; geometric anisotropy ratio = 2)

Figs. B.19 and B.21 show microscopic images of the cross-section of struts in foam A, B and C.

Fig. B.19 Cross-section of struts in rigid polyurethane foam A ($\rho = 23.3\,\mathrm{kg}/\mathrm{m}^3$; geometric anisotropy ratio = 2.5)
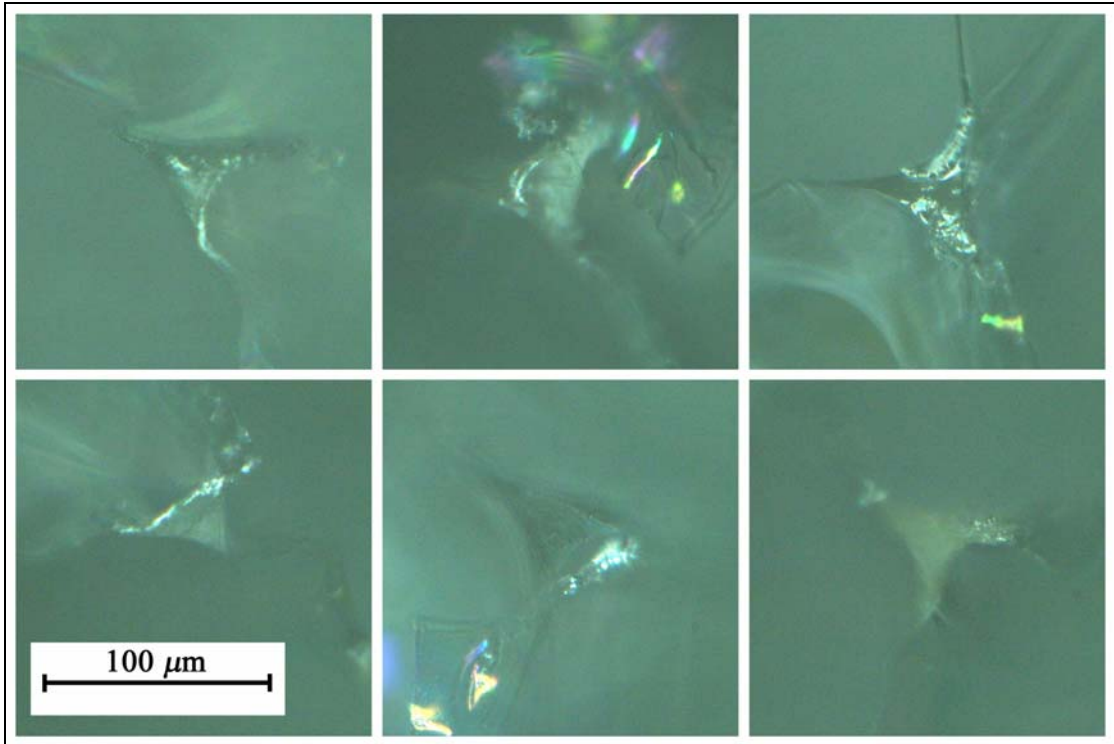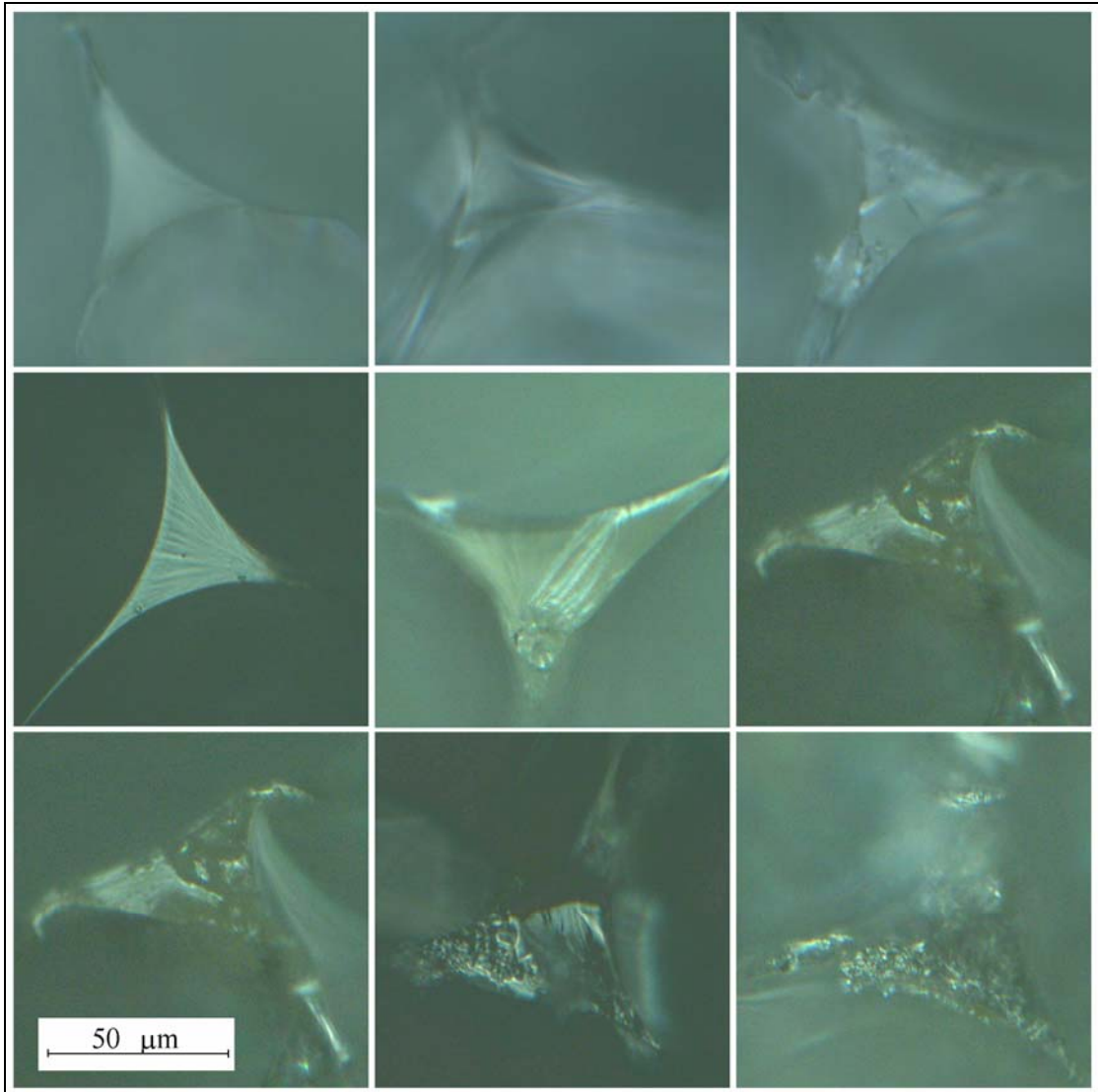
Fig. B.20 Cross-section of struts in rigid polyurethane foam B ($\rho = 29.5 \, \text{kg}/\text{m}^3$; geometric anisotropy ratio = 2)
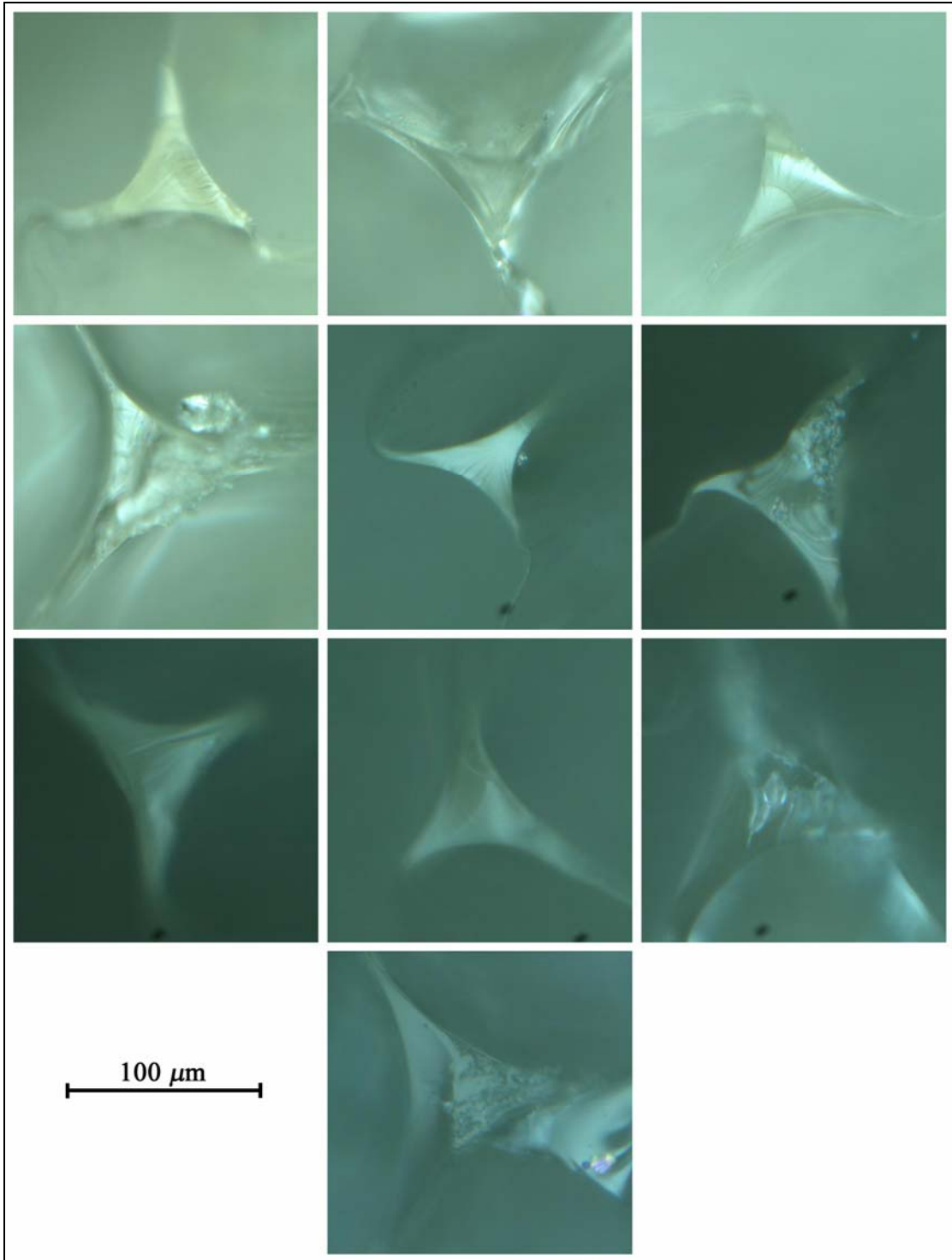
Fig. B.21 Cross-section of struts in rigid polyurethane foam C ($\rho = 35.2\,\mathrm{kg}/\mathrm{m}^3$; geometric anisotropy ratio = 1.7)

Table B.1 shows measurements of strut cross-section dimensions obtained from microscopic observation discussed in Section 3.5. Table B.2 shows measurements of the length of rigid segments in struts in foam B ($\rho = 29.5\,\mathrm{kg}/\mathrm{m}^3$; geometric anisotropy ratio = 2), obtained from the observations discussed in Section 3.6.2.

Table B.1 Strut dimensions

Foam A		Foam B		Foam C	
r	*R*	*r*	*R*	*r*	*R*
11.0	41.1	10.0	37.3	17.1	63.8
15.5	57.8	10.0	37.3	15.0	56.0
14.0	52.2	12.5	46.7	17.5	65.3
15.0	56.0	12.0	44.8	24.5	91.4
11.5	42.9	15.5	57.8	13.2	49.2
12.5	46.7	13.5	50.4	15.1	56.5
		17.0	63.4	13.9	51.9
		16.5	61.6	12.6	47.1
		17.0	63.4	16.9	63.1
				12.2	45.5
average					
13.3	49.4	13.8	51.4	15.8	59.0

Table B.2 Dimensions of rigid segments in struts in foam B ($\rho = 29.5\,\text{kg}/\text{m}^3$; geometric anisotropy ratio = 2)

Length of strut (μm)	Length of rigid segment (μm)	
659.3	60.4	44.0
648.4	60.4	44.0
461.5	60.4	44.0
362.6	44.0	60.4
379.1	54.9	44.0
538.5	54.9	49.5
527.5	49.5	49.5
302.2	60.4	44.0
379.1	49.5	44.0
368.1	44.0	44.0
423.1	49.5	49.5
439.6	54.9	38.5
329.7	44.0	44.0
390.1	49.5	54.9
274.7	44.0	44.0
373.6	44.0	44.0
395.6	49.5	38.5
456.0	54.9	38.5
560.4	49.5	49.5
average	45.6	